

Les Houches 2013: Physics at TeV Colliders Standard Model Working Group Report

Conveners

Higgs physics: SM issues

D. De Florian (Theory), M. Kado (ATLAS), A. Korytov (CMS),
S. Dittmaier (Electroweak Contact)

SM: Loops and Multilegs

N. Glover (Theory), J. Huston (ATLAS), G. Dissertori (CMS),
S. Dittmaier (Electroweak Contact)

Tools and Monte Carlos

F. Krauss (Theory), J. Butterworth (ATLAS), K. Hamilton (MC-NLO Contact),
G. Soyez (Jets Contact)

Abstract

This Report summarizes the proceedings of the 2013 Les Houches workshop on Physics at TeV Colliders. Session 1 dealt primarily with (1) the techniques for calculating standard model multi-leg NLO and NNLO QCD and NLO EW cross sections and (2) the comparison of those cross sections with LHC data from Run 1, and projections for future measurements in Run 2.

Acknowledgements

We would like to thank the organizers (G. Belanger, F. Boudjema, P. Gras, D. Guadagnoli, S. Gascon, J.P. Guillet, B. Herrmann, S. Kraml, G.H. de Monchenault, G. Moreau, E. Pilon, P. Slavich and D. Zerwas) and the Les Houches staff for the stimulating environment always present at Les Houches.

Authors

J. R. Andersen¹, S. Badger², L. Barzè³, J. Bellm⁴, F. U. Bernlochner⁵, A. Buckley⁶, J. Butterworth⁷, N. Chanon⁸, M. Chiesa⁹, A. Cooper-Sarkar¹⁰, L. Cieri¹¹, G. Cullen¹², H. van Deurzen¹³, G. Dissertori⁸, S. Dittmaier¹⁴, D. de Florian¹⁵, S. Forte¹⁶, R. Frederix³, B. Fuks^{3,17}, J. Gao¹⁸, M.V. Garzelli¹⁹, T. Gehrmann²⁰, E. Gerwick²¹, S. Gieseke²², D. Gillberg²³, E. W. N. Glover¹, N. Greiner¹³, K. Hamilton⁷, T. Hapola¹, H.B. Hartanto²⁴, G. Heinrich¹³, A. Huss¹⁴, J. Huston²⁵, B. Jäger²⁶, M. Kado²⁷, A. Kardos²⁸, U. Klein²⁹, F. Krauss¹, A. Kruse³⁰, L. Lönnblad³¹, G. Luisoni¹³, Daniel Maître¹, P. Mastrolia^{13,32}, O. Mattelaer³³, J. Mazzitelli¹⁵, E. Mirabella¹³, P. Monni³⁴, G. Montagna⁹, M. Moretti³⁵, P. Nadolsky¹⁸, P. Nason³, O. Nicrosini³⁶, C. Oleari²⁸, G. Ossola^{37,38}, S. Padhi³⁹, T. Peraro¹³, F. Piccinini³⁶, S. Plätzer⁴⁰, S. Prestel⁴⁰, J. Pumplin²⁵, K. Rabbertz²², Voica Radescu⁴⁰, L. Reina⁴¹, C. Reuschle⁴², J. Rojo³, M. Schönherr¹, J. M. Smillie⁴³, J.F. von Soden-Fraunhofen¹³, G. Soyez⁴⁴, R. Thorne⁷, F. Tramontano⁴⁵, Z. Trocsanyi¹⁹, D. Wackerroth⁴⁶, J. Winter¹³, C-P. Yuan²⁵, V. Yundin¹³, K. Zapp³

- ¹ Institute for Particle Physics Phenomenology, Department of Physics, University of Durham, Durham DH1 3LE, UK
- ² Niels Bohr Institute (NBI), University of Copenhagen, Blegdamsvej 17 DK-2100 Copenhagen, Denmark
- ³ PH Department, TH Unit, CERN, CH-1211, Geneva 23, Switzerland
- ⁴ Institute for Theoretical Physics, Karlsruhe Institute of Technology, D - 76128 Karlsruhe, Germany
- ⁵ University of Victoria, Victoria, British Columbia, Canada V8W 3P
- ⁶ School of Physics & Astronomy, University of Glasgow, Glasgow, UK
- ⁷ Department of Physics and Astronomy, University College London, Gower Street, London WC1E 6BT, UK
- ⁸ Institute for Particle Physics, ETH Zurich, 8093 Zurich, Switzerland
- ⁹ Dipartimento di Fisica, Università di Pavia and INFN, Sezione di Pavia, Via A. Bassi, 6, 27100 Pavia, Italy
- ¹⁰ Department of Physics, University of Oxford, Denys Wilkinson Building, Keble Road, Oxford OX1 3RH, UK
- ¹¹ Dipartimento di Fisica, Università di Roma La Sapienza and INFN, Sezione di Roma, I-00185 Rome, Italy
- ¹² DESY, Zeuthen, Platanenallee 6, D-15738 Zeuthen, Germany
- ¹³ Max-Planck-Institut für Physik, Werner-Heisenberg-Institut, Föhringer Ring 6, D-80805 München, Germany
- ¹⁴ Physikalisches Institut, Albert-Ludwigs-Universität Freiburg, D-79104 Freiburg, Germany
- ¹⁵ Departamento de Física, Facultad de Ciencias Exactas y Naturales, Universidad de Buenos Aires, Pabellon I, Ciudad Universitaria (1428), Capital Federal, Argentina
- ¹⁶ Dipartimento di Fisica, Università degli Studi di Milano and INFN, Sezione di Milano, Via Celoria 16, I-20133 Milan, Italy
- ¹⁷ Institut Pluridisciplinaire Hubert Curien, Department Recherches Subatomiques, Université de Strasbourg, CNRS-IN2P3, 23 rue du Loess, F-67037 Strasbourg, France
- ¹⁸ Southern Methodist University, Dept. of Physics, Dallas, TX 75275, USA
- ¹⁹ MTA-DE Particle Physics Research Group, University of Debrecen, H-4010 Debrecen P.O.Box 105, Hungary

- ²⁰ Institute for Theoretical Physics, University of Zurich, Winterthurerstrasse 190, CH-8057 Zurich, Switzerland
- ²¹ II. Physikalisches Institut, Universität Göttingen, Germany
- ²² Institut für Experimentelle Kernphysik, Karlsruher Institut für Technologie, D-76131 Karlsruhe, Germany
- ²³ CERN, CH-1211 Geneva 23, Switzerland
- ²⁴ Institut für Theoretische Teilchenphysik und Kosmologie, RWTH Aachen University, D-52056 Aachen, Germany
- ²⁵ Department of Physics and Astronomy, Michigan State University, East Lansing, MI 48824, USA
- ²⁶ PRISMA Cluster of Excellence and Institute of Physics, Johannes Gutenberg University, D-55099 Mainz, Germany
- ²⁷ Laboratoire de l'Accélérateur Linéaire, CNRS/IN2P3, F-91898 Orsay CEDEX, France
- ²⁸ Università di Milano-Bicocca and INFN, Sezione di Milano-Bicocca, Piazza della Scienza 3, 20126 Milan, Italy
- ²⁹ University of Liverpool, Dept. of Physics Oliver Lodge Lab, Oxford St. Liverpool L69 3BX, UK
- ³⁰ Univ. of Wisconsin, Dept. of Physics, High Energy Physics, 2506 Sterling Hall 1150 University Ave, Madison, WI 53706, USA
- ³¹ Theoretical High Energy Physics, Department of Theoretical Physics, Lund University, Sölvegatan 14A, SE-223 62 Lund, Sweden
- ³² Dipartimento di Fisica e Astronomia, Università di Padova, and INFN Sezione di Padova, Via Marzolo 8, I-35131 Padova, Italy
- ³³ Centre for Cosmology, Particle Physics and Phenomenology (CP3), Université Catholique de Louvain, B-1348 Louvain-la-Neuve, Belgium
- ³⁴ Rudolf Peierls Centre for Theoretical Physics, University of Oxford, 1 Keble Road, Oxford OX1 2NP, UK
- ³⁵ Dipartimento di Fisica e Scienze della Terra, Università di Ferrara, and INFN Sezione di Ferrara, Via Saragat 1, 44100 Ferrara, Italy
- ³⁶ INFN, Sezione di Pavia, Via A. Bassi 6, 27100 Pavia, Italy
- ³⁷ Physics Department, New York City College of Technology, The City University of New York, 300 Jay Street Brooklyn, NY 11201, USA
- ³⁸ The Graduate School and University Center, The City University of New York, 365 Fifth Avenue, New York, NY 10016, USA
- ³⁹ Department of Physics, University of California at San Diego, La Jolla, CA 92093, USA
- ⁴⁰ DESY, Notkestrasse 85, D-22607 Hamburg, Germany
- ⁴¹ Physics Department, Florida State University, Tallahassee, FL 32306-4350, USA
- ⁴² Institute for Theoretical Physics, Karlsruhe Institute of Technology, D - 76128 Karlsruhe, Germany
- ⁴³ The Higgs Centre for Theoretical Physics, University of Edinburgh, Mayfield Road, Edinburgh, EH9 3JZ
- ⁴⁴ IPhT, CEA Saclay, Orme des Merisiers, Bat 774, F-91191 Gif-sur-Yvette, cedex, France
- ⁴⁵ Dipartimento di Fisica, Università di Napoli Federico II, and INFN, Sezione di Napoli, Complesso di Monte Sant'Angelo, via Cintia I-80126 Napoli, Italy
- ⁴⁶ Department of Physics, SUNY at Buffalo, Buffalo, NY 14260-1500, USA

Contents

| | | |
|------------|---|-----------|
| 1 | Introduction ¹ | 1 |
| 2 | Dictionary for electroweak corrections ² | 11 |
| I | NLO automation and (N)NLO techniques | 26 |
| 1 | The first use case for BLHA2 extensions: NJET plus Herwig++/Matchbox ³ | 26 |
| 2 | GoSam plus Herwig++/Matchbox ⁴ | 31 |
| II | Parton distribution functions | 37 |
| 1 | PDF dependence of the Higgs production cross section in gluon fusion from HERA data ⁵ | 37 |
| 2 | Dataset sensitivity of the $gg \rightarrow H$ cross-section in the NNPDF analysis ⁶ | 56 |
| 3 | New access to PDF data via LHAPDF6 ⁷ | 64 |
| III | Phenomenological studies | 70 |
| 1 | Inclusive jet cross section at the LHC and the impact of weak radiative corrections ⁸ | 70 |
| 2 | NNLO QCD and NLO EW Drell Yan background predictions for new gauge boson searches ⁹ | 80 |
| 3 | Electroweak Sudakov corrections to $Z/\gamma +$ jets at the LHC ¹⁰ | 91 |
| 4 | Jet rates from recursion relations ¹¹ | 96 |
| 5 | Study of the average number of hard jets ¹² | 100 |
| 6 | Uncertainties in $pp \rightarrow h + 2$ jets production through gluon fusion ¹³ | 105 |
| 7 | Higgs boson plus di- and tri-jet production at NLO in QCD ¹⁴ | 117 |
| 8 | Jet-bin uncertainties estimate through jet efficiencies ¹⁵ | 126 |
| 9 | Higgs production in association with top quarks at the LHC: comparison of different approaches for NLO QCD simulations matched with parton shower ¹⁶ | 132 |
| 10 | Next-to-next-to-leading order corrections to Higgs boson pair production at the LHC ¹⁷ | 142 |
| 11 | Photon isolation studies ¹⁸ | 145 |

¹G. Dissertori, S. Dittmaier, N. Glover, J. Huston, A. Korytov, F. Krauss

²S. Dittmaier

³S. Badger, S. Plätzer, V. Yundin

⁴J. Bellm, S. Gieseke, N. Greiner, G. Heinrich, S. Plätzer, C. Reuschle and J.F. von Soden-Fraunhofen

⁵A. Cooper-Sarkar, S. Forte, J. Gao, J. Huston, P. Nadolsky, J. Pumplin, V. Radescu, J. Rojo, R. Thorne and C.-P. Yuan

⁶S. Forte and J. Rojo

⁷A. Buckley

⁸S. Dittmaier, A. Huss and K. Rabbertz

⁹U. Klein

¹⁰M. Chiesa, L. Barzè, G. Montagna, M. Moretti, O. Nicrosini, F. Piccinini, F. Tramontano

¹¹E. Gerwick, S. Plätzer

¹²J.R. Andersen, D. Maître

¹³J.R. Andersen, F.U. Bernlochner, D. Gillberg, K. Hamilton, T. Hapola, J. Huston, A. Kruse, L. Lönnblad, P. Nason, S. Prestel, M. Schönherr, J.M. Smillie, K. Zapp

¹⁴G. Cullen, H. van Deurzen, N. Greiner, J. Huston, G. Luisoni, P. Mastrolia, E. Mirabella, G. Ossola, T. Peraro, F. Tramontano, J. Winter and V. Yundin

¹⁵P. F. Monni (Work in collaboration with A. Banfi, G.P. Salam, and G. Zanderighi)

¹⁶M.V. Garzelli, H.B. Hartanto, B. Jäger, A. Kardos, L. Reina, Z. Trócsányi, D. Wackerroth

¹⁷D. de Florian and J. Mazzitelli

¹⁸L. Cieri and D. de Florian

| | | |
|--|---|------------|
| 12 | Diphotons and jets at NLO ¹⁹ | 152 |
| IV MC tuning and output formats | | 158 |
| 1 | Extensions to the Les Houches Event Format ²⁰ | 158 |
| 2 | Proposed updates for HepMC event record ²¹ | 162 |
| 3 | Improvements in the Rivet MC analysis toolkit ²² | 164 |

¹⁹N. Chanon, T. Gehrmann, N. Greiner, G. Heinrich

²⁰A. Buckley, J. Butterworth, R. Frederix, B. Fuks, F. Krauss, L. Lonnblad, O. Mattelaer, P. Nason, C. Oleari, S. Padhi, S. Plätzer, S. Prestel

²¹A. Buckley, J. Butterworth, F. Krauss, L. Lonnblad, S. Plätzer, S. Prestel

²²A. Buckley

1 Introduction¹

The Les Houches Workshop in 2011 was the first for which data from the LHC was available. In 2013, we had high statistics data for the first time, at both 7 TeV and 8 TeV, and, most importantly, the discovery of the Higgs boson to contemplate. The LHC data for Standard Model (SM) processes encompassed a very wide kinematic range, accessing transverse momenta and masses on the order of a TeV or greater. For precision understanding at such scales, higher-order electroweak (EW) corrections need to be taken into account in addition to higher-order QCD corrections. There was perhaps more emphasis on EW physics and corrections in the 2013 Les Houches than in previous workshops. As for the 2011 workshop, there was no evidence of beyond-SM (BSM) processes; if such events are present in the data, they are hiding well, indicating even more the need for precision SM calculations to indicate the presence of any deviations.

The SM data taken at 7 TeV and 8 TeV, with its small statistical errors and decreasing (with time) systematic errors, is useful not only to test the theoretical predictions, but to serve as input for the global parton distribution function (PDF) fits. Currently, the PDF fits are dominated by data taken at HERA and at fixed target deep-inelastic experiments, especially in the parton x range from around 0.01 to 0.1. This kinematic range is especially important for Higgs production, and in particular for the process $gg \rightarrow \text{Higgs}$. The PDF($+\alpha_s$) uncertainty is the largest theoretical uncertainty for this important process. As more (and better) data is taken at the LHC, there is the possibility for PDF uncertainties to be reduced, especially in the TeV mass range. Until now, EW and QED corrections to PDFs have been mostly ignored, but again, given the mass scales being considered (and the importance of processes such as $\gamma\gamma \rightarrow WW$ at those mass scales), such considerations will become increasingly important.

The rapid rate of progress beyond leading-order (LO) calculations has continued on the theoretical side, in terms of semi-automated calculations of multi-leg next-to-leading order (NLO) QCD processes, advances in next-to-next-to-leading order (NNLO) QCD calculations, and advances in NLO EW, and mixed EW+QCD, calculations. In the last two years, we have seen the NLO calculation of complex multi-leg processes such as for the production of 5 jets [1], $W + 5$ jets [2], and Higgs + 3 jets [3] as well as the further development of general purpose NLO codes such as GoSaM [4], HELAC-NLO [5], MadLoop [6], OpenLoops [7], and Recola [8]. At NNLO, there have been new results for diphoton [9] and $Z\gamma$ production [10]. The complete NNLO $t\bar{t}$ cross section calculation is available [11–14], along with the partial (gluons only) calculation for dijet production [15, 16] and for Higgs + 1 jet production [17], with the likelihood of further progress within the near future. The sticking point for processes with coloured final-state particles has been the infrared subtraction. Now several subtraction schemes have been developed [18–20] and the techniques have been applied to the processes listed above. Based on these experiences, further progress should come more quickly. In some sense, part of the frontier is now NNNLO, where some approximate $gg \rightarrow \text{Higgs}$ calculations have been performed [21, 22], and a full calculation might be possible within the next few years [23–25].

Naively, NLO EW corrections are roughly as important as NNLO QCD corrections. However, NLO $\mathcal{O}(\alpha)$ EW corrections can be magnified by the presence of large logarithms and/or kinematical effects, such as when the hard scale(s) in the process are large compared to the W -boson mass. When all invariants for the 4-vectors of pairs of particles become large compared to the W mass, this is referred to as the Sudakov regime, or ‘Sudakov zone’. There is a need in principle for mixed QCD+EW calculations of order $\alpha_s\alpha$. Sadly, however, in most cases, the multi-scale NNLO calculations required at this order are currently out of reach, and we have to rely on approximations as to whether for example QCD and EW corrections are additive or multiplicative.

¹G. Dissertori, S. Dittmaier, N. Glover, J. Huston, A. Korytov, F. Krauss

The Les Houches NLO Wish List, constructed in 2005, and added to in 2007 and 2009, was formally dis-continued in 2011, due to the progress in NLO automation evident at that time. Instead in 2011, an NNLO Wish List was started, with a few essential processes given high priority. These included the processes listed above, in addition to vector-boson + jet production and double-vector-boson production. In 2013, we have gone beyond the 2011 list, and have constructed a *High Precision Wish List* that has to be considered as extremely ambitious, and that will no doubt still exist several Les Houches Workshops from now. The calculation of the processes on this list will allow us to fully exploit the data to come at the LHC at 14 TeV, and hopefully to understand the SM to such an extent that any evidence of new physics encountered will be unambiguous.

As stressed in earlier Les Houches Workshops, it is important not only for advanced QCD+EW calculations to be completed, but for the calculations and their results to be available to experimenters. This has been made easier in recent years with the use of the ROOT output format and with Rivet routines. It is now standard technology as well to allow for ‘on-the-fly’ re-weighting of matrix element results for new PDFs, new scales and even new jet algorithms, and this should be incorporated, where possible, in public programs.

In addition to progress on fixed-order calculations, there has also been progress on resummation calculations, in particular for cross sections with jet vetoes, or jet binning, such as used for Higgs+jets production through gg fusion, that has led to the restoration of the accuracy present in the related inclusive cross section predictions.

Another area of rapid theoretical progress has been in the combination of the fixed-order results with a parton shower, leading to particle-level predictions with improved perturbative accuracy. The principles of *matching* a parton shower with NLO calculations for a particular final state are well established and have been partially or fully automated [6, 26–29] to exploit the automated NLO codes. Alternatively, the description of multi-jet final states with parton showers can be improved by *merging* matrix element calculations of varying multiplicity with a parton shower. This approach has recently been refined and extended, leading to algorithms [30, 31] which can combine multiple NLO calculations of varying multiplicity into a single, inclusive simulation. The MINLO method [32] for choosing the factorisation and renormalisation scales accounts for Sudakov suppression effects and enables NLO calculations to extrapolate to zero jet transverse momentum, thus offering the opportunity to match to NNLO calculations for a limited class of processes and observables [33, 34]. Other ideas have been floated for matching NNLO parton-level calculations with a parton shower [35] and one hopes that in the next few years the precision of event generators for collider physics can be improved to NNLO accuracy.

For the first time, the Les Houches Workshop coincided with a Snowmass Workshop in the US. There was a great deal of synergy between the two workshops with regards to QCD and EW calculations and measurements. This was especially true as the focus of the two workshops were different, with Les Houches being concerned with physics of the present-day, or near-future, and Snowmass being concerned with the physics possible in the future with higher-energy machines. It was very informative, for example to extrapolate theoretical predictions and corrections from 8–14 TeV to the higher energies being considered at Snowmass.

The structure of the proceedings is as follows. Later in the introduction, we discuss the new Les Houches Wish List. Then follows in Section 2 a ‘dictionary’ for EW corrections. Chapter I has contributions related to NLO automation and NNLO techniques. In Chapter II are contributions related to PDF studies, including the gg → Higgs study mentioned above, and in Chapter III are contributions related to phenomenological studies. Finally, in Chapter IV are contributions related to Monte Carlo tuning and output formats.

1.1 The Les Houches High Precision Wish List

Below we discuss the revised High Precision Wish List. As mentioned above, the list is ambitious, but not out of the question for the advances that might be expected in the next 5 years, or over the span of Run 2 at the LHC. Historically, reducing the theoretical uncertainty by a factor of two typically takes $\mathcal{O}(10\text{--}15)$ years and one might expect that over the remaining lifetime of the LHC, a further factor of two improvement is feasible.

For convenience, we have divided the wish list into three parts;

1. Final states involving the Higgs Boson,
2. Final states involving Jets or Heavy Quarks,
3. Final states involving Electroweak Gauge Bosons.

In each case, Tables 1.1, 1.1.2, and 1.1.3 show the final state, what is currently known, and the desired accuracy. Throughout, $V = Z$ or W^\pm . We systematically use the shorthand $d\sigma$ to indicate the fully differential cross section while the accuracy is specified after the ampersand according to the following notation;

- LO $\equiv \mathcal{O}(1)$,
- NLO QCD $\equiv \mathcal{O}(\alpha_s)$,
- NNLO QCD $\equiv \mathcal{O}(\alpha_s^2)$,
- NLO EW $\equiv \mathcal{O}(\alpha)$,
- NNNLO QCD $\equiv \mathcal{O}(\alpha_s^3)$,
- NNLO QCD+EW $\equiv \mathcal{O}(\alpha_s\alpha)$.

This counting of orders \mathcal{O} is done relative to LO QCD, which is $\mathcal{O}(1)$ by definition, independent of the absolute power of α_s in its cross section. Note that it is simplified in two respects: Firstly, it suppresses the possibility (as in $t\bar{t}$ or dijet production) that there is no uniform scaling in α_s and α at tree or at the lowest loop level. In this case EW corrections involve orders $\mathcal{O}(\alpha/\alpha_s)$ relative to LO as well. Secondly, the counting can depend on the observable, as e.g. in inclusive Higgs-boson production, where the NLO correction to the total cross section comprises only a LO prediction for the transverse-momentum distribution for the Higgs boson.

Parametrically, $\alpha \sim \alpha_s^2$ so that NNLO QCD and NLO EW effects are naively of a similar size (although there may well be regions of phase space where one dominates over the other). In this notation, $d\sigma @ \text{NNLO QCD} + \text{NLO EW}$ would indicate a single code computing the fully differential cross section including both $\mathcal{O}(\alpha_s^2)$ and $\mathcal{O}(\alpha)$ effects.

The following lists of LHC processes are very comprehensive, rendering it impossible to quote all relevant higher-order calculations to each process here. We, therefore, mostly restrict the explicitly given theoretical references to the relevant publications of the last 2–3 years, while references to previous work can be found in the recent papers. Whenever possible, we point to specific reviews as well. We did also not spell out the obvious desire to have all NLO predictions matched to QCD parton showers, as obtained for instance in the MC@NLO [36] or Powheg [37] approaches. Similarly, the experimental references are not intended to be exhaustive either, but are cited to support the current or expected experimental precisions.

Note also that we did not compile a separate wish list for decay sub-processes, but indicate the inclusion of particle decays whenever relevant in the context of production processes. The description of Higgs-boson decays and their accuracy have been discussed in Refs. [38–40] in great detail. At the level of some percent the approach of describing full processes in the factorized approach (production cross section) \times (decay branching ratio) is limited. Instead the full resonance process, with possible interference effects with background, should be considered.

| Process | State of the Art | Desired |
|---------------------|---|---|
| H | $d\sigma$ @ NNLO QCD (expansion in $1/m_t$) full m_t/m_b dependence @ NLO QCD and @ NLO EW NNLO+PS, in the $m_t \rightarrow \infty$ limit | $d\sigma$ @ NNNLO QCD (infinite- m_t limit) full m_t/m_b dependence @ NNLO QCD and @ NNLO QCD+EW NNLO+PS with finite top quark mass effects |
| H + j | $d\sigma$ @ NNLO QCD (g only) and finite-quark-mass effects @ LO QCD and LO EW | $d\sigma$ @ NNLO QCD (infinite- m_t limit) and finite-quark-mass effects @ NLO QCD and NLO EW |
| H + 2j | $\sigma_{\text{tot}}(\text{VBF})$ @ NNLO(DIS) QCD $d\sigma(\text{VBF})$ @ NLO EW $d\sigma(\text{gg})$ @ NLO QCD (infinite- m_t limit) and finite-quark-mass effects @ LO QCD | $d\sigma(\text{VBF})$ @ NNLO QCD + NLO EW $d\sigma(\text{gg})$ @ NNLO QCD (infinite- m_t limit) and finite-quark-mass effects @ NLO QCD and NLO EW |
| H + V | $d\sigma$ @ NNLO QCD $d\sigma$ @ NLO EW $\sigma_{\text{tot}}(\text{gg})$ @ NLO QCD (infinite- m_t limit) | with $H \rightarrow b\bar{b}$ @ same accuracy $d\sigma(\text{gg})$ @ NLO QCD with full m_t/m_b dependence |
| tH and $\bar{t}H$ | $d\sigma(\text{stable top})$ @ LO QCD | $d\sigma(\text{top decays})$ @ NLO QCD and NLO EW |
| ttH | $d\sigma(\text{stable tops})$ @ NLO QCD | $d\sigma(\text{top decays})$ @ NLO QCD and NLO EW |
| gg \rightarrow HH | $d\sigma$ @ NLO QCD (leading m_t dependence) $d\sigma$ @ NNLO QCD (infinite- m_t limit) | $d\sigma$ @ NLO QCD with full m_t/m_b dependence |

Table 1: Wishlist part 1 – Higgs ($V = W, Z$)

In the context of Higgs-boson observables, this issue is discussed in some detail in Refs. [39, 40] (see also references therein); general considerations about this issue can also be found in Section 2.8.

1.1.1 Final states involving the Higgs Boson

Now that the Higgs boson has been discovered, the next key step is the detailed measurement of its properties and couplings. Already much has been accomplished during the 2011–2012 running at the LHC, but differential measurements, for example, are still in their infancy, due to the lack of statistics. Given its importance, a great deal of theoretical attention has already been given to calculations of the Higgs-boson production sub-processes for each of the production modes [38–40] including a concise summary of the predictions available for each channel.² Nevertheless, as indicated in Table 1.1, more precise calculations are needed.

H: The current situation is well summarized in Refs. [38–40]: we know the production cross section for the gg fusion subprocess to NNLO QCD in the infinite- m_t limit and including finite-quark-mass effects at NLO QCD and NLO EW. The current experimental uncertainties associated with probing the $gg \rightarrow H$ process cross section are of the order of 20–40%, depending on the amount of model-dependent assumptions. Theoretically, the uncertainty is of the order of 15%, with the uncertainties due to PDF+ α_s and higher-order corrections, as estimated through scale variations, both being on the order of 7–8%. The accuracy of the experimental cross section is statistically limited, with the total error expected to decrease to the order of 10% with 300 fb^{-1} in Run 2, running at an energy close

²For more references, see also Ref. [41].

to 14 TeV [42]. Thus, the desire is to improve upon our knowledge of the higher-order corrections to gg fusion, in parallel with improvements to the PDF+ α_s uncertainty. NNLO QCD corrections to gg fusion in the infinite- m_t limit are already underway [23–25] and could reduce the residual scale dependence to below 5%. Ultimately, one may need to know the NNLO QCD and mixed NNLO QCD+EW contributions retaining finite top-quark mass effects. Currently, experimental physicists are using parton-shower programs which include the cross sections for Higgs production to NLO. An NNLO+PS simulation for Higgs boson production, in the infinite top mass limit, has already been presented in [33, 34] (which could be extended to include finite top mass effects).

- H + j: The first attempts at differential Higgs+jets measurements were made in the diphoton channel with the 8 TeV data in ATLAS [43]. At 14 TeV, with 300 fb^{-1} , there will be a very rich program of differential jet measurements, with on the order of 3000 events per experiment (in the diphoton channel) with jets above the top mass scale, thus probing inside the top-quark loop in the gg production process. Currently, the NNLO QCD Higgs+jet cross section for the gluons-only process in the infinite- m_t limit is known [17], and the full cross section is expected later this year. The (LO) one-loop QCD and EW contributions retaining the dependence on the masses of the particles circulating in the loop are also known, but as for the inclusive case, the finite-mass contributions to the Higgs+jet cross section at NLO QCD and NLO EW may also be needed.
- H + 2j: The Higgs+2jet channel is crucial in order to understand Higgs couplings, and in particular to understand the coupling to vector bosons through the vector-boson fusion (VBF) channel. VBF production itself is known to NNLO QCD in the double-DIS approximation together with QCD and EW effects at NLO, while the gg fusion channel is available at NLO QCD in the infinite- m_t limit [44, 45] and to LO QCD retaining finite-mass effects. With 300 fb^{-1} , there is the possibility of measuring the HWW coupling strength to the order of 5% which could require both the VBF and gluon fusion Higgs+2jet cross sections to NNLO QCD and finite-mass effects to NLO QCD and NLO EW accuracy [42].
- H + V: Two important, but poorly known, couplings of the Higgs boson are to the top and bottom quarks. Currently the couplings are known to the order of 50% or more for the bottom quark and 100% for the top quark. Higgs $\rightarrow b\bar{b}$ is primarily measured through the Higgs + vector-boson final state. Currently, the production cross section is known at NNLO QCD and at NLO EW, recently generalized to differential cross section including leptonic Z-boson and W/Z-boson decays at NNLO QCD [46] and NLO EW order [47], respectively. The gg $\rightarrow \text{HZ}$ channel, which is known [48] at NLO QCD in the infinite- m_t limit for the total cross section, contributes about 14% to the cross section at the LHC for 14 TeV and significantly increases the scale uncertainty. The scale uncertainty is about 1%(4%) for HW(HZ) production, the PDF uncertainty is about 3.5%. The $b\bar{b}$ decay is currently linked to the HV production process to NLO QCD in the narrow-width approximation (NWA) [49], but it is desirable to combine Higgs production and decay processes to the same order, i.e., NNLO in QCD and NLO in EW for the Higgs-strahlung process. The NNLO QCD corrections to the H $\rightarrow b\bar{b}$ decay, in fact, are known fully differentially [50]. With 300 fb^{-1} at a 14 TeV LHC, the signal strength for the Higgs $\rightarrow b\bar{b}$ final state should be measured to the 10–15% level, shrinking to 5% for 3000 fb^{-1} [42].
- tH, $\bar{t}H$, $t\bar{t}H$: In the presence of CP violation, the Higgs–top coupling may have both scalar and pseudoscalar components, κ_t and $\tilde{\kappa}_t$, which are weakly bounded by the present experimental constraints. These couplings can be probed using measurements of H production in association with $t\bar{t}$, single t, or single \bar{t} [51]. With $300(3000) \text{ fb}^{-1}$, the top-quark Yukawa coupling should be measured to approximately 15% (5–10%) [42]. The $t(\bar{t})[t\bar{t}]$ Higgs cross section is currently known at LO (LO) [NLO] QCD, respectively, and with stable top

| Process | State of the Art | Desired |
|-------------------|---|--|
| $t\bar{t}$ | $\sigma_{\text{tot}}(\text{stable tops}) @ \text{NNLO QCD}$ $d\sigma(\text{top decays}) @ \text{NLO QCD}$ $d\sigma(\text{stable tops}) @ \text{NLO EW}$ | $d\sigma(\text{top decays}) @ \text{NNLO QCD} + \text{NLO EW}$ |
| $t\bar{t} + j(j)$ | $d\sigma(\text{NWA top decays}) @ \text{NLO QCD}$ | $d\sigma(\text{NWA top decays}) @ \text{NNLO QCD} + \text{NLO EW}$ |
| $t\bar{t} + Z$ | $d\sigma(\text{stable tops}) @ \text{NLO QCD}$ | $d\sigma(\text{top decays}) @ \text{NLO QCD} + \text{NLO EW}$ |
| single-top | $d\sigma(\text{NWA top decays}) @ \text{NLO QCD}$ | $d\sigma(\text{NWA top decays}) @ \text{NNLO QCD} + \text{NLO EW}$ |
| dijet | $d\sigma @ \text{NNLO QCD (g only)}$ $d\sigma @ \text{NLO EW (weak)}$ | $d\sigma @ \text{NNLO QCD} + \text{NLO EW}$ |
| 3j | $d\sigma @ \text{NLO QCD}$ | $d\sigma @ \text{NNLO QCD} + \text{NLO EW}$ |
| $\gamma + j$ | $d\sigma @ \text{NLO QCD}$ $d\sigma @ \text{NLO EW}$ | $d\sigma @ \text{NNLO QCD} + \text{NLO EW}$ |

Table 2: Wishlist part 2 – Jets and Heavy Quarks

quarks. In all three cases, it is necessary to know the cross section (with top decays) at NLO QCD, possibly including NLO EW effects.

HH: The self-coupling of the Higgs boson arises from the EW symmetry breaking of the Higgs potential and measuring the triple-Higgs-boson coupling then directly probes the EW potential. Double-Higgs production via gluon fusion, used to measure the triple-Higgs coupling, is known at LO QCD with full top mass dependence, including the leading finite-mass effects at NLO QCD [52,53] and at NNLO QCD in the infinite- m_t limit [54]. It may be necessary to compute the full top mass dependence at NLO QCD. The production cross section for double-Higgs production is small, and the backgrounds non-negligible. Nonetheless, it is hoped that a 50% precision on the self-coupling parameter may be possible with 3000 fb^{-1} at 14 TeV [42]. Other double-Higgs production processes, such as via gluon fusion or associated production with W/Z bosons, are mostly known to NLO QCD (excluding final states with top quarks) and were recently discussed in Refs. [55,56]. Owing to the strong suppression of their cross sections, their observability at the LHC is extremely challenging.

1.1.2 Final states involving Jets or Heavy Quarks

$t\bar{t}$: Precision top physics is important for a number of reasons. It is by far the most massive quark, and it is possible that new physics might have a strong coupling to top quarks; hence the need for precision predictions. For example, a forward–backward asymmetry has been observed at the Tevatron larger than predicted by NLO QCD+EW predictions. The larger than expected asymmetry may be the result of new physics, due to missing higher-order corrections, or caused by unknown problems in the experimental analysis. At the LHC, the dominant production mechanism for top pair production is through gg fusion, for basically all kinematic regions. Thus, a comparison of precise top-quark measurements with similar predictions can greatly help the determination of the gluon PDF, especially at high x where the current uncertainty is large. The present experimental uncertainty on the total top-quark pair cross section is on the order of 5% for the dilepton final state, and should improve for the lepton + jets final state to be of the same order [57,58]. Note that a sizeable portion of that uncertainty is due to the luminosity

uncertainty, emphasizing the utility of using the top pair cross section as a handle on precision normalizations. Currently, the total cross section is known in NNLO QCD [11–14] and to NLO EW for stable tops (see, e.g., Ref. [59] and older references therein), but only to NLO QCD with decays of on-shell [60] or off-shell [61–64] top quarks. The theoretical uncertainty for predictions for the total cross section is 4%, while differential predictions have a larger uncertainty (currently at the NLO level). It is expected that fully differential NNLO QCD predictions will be known in the near future, perhaps even this year. This is very important, especially for a better understanding of $t\bar{t}$ asymmetry measurements at the Tevatron and LHC. Note that a non-negligible contribution to the experimental uncertainty for the top-quark cross section is the extrapolation from the fiducial phase space to the full phase space. To fully exploit the physics potential, we need to be able to compare experimental fiducial cross sections to theoretical fiducial cross sections, requiring a knowledge of top-quark pair production (with decays) including NNLO QCD and NLO EW effects.

- $t\bar{t} + j(j)$: Due to the dominant gg sub-process production mechanism, and the large phase space for gluon emission at the LHC, most $t\bar{t}$ final states also contain one or more jets. Extending previous work on stable top quarks [65–67], the NLO QCD corrections to $t\bar{t} + \text{jet}$ production (supplemented by parton-shower effects in Ref. [68]) were calculated with on-shell top decays including spin correlation effects in Ref. [69]. In the future, a knowledge of $t\bar{t} + \text{jet}$ production (with decays) including NNLO QCD and NLO EW effects may be necessary. For $t\bar{t} + 2\text{jet}$ production NLO QCD corrections were first worked out for on-shell top quarks [70, 71] and were recently generalized to include spin-correlated top-quark decays in LO as well as a consistent merge with a QCD parton shower [72]. At least the inclusion of QCD corrections to the top-quark decays is desirable also in this case.
- $t\bar{t} + W/Z$: Top pair production in association with a vector boson is an important process for comparing with $t\bar{t}\text{Higgs}$ production, but also for measuring the coupling of the top quark with the W or Z. The NLO QCD corrections in the NWA with on-shell top decays including spin correlation effects are known [73–76] (generalizing earlier work on $t\bar{t}Z$ with stable top quarks [77]). It may be necessary to study the effect of hard radiation in the top decay. Evidence for the production of a $t\bar{t} + Z$ final can be found in Ref. [78].
- single-top: Measurements of single-top production are important for precision top physics, and specifically the measurement of V_{tb} . The current experimental cross section precision is on the order of 10%, and a precision of $>5\%$ during Run 2 is likely [79]. The single-top processes tW and tZ are more problematic. Both ATLAS [80] and CMS [81] have results (but less than 5σ significance) from Run 1 (7 TeV) for the first channel, while the measurement of the second channel may be possible with the 8 TeV data, but with some difficulty. The tW cross section has been measured with an approximately 40% uncertainty, dominated by statistical errors, and by the incomplete knowledge of the backgrounds. These uncertainties should decrease significantly with the 8 TeV data, and certainly will with the 14 TeV data.
Currently the single-top cross section in the various channels (including decay) is known to NLO in QCD [82–84] and including dominant soft-gluon and threshold effects at NNLO QCD [85, 86], with a theoretical uncertainty of the order of less than 10% (tW) and less than 5% (tZ). A theoretical uncertainty much less than the experimental precision is desired, leading to the need for a calculation of the single-top cross section to NNLO in QCD and including NLO EW effects.
- dijet: Dijet production at the LHC probes the smallest distance scales measurable, and thus is an obvious place to search for the impact of new physics. The cross section has been known to NLO QCD for over 20 years, and considerable effort to extend the calculation to

NNLO QCD has been made and the partial (gluons only) calculation is available [15, 16] with the expectation of further progress in the near future. The cross section is also known at NLO EW (weak, non-photon corrections only) [87], with the weak corrections being potentially very important at high transverse momentum. The current state of the art for global PDF fitting is NNLO QCD, with the processes currently included in the fits all known at NNLO QCD, except for inclusive jet production. Thus, a complete calculation incorporating both NNLO QCD and NLO EW effects is vital. Currently, the experimental uncertainty for the inclusive jet cross section is between 5% and 10% (in the jet transverse momentum range roughly from 200 GeV to 1 TeV), necessitating a theoretical uncertainty below that [88–90].

- 3j: The 3-jet to 2-jet ratio is a useful process to measure the running of the strong coupling constant over a wide dynamic range, in a way that removes much of the sensitivity to the gluon distribution. Because this measurement is the ratio of two related cross sections, many of the experimental systematic errors cancel. For example, the jet energy scale uncertainty for the ratio can be reduced to less than or equal to 1% [91]. The measurements are currently statistically limited for jet transverse momenta below the TeV range, but this will not be the case for the high luminosity running at 14 TeV. The largest uncertainties are those from the residual scale dependence at NLO QCD [92, 93], typically of the order 5% at high p_T . For this reason, it is desirable to know the cross section for 3-jet production to NNLO QCD and NLO EW, as for dijet production.
- $\gamma + j$: Photon + jet production is another process that will be extremely useful for the determination of the gluon distribution, especially at high parton momentum fraction x . Due to the relatively clean measurement of the photon 4-vector, an experimental precision better than with dijet production is possible. To put the two processes on an equal theoretical basis, the calculation of photon + jet to NNLO QCD + NLO EW is desirable.

1.1.3 Final states involving EW Gauge Bosons

- V: Vector-boson production is one of the key benchmark processes at hadron colliders. Experimentally, the cross sections can be measured with great precision (on the order of 1–2%, excluding luminosity uncertainties [94, 95]), while the current best theoretical calculations at NNLO QCD and NLO EW have small uncertainties (see, e.g., Ref. [96] and references therein). The resulting comparisons of data to theory thus serve both as precision tests of QCD and sensitive probes of PDFs. For example, measurements of W and Z boson rapidity distributions have indicated that the strange quark distribution may be larger than presented in current PDFs [97]. To take full advantage of the experimental precision, it is necessary to know the cross section to NNNLO QCD and NNLO QCD+EW, and to implement such a cross section in a NNLO+PS format.
- V + j(j): Vector boson + 1,2 jets are useful both for PDF determination (for example, the Z+jet cross section for the gluon distribution and the W+charm cross section for the strange quark PDF) as well as a well-known system in which to study the systematics of multiple jet production, with an accessible wide kinematic range (useful for example to understand the parallel dynamics of Higgs+jet(s) systems). Currently, the V+jet and V+2jet cross sections are known to NLO QCD. The NLO EW corrections are known for V+jet, including V decays and off-shell effects [98–100]. For Z+2jet production, the NLO EW corrections are known for on-shell Z bosons [8] and are in progress for the off-shell case [101]. The resulting differential uncertainties can reach 10–20% for high jet momenta, exceeding the experimental uncertainties [102]. It is desirable to know both types of cross sections at NNLO QCD + NLO EW.

| Process | State of the Art | Desired |
|---------------------|--|---|
| V | $d\sigma(\text{lept. V decay}) @ \text{NNLO QCD}$ $d\sigma(\text{lept. V decay}) @ \text{NLO EW}$ | $d\sigma(\text{lept. V decay}) @ \text{NNNLO QCD}$ and $@ \text{NNLO QCD+EW}$ NNLO+PS |
| V + j(j) | $d\sigma(\text{lept. V decay}) @ \text{NLO QCD}$ $d\sigma(\text{lept. V decay}) @ \text{NLO EW}$ | $d\sigma(\text{lept. V decay})$ $@ \text{NNLO QCD} + \text{NLO EW}$ |
| VV' | $d\sigma(\text{V decays}) @ \text{NLO QCD}$ $d\sigma(\text{on-shell V decays}) @ \text{NLO EW}$ | $d\sigma(\text{decaying off-shell V})$ $@ \text{NNLO QCD} + \text{NLO EW}$ |
| gg \rightarrow VV | $d\sigma(\text{V decays}) @ \text{LO QCD}$ | $d\sigma(\text{V decays}) @ \text{NLO QCD}$ |
| V γ | $d\sigma(\text{V decay}) @ \text{NLO QCD}$ $d\sigma(\text{PA, V decay}) @ \text{NLO EW}$ | $d\sigma(\text{V decay})$ $@ \text{NNLO QCD} + \text{NLO EW}$ |
| Vbb | $d\sigma(\text{lept. V decay}) @ \text{NLO QCD}$ massive b | $d\sigma(\text{lept. V decay}) @ \text{NNLO QCD}$ + NLO EW, massless b |
| VV' γ | $d\sigma(\text{V decays}) @ \text{NLO QCD}$ | $d\sigma(\text{V decays})$ $@ \text{NLO QCD} + \text{NLO EW}$ |
| VV'V'' | $d\sigma(\text{V decays}) @ \text{NLO QCD}$ | $d\sigma(\text{V decays})$ $@ \text{NLO QCD} + \text{NLO EW}$ |
| VV' + j | $d\sigma(\text{V decays}) @ \text{NLO QCD}$ | $d\sigma(\text{V decays})$ $@ \text{NLO QCD} + \text{NLO EW}$ |
| VV' + jj | $d\sigma(\text{V decays}) @ \text{NLO QCD}$ | $d\sigma(\text{V decays})$ $@ \text{NLO QCD} + \text{NLO EW}$ |
| $\gamma\gamma$ | $d\sigma @ \text{NNLO QCD} + \text{NLO EW}$ | q_T resummation at NNLL matched to NNLO |

Table 3: Wishlist part 3 – Electroweak Gauge Bosons (V = W, Z)

VV': With precision measurements of double-vector-boson production (VV'), one has a handle on the determination of triple gauge couplings, and a possible window onto new physics. Currently, the cross sections are known to NLO QCD (with V decays) and to NLO EW (with on-shell or at least resonant V's). WZ cross sections currently have a (non-luminosity) experimental uncertainty on the order of 10% or less, dominated by the statistical error [103, 104]. The current theoretical uncertainty is on the order of 6%. Both the experimental statistical and systematic errors will improve with more data, necessitating the need for a calculation of VV' to NNLO QCD + NLO EW (with V decays). Recently the well-known NLO QCD corrections have been complemented by the NLO EW corrections, first for stable W and Z bosons [105–107], and in the WW case also including corrections to leptonic W-boson decays [108]. Moreover, the EW corrections to on-shell VV' production have been implemented in the Herwig Monte Carlo generator in an approximative way [109].

A thorough knowledge of the VV production cross section is needed, because of measurements of triple gauge couplings and since that final state forms a background for Higgs measurements in those channels. The non-luminosity errors for the VV final state are of the order of 10% or less, with the theoretical uncertainties approximately half that [103, 104, 110–113].

gg \rightarrow VV: An important piece of the VV cross section is that resulting from a gg initial state. Formally, the gg production sub-process is suppressed by a factor of α_s^2 with respect to the dominant $q\bar{q}$ sub-process, but still contributes 5–10% to the cross section for typical event-selection cuts due to the large gluon flux at the LHC. As background to Higgs-boson studies, it can even be enhanced to the level of some 10% (see, e.g., discussions in Refs. [38–40]

and references therein). Currently, this subprocess is known (with lepton decays) at LO QCD. It is desirable to know the cross section to NLO. An approximative approach has been suggested recently in Ref. [114].

- $V\gamma$: $V\gamma$ measurements serve for precision tests of the EW sector and also as a probe of new physics appearing for example in anomalous triple-gauge-boson couplings or in production of new vector-meson resonances decaying into $V\gamma$. Experimental uncertainties are currently of the order of 10% and the theoretical errors are on the order of 5–10% [115,116]. Currently, $W\gamma$ production is known (with decays) at NLO QCD, $Z\gamma$ production even at NNLO QCD [10]. The NLO EW corrections are known in the pole approximation (resonant V bosons with decays) in either case. It is desirable to fully know the cross sections to NNLO QCD + NLO EW.
- $Vb\bar{b}$: Associated Higgs-boson production (VH) with the Higgs boson decaying into a $b\bar{b}$ final state is a key process to measure the coupling of the Higgs boson into b-quarks. There is a significant background to this final state from $Vb\bar{b}$ production. The state of the art for calculating $Vb\bar{b}$ production is at NLO QCD (including b-quark mass effects). Currently, both the experimental and theoretical systematic errors are at the order of 20%. The experimental errors will improve with more data. Thus, it is crucial to improve the theoretical accuracy by extending the QCD calculation to NNLO (for massless b quarks). This includes a proper understanding of uncertainties in the approaches based on four or five active quark flavours.
- $VV'V''$: Cross sections for triple-gauge-boson production are currently known to NLO QCD, but only the NLO EW corrections to WWZ are known in the approximation of stable W and Z bosons [117]. Triple-gauge-boson production processes serve as channels for the determination of quartic gauge boson couplings and will allow for a better understanding of EW symmetry breaking. Currently, all of these final states are very statistically limited (no measurements have been published by ATLAS or CMS for example although analyses are currently underway for the 8 TeV data), but precision measurements will be possible in Run 2. Thus, it is desired for the calculation of these final states to NLO QCD + NLO EW.
- $VV' + j(j)$: The reasoning above applies as well to the $VV' + j(j)$ final states, whose production cross sections are currently known to NLO QCD. $VV' + j$ production is useful as a background to Higgs-boson production and for BSM searches, while $VV' + jj$ production contains the EW vector-boson scattering sub-process that is particularly sensitive to EW quartic gauge-boson couplings and to details of EW symmetry breaking. EW corrections to these process classes are yet unknown, although they are certainly as important as QCD corrections in the vector-boson scattering channels.
- $\gamma\gamma$ Diphoton production is a very clean channel in which to carry out precision tests of perturbative QCD, as well as one of the primary decay modes used first for the discovery of the Higgs bosons and now for detailed measurements of the same. Although sideband subtraction is a very powerful tool in which to separate resonant Higgs boson production from the non-resonant diphoton background, it is still important to gain as much understanding of the QCD mechanisms for diphoton production as possible. The diphoton cross section has been recently calculated at NNLO [9] and the NLO EW corrections are also known [106]. Detailed measurements of the diphoton final state system have been carried out [118,119], with a considerable improvement in agreement between data and theory resulting from the calculation at NNLO. The next theoretical improvement needed is a q_T resummation at NNLL matched to the NNLO calculation. If Drell-Yan and Higgs production are known in fully differential form at NNNLO, then it should be possible to extend those calculations to include all colorless final states (including $\gamma\gamma$) at NNNLO.

2 Dictionary for electroweak corrections³

In the coming years, the LHC explores particle phenomena at the TeV scale at its full centre-of-mass energy $\sqrt{s} = 13\text{--}14\text{TeV}$ with an increasingly higher luminosity, so that plenty of particle processes can be investigated at the accuracy level of several percent. This perspective, and already several measurements at lower energies in the previous LHC run, are calling for theoretical predictions at the level of few percent, i.e. electroweak (EW) radiative corrections have to be taken into account in predictions beyond the level of crude approximations. Since QCD radiative corrections are substantial in predictions for hadronic collisions, their structure and general features are much better known in the experimental community than their EW counterparts, which are smaller in general.

The following survey of EW higher-order issues is meant as orientation guide for non-experts in view of EW radiative corrections. Particular attention is paid to those EW effects that can enhance NLO EW corrections (expected to be of the small size α/π) to a size that can compete with or even exceed the size of QCD corrections in specific situations (e.g. final-state radiation, EW corrections at high energies). Moreover, some subtle aspects in the calculation of EW corrections are discussed that are crucial for consistent predictions (e.g. photon-jet separation, treatment of unstable particles).

2.1 Input-parameter scheme – choice of α

A convenient choice for the input parameters of the SM is: the electromagnetic coupling $\alpha = e^2/(4\pi)$, the strong coupling constant $\alpha_s = g_s^2/(4\pi)$, the weak gauge-boson masses M_W and M_Z , the Higgs-boson mass M_H , the fermion masses m_f , and the CKM matrix V .

The masses can all be defined as *pole masses*, defined by the locations of the particle poles in the respective propagators, but for the quarks it is often useful to switch to a running mass at some appropriate scale. Properly defined observables and their predictions should be insensitive to the perturbatively problematic light-quark masses, as discussed below in more detail. Recall that the Yukawa couplings do not represent free parameters, but are fixed by the fermion masses and the other EW input parameters. Disturbing the relation between Yukawa couplings and fermion masses, in general, violates EW gauge invariance and can lead to inconsistent and wrong predictions, especially in the calculation of EW corrections.

The definition of the CKM matrix in the presence of EW corrections, in general, is a non-trivial task. However, apart from applications in flavour physics, for high-energy scattering the approximations of taking all quarks other than bottom and top massless and ignoring mixing with the third generation are appropriate. In this approximation, the CKM matrix can only become relevant in charged-current quark–antiquark annihilation channels, such as Drell–Yan-like W-boson production, and leads to global factors $|V_{ij}|^2$ to partonic channels with $q_i\bar{q}_j$ or $q_j\bar{q}_i$ annihilation. Note that this statement holds at the level of NLO EW corrections as well, because of the mass degeneracy in the first two quark generations where the mixing takes place.

For the boson masses M_W , M_Z , and M_H , real on-shell masses are usually employed. Details about different schemes are discussed in Sect. 2.8 in the context of the description of instability effects. Here, we only emphasize that the weak mixing angle θ_W is not an independent input parameter. The most common choice in EW physics follows the on-shell prescription which defines $c_w \equiv \cos\theta_W \equiv M_W/M_Z$ and $s_w = \sqrt{1 - c_w^2}$ via the on-shell W/Z-boson masses. Taking s_w as independent parameter in addition to M_W and M_Z , e.g. by setting it to some ad hoc value or to the sine of the effective weak mixing angle measured at the Z pole, in general breaks gauge invariance, destroys gauge cancellations, and can lead to totally wrong results.

For the electromagnetic coupling α basically the choice is between three different values:

³S. Dittmaier

the fine-structure constant $\alpha(0) \approx 1/137$ (“ $\alpha(0)$ -scheme”), the effective value $\alpha(M_Z) \approx 1/129$ (“ $\alpha(M_Z)$ -scheme”), where $\alpha(0)$ is evolved via renormalization-group equations from zero-momentum transfer to the Z pole, and an effective value derived from the Fermi constant G_F leading to $\alpha_{G_F} = \sqrt{2}G_F M_W^2(1 - M_W^2/M_Z^2)/\pi \approx 1/132$, defining the so-called “ G_F -scheme”. The various choices for α differ by 2–6% and represent an important part of the so-called *input-parameter scheme*. Which scheme is the most appropriate in practice, depends on the nature of the process under consideration. Whatever scheme will be used, it is crucial that a common coupling factor α^n is used in complete gauge-invariant subsets of diagrams, otherwise important consistency relations (compensation of divergences, unitarity cancellations, etc.) will be destroyed. Note that this does not necessarily mean that there is only one value of α , but that all α -factors are global factors to gauge-invariant pieces of amplitudes.

In the following we describe which input-parameter scheme is appropriate for a contribution to a cross section (or squared matrix element) whose LO contribution is proportional to a fixed order $\alpha_s^m \alpha^n$, i.e. NLO EW contributions scale like $\alpha_s^m \alpha^{n+1}$. Corrections to LO contributions scaling with different powers m or n belong to disjoint gauge-invariant contributions, which can, thus, be treated independently. The standard QED definition of α employs an on-shell renormalization condition in the Thomson limit (photon momentum transfer $Q = 0$), leading to the renormalized value $\alpha = \alpha(0)$ of the $\alpha(0)$ -scheme. Our notation and conventions used below for field-theoretical quantities and renormalization constants follow Ref. [120]. The “best” scheme is the one that absorbs most of the universal corrections resulting from EW renormalization into the corresponding lowest-order prediction, thereby leading to smaller corrections. The most prominent EW renormalization effect is the the running of α , i.e. the question whether an EW coupling naturally takes place at low ($Q^2 = 0$) or high ($|Q^2| \gtrsim M_W^2$) momentum transfer Q^2 . Let us first consider a process without external photons in the initial or final state. In the $\alpha(0)$ -scheme with the on-shell charge renormalization, each of the n EW couplings leads to a relative correction $2\delta Z_e$. The charge renormalization constant δZ_e contains mass-singular terms like $\alpha \ln m_f$ from each light fermion f which remain uncanceled in the EW corrections. These terms are contained in the quantity

$$\Delta\alpha(M_Z) = \Pi_{f \neq t}^{\gamma\gamma}(0) - \text{Re}\{\Pi_{f \neq t}^{\gamma\gamma}(M_Z^2)\} \approx \frac{\alpha(0)}{3\pi} \sum_{f \neq t} N_f^c Q_f^2 \left[\ln\left(\frac{M_Z^2}{m_f^2}\right) - \frac{5}{3} \right], \quad (1)$$

with $\Pi_{f \neq t}^{\gamma\gamma}$ denoting the photonic vacuum polarization induced by all fermions f (with charge Q_f) other than the top quark (see also Ref. [120]), and $N_l^c = 1$ and $N_q^c = 3$ are the colour factors for leptons and quarks, respectively. The correction $\Delta\alpha(M_Z) \approx 6\%$ quantifies the running of α from $Q^2 = 0$ to the high scale $Q^2 = M_Z^2$ induced by vacuum polarization effects of the light fermions,

$$\alpha(M_Z) = \alpha(0)/[1 - \Delta\alpha(M_Z)], \quad (2)$$

a quantity that is non-perturbative, signalled by its sensitivity to the light-quark masses. The numerical value for $\alpha(M_Z)$ is obtained from an experimental analysis of e^+e^- annihilation into hadrons at low energies below the Z -boson resonance, combined with theoretical arguments using dispersion relations [121]. Eliminating $\alpha(0)$ in favour of $\alpha(M_Z)$ in the LO prediction, i.e. going over to the $\alpha(M_Z)$ -scheme, effectively subtracts the $\Delta\alpha(M_Z)$ terms from the EW corrections and, thus, cancels all light-fermion logarithms resulting from charge renormalization in the EW correction. This cancellation happens at any loop order in α , i.e. employing the $\alpha(M_Z)$ -scheme resums the dominant effects from the running of α and, at the same time, removes the (perturbatively unpleasant) light-quark masses, which should have been taken from a fit to $\Pi_{f \neq t}^{\gamma\gamma}(Q^2)$ otherwise. For high-energy processes without external photons the $\alpha(M_Z)$ -scheme is appropriate from this point of view.

For processes with l external photons ($l \leq n$), however, the relative EW correction comprises l times the photonic wave-function renormalization constant δZ_{AA} , which exactly cancels the light-fermion mass logarithms appearing in $2\delta Z_e$. This statement expresses the fact that external, i.e. real photons effectively couple with the scale $Q^2 = 0$. Consequently, the coupling factor α^n in the LO cross section should be parametrized as $\alpha(0)^l \alpha(M_Z)^{n-l}$, and the corresponding $\Delta\alpha(M_Z)$ terms should be subtracted only $(n-l)$ times from the EW correction, in order to absorb the large effects from $\Delta\alpha(M_Z)$ into the LO prediction. For $l = n$, this scaling corresponds to the pure $\alpha(0)$ -scheme, but for $l < n$ to a mixed scheme.

The G_F -scheme, finally, offers the possibility to absorb some significant universal corrections connected with the renormalization of the weak mixing angle into LO contributions. At NLO, the G_F - and $\alpha(0)$ -schemes are related according to

$$\alpha_{G_F} \equiv \frac{\sqrt{2}G_F M_W^2 (M_Z^2 - M_W^2)}{\pi M_Z^2} = \alpha(0) \left(1 + \Delta r^{(1)}\right) + \mathcal{O}(\alpha^3), \quad (3)$$

where $\Delta r^{(1)}$ is the NLO EW correction to muon decay [120, 122]. The quantity $\Delta r^{(1)}$ can be decomposed according to $\Delta r^{(1)} = \Delta\alpha(M_Z) - \Delta\rho^{(1)}c_w^2/s_w^2 + \Delta r_{\text{rem}}$ with $\Delta\alpha(M_Z)$ from above, the universal (top-mass-enhanced) correction $\Delta\rho^{(1)} = 3G_\mu m_t^2/(8\sqrt{2}\pi^2)$ to the ρ -parameter, and a very small remainder Δr_{rem} . In view of the running of α , the G_F -scheme corresponds to an α at the EW scale similar to the $\alpha(M_Z)$ -scheme, since $\Delta r^{(1)}$ contains exactly one unit of $\Delta\alpha(M_Z)$. The G_F -scheme is, thus, similar to the $\alpha(M_Z)$ -scheme as far as the running of α is concerned, i.e. it is better than the $\alpha(0)$ -scheme except for the case of external photons. The choice between the G_F - or $\alpha(M_Z)$ -scheme is driven by the appearance of s_w in the EW couplings. Whenever s_w (or c_w) is involved in an EW coupling, the corresponding EW correction receives a contribution from $\Delta\rho^{(1)}$ according to $s_w^2 \rightarrow s_w^2 + \Delta\rho^{(1)}c_w^2$. Using (3), it is easy to see that the combination α/s_w^2 , which corresponds to the SU(2) gauge coupling, does not receive this universal correction, since the $\Delta\rho^{(1)}$ terms from $\Delta r^{(1)}$ and the correction associated with s_w^2 cancel. In other words, employing the G_F -scheme for SU(2) gauge couplings absorbs the leading correction to the ρ -parameter into the LO coupling. This statement also holds at the two-loop level [123]. The G_F -scheme is, thus, most appropriate for describing couplings of W bosons. For Z bosons this scheme absorbs at least part of the $\Delta\rho^{(1)}$ corrections because of additional c_w factors in the coupling from the weak mixing, while the scheme is actually not appropriate for photonic couplings. However, also here it should be kept in mind that a fixed scheme with a global definition of couplings has to be employed within gauge-invariant subsets of diagrams. In most cases, it is advisable to use the G_F -scheme for couplings that involve weak bosons, although the gauge-invariant subsets of diagrams, in general, also contain internal photons.

The application of the various input-parameter schemes to the neutral- and charged-current Drell–Yan processes, including also leading EW effects beyond NLO, is discussed in Refs. [124–126].

2.2 Electroweak corrections at high energies

At high energies, where scattering processes involve large scales $Q^2 \gg M_W^2$, EW corrections develop large logarithmic contributions such as $(\alpha/s_w^2) \ln^2(Q^2/M_W^2)$ and $(\alpha/s_w^2) \ln(Q^2/M_W^2)$ at NLO, and powers of those beyond NLO. These mass-singular corrections originate from soft and/or collinear exchange of EW gauge bosons in loop diagrams. The corresponding logarithms grow to tens of percent in the TeV range, i.e. EW corrections become very significant at high energies.

The kinematic regime in which such EW corrections are most pronounced is characterized by the situation that all invariants $s_{ij} = 2k_i \cdot k_j$ for pairs of particles' four-momenta $k_{i,j}$

become large ($s_{ij} \gg M_W^2$) and is known as *Sudakov regime*. The structure of EW corrections in this domain has been investigated in detail at $\mathcal{O}(\alpha)$ and beyond by several groups (see e.g. Refs. [127–137] and references therein). As described for example in Refs. [131, 134, 137], the leading EW logarithmic corrections, which are enhanced by large factors $L = \ln(s_{ij}/M_W^2)$, can be divided into an $SU(2) \times U(1)$ -symmetric part, an electromagnetic part, and a subleading part induced by the mass difference between W and Z bosons. The last part does not contribute to corrections $\propto (\alpha L^2)^n$. The leading (Sudakov) logarithms $\propto (\alpha L^2)^n$ of electromagnetic origin cancel between virtual and real (soft) bremsstrahlung corrections, so that the only source of leading logarithms is, thus, the symmetric EW part, which can be characterized by comprising W bosons, Z bosons, and photons of a common mass M_W . These leading EW Sudakov corrections can be obtained to all orders from the respective NLO result via exponentiation. For the subleading EW high-energy logarithms corresponding resummations are not fully proven, but the corrections are expected to obey so-called infrared evolution equations, a statement that is backed by explicit two-loop calculations.

The detailed knowledge of the tower of EW high-energy logarithms is important for a deeper understanding of EW dynamics, but making use of it in predictions is a subject that deserves care:

- It is certainly advisable to make use of full NLO EW corrections, i.e. without applying expansions for high energies, whenever possible for a given process. Non-logarithmic corrections typically amount to some percent, depending on the process under consideration. A safe assessment of the quality of logarithmic approximations usually requires the comparison to full NLO results.
- Beyond NLO, the knowledge of higher-order EW logarithms can be very useful and exploited to improve pure NLO predictions. However, particular care has to be taken if the EW logarithms show large cancellations between leading and subleading terms, as for instance observed in the case of neutral-current fermion–antifermion scattering [135]. If the full tower of logarithms of a fixed perturbative order is not known, it is not clear to which accuracy truncated towers approximate the full correction. However, the known part of the tower can at least deliver estimates for the size of missing corrections and be used in the assessment of theoretical uncertainties.
- While the analytical structure of EW corrections was studied in the literature at very detail for the Sudakov regime, there is only little knowledge on EW corrections beyond NLO in more general kinematical situations where not all invariants s_{ij} are large. Note that there are many cross sections that are in fact not dominated by the Sudakov regime in the high-energy limit, including all processes that are dominated by t -channel diagrams. For example, unless specifically designed cuts are applied, reactions like W-boson pair production via e^+e^- , pp , or $\gamma\gamma$ collisions are dominated by the *Regge limit*, where the Mandelstam variable t remains small while s gets large. Moreover, it often depends on the specific observable which regime is probed in high-energy tails of kinematical distributions. Taking Drell–Yan processes (see, e.g., Refs. [124–126]) and dijet production [87] at the LHC as examples, differential distributions in the transverse momenta of the produced leptons or jets probe the Sudakov regime in the high-momentum tails. On the other hand, the invariant-lepton- or jet-mass distributions of these processes are not dominated by this regime at high scales, so that the EW high-energy logarithms derived in the Sudakov regime do not approximate the EW corrections well in those observables.
- Since the EW high-energy logarithmic corrections are associated with virtual soft and/or collinear weak-boson or photon exchange, they all have counterparts in real weak-boson or photon-emission processes which can partially cancel the large negative virtual corrections (but not completely, see Ref. [129]). This cancellation will not be complete, since $SU(2)$

doublets are in general not treated inclusively in EW corrections—a fact that is by some abuse of language called *Bloch–Nordsieck violation*.⁴ To which extent the cancellation occurs depends on the experimental capabilities to separate final states with or without weak bosons or photons. Logarithmic approximations, as recently implemented in the PYTHIA shower [138] can deliver first estimates, but solid predictions have to be based on complete matrix elements. The general issue and specific examples have been discussed for example in Refs. [139–142]. For instance, the numerical analysis [140] of neutral-current Drell–Yan production demonstrates the effect of real weak-boson emission in the distributions in the transverse lepton momentum $p_{T,l}$ and in the invariant mass M_{ll} of the lepton pair. At the LHC, at $M_{ll} = 2\text{TeV}$ the EW corrections are reduced from about -11% to -8% by weak-boson emission. At $p_{T,l} = 1\text{TeV}$ the corresponding reduction from about -10% to -3% is somewhat larger.

2.3 Photonic final-state radiation off leptons

The emission of photons collinear to incoming or outgoing charged leptons l leads to corrections that are enhanced by large logarithms of the form $\alpha^n \ln^n(m_l^2/Q^2)$ with Q denoting a characteristic scale of the process. For lepton colliders, such as a high-energy e^+e^- collider, this collinear initial-state radiation (ISR) leads to pronounced photonic corrections, which are particularly large whenever the underlying total or differential cross section shows strong variations (e.g. near resonances or thresholds). In the following we focus on final-state radiation (FSR) off leptons, the situation that is also relevant at hadron colliders. Both for ISR and FSR, the logarithmically enhanced corrections are universal in the sense that they do not change the nature of the cross section of the underlying hard scattering process, but depend only on the type and kinematics of the incoming or outgoing charged particles. More precisely, ISR distorts cross sections in terms of some convolution over the radiative energy loss in the initial state of the hard scattering, while FSR only influences the kinematics and acceptance of the outgoing particles. The first-order logarithm $\alpha \ln(m_l^2/Q^2)$ is, of course, contained in a full (process-dependent) NLO EW $\mathcal{O}(\alpha)$ correction, and likewise for higher orders, so that Q is unambiguously fixed in any completely calculated order. In a fixed perturbative order that is not completely taken into account, but where ISR or FSR is included in logarithmic accuracy, the ambiguity in the scale Q is part of the remaining theoretical uncertainty.

The universal logarithmic corrections can be evaluated in the so-called *structure-function approach* (see Ref. [143,144] and references therein), where these logarithms are derived from the universal factorization of the related mass singularity, or by dedicated photonic parton showers (see e.g. Refs. [145–147]). For FSR in a process in which a lepton l with momentum k_l is produced, the incorporation of the mass-singular logarithms takes the form of a convolution integral over the LO cross section σ^{LO} ,

$$\sigma_{\text{LLFSR}} = \int d\sigma^{\text{LO}}(k_l) \int_0^1 dz \Gamma_{\text{ll}}^{\text{LL}}(z, Q^2) \Theta_{\text{cut}}(zk_l), \quad (4)$$

where $\Gamma_{\text{ll}}^{\text{LL}}$ is the structure function describing the radiation in logarithmic accuracy. The variable $(1-z)$ is the momentum fraction of the respective lepton lost by collinear (single or multiple) photon emission, and the step function Θ_{cut} is equal to 1 if the event passes the cuts on the rescaled lepton momentum zk_l and 0 otherwise. The structure function is known to $\mathcal{O}(\alpha^5)$ in the literature, including the resummation of soft-photon effects. At NLO, i.e. in $\mathcal{O}(\alpha)$, the structure function has the well-known form

$$\Gamma_{\text{ll}}^{\text{LL},1}(z, Q^2) = \frac{\beta_l}{4} \left(\frac{1+z^2}{1-z} \right)_+ \quad (5)$$

⁴The Bloch–Nordsieck theorem simply does not apply to non-Abelian gauge theories.

with the variable

$$\beta_1 = \frac{2\alpha(0)Q_l^2}{\pi} \left[\ln\left(\frac{Q^2}{m_l^2}\right) - 1 \right], \quad (6)$$

quantifying the large logarithm, with Q_l denoting the electric charge of the lepton l . Here we also indicated that $\alpha(0)$ is the appropriate electromagnetic coupling constant to describe these photon radiation effects. Note that in contrast to the parton-shower approaches to photon radiation, the structure-function approach neglects the photon momenta transverse to the lepton momentum.

For FSR the *Kinoshita–Lee–Nauenberg* (KLN) theorem [148, 149] guarantees that these logarithms cancel if collinear lepton–photon systems are treated fully inclusively, like in a total cross section, defined without any phase-space cuts. Such observables are called *collinear safe*. In the presence of phase-space cuts and in differential cross sections, in general, mass-singular contributions survive, leading to enhanced radiation effects, since the necessary inclusiveness for their compensation is disturbed. At NLO, these features can be easily understood from the explicit analytic form shown in Eq. (5), where the integral over the plus distribution vanishes when taken over the full z range (i.e. $\Theta_{\text{cut}}(zk_l) = 1$ for all z). For differential observables the level of inclusiveness necessary for collinear safety can be restored by a procedure known as *photon recombination*, which treats collinear lepton–photon systems as one quasi-particle. This procedure is similar to the application of a jet algorithm in QCD. For final-state electrons, photon recombination automatically is involved in their reconstruction from electromagnetic showers detected in calorimeters. Muons, on the other hand, can be observed as *bare* leptons from their tracks in the muon chambers, but in order to reduce large FSR corrections, observed muons are sometimes also reconstructed as *dressed* leptons via photon recombination, as e.g. described in Ref. [150] for an ATLAS analysis. Working with dressed leptons, where mass-singular FSR effects cancel, has the advantage that the resulting cross section does not depend on the mass (and thus on the flavour) of the charged lepton, i.e. the reconstructed lepton looks universal (at least electrons and muons).

We conclude this part by an appeal to experimentalists. Obviously data should be stored for future use in such a way that measured total and differential cross sections can be unambiguously confronted with new calculations in the future. This requires that there should be at least one set of results without any unfolding or presubtraction of FSR effects, because unfolded results depend on details (including version dependences) and intrinsic uncertainties of the tool used in the unfolding. Data should be free of such conventions (which most often are not sufficiently well documented) and limitations. Making use of some standard definition of dressed leptons (cf. Ref. [150]), could be a step towards the right direction, since photon recombination reduces unpleasantly large FSR corrections.

2.4 QED-corrected parton distribution functions

The inclusion of NLO EW $\mathcal{O}(\alpha)$ corrections to hadronic cross sections conceptually proceeds along the same lines as the incorporation of NLO QCD corrections, with the slight generalization that the photon appears as parton in the hadron as well. The $\mathcal{O}(\alpha)$ -corrected parton cross sections contain mass singularities which are due to collinear photon radiation off the initial-state quarks or due to a collinear splitting $\gamma \rightarrow q\bar{q}$ for initial-state photons. If small quark masses are used as regulators for collinear divergences, these singularities appear as terms of the form $\alpha \ln(m_q)$, in dimensional regularization with strictly massless quarks they appear as poles $\propto \alpha/\epsilon$ in $D = 4 - 2\epsilon$ dimensions. In complete analogy to factorization in NLO QCD calculations, these collinear singularities are absorbed into the quark and photon distributions. The explicit form of the redefinition of PDFs can, e.g., be found in Ref. [126]. The *factorization scheme* for the QED part of the redefinition is determined by the $\mathcal{O}(\alpha)$ part of the so-called *coefficient functions*,

and the $\overline{\text{MS}}$ and DIS-like schemes are defined in complete analogy to QCD. The $\overline{\text{MS}}$ scheme is motivated by formal simplicity, because it merely rearranges the infrared-divergent terms (plus some trivial constants) as defined in dimensional regularization. The DIS-like scheme is defined in such a way that the DIS structure function F_2 does not receive any corrections; in other words, the radiative corrections to electron–proton DIS are implicitly contained in the PDFs in this case. Whatever scheme has been adopted in the extraction of PDFs from experimental data, the same scheme has to be used when predictions for other experiments are made using these PDFs.

In complete analogy to the pure QCD case, a factorization scale $\mu_{\text{fact,QED}}$ rules up to which scale collinear QED splitting processes in the initial state are considered to be part of the colliding hadron. The absorption of the collinear singularities of $\mathcal{O}(\alpha)$ into PDFs requires the inclusion of the corresponding $\mathcal{O}(\alpha)$ corrections into the Dokshitzer–Gribov–Lipatov–Altarelli–Parisi (DGLAP) evolution of these distributions, which describe the dependence of the PDFs on the factorization scales. Note, however, that the two factorization scales $\mu_{\text{fact,QCD}}$ and $\mu_{\text{fact,QED}}$ have to be identified, $\mu_{\text{fact}} = \mu_{\text{fact,QCD}} = \mu_{\text{fact,QED}}$, if the DGLAP equations are to keep their usual form as integro-differential equation in one scale, which is the common practice.

The first set of parton distributions including QED corrections was MRST2004QED [151], which takes into account $\mathcal{O}(\alpha)$ corrections to the DGLAP evolution, but uses a theoretical model as ansatz for the photon PDF at some starting scale. In 2013 the new set NNPDF2.3QED [152] of QED-corrected PDFs became available, which also provides error estimates for the PDFs and, for the first time, employed data to fit the photon distribution function. For typical scales relevant for LHC processes, the NNPDF photon density confirms the older MRST result for x -values $\gtrsim 0.03$, but is somewhat smaller for lower values of x . Generically the impact of QED corrections on quark PDFs is below the percent level for $x \lesssim 0.4$. There are some slight shortcomings in those sets of QED-corrected PDF sets concerning the issue of the QED factorization scheme. The QED evolution is treated in LO only, and EW corrections are ignored in the fit of the PDFs to data. This means that there is some mismatch in the use of the PDFs at the level of non-enhanced $\mathcal{O}(\alpha)$ terms, which should be quite small, and that a very conservative error estimate should treat the difference between results obtained with various QED factorization schemes as theoretical uncertainty. However, as discussed in Refs. [152, 153] the neglect of EW corrections in the PDF fit to data favours the central value of the DIS scheme for EW corrections. Thus, the recommendation for the NNPDF2.3QED PDF set is to use a mixed scheme which follows the $\overline{\text{MS}}$ scheme for QCD and the DIS scheme for EW NLO corrections.

2.5 Photon-induced processes

The inclusion of the photon in the set of partons inside hadrons leads to so-called photon-induced processes, i.e. partonic channels with photons in the initial state, in addition to the partonic channels of QCD. At NLO EW level, contributions from photon-induced processes always result as crossed counterparts of photonic bremsstrahlung corrections. For instance, quark-initiated qq , $q\bar{q}$, $\bar{q}q$ channels always receive (real) $\mathcal{O}(\alpha)$ corrections from $q\gamma$ and/or $\bar{q}\gamma$ scattering, where the additional q or \bar{q} in the final state leads to an additional jet with respect to the LO signature, similar to real NLO QCD corrections. For specific final states with charged particles, but without net electric charge, there is also a contribution from $\gamma\gamma$ scattering with LO kinematics and without additional partons in the final state. This is, for instance, the case for $\mu^+\mu^-$ or W^+W^- production.

For processes, where the diagrams of the $q\gamma$ -induced corrections have direct counterparts in the qg channels of the NLO QCD corrections, the $q\gamma$ channels typically contribute at the percent level to the hadronic cross section. This suppression originates from the relative coupling

factor α/α_s and from the fact that the photon and gluon PDFs are similar in shape, but the gluon PDF is larger by about two orders of magnitude for scales and x values of typical LHC processes. A similar statement holds for $\gamma\gamma$ channels whenever similar $g\gamma$ or gg channels exist. More significant contributions from photon-induced processes can only arise if the photonic channels involve diagrams without QCD counterparts, i.e. diagrams where the photon couples to colour-neutral charged particles like muons or W bosons. Recently discussed examples for enhanced photon-induced contributions are the channels $\gamma\gamma \rightarrow l^+l^-$ [96, 126, 154] and $\gamma\gamma \rightarrow W^+W^-$ [105–108], where the $\gamma\gamma$ channels comprise more than 10% in certain regions of phase space.

2.6 Photon–jet separation

Including QCD and EW corrections in predictions for the production of a specific final state F in association with a hard jet or a hard photon necessarily raises the issue of a proper separation of jets and photons, since the real corrections to $F + \text{jet}$ and $F + \gamma$ production both involve final states with $F + \text{jet} + \gamma$ final states. The process of $F + \text{jet} + \gamma$ production contributes to the NLO EW corrections to $F + \text{jet}$ production and to the NLO QCD corrections to $F + \gamma$ production at the same time. A consistent isolation of $F + \text{jet}$ from $F + \gamma$ signatures at full (QCD+EW) NLO accuracy requires a photon–jet separation that guarantees a proper cancellation of all infrared (soft and collinear) singularities on the theory side and is experimentally feasible at the particle level.

Since calorimetric information is decisive for the reconstruction of jets and photons, it is natural to take the electromagnetic energy fraction inside some hadronic/electromagnetic shower as criterion to decide whether it is called a jet or a photon. Note that this criterion, however, necessarily leads to an incomplete cancellation of collinear singularities for photon emission off (anti)quarks. This can be explicitly seen by inspecting the integral (4) with the structure function (5) interpreting l as the radiating (anti)quark. The selection criterion cuts into the z -integration and destroys the cancellation of the collinear singularity, which would require the integration to be taken over the full z -range. Two different methods have been suggested in the literature to cope with this situation: one method introduces a phenomenological *quark-to-photon fragmentation function* that absorbs the collinear singularity in the same way as the PDFs absorb collinear singularities from the initial state. Another method, known as *Frixione isolation*, shifts the complete collinear singularity to the jet side upon designing a specially adapted definition of the allowed hadronic energy fraction in a photonic shower:

- *Quark-to-photon fragmentation function*

The quark-to-photon fragmentation function $D_{q \rightarrow \gamma}(z_\gamma)$ describes the probability of a quark fragmenting into a jet containing a photon carrying the fraction z_γ of the total jet energy. Since fragmentation is a long-distance process, it cannot be calculated entirely in perturbation theory, but receives two types of contributions: (a) the perturbatively calculable radiation of a photon off a quark, which contains a collinear divergence; (b) the non-perturbative production of a photon during the hadronization of the quark, which is described by a bare non-perturbative fragmentation function $D_{q \rightarrow \gamma}^{\text{bare}}(z_\gamma)$. The latter contributes to the photon-emission cross section as

$$d\sigma^{\text{frag}}(z_{\text{cut}}) = d\sigma^{\text{LO}} \int_{z_{\text{cut}}}^1 dz_\gamma D_{q \rightarrow \gamma}^{\text{bare}}(z_\gamma), \quad (7)$$

where z_{cut} is the smallest photon energy fraction required in the collinear photon–quark system to be identified as a photon. The perturbative and non-perturbative (bare) contributions to the fragmentation function are sensitive to the infrared dynamics inside the quark jet and can a priori not be separated from each other in a unique way. Since

the infrared singularity present in the perturbative contribution must be balanced by a divergent piece in the bare fragmentation function, $D_{q \rightarrow \gamma}^{\text{bare}}(z_\gamma)$ can be decomposed at a factorization scale μ_F into a universal divergent piece and a phenomenological contribution $D_{q \rightarrow \gamma}(z_\gamma, \mu_F)$, which has to be taken from experiment,

$$D_{q \rightarrow \gamma}^{\text{bare,DR}}(z_\gamma) = \frac{\alpha Q_q^2}{2\pi} \frac{1}{\epsilon} \left(\frac{4\pi\mu^2}{\mu_F^2} \right)^\epsilon \frac{1}{\Gamma(1-\epsilon)} P_{ff}(1-z_\gamma) + D_{q \rightarrow \gamma}(z_\gamma, \mu_F), \quad (8)$$

where Q_q is the electric charge of the massless quark q and $P_{ff}(z) = (1+z^2)/(1-z)$ is the $q \rightarrow q + \gamma$ splitting function. Here, the collinear singularity is regularized in $D = 4 - 2\epsilon$ dimensions (with the arbitrary reference mass μ) and isolated by an $\overline{\text{MS}}$ -type factorization scheme; the respective result for mass regularization with a small quark mass can be found in Ref. [155].

In Ref. [156] a method was proposed how to measure $D_{q \rightarrow \gamma}(z_\gamma, \mu_F)$ upon analyzing the process $e^+e^- \rightarrow n \text{ jet} + \text{photon}$. The key feature of the proposed method is the democratic clustering of both hadrons and photons into jets, while keeping track of the photonic energy fraction in the jet, i.e. technically one has to deal with identified particles in the final state that lead to infrared-non-safe observables (with respect to collinear singularities). The treatment of this situation with one-cut-off phase-space slicing and dipole subtraction is described in Refs. [156] and [155], respectively. The first determination of $D_{q \rightarrow \gamma}(z, \mu_0)$ was performed by the ALEPH collaboration [157] using the ansatz

$$D_{q \rightarrow \gamma}^{\text{ALEPH}}(z_\gamma, \mu_F) = \frac{\alpha Q_q^2}{2\pi} \left[P_{ff}(1-z_\gamma) \ln \left(\frac{\mu_F^2}{\mu_0^2} \frac{1}{(1-z_\gamma)^2} \right) + C \right], \quad (9)$$

with two fitting parameters, $C = -12.1$ and $\mu_0 = 0.22 \text{ GeV}$.

– *Frixione isolation* [158]

This procedure defines isolated hard photons by the requirement that only soft partons can become collinear to the photon. In detail, the total transverse energy $\sum_i E_{T,i}$ of all partons i with small distances $R_{i\gamma} = \sqrt{(\eta_i - \eta_\gamma)^2 + (\phi_i - \phi_\gamma)^2}$ to the photon in the pseudo-rapidity–azimuthal-angle plane is required to go to zero with the maximally allowed distance $R_{i\gamma}$, i.e.

$$\sum_i E_{T,i} \theta(\delta - R_{i\gamma}) \leq \mathcal{X}(\delta) \quad \text{for all } \delta \leq \delta_0, \quad (10)$$

where δ_0 is a measure for the size of the cone around the photon, in which the criterion is used, and $\mathcal{X}(\delta)$ is an appropriate function with $\mathcal{X}(\delta) \rightarrow 0$ for $\delta \rightarrow 0$. Specifically, the form

$$\mathcal{X}(\delta) = E_{T,\gamma} \epsilon_\gamma \left(\frac{1 - \cos \delta}{1 - \cos \delta_0} \right)^n \quad (11)$$

is suggested in Ref. [158] for a photon of transverse energy $E_{T,\gamma}$, where the two parameters ϵ_γ and n can just be taken to be 1. This condition excludes any hard jet activity collinear to the photon, but still takes into account soft jet activity at a sufficiently inclusive level to guarantee the proper cancellation of infrared singularities when calculating NLO QCD corrections to $F + \gamma$ production with γ being the isolated photon. Taking the inverse procedure to define $F + \text{jet}$ production, i.e. interpreting $F + \text{jet} + \gamma$ production as photonic EW correction to $F + \text{jet}$ if condition (10) is not fulfilled, formally shifts the complete contribution of the quark-to-photon fragmentation function to $F + \text{jet}$ production. Whether this means that $F + \gamma$ production is really insensitive to non-perturbative corrections is not proven and sometimes under debate. Moreover, the implementation of condition (10) at the experimental level raises issues, in particular concerning shower effects on the hard photon kinematics and the realizability at the apex of the cone.

At the LHC, a prominent example for photon–jet separation is given by W/Z production in association with a jet or a photon, where the NLO EW corrections to W/Z+jet production [98–100] and the NLO QCD corrections to W/Z+ γ production (e.g. implemented in MCFM [159]) overlap. Comparing, for instance, results on W+ γ production obtained with the two separation procedures as implemented in MCFM reveals differences at the level of $\sim 2\%$ only. Note, however, that it is not possible to make generic, process-independent statements on such differences.

2.7 Combination of QCD and electroweak corrections

Naively a comparison of coupling strengths suggests that along with NLO $\mathcal{O}(\alpha_s)$ and NNLO $\mathcal{O}(\alpha_s^2)$ QCD corrections simply taking into account NLO EW corrections of $\mathcal{O}(\alpha) \sim \mathcal{O}(\alpha_s^2)$ would be adequate in predictions. However, as explained in the previous sections, EW $\mathcal{O}(\alpha)$ corrections can be significantly enhanced compared to the small value of α/π by large logarithms and/or kinematical effects, raising the question about mixed QCD–EW corrections of $\mathcal{O}(\alpha_s\alpha)$. In spite of the great progress of recent years in NNLO QCD calculations, the required multi-scale NNLO calculations needed at $\mathcal{O}(\alpha_s\alpha)$ are still out of reach at present. As long as this is the case, we have to rely on approximations—an issue that already comes up in the combination of NLO QCD and EW corrections ($\delta_{\text{QCD}}^{\text{NLO}}$ and $\delta_{\text{W}}^{\text{NLO}}$) in cross-section predictions. Schematically, the choice is between the two extreme variants of adding, $1 + \delta^{\text{NLO}} = 1 + \delta_{\text{QCD}}^{\text{NLO}} + \delta_{\text{W}}^{\text{NLO}}$, or multiplying relative corrections, $1 + \delta^{\text{NLO}} = (1 + \delta_{\text{QCD}}^{\text{NLO}}) \times (1 + \delta_{\text{W}}^{\text{NLO}})$, and variants in between these two extreme cases. The differences between different variants are of $\mathcal{O}(\alpha_s\alpha)$, and the optimal choice should minimize the remaining corrections of this order for the most important observables.

Since long-distance effects such as soft or collinear parton emission off quarks or gluons and collinear final-state photon radiation off leptons are known to factorize from the actual hard scattering, the variant of factorizing QCD and EW corrections seems to be preferable in many cases. For the prediction of a cross section which is differential in some observable x at the parton level, this idea of factorization can be translated into the recipe

$$\frac{d\sigma}{dx} = \frac{d\sigma_{\text{QCD}}}{dx} \times \left[1 + \delta_{\text{W}}^{\text{NLO}}(x) \right] + \frac{d\sigma_{\gamma}}{dx}, \quad (12)$$

where σ_{QCD} stands for the best available QCD prediction for the cross section, $\delta_{\text{W}}^{\text{NLO}}(x)$ is the relative EW correction differential in x , and σ_{γ} denotes the contribution from photon-induced processes. This approach is, e.g., useful if the various contributions are calculated independently, possibly even by independent programs. For instance, the state-of-the-art predictions for Higgs production via vector-boson fusion and Higgs-strahlung provided by the LHC Higgs Cross Section Working Group [38–40] are calculated in this way.

Similar factorization approaches can also be directly included in the event generation within QCD-based event generators upon applying differential reweighting factors for the EW corrections. In simple cases where the relative EW correction $\delta_{\text{W}}^{\text{NLO}}$ depends mainly on a single kinematical variable x , while $\delta_{\text{W}}^{\text{NLO}}$ is flat in the other relevant kinematical variables, generated events can simply be reweighted by the factor $1 + \delta_{\text{W}}^{\text{NLO}}(x)$. As discussed in Ref. [160] (Section 19), this method is quite successful for Higgs production via vector-boson fusion, where x can be identified with the transverse momentum of the Higgs boson. Specifically, in Ref. [160] the QCD-based prediction of HERWIG [161] was dressed with the relative EW correction from HAWK [162, 163]. A similar approach has been advocated recently in Ref. [109] where the EW corrections [105, 106] to on-shell diboson production (neglecting corrections to W/Z decays) were included in HERWIG++ [164, 165] by reweighting factors that are double-differential in the partonic scattering energy and the angle of the LO kinematics. It should be kept in mind

that generally such reweighting procedures represent some approximative compromise with advantages and weaknesses. As in the two examples mentioned above, usually no hard photon is generated along with the EW reweighting, but photon emission is integrated over, i.e. in the real-photonic bremsstrahlung corrections the kinematic effects from hard photon emission are neglected. While observables that are not sensitive to photonic recoil effects can be described well via the reweighting approach (see, e.g., Ref. [109] for examples in diboson production), the method is expected to fail whenever photonic recoil is important (see, e.g., the transverse momentum of the dilepton system in W -pair production as discussed in Ref. [108]). Before applied in practice, the applicability and reliability of the reweighting approach should be checked by a comparison to fully differential results.

This discussion reveals one of the crucial problems in the combination of NLO QCD and NLO EW corrections when following the factorization idea: The QCD and EW corrections of the two different factors are in general defined on different phase spaces. Only a complete calculation of $\mathcal{O}(\alpha_s\alpha)$ corrections can fully solve this problem. Since matrix elements and phase spaces for jet and/or photon emission factorize in the soft and/or collinear limits of the radiated particle, there is at least the possibility to correctly describe the leading soft and/or collinear $\mathcal{O}(\alpha_s\alpha)$ effects at the fully differential level. Based on this idea, Monte Carlo generators such as HERWIG++ [164,165] and SHERPA [166] already dress QCD-based predictions with soft and/or collinear photon radiation (at least off final-state leptons), in order to catch some leading $\mathcal{O}(\alpha_s\alpha)$ effects and even higher-order effects in α . Likewise dedicated Monte Carlo programs for Drell–Yan processes such as RESBOS-A [167], HORACE [168], and WINHAC [169] proceed similarly.

Finally, we comment on the issue of *matching* fixed-order NLO calculations of $\mathcal{O}(\alpha_s)$ and $\mathcal{O}(\alpha)$ with parton showers that take into account multiple jet and/or photon emission in some leading logarithmic approximation. Here the central issue is to avoid double-counting effects at the level of one-parton and one-photon emission and to keep full NLO accuracy after the matching. In pure QCD, two matching prescriptions are widely in use: MC@NLO [36] and POWHEG [37,170]. When matching NLO QCD+EW calculations to a pure QCD parton shower (as e.g. done in Ref. [171] for Drell–Yan processes in the POWHEG framework), thus, improves the NLO prediction not only in the pure QCD sector, but also in $\mathcal{O}(\alpha_s\alpha)$ by dressing $\mathcal{O}(\alpha)$ effects with soft/collinear QCD radiation. If the matched shower even includes photon radiation, where the POWHEG matching has to be generalized as described in Refs. [172,173] for Drell–Yan processes, then the effectively included $\mathcal{O}(\alpha_s\alpha)$ effects account for $\mathcal{O}(\alpha_s)$ effects dressed with soft/collinear photon radiation.

As long as complete corrections of $\mathcal{O}(\alpha_s\alpha)$ are missing, they are one particular source for theoretical uncertainties. Their size can be conservatively estimated upon comparing the results obtained from the additive and multiplicative approaches to combine NLO QCD and EW corrections. If leading effects of $\mathcal{O}(\alpha_s\alpha)$, which show factorization properties (such as photonic FSR or EW Sudakov logarithms), are properly included, those effects should be excluded from the assessment of uncertainties at $\mathcal{O}(\alpha_s\alpha)$.

2.8 Instability effects and the treatment of W/Z resonances

Although external W and Z bosons always appear as resonances in experiments which have to be reconstructed from their decay products, LO predictions for W/Z production processes often start from the approximation of stable W/Z bosons on their mass shell. The more realistic treatment as resonance processes changes cross-section predictions typically at the level of $\mathcal{O}(\Gamma_V/M_V) \sim 3\%$ ($M_V =$ mass, Γ_V decay width of $V = W, Z$) when the resonances are integrated over. For such observables off-shell effects of the weak gauge bosons, derived from LO calculations for the resonant and non-resonant production of the decay products, can be counted as $\mathcal{O}(\alpha)$ corrections. The remaining $\mathcal{O}(\alpha)$ corrections can be calculated from virtual

one-loop and real emission corrections to on-shell W/Z production if the decays of the weak gauge bosons are treated inclusively.

For an inclusion of the W/Z decays in predictions, the simplest (but somewhat crude) way is to employ the *narrow-width approximation* (NWA), which treats the W/Z bosons as “stable intermediate states”, i.e. the full process is decomposed into on-shell W/Z production and on-shell W/Z decays. This decomposition results from the limit $\Gamma_V \rightarrow 0$ in the squared matrix element of the full resonance process, where the squared propagator factor (momentum transfer k) behaves like

$$\frac{1}{|k^2 - M_V^2 + iM_V\Gamma_V|^2} \simeq \Gamma_V \rightarrow 0 \frac{\pi}{M_V\Gamma_V} \delta(k^2 - M_V^2). \quad (13)$$

The $1/\Gamma_V$ factor on the r.h.s. is part of the well-known *branching ratio* which emerges after the inclusive integration over the V decay phase space. If cuts are imposed on the decay products, or if distributions in kinematical variables of those are considered, in general effects of spin correlations between W/Z production and decay (or between various decaying gauge bosons) appear. The naive NWA, which employs unpolarized production cross sections and decay widths, can be easily improved to include these correlations by properly combining production and decay parts for definite polarization states. Note that $\mathcal{O}(\alpha)$ corrections to a cross section in NWA do not only consist of corrections to the V -production cross section and to the relevant branching ratio, but also comprise the off-shell effects of $\mathcal{O}(\Gamma_V/M_V)$ mentioned above. Furthermore, it has been shown [174] that naive estimates often underestimate the theoretical uncertainties of the NWA; in scenarios with cascade decays, which are quite common in non-standard models, the NWA can even fail completely, as demonstrated in Ref. [175].

A detailed description of a resonance process, keeping the full differential information of the kinematics of the decay products, has to be based on complete matrix elements for the full process, including both resonant and non-resonant diagrams. Note that in standard perturbation theory, particle propagators do not include decay widths. The decay widths rather appear in the propagator denominators only after a Dyson summation of self-energy diagrams (or at least the imaginary parts thereof near resonances). Depending on the details of the field-theoretical definition of the unstable particle’s mass, different results are obtained for the resonant propagator. Writing generically

$$P_V(k) = \frac{1}{k^2 - M_V^2 + iM_V\Gamma_V(k^2)} \quad (14)$$

for the V -propagator factor, two frequently used versions are:

- *Fixed width* (FW): $\Gamma_V(k^2) = \Gamma_V = \text{const.}$
 In this parametrization, the complex squared mass $M_V^2 - iM_V\Gamma_V$ plays the role of the complex location of the pole in the propagator, i.e. it is a field-theoretically sound, gauge-invariant quantity resulting from an all-order definition (see Ref. [176, 177] and older references therein). The real and imaginary parts of this complex quantity define the *pole mass* and its associated *pole width*.
- *Running width* (RW): $\Gamma_V(k^2) = \Gamma_V \times k^2/M_V^2 \times \theta(k^2)$.
 This behaviour results from the so-called *on-shell definition* (OS) of the gauge-boson masses (see, e.g., Ref. [120]), M_V^{OS} , which are tied to the zeroes of the real parts of the respective self-energies. This definition has the drawback that it is gauge dependent at the two-loop level and beyond. The values for the Z- and W-boson masses have, however, been determined within this scheme at LEP and the Tevatron.

For reasons of theoretical consistency, the pole definition of mass and width are clearly preferable.

Fortunately, there is a simple translation from one scheme to the other [178, 179]:

$$M_V = \frac{M_V}{\sqrt{1 + \Gamma_V^2/M_V^2}} \Big|_{\text{OS}}, \quad \Gamma_V = \frac{\Gamma_V}{\sqrt{1 + \Gamma_V^2/M_V^2}} \Big|_{\text{OS}}, \quad (15)$$

so that $M_{Z,\text{OS}} - M_Z \approx 34\text{MeV}$ and $M_{W,\text{OS}} - M_W \approx 27\text{MeV}$. For precision EW physics, in particular for a precision M_W measurement, it is important to be consistent in the use of a scheme and the respective input.

The FW and the RW prescriptions represent different parametrizations of resonances, but none of them represents a consistent scheme to calculate full cross sections for resonance processes, since both in general lead to gauge-dependent results. This is due to the fact that using Eq. (14) for propagator factors necessarily mixes different orders in perturbation theory in practice, since the width term in the propagator results from partial all-order resummations, but the cross-section calculation stops at some finite loop level. While the FW usually at least leads to acceptable LO results, the k^2 -dependence of the width term in the RW propagator can enhance gauge-breaking terms already in LO predictions to a level that completely destroys predictions. Various examples are, e.g., discussed in Refs. [179–181]. Proper cross-section predictions should be based on consistent, gauge-invariant schemes, or at least be validated by comparing to such results.

In a nutshell, we briefly describe the schemes that are most frequently used in LHC physics to deliver gauge-invariant predictions at LO and NLO:

– *Factorization schemes*

Different variants of factorizing resonant structures from amplitudes have been suggested and used in the literature, but they all share the idea to separate a simple resonance factor from complete (gauge-invariant) amplitudes or from gauge-invariant subsets of diagrams. In Ref. [124], for instance, the virtual electroweak correction to Drell–Yan-like W production was factorized from the resonant LO amplitude, so that the relative correction factor did not involve resonance factors anymore. At first sight, such schemes seem to be very simple, but for more complicated processes it is highly non-trivial to guarantee the aimed precision (e.g. NLO) everywhere in phase space and to match virtual and real corrections. Simply modifying LO cross sections with fudge factors containing decay widths for resonances in general introduces spurious $\mathcal{O}(\alpha)$ terms destroying NLO EW accuracy. A consistent implementation of weak NLO corrections to Z-boson production in a factorization scheme is, e.g., described in Ref. [126].

– *Pole scheme*

The pole scheme exploits the fact that both the location of the V propagator pole and its residue in amplitudes are gauge-independent quantities. The idea [182, 183] is, thus, to first isolate the residue for the considered resonance and subsequently to introduce a finite decay width only in the gauge-independent resonant part. If done carefully this procedure respects gauge invariance and can be used to make uniform predictions in resonant and non-resonant phase-space regions. There is some freedom in the actual implementation of the scheme, because the resonant part of an amplitude is not uniquely determined by the propagator structure alone, but depends on a specific phase-space parameterization and in most cases also on the separation of polarization-dependent parts (spinors, polarization vectors). Taking the pole prescription literally, the scattering amplitude on the resonance pole (i.e. with k^2 being complex) involves matrix elements with complex kinematical variables, which is a subtle issue [184]. This *complex pole scheme* was applied to Higgs production via gluon fusion at the LHC in Ref. [185], with particular emphasis on a heavy, i.e. very broad, Higgs boson. For narrow resonances such as the weak gauge bosons

$V = W, Z$, the complex kinematics can be avoided by suitable expansions in Γ_V/M_V , as e.g. done in Ref. [126] for single-Z production.

The pole scheme offers a well-defined separation between resonant and non-resonant parts of a cross section, i.e. in some sense a definition of *signal* and *background* for the production of a resonance. This scheme is, thus, ideal for a parametrization of a resonance by so-called *pseudo-observables*, such as total and partial decay widths, peak cross sections, effective couplings, etc. Moreover, the consistent separation of signal and background contributions is an ideal starting point to further improve the description of the signal by higher-order corrections, a point that is particularly important if the signal dominates over the background and, thus, deserves higher precision.

– *Pole approximation*

A pole approximation—in contrast to a full pole-scheme calculation—results from a resonant amplitude defined in the pole scheme upon neglecting non-resonant parts. Consequently, NLO calculations in pole approximation deliver NLO accuracy only in the neighborhood of resonances, but not in off-shell tails. Note that NLO corrections in pole approximations do not only involve independent corrections to the production and to the decay of resonances (called *factorizable* corrections), but also comprise soft-photon or soft-gluon exchange between production and decay subprocesses (called *non-factorizable* corrections). Different variants of *double-pole approximations* have, for instance, been employed to describe W-pair production with decays in e^+e^- annihilation at LEP2 (reviewed, e.g., in Ref. [186]). Recently, this concept has been applied to W-pair production at the LHC in Ref. [108].

– *Effective field theories*

Approaches [187–189] via effective field theories (EFT) deliver a field-theoretically elegant way to carry out pole expansions owing to their formulation via Lagrangians and effective actions. Like pole approximations, their validity is restricted to the resonance region, but they offer the combination with further expansions, e.g. around thresholds, and suggest better possibilities to carry out dedicated resummations. The EFT shows limitations or complications if detailed information on differential properties of observables is needed, since different degrees of freedom are integrated out. For e^+e^- collisions the EFT approach was, for instance, used to evaluate NLO EW corrections to the W-pair production cross section near the WW threshold [190], including leading EW higher-order effects beyond NLO. Currently, the formalism is applied to the NLO QCD corrections to top-quark pair production at the LHC, with first results on the quark–antiquark annihilation channel [191].

– *Complex-mass scheme*

This scheme was introduced in Ref. [180] for LO calculations and generalized to NLO in Ref. [192]. In this approach the squared W- and Z-boson masses are consistently identified with the complex values $M_V^2 - iM_V\Gamma_V$ ($V = W, Z$), not only in the V -propagators, but also in the couplings, which therefore become complex and involve a complex weak mixing angle via $c_w^2 = 1 - s_w^2 = (M_W^2 - iM_W\Gamma_W)/(M_Z^2 - iM_Z\Gamma_Z)$. Otherwise the usual perturbative calculus with Feynman rules and counterterms works without modification. All relations following from gauge invariance are respected, because the gauge-boson masses are modified only by an analytic continuation. NLO calculations deliver uniform predictions with NLO accuracy everywhere in phase space, i.e. both in resonant and non-resonant regions. Spurious terms spoiling unitarity are unproblematic, since they are of (N)NLO in an (N)LO calculation (i.e. of higher order) without any unnatural amplification, because unitarity cancellations, which are ruled by gauge invariance, are respected.

The complex-mass scheme, first used for four-fermion production in e^+e^- physics [192],

is frequently used in NLO calculations for weak gauge-boson or Higgs-boson processes at the LHC, for example for the off-shell Higgs-boson decays $H \rightarrow WW/ZZ \rightarrow 4$ fermions at NLO accuracy in the Monte Carlo program PROPHECY4F [193, 194] and in the previously mentioned NLO EW calculations for single-Z [126] and $W/Z + \text{jet}$ [98–100] at the LHC. As discussed in the context of the (two-loop) calculation of NLO EW corrections to Higgs production via gluon fusion [195, 196], the complex-mass scheme delivers also a sound description of particle thresholds in loop amplitudes (which can be viewed as resonances inside loops).

Finally, we want to reemphasize that this survey is just meant to assist non-experts in the field in finding their bearings upon putting some keywords into context. It is by no means comprehensive or complete, i.e. several issues concerning unstable particles are left untouched here, such as signal–background interferences or many technical details and subtleties. There is still much work to be done until all relevant resonance processes at the LHC are theoretically described in a satisfactory way—a statement that is also backed by the recent report of the Higgs CAT [197].

Acknowledgments

The author (S.D.) is grateful to A. Denner and A. Mück for valuable discussions and comments on this contribution.

Chapter I

NLO automation and (N)NLO techniques

1 The first use case for BLHA2 extensions: N_{JET} plus Herwig++/Matchbox¹

We present first results from interfacing N_{JET} to Herwig++/Matchbox. This combination has provided the first working example for extensions of the BLHA interface regarding tree-level, as well as colour and spin correlated matrix elements on top of virtual corrections.

1.1 Introduction

We explore the possibility of a more general interface between next-to-leading order (NLO) Monte-Carlo event generators and automated matrix element generators. Apart from specialized implementations, currently the BLHA [198] has been used to provide loop level matrix elements. The purpose of this study is to use the updated BLHA2 accord [199] to provide more general matrix elements to the Monte-Carlo program for use in the real radiation contributions as NLO.

Our starting point is the differential cross section to NLO accuracy in QCD in hadron-hadron collisions written using the Catani-Seymour subtraction scheme [200]:

$$d\sigma_n(\mu_R, \mu_F; H_1(p_1) + H_2(p_2) \rightarrow X) = \sum_{k=0}^K d\sigma_n^{\text{N}^k\text{LO}}(\mu_R, \mu_F; H_1(p_1) + H_2(p_2) \rightarrow X) + \mathcal{O}(\alpha_s^{n-1+K}) \quad (\text{I.1})$$

$$d\sigma_n^{\text{LO}}(\mu_R, \mu_F; H_1(p_1) + H_2(p_2) \rightarrow X) = \sum_{i,j} f_{i/H_1}(x_1, \mu_F) f_{j/H_2}(x_2, \mu_F) d\hat{\sigma}_n^B(\mu_R, \mu_F; i(x_1 p_1) + j(x_2 p_2) \rightarrow X) dx_1 dx_2 \quad (\text{I.2})$$

$$\begin{aligned} d\sigma_n^{\text{NLO}}(\mu_R, \mu_F; H_1(p_1) + H_2(p_2) \rightarrow X) = & \sum_{i,j} f_{i/H_1}(x_1, \mu_F) f_{j/H_2}(x_2, \mu_F) d\hat{\sigma}_n^V(\mu_R, \mu_F; i(x_1 p_1) + j(x_2 p_2) \rightarrow X) dx_1 dx_2 \\ & + \sum_{i,j} f_{i/H_1}(x_1/z, \mu_F) f_{j/H_2}(x_2, \mu_F) d\hat{\sigma}_n^I(\mu_R, \mu_F, z; i(x_1 p_1) + j(x_2 p_2) \rightarrow X) dx_1 dx_2 dz \\ & + \sum_{i,j} f_{i/H_1}(x_1, \mu_F) f_{j/H_2}(x_2/z, \mu_F) d\hat{\sigma}_n^I(\mu_R, \mu_F, z; i(x_1 p_1) + j(x_2 p_2) \rightarrow X) dx_1 dx_2 dz \\ & + \sum_{i,j} f_{i/H_1}(x_1, \mu_F) f_{j/H_2}(x_2, \mu_F) d\hat{\sigma}_n^{\text{RS}}(\mu_R, \mu_F; i(x_1 p_1) + j(x_2 p_2) \rightarrow X) dx_1 dx_2 \end{aligned} \quad (\text{I.3})$$

where $f_{i/H}(x, \mu_F)$ is the parton distribution function giving the probability of finding a parton i with momentum fraction x inside the hadron H . The partonic cross sections can then be written in terms of matrix elements and dipole subtraction terms as follows:

$$d\hat{\sigma}_n^B = c(\alpha_s, \mu_R) d\text{PS}_n \sum_{\lambda_h=\pm} B_n(\{\lambda_h\}) \quad (\text{I.4})$$

$$d\hat{\sigma}_n^V = c(\alpha_s, \mu_R) \alpha_s(\mu_R) d\text{PS}_n \sum_{\lambda_h=\pm} V_n(\mu_R, \{\lambda_h\}) \quad (\text{I.5})$$

$$d\hat{\sigma}_n^I = c(\alpha_s, \mu_R) \alpha_s(\mu_R) d\text{PS}_n \sum_{k,l} \sum_{\lambda_h=\pm} \tilde{B}_n^{kl}(\{\lambda_h\}) \mathcal{D}^{kl}(z) \quad (\text{I.6})$$

¹S. Badger, S. Plätzer, V. Yundin

$$d\widehat{\sigma}_n^{RS} = c(\alpha_s, \mu_R) \alpha_s(\mu_R) d\text{PS}_{n+1} \left\{ \sum_{\lambda_h=\pm} B_{n+1}(\{\lambda_h\}) - \sum_{k,l} S_{n+1}^{kl}(\{\lambda_h\}) \right\} \quad (\text{I.7})$$

where

$$B_n(\{\lambda_h\}) = \sum_{i,j} \left(A_i^{(0)}(p_1^{\lambda_1}, \dots, p_n^{\lambda_n}) \right)^\dagger C_{ij}^{(0)} A_j^{(0)}(p_1^{\lambda_1}, \dots, p_n^{\lambda_n}) \quad (\text{I.8})$$

$$V_n(\mu_R, \{\lambda_h\}) = \sum_{i,j} \left(A_i^{(0)}(p_1^{\lambda_1}, \dots, p_n^{\lambda_n}) \right)^\dagger C_{ij}^{(1)} A_j^{(1)}(\mu_R, p_1^{\lambda_1}, \dots, p_n^{\lambda_n}) \quad (\text{I.9})$$

$$\tilde{B}_n^{kl}(\{\lambda_h\}) = \sum_{i,j} \left(A_i^{(0)}(p_1^{\lambda_1}, \dots, p_n^{\lambda_n}) \right)^\dagger \tilde{C}_{ij}^{(0),kl} A_j^{(0)}(p_1^{\lambda_1}, \dots, p_n^{\lambda_n}) \quad (\text{I.10})$$

$$S_{n+1}(\{\lambda_h\}) = \left| \sum_{\lambda_P=\pm} \mathcal{A}_n(p_1^{\lambda_1}, \dots, p_{k-1}^{\lambda_{k-1}}, p_{k+l}^{\lambda_P}, p_{k+1}^{\lambda_{k+1}}, \dots, p_{l-1}^{\lambda_{l-1}}, p_{l+1}^{\lambda_{l+1}}, \dots, p_{n+1}^{\lambda_{n+1}}) \mathcal{S}^{kl \rightarrow P}(-p_{k+l}^{-\lambda_P}; p_k^{\lambda_k}, p_l^{\lambda_l}) \right|^2 \quad (\text{I.11})$$

\mathcal{D}^{kl} are the integrated dipoles and \mathcal{S} represents a polarized splitting function. The colour sums over the indices i and j run over the independent set of primitive amplitudes defined together with the colour matrices $C_{ij}^{(L)}$ and colour correlated matrices $\tilde{C}_{ij}^{(L),lm}$ whose entries are polynomials in N_c .

The subtraction terms must be expanded before they can be written in terms of helicity and colour correlated tree-level matrix elements. There are clearly four terms in the expansion though only two are independent due to parity symmetry. These are labelled using $\lambda_P = \pm$ in the amplitude and $\lambda_P^\dagger = \pm$ in the conjugate amplitude. The first of these, $(\lambda_P, \lambda_P^\dagger) = (+, -)$, is the same colour correlated born amplitudes appearing in the integrated subtraction terms while the second involves the off-diagonal elements $(\lambda_P, \lambda_P^\dagger) = (+, +)$. This term is the spin-correlated born amplitude can be written as a usual colour correlated born together with flipping the helicity of the P^{th} particle in the conjugate amplitude:

$$B_n^{\text{flip}(P),kl}(\lambda_1, \dots, \lambda_n) = \sum_{i,j} \left(A_i^{(0)}(p_1^{\lambda_1}, \dots, p_P^{-\lambda_P}, \dots, p_n^{\lambda_n}) \right)^\dagger \tilde{C}_{ij}^{(0),kl} A_j^{(0)}(p_1^{\lambda_1}, \dots, p_P^{\lambda_P}, \dots, p_n^{\lambda_n}) \quad (\text{I.12})$$

Once collected in terms of helicity summed objects, the real-subtraction terms are,

$$\sum_{\lambda_h=\pm} S_{n+1}^{kl}(\{\lambda_h\}) = D^{kl \rightarrow p}(p_k, p_l) \sum_{\lambda'_h=\pm} B_n^{kl}(\{\lambda'_h\}) + \left(D^{\text{flip}(P),kl \rightarrow P}(p_k, p_l) \sum_{\lambda'_h=\pm} B_n^{\text{flip}(P),kl}(\{\lambda'_h\}) + (c.c) \right), \quad (\text{I.13})$$

where $\{\lambda'_h\}$ is are the n -point helicity configurations. Note that we have used parity symmetry to write,

$$\sum_{\lambda_h=\pm} \tilde{B}_n^{kl}(\{\lambda_{h=1,n}\}) = 2 \sum_{\lambda_h=\pm} \tilde{B}_n^{kl}(\{+, \lambda_{h=2,n}\}). \quad (\text{I.14})$$

While the first term proportional to the dipole $D^{kl \rightarrow P}$ is phase independent, the spin correlated term depends on a complex phase which cancels with the phase in $D^{\text{flip}(P),kl \rightarrow P}$. When passing spin correlated amplitudes via the BLHA interface the necessary phase information is extracted using the polarization vector $\varepsilon_+^\mu(p, q)$ provided via the function,

PolVec(double* p, double* q, double* eps)

For the current set-up we pass the helicity summed objects between NJET [201] and the Herwig++/Matchbox [164]. The BLHA2 keyword `AmplitudeType` takes options defined as follows

| <code>AmplitudeType</code> | function |
|----------------------------|---|
| <code>loop</code> | $\sum c(1, \mu_R) V_{\mu_R, n}(h)$ |
| <code>tree</code> | $\sum c(1, \mu_R) B_n(h)$ |
| <code>cctree</code> | $\sum c(1, \mu_R) B_n^{kl}(h)$ |
| <code>sctree</code> | $\sum c(1, \mu_R) B_n^{\text{flip}(P), kl}(h, m)$ |

The colour correlated tree amplitudes form a real symmetric $n \times n$ matrix which is accessed using the `OLP_EvalSubProcess2` function to return a $n(n-1)/2$ array of type `double` where B^{kl} is the $k + l(l-1)/2$ -th element. The spin correlated amplitudes form a complex $n \times n$ matrix which is accessed using the `OLP_EvalSubProcess2` function to return a $2n^2$ array of type `double` where $\text{Re}(B^{\text{flip}(P), kl})$ is the $(2k + 2nl)$ -th element and $\text{Im}(B^{\text{flip}(P), kl})$ is the $(2k + 2nl + 1)$ -th element.

1.2 Proof of Concept and Validation: Multi-jet Production

In this section we describe the application of the BLHA2 interface to calculate jet production at NLO QCD. We have compared all tree-level and one-loop amplitudes required for two and three jet production, as well as selected colour and spin correlated matrix elements to NLOJet++ [93] (via a dedicated interface [202]) and found full agreement. Let us stress that the comparison of the one loop contributions, *i.e.* one loop matrix elements and integrated subtraction dipoles, also provided another non-trivial check of the framework, since the conventions of the finite one loop pieces differ between NLOJet++ and the BLHA2 interface. On top of this, there are different regularization schemes used, however both of these complications did not complicate the implementation as Matchbox provides a transparent way of communicating conventions on the one loop contributions to the integrated dipoles. To present few more details on how the interface is working, we show an example BLHA2 order file produced by Herwig++ for the $d\bar{d} \rightarrow gg$ channel, and the contract file produced by `njet.py` in figure I.1. These files are automatically processed; Herwig++ is run as with any other builtin process by a simple addition to the Matchbox input file,

```
library HwMatchboxNJet.so
cd /Herwig/MatrixElements/Matchbox/Amplitudes
create Herwig::NJetAmplitude NJet
insert /Herwig/MatrixElements/Matchbox/PPFactory:Amplitudes 0 NJet
```

and the process of interest, say three-jet production, is enabled by

```
set /Herwig/MatrixElements/Matchbox/PPFactory:OrderInAlphaS 3
do /Herwig/MatrixElements/Matchbox/PPFactory:Process p p j j j
```

Note that the coupling power is always taken with respect to the leading order process.

Besides the low-level check of matrix elements on a point-by-point basis, Matchbox offers a variety of checks to enable a full NLO cross section calculation, including the cancellation of ϵ -poles between integrated subtraction terms and one-loop amplitudes, as well as tests of the singularity cancellation in the unresolved limit of the real emission matrix element. In figures I.2 and I.3 we present few examples of this kind, showing full functionality of the setup.

1.3 Outlook & Conclusions

We have implemented a tested the BLHA2 interface as a method to pass all loop-level and tree-level-type matrix elements relevant for all components of the NLO calculation. The new

```

# OLP order file created by Herwig++/Matchbox
InterfaceVersion BLHA2
Model SM
CorrectionType QCD
IRregularisation CDR
Extra HelAvgInitial no
Extra ColAvgInitial no
Extra MCSymmetrizeFinal no
NJetReturnAccuracy yes
NJetRenormalize yes
NJetNf 2
AlphasPower 2
AlphaPower 0
AmplitudeType loop
1 -1 -> 21 21
AmplitudeType cctree
1 -1 -> 21 21
AmplitudeType sctree
1 -1 -> 21 21
AlphasPower 3
AmplitudeType tree
1 -1 -> 21 21 21

```

```

# OLP order file created by Herwig++/Matchbox
# Generated by njet.py, do not edit by hand.
# Signed by NJet 364882640.
# 1021 1 1e-05 0.01 2 3 1 1 3 2
InterfaceVersion BLHA2 | OK
Model SM | OK
CorrectionType QCD | OK
IRregularisation CDR | OK
Extra HelAvgInitial no | OK
Extra ColAvgInitial no | OK
Extra MCSymmetrizeFinal no | OK
NJetReturnAccuracy yes | OK
NJetRenormalize yes | OK
NJetNf 2 | OK
AlphasPower 2 | OK
AlphaPower 0 | OK
AmplitudeType loop | OK
1 -1 -> 21 21 | 1 1 # 2 1 0 1 (-1 -2 3 4)
AmplitudeType cctree | OK 1 -1 -> 21 21 | 1 2 # 2 1
0 3 (-1 -2 3 4)
AmplitudeType sctree | OK
1 -1 -> 21 21 | 1 3 # 2 1 0 5 (-1 -2 3 4)
AlphasPower 3 | OK
AmplitudeType tree | OK
1 -1 -> 21 21 21 | 1 4 # 6 1 0 2 (-1 -2 3 4 5)

```

Fig. I.1: Example order and contract files of the BLHA2 interface.

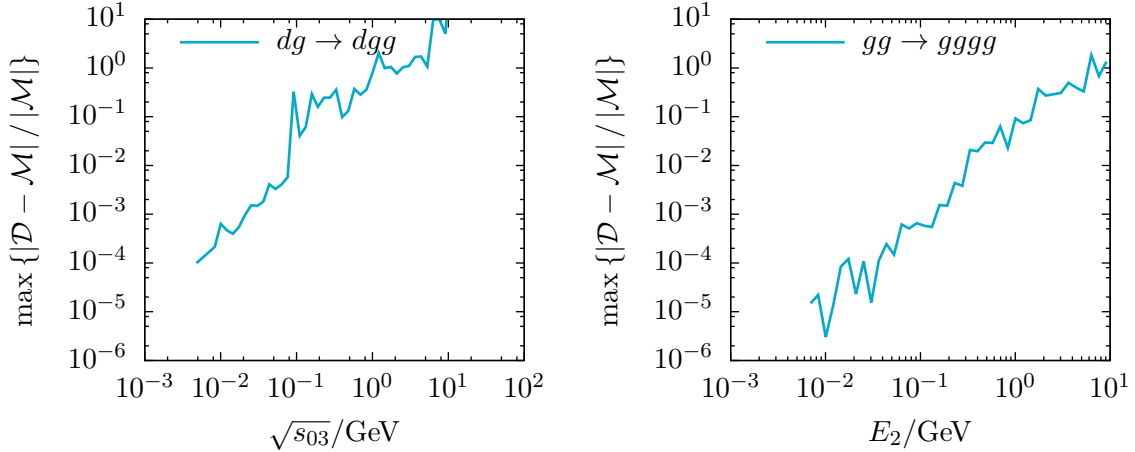


Fig. I.2: Validation of the subtraction for a collinear (left) and a soft limit (right). We show the maximum relative deviation of the subtraction terms to the real emission matrix element, as a function of $s_{03} = 2p_0 \cdot p_3$ for configurations which are collinear but not soft, and as a function of the gluon energy E_2 for purely soft configurations. The incoming partons are labelled 0,1 and outgoing partons are numbered from 2 onwards.

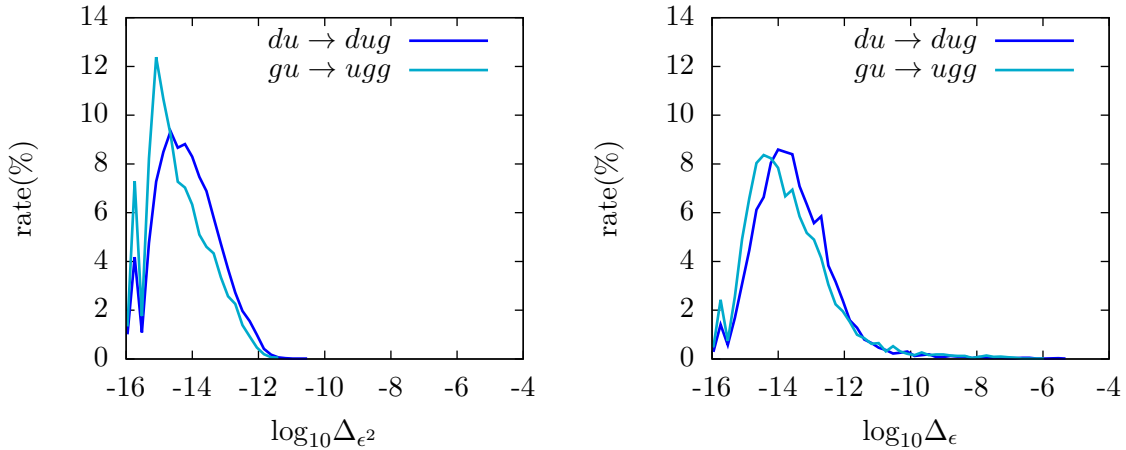


Fig. I.3: Validation of the integrated subtraction terms. We show the distribution of events as a function of the relative difference of the ϵ^2 and ϵ pole coefficients, Δ_{ϵ^2} and Δ_{ϵ} respectively.

features of the BLHA2 allow this to be done in a relatively clean way allowing us to make maximum use of the matrix elements computed by automated codes. The code used to produce the matrix elements is publicly available from <https://bitbucket.org/njet/njet/>. The Herwig++ counterpart of the interface will be included in the next 2.7.x series release of Herwig++, see <http://herwig.hepforge.org>, and the present work has formed the basis for interfacing Herwig++ to other OLP codes as well [203].

Helicity sampling has been shown to be advantageous in a number of cases. From the formalism we used here it is clear that the born, virtual and integrated subtraction contributions can have the sum over helicity trivially moved into the MC program at the cost of passing one extra integer defining the helicity configuration. The real+subtraction terms on the other hand are not so trivial to decompose since the sum of dipoles does not commute with the sum over helicities. It would be interesting to apply the techniques developed in reference [204] for future applications of the BLHA interface. We would also like to point out further work in extending the BLHA2 standard to a level where actual amplitudes can be interfaced, this being very beneficial to enable recent developments on improved parton showering along the lines of [205, 206]. We will of course also explore phenomenological studies on multi-jet production within a matched or merged simulation setup.

Acknowledgements

We would like to thank the Les Houches workshop for hospitality offered during which some of the work contained herein was performed. SP acknowledges partial support from the Helmholtz Alliance ‘Physics at the Terascale’. VY acknowledges support by the Alexander von Humboldt Foundation, in the framework of the Sofja Kovaleskaja Award 2010, endowed by the German Federal Ministry of Education and Research.

2 GoSam plus Herwig++/Matchbox²

We describe how GOSAM and HERWIG++ are linked via the new version of the Binoth-Les Houches-interface (BLHA2), emphasizing new features of the interface. We also give a phenomenological example and comment on prospects to match NLO calculations with a parton shower and hadronisation in a fully automated way.

2.1 Introduction

Next-to-leading order (NLO) calculations matched to a Monte Carlo program which can provide not only the phase space integration, but also a parton shower and subsequent hadronisation, should be the new standard for LHC data analysis.

To this aim, automated tools providing the various ingredients of an NLO calculation at parton level are indispensable. These tools comprise a part providing the one-loop virtual corrections, and parts providing the ingredients which do not involve loops, i.e. the real radiation matrix element, the subtraction terms for the infrared singularities, and the Born matrix element. The full NLO code therefore can be divided into the categories “one-loop provider” (OLP) and “Monte Carlo program” (MC).

The past years have seen enormous progress in the development of programs for automated one-loop calculations for multi-particle final states [4–8, 201, 207–210]. On the Monte Carlo side, a lot of progress has been achieved in matching NLO real radiation matrix elements with a parton shower, see e.g. [26, 28–30, 37, 211].

The various one-loop matrix element generators and Monte Carlo programs each have different focuses and strengths. Therefore, in order to achieve maximal flexibility in connecting various OLP’s with different MC’s, it is desirable to have a standard interface allowing to link these two parts smoothly. Such an interface has been initiated at the Les Houches 2009 workshop [198], known as the “Binoth-Les Houches-Accord” (BLHA) and has been updated in 2013 [199]. The latter update will be called BLHA2 in the following.

Here we present the combination of the one-loop program GOSAM [4] with the Monte Carlo program HERWIG++ [164, 212] based on the BLHA2 interface, with particular emphasis on the new features of the interface.

2.2 Linking GoSam and Herwig++/Matchbox via the BLHA2 interface

Various function calls, as defined according to BLHA2, have been implemented on both sides in order to enable the communication between OLP and MC.

2.2.1 Herwig++/Matchbox

On the side of HERWIG++ the interface has been realized within the MATCHBOX module [28], providing functionality to perform hard process generation at the level of NLO QCD accuracy and easing the setup of run time interfaces to external codes for hard process generation. HERWIG++/MATCHBOX provides thereby the phase space generation and integration, as well as the organization of the matrix elements and of the appropriate real radiation subtraction terms for the infrared singular regions. The class `GoSamAmplitude` has been implemented in the MATCHBOX module, to be included through the shared object file `HwMatchboxGoSam.so`, which itself is globally operated through the class `MatchboxOLPME`.

To configure HERWIG++ accordingly a prefix with the installation path (DIR) to GOSAM has to be specified prior to the installation: `./configure -with-gosam=DIR`.

²J. Bellm, S. Gieseke, N. Greiner, G. Heinrich, S. Plätzer, C. Reuschle and J.F. von Soden-Fraunhofen

The user only needs to enable the interface from the HERWIG++/MATCHBOX process input files, using for example the following syntax:

```
library HwMatchboxGoSam.so
cd /Herwig/MatrixElements/Matchbox/Amplitudes
create Herwig::GoSamAmplitude Gosam
set Gosam:GoSamSetup /desiredpath/gosam_setup.in
insert /Herwig/MatrixElements/Matchbox/PPFactory:Amplitudes 0 Gosam
```

where a `GoSamAmplitude` object `Gosam` will be created. This amplitude can be used to calculate a specific process, which can be enabled from the HERWIG++/MATCHBOX process input files, as is usual for a HERWIG++/MATCHBOX calculation, using for example the following syntax:

```
do PPFactory:Process p p e+ e- j
```

upon which the calculation will be performed fully automatically. This includes Catani-Seymour dipole subtraction for NLO calculations as well as matching procedures if required from the input file, etc. From a user point of view this means that, except for creating and inserting the `GoSamAmplitude` object, nothing changes.

Internally, according to BLHA, the process setup is communicated between OLP and MC by exchanging an order file and a contract file. On the side of HERWIG++/MATCHBOX this is attended to by the functions `GoSamAmplitude::fillOrderFile()` and `GoSamAmplitude::checkOLPContract()`, where an intermediate process-ID map is used to translate the numbering of the process ID's between GOSAM and HERWIG++/MATCHBOX. The contract is "signed" by calling the appropriate GOSAM-OLP python script within the function `GoSamAmplitude::signOLP()`, whereupon the GOSAM-OLP python script reads the GOSAM configuration input file `/desiredpath/gosam_setup.in`³. Subsequently the process setup is started and the corresponding FORTRAN90 matrix elements are created by GOSAM, organized into the various subprocesses and helicity configurations thereof. The function `GoSamAmplitude::buildGoSam()` then calls the appropriate `make` routine, provided by GOSAM, whereupon the compilation of the various FORTRAN90 matrix elements is performed.

Since HERWIG++/MATCHBOX does momentarily not possess the means to create its own tree-level matrix elements, GOSAM is also used to provide the various tree-level matrix elements (usual Born matrix elements as well as spin- and colour-correlated Born matrix elements). The various subprocesses, specified in the order/contract file, are therefore grouped into various amplitude types (`Tree`, `ccTree`, `scTree` and `Loop`) as well as the different powers of α_s , as specified according to BLHA2.

The function `GoSamAmplitude::startOLP()` loads the object file `libgolem_olp.so` from the FORTRAN90 matrix element compilation. It also calls the GOSAM FORTRAN90 function `OLP_Start()`, as well as the GOSAM FORTRAN90 function `OLP_SetParameter()` to set the initial parameters of the calculation. If required, it also calls for the GOSAM FORTRAN90 function `OLP_PrintParameter()`, which prints the parameters of the calculation into an output file. From the HERWIG++/MATCHBOX process input files this feature can be enabled as follows (see example above):

```
set Gosam:PrintParameter On
```

The runtime evaluation for each phase-space point is performed by the functions

```
GoSamAmplitude::evalSubProcess(),
GoSamAmplitude::evalColourCorrelator(),
GoSamAmplitude::evalSpinColourCorrelator(),
```

³Various GOSAM specific options can be set within the GOSAM configuration input file.

depending on the various amplitude types. Within those functions the GOSAM FORTRAN90 function `OLP_Eval_SubProcess2()` is called, where the type of output depends on the amplitude type in question.

To acquire the spin-correlated Born matrix elements the exchange of the polarization vectors of the associated gluons is required. For a specific spin-correlation the corresponding polarization vector is communicated through the function `GoSamAmplitude::plusPolarization()` and the GOSAM FORTRAN90 function `OLP_Polvec()`, as specified according to BLHA2. The spin-colour-correlated Born matrix element can be written as

$$\langle \mathcal{M}_\mu | \mathbf{C}_{ij} C^{\mu\nu} | \mathcal{M}_\nu \rangle = \frac{1}{Q^2} \left[\langle \mathcal{M} | \mathbf{C}_{ij} | \mathcal{M} \rangle \left(-CQ^2 + |\epsilon_+ \cdot q|^2 \right) + 2\text{Re} \left((\epsilon_+ \cdot q)^2 \begin{cases} \langle \mathcal{M}_- | \mathbf{C}_{ij} | \mathcal{M}_+ \rangle & \text{outgoing } g \\ \langle \mathcal{M}_+ | \mathbf{C}_{ij} | \mathcal{M}_- \rangle & \text{incoming } g \end{cases} \right) \right] \quad (\text{I.15})$$

where \mathcal{M}_\pm refers to the amplitude with positive/negative gluon helicity and a sum over helicities is understood if \mathcal{M} carries no subscript. The polarization vector which is communicated through the function `OLP_Polvec()` is hereby ϵ_+ [199] and the standard is that of outgoing gluons, i.e. $\langle \mathcal{M}_- | \mathbf{C}_{ij} | \mathcal{M}_+ \rangle$ for the spin-correlated result. In the case of incoming gluons the polarization vectors are simply complex conjugated within the function `GoSamAmplitude::plusPolarization()`, which yields the correct result since only the real part is of interest here.

The calls to the FORTRAN90 functions of GOSAM are realized by external function calls in the class `GoSamAmplitude`:

```
extern "C" void OLP_Start(const char*, int*);
extern "C" void OLP_Polvec(double*, double*, double*);
extern "C" void OLP_SetParameter(char*, double*, double*, int*);
extern "C" void OLP_PrintParameter(char*);
extern "C" void OLP_EvalSubProcess2(int*, double*, double*, double*, double*);
```

The class `GoSamAmplitude` also provides an automated way to hand over the correct electroweak parameters according to the chosen electroweak scheme in the HERWIG++ process input files, via the function `OLP_SetParameter()`. GOSAM automatically chooses the appropriate scheme upon recognizing the corresponding electroweak parameters. Note also that, regarding regularization schemes, conventional dimensional regularization (`cdr`) as well as dimensional reduction (`dred`) are supported and yield the same results.

2.2.2 GoSam

On the GOSAM side, dedicated OLP modules are provided which host the interface. It should be emphasized again that the user does not need to have a detailed knowledge of these modules, but only interacts via the user interface of the Monte Carlo program, in the present case the HERWIG++ process input files.

The function `OLP_Start(char* fname, int* ierr)`, which was already in place with the first version of the BLHA interface, takes the name of the contract file as first argument and initializes the OLP setup. The function `OLP_Info(char olp_name, char olp_version, char message)` prints the GOSAM version, svn revision number and references which should be cited when using the program.

An important new feature of BLHA2 is the function `OLP_SetParameter()`, which allows to set parameters like α_s , α , masses, widths etc. These parameters are set in the HERWIG++ process input files. Note that this function can also be used to exchange dynamic parameters like $\alpha_s(\mu^2)$ at runtime.

| | |
|---|---|
| <pre> # OLP order file created by # Herwig++/Matchbox for GoSam InterfaceVersion BLHA2 MatrixElementSquareType CHsummed CorrectionType QCD IRregularisation CDR AlphasPower 1 AmplitudeType ccTree 1 -1 - > -11 11 21 ... 21 3 - > -11 3 11 AmplitudeType scTree 1 -1 - > -11 11 21 ... 21 3 - > -11 3 11 AmplitudeType Loop 1 -1 - > -11 11 21 ... 21 3 - > -11 3 11 AlphasPower 2 AmplitudeType Tree 1 1 - > -11 1 1 11 ... 21 21 - > -11 -3 3 11 </pre> | <pre> # vim: syntax=olp #@OLP GOSAM 2.0.beta #@IgnoreUnknown False #@IgnoreCase False #@SyntaxExtensions InterfaceVersion BLHA2 OK MatrixElementSquareType CHsummed OK CorrectionType QCD OK IRregularisation CDR OK AlphasPower 1 OK AmplitudeType ccTree OK 1 -1 - > -11 11 21 1 131 ... 21 3 - > -11 3 11 1 70 AmplitudeType scTree OK 1 -1 - > -11 11 21 1 145 ... 21 3 - > -11 3 11 1 71 AmplitudeType Loop OK 1 -1 - > -11 11 21 1 137 ... 21 3 - > -11 3 11 1 63 AlphasPower 2 OK AmplitudeType Tree OK 1 1 - > -11 1 1 11 1 42 ... 21 21 - > -11 -3 3 11 1 106 </pre> |
|---|---|

Fig. I.4: Automatically created order and contract file for Z+jet. The various subprocesses are given a process ID by the OLP.

At runtime, the OLP returns the values for the virtual amplitude to the MC via the function `OLP_EvalSubProcess2()`. As compared to the original function `OLP_EvalSubProcess()`, the new function `OLP_EvalSubProcess2()` does not contain the passing of coupling constants anymore, as their values are now passed separately by using `OLP_SetParameter()`⁴. It also has a new argument appended which serves to assess the accuracy of the result returned by the OLP. The arguments of `OLP_EvalSubProcess2()` are described in detail in ref. [199]. Here we point out that the amplitude types `scTree` and `ccTree`, denoting spin- and colour-correlated Born matrix elements, can also be provided by GOSAM, as described already in section 2.2.1. This allows HERWIG++/MATCHBOX to construct the real radiation subtraction terms for the infrared singular regions. To this end GOSAM also provides the function `OLP_Polvec()` as described in section 2.2.1.

At this point we would like to stress another useful feature of GOSAM, which is the ability to read in model files in the UFO (Universal Feynrules Output) [213] format and which is particularly useful for calculations beyond the Standard Model. The UFO format also provides human readable name attributes for the model parameters, as well as the SLHA identifiers [214], which are processed by the subroutine `read_slha_file`.

2.3 Example Z+jet at NLO

As an example we use the built-in process $pp \rightarrow Z/\gamma^* + \text{jet} \rightarrow e^+e^- + \text{jet}$ of HERWIG++/MATCHBOX and compare it against the same automatically generated GOSAM process. The corresponding, yet

⁴The function `OLP_EvalSubProcess()`, using BLHA1 conventions, is also still in operation in GoSAM.

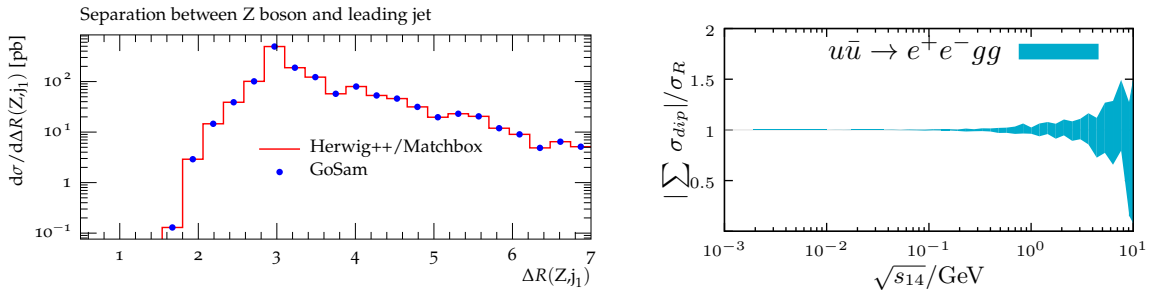


Fig. I.5: Left: The fixed order parton level R-separation between the Z boson and the leading jet in Z+jet production at NLO. Right: Testing the numerical stability in the collinear and soft region shows the expected behaviour. As an example we show the sum over all Catani-Seymour-dipoles [200] divided by the real contribution, at phase-space points where the $\bar{u}g_1$ invariant mass is smaller than 10 GeV. Here s_{14} denotes the invariant mass between the \bar{u} and the first gluon in the list.

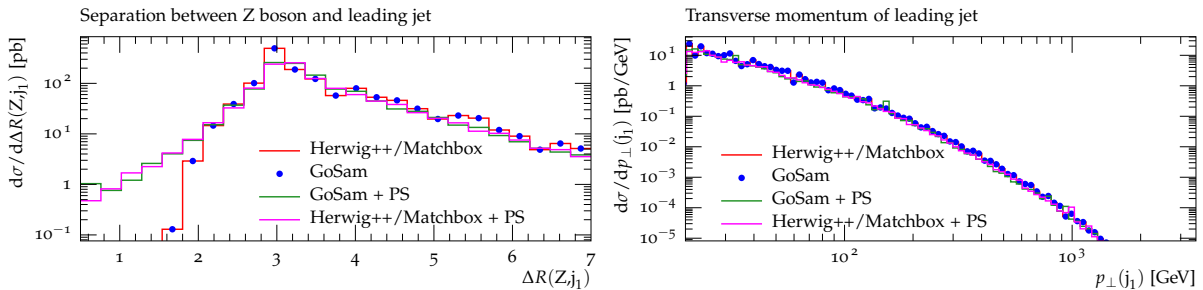


Fig. I.6: Left: The R-separation between the Z-boson and the leading jet in Z+jet production. Right: The transverse momentum of the leading jet. Both with and without parton shower matching. The – for this process – inclusive observable p_\perp of the first jet is hardly affected by the parton shower. The red and pink lines show the results with the HERWIG++/MATCHBOX built-in matrix elements, the blue dots and green lines show the results of HERWIG++/MATCHBOX with the GOSAM matrix elements.

shortened, order and contract files are shown in fig. I.4. Here we want to stress again that the whole computation proceeds fully automatically only upon a few commands in the HERWIG++ input files, which includes the automatic generation of the order and the contract file. To get agreement between the HERWIG++/MATCHBOX built-in and the GOSAM matrix elements, we need to make the same assumptions on both sides: While in the HERWIG++/MATCHBOX built-in matrix elements the diagrams with photon- and Z-radiation from bottom- and top-triangles are not implemented, because they are numerically negligible, GOSAM produces these by default. For the comparison, these contributions were eliminated by using the appropriate filter options in the GOSAM configuration input file.

To calculate the cross sections and distributions shown in fig. I.5 and fig. I.6 we use the minimal set of cuts

$$66 \text{ GeV} < m_{e^+e^-} < 116 \text{ GeV}, \quad p_{T,j} > 20 \text{ GeV}, \quad |\eta_j| < 5,$$

and the dynamical scale

$$\mu_r = \mu_F = m_{e^+e^-}.$$

The scale choice may not be ideal from a phenomenological point of view, but it shows that dynamical scales work fine within the interface. The shower matched distributions are

obtained using the dipole shower outlined in [215] and a modified version of the MC@NLO-type matching described in [28], which accounts for subleading colour contributions. The matching can be enabled, as is usual for MATCHBOX processes, with a single command line:

```
set PPFactory:ShowerApproximation DipoleMatching
```

2.4 Conclusions & Outlook

The combination of one-loop providers (OLP) and Monte Carlo programs (MC) using a standardized interface has been proven to be a successful strategy for automated NLO calculations. We have presented phenomenological results obtained through the automatized combination of the Monte Carlo program HERWIG++/MATCHBOX with the one-loop program GOSAM. The link between the two codes is based on the new version of the Binoth-Les-Houches interface (BLHA2), which has been worked out at the Les Houches 2013 workshop, including proof-of-concept interfaces to other OLPs, [216]. In particular, the new feature to pass spin- and colour-correlated tree level matrix elements from the one-loop provider to the Monte Carlo program allows the HERWIG++/MATCHBOX module to provide the full NLO real radiation part. As a first application we calculated the NLO QCD corrections to Z+jet production at the LHC. We validated the results with the GOSAM matrix elements against a corresponding built-in implementation in HERWIG++/MATCHBOX.

In combination with the HERWIG++ shower, the full chain from process definition to the production of showered event samples at NLO accuracy is thus provided in a fully automated way. This opens the door for a multitude of phenomenological applications. As both GOSAM and HERWIG++ are also able to import model files in UFO format, and offer various features which are important for calculations involving unstable particles, the applications are not limited to QCD, but also well suited for electroweak corrections and BSM calculations.

Acknowledgements

This work was supported in part by the Marie Curie Initial Training Network *MCnetITN*, the German Federal Ministry of Education and Research (BMBF), the Helmholtz Alliance “Physics at the Terascale” and the Karlsruhe School of Elementary Particle and Astroparticle Physics (KSETA).

Chapter II

Parton distribution functions

1 PDF dependence of the Higgs production cross section in gluon fusion from HERA data¹

We document a detailed comparison of theoretical settings and fitting methodologies employed in the determination of parton distribution functions (PDFs) of the proton, focusing on the factors driving the PDF uncertainty in Higgs boson production in the gluon fusion channel. In order to understand the moderate discrepancies among predictions obtained using CT10, HERAPDF1.5, MSTW08 and NNPDF2.3 PDF ensembles, we first complete a benchmarking comparison of computations of NNLO neutral current DIS cross sections used in the fitting codes of these groups. Then, we compare results of the fits performed by following the methodologies of the four groups to a reduced common set of DIS data from HERA experiments. We conclude that the predictions for $gg \rightarrow H$ observables, obtained when the PDFs are constrained using only the HERA DIS data, are in fairly good agreement, within the PDF uncertainty.

1.1 Introduction

Following the discovery of the Higgs boson at the LHC, it is crucial to measure all of its properties precisely in order to identify the underlying mechanism of electroweak symmetry breaking. PDF uncertainty is one of the limiting factors in the accuracy with which one can extract the Higgs boson couplings from experimental data. Its control is needed for precise Higgs characterization [40].

It has been shown that recent NNLO PDFs from various PDF analysis groups are in generally good agreement. However, moderate differences due to the gluon PDFs are observed around the Higgs mass region, at ≈ 125 GeV. This leads to discrepancies at the level of 1 to 2 standard deviations [217] in the predictions for the Higgs production cross sections through gluon fusion, which is the dominant production channel at the LHC. In part because the origin of this spread in the results is not understood, the PDF4LHC convention [218], adopted by the Higgs working group [38, 40], recommends a conservative estimate for the combined PDF+ α_s uncertainty based on the envelope of results obtained using different PDF sets. If this sizable uncertainty is of theoretical origin, it would remain irreducible unless its source is identified. Whereas the problem may be resolved after including more experimental data, this is by no means guaranteed, and thus it is important to investigate the origin of the differences among the various PDF sets and, if possible, reduce or even eliminate it.

There have been in the past several related PDF benchmarking studies, some in the context of other Les Houches workshops. The evolution of PDFs was benchmarked in ref. [219], where the HOPPET [220] and PEGASUS [221] codes were compared, including the effect of scale variations. This exercise was extended within the context of the HERA-LHC workshop to NNLO evolution and polarized PDF evolution [222]. Differences in general-mass heavy-quark schemes for DIS charm structure functions, $F_{2,c}$, were studied in detail in ref. [160], where good agreement between the ACOT, FONLL and TR schemes was found up to different treatments of powerlike corrections. Finally, other recent benchmarking exercises have focused on the comparison of PDFs and their predictions for LHC cross sections [217, 223–227], and the

¹A. Cooper-Sarkar, S. Forte, J. Gao, J. Huston, P. Nadolsky, J. Pumplin, V. Radescu, J. Rojo, R. Thorne and C.-P. Yuan

mentioned differences in the gluon PDFs were already noted.

The main goal of this contribution is to begin a benchmarking exercise aimed at advancing the control of PDF dependence of the $gg \rightarrow H$ cross section. We will restrict ourselves to the comparison of the PDFs based on the general-mass schemes for heavy-quark scattering contributions, as it has been noted in a number of studies [228–231] that the PDFs (and α_s) can differ rather significantly if a fixed-flavor number (FFN) scheme is used.² The recent NNLO sets utilizing the general-mass schemes include CT10 [233], HERAPDF1.5 [234], MSTW2008 [235] and NNPDF2.3 [236]. Except for HERAPDF1.5, which is based on inclusive HERA data only, three other PDF sets include information from a variety of data sets from fixed-target and collider DIS, as well as from hadron-hadron scattering processes, including, in some cases, the LHC data. Detailed comparisons of these NNLO PDFs and the respective LHC predictions can be found in a recent benchmarking study [217]. In all these fits, the backbone of the fit is provided by the combined HERA-1 inclusive DIS data [237], which also plays an important role in constraining the gluon PDFs in the Higgs mass region [238]. Recently combined charm quark production measurements at HERA have also been published [239], which introduce an additional constraint on the gluon PDF.

Given the relevance of the HERA data for pinning down the gluon PDF, and the fact that this data set underwent careful examination of all the experimental uncertainties, we have chosen to initiate this benchmarking exercise by first studying the fits that include exclusively the HERA-1 data. In this highly controlled environment, we can compare the output from the different fitting codes and try to isolate possible sources of discrepancy related to, for example, implementation of reduced cross section calculations, alternative parametrizations, kinematical cuts used in the fits, and the different definitions of χ^2 used in determining the fit quality. We can then study how these differences translate into the predictions for Higgs cross sections in the gluon fusion channel.

As a prerequisite for this benchmarking exercise, we compared the NNLO QCD predictions for the neutral-current DIS cross sections from four different codes, but always using the same PDF set. This is an important starting point: we show that, when all groups use common PDFs and settings, they find good agreement among their NC DIS cross sections, with (small) remaining differences arising from known sources such as the selection of the heavy-quark scheme.

This contribution is organized as follows. In Section 2 we briefly recall the status of the PDF dependence of the NNLO Higgs cross section in gluon fusion. In Section 3 we present the results of the benchmarking of the NNLO neutral current DIS structure functions from different groups using a common PDF set. Section 4 contains the main results of this study, where fits to HERA only data are performed, and the impact of various theoretical and methodological settings is assessed. Finally in Section 5 we summarize our main results and outline the continuation of this benchmarking exercise beyond the HERA-only fits.

1.2 The Higgs cross section via gluon fusion obtained with recent NNLO PDF sets

We first review the settings of the four recent NNLO PDF determinations that will be studied in this paper. Table II.1 summarizes the heavy-quark scheme, the scale at which the PDFs are parametrized, the charm-quark mass, and the kinematic cuts on DIS data. Note that, in addition to these differences in settings, the four PDF analyses also differ in the data sets that they include. We compare the corresponding predictions for the Higgs cross section in the gluon fusion channel in Table II.2 and Fig. II.1. These predictions use versions of the PDF sets with a common $\alpha_s(M_Z)$ value of 0.118 and are calculated with iHixs1.3 [240] at NNLO in QCD,

²Studies of the gluon PDF and predictions for the Higgs and other benchmark LHC cross sections in the FFN scheme are available in [226, 227, 232].

with both Higgs boson mass and QCD scales set to 125 GeV in the heavy top-quark limit. We show the PDF uncertainties at the 68% confidence level (c.l.). For the LHC at 8 TeV, the two extreme results, CT10 and NNPDF2.3, differ by about 4%, or 2σ if their uncertainties are added in quadrature. This spread is the origin of the significant PDF+ α_s uncertainty in the $gg \rightarrow H$ channel [40]. A similar results holds for the LHC at 14 TeV.

| PDFs set | Ref. | Initial scale [GeV] | Heavy-quark scheme | m_c mass [GeV] | Q^2 cut $\geq \text{GeV}^2$ | W^2 cut $\geq \text{GeV}^2$ |
|------------------------|-------|---------------------|----------------------|------------------|-------------------------------|-------------------------------|
| CT10 | [233] | 1.3 | S-ACOT- χ [241] | 1.3 | 4 | 12.25 |
| HERAPDF1.5 | [234] | 1.378 | default TR' | 1.4 | 3.5 | N.A.* |
| MSTW'08 | [235] | 1.0 | default TR' [242] | 1.4 | 2.0 | 15.0 |
| NNPDF2.3 ($N_f = 5$) | [236] | 1.414 | FONLL-C [243] | 1.414 | 3.0 | 12.5 |

*All HERA data have $W^2 > 350 \text{ GeV}^2$.

Table II.1: Basic inputs of the recently published NNLO PDFs based on a GM-VFN scheme.

| σ_H [pb] | CT10 | MSTW'08 | NNPDF2.3 | HERAPDF 1.5 |
|-----------------|------------------|------------------|------------------|------------------|
| LHC 8 TeV | 18.36 ± 0.35 | 18.78 ± 0.31 | 19.23 ± 0.21 | 18.63 ± 0.23 |
| LHC 14 TeV | 47.60 ± 1.02 | 48.71 ± 0.77 | 49.76 ± 0.47 | 48.18 ± 0.47 |

Table II.2: Predictions for inclusive cross sections of SM Higgs boson production through gluon fusion utilizing recently published NNLO PDFs.

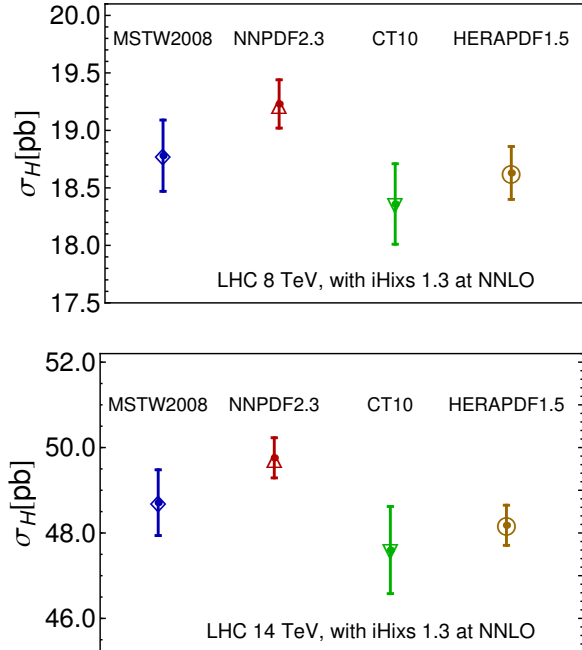


Fig. II.1: Predictions for inclusive cross sections of the SM Higgs boson production through gluon fusion based on recently published NNLO PDFs.

These discrepancies of the Higgs cross sections can be traced back to the differences in the normalization and shape of the corresponding gluon PDFs, as shown in Fig. II.2. In this plot all gluon PDFs are normalized to the gluon PDF of the first, or central, set of the NNPDF2.3

ensemble, and only the PDF uncertainty of the NNPDF2.3 ensemble is shown in the figure for simplicity. The three vertical lines indicate the x values of 0.005, 0.01, and 0.02, covering typical x values for Higgs production in the central rapidity region, $x = m_H/\sqrt{s} \sim 0.016$ (0.009) for LHC 8 (14) TeV. We can see that at $Q = 85$ GeV, and for x from 0.005 to 0.1, the gluon PDF from CT10 lies below that of NNPDF2.3. MSTW lie in between, while HERAPDF is close to CT10 at $x < 0.02$ and larger than CT10 at $x > 0.02$. Fig. II.3 shows a comparison of the gluon-gluon parton luminosity as a function of the invariant mass of the final state. The factorization scale is set to the invariant mass. The vertical line indicates the mass of the SM Higgs boson at 125 GeV. For higher invariant masses (> 400 GeV), all predictions are within 68% c.l. uncertainties of NNPDF2.3 until very high masses, (> 1000 GeV).

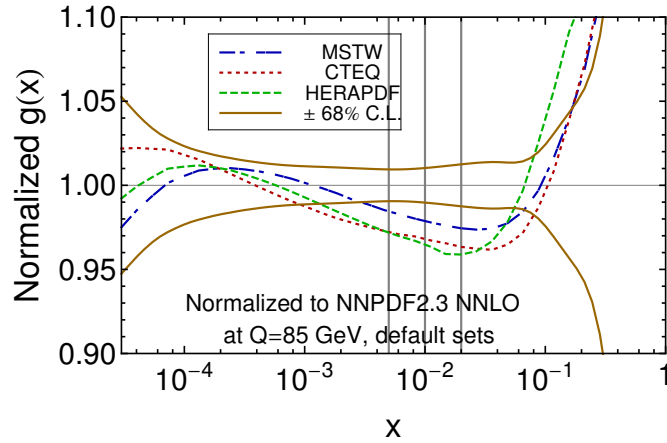


Fig. II.2: Comparison of central gluon PDFs from recently published NNLO PDF sets at a common scale $Q = 85$ GeV, normalized to the NNPDF2.3 gluon PDF and superimposed on the NNPDF2.3 68% c.l. PDF uncertainty.

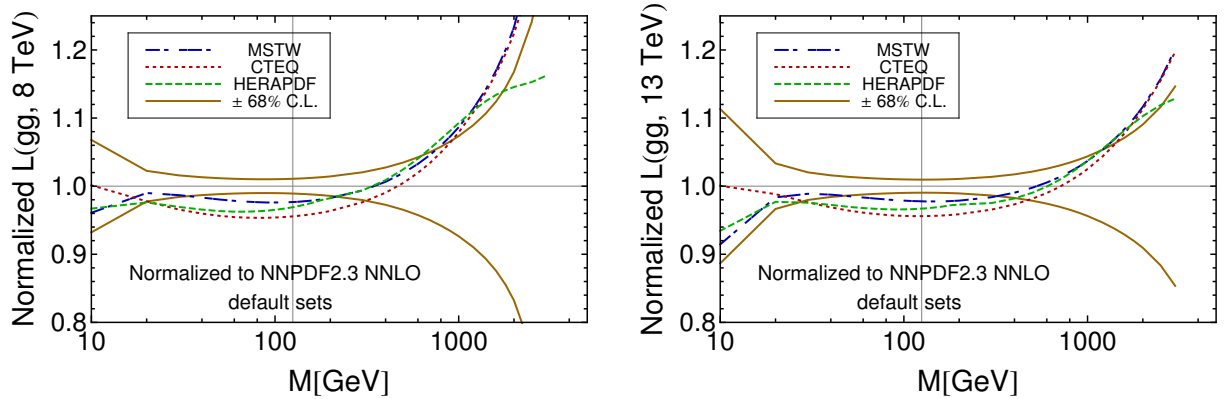


Fig. II.3: Comparison of the gluon-gluon parton luminosity as a function of invariant mass at the LHC 8 and 13 TeV from recently published NNLO PDFs, normalized to the NNPDF 2.3 central prediction. The factorization scale is set to the invariant mass. The vertical line corresponds to the mass of the SM Higgs boson.

To illustrate the sensitivity of the Higgs cross section to the gluon PDF, we also plot the rapidity distribution of the Higgs boson from gluon fusion in Fig. II.4. The predictions are calculated at NLO using MCFM 6.0 [209], with both the Higgs mass and QCD scales set at 125

GeV, and knowing that the NNLO/NLO K -factors cancel well in these ratios. We see that in the central production region ($|y| < 1$), which contributes the bulk of the total cross section, the difference between CT10 and NNPDF2.3 can reach 6%, i.e., it is larger than in the inclusive rate. At higher rapidities the predictions of all groups overshoot that of NNPDF2.3, reflecting the behavior of their large- x gluon PDFs in Fig. II.2.

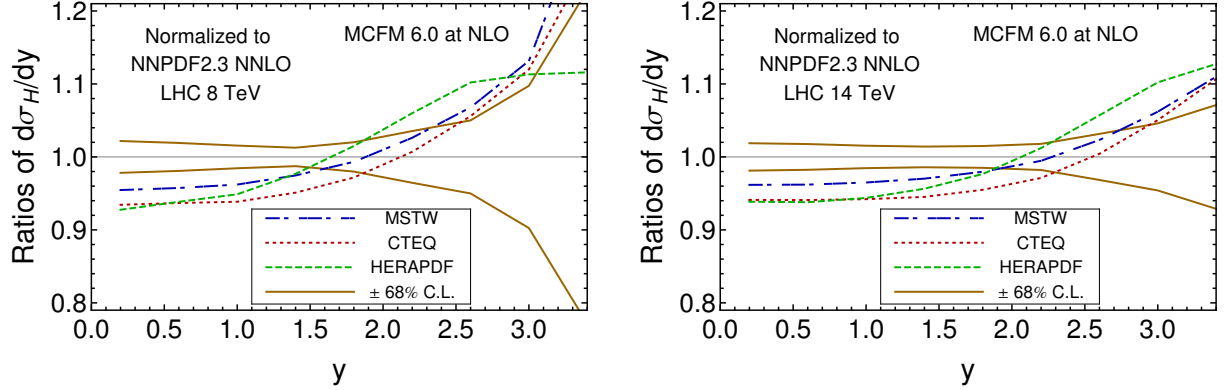


Fig. II.4: Comparison of the rapidity distribution of the SM Higgs boson in production through gluon fusion from recently published NNLO PDFs, normalized to the NNPDF 2.3 central prediction. The matrix elements of hard scattering are calculated at NLO.

In Section 4 we will investigate the origin of these differences in the gluon PDFs in a simpler scenario than that of the global fit, namely, by comparing the PDF fits of the HERA-1 DIS data set alone. However, before doing that, we want to make sure that the differences among the theoretical predictions for NNLO DIS neutral current cross sections in different fitting codes are under control, and with this aim we discuss now a new benchmarking of DIS structure functions.

1.3 Benchmark comparisons of NNLO neutral current DIS cross sections

As in the previous benchmarking studies, in this section we adopt the Les Houches toy PDFs and settings [160]. The corresponding LHAPDF grid file was generated with the APFEL program [244] by evolving the Les Houches toy PDFs from the starting scale $Q_0^2 = 2 \text{ GeV}^2$. We set the bottom and top masses to infinity, and use as a boundary condition $\alpha_s(\mu) = 0.35$ at a scale μ approaching Q_0 from below. Theoretical predictions are made at the (x, Q^2) values of the neutral current positron HERA-1 combined data set [237] for $Q^2 \geq 3.5 \text{ GeV}^2$.

Modern GM-VFN schemes, like FONLL-C [243] used by NNPDF, TR [229] used by MSTW and HERAPDF, and S-ACOT- χ [241] used by CTEQ, are expected to be very similar at NNLO, and we will demonstrate the convergence here.

For the comparisons of this section, the MSTW and HERAPDF results will both use the optimal TR heavy-quark scheme [229], instead of the standard scheme that is used in the published NNLO PDF sets. As noted in [229], the change in the TR scheme leads to only an extremely small change in the MSTW fit quality and the resulting PDFs at NNLO, i.e. small fractions of a percent in the Higgs cross section at the LHC. The NNPDF2.3 results for structure functions will be obtained using the APFEL code, instead of using the FastKernel NNPDF fitting code, because of its ease of use (the predictions of the two codes agree at the per mille level anyway.). The HERAPDF results on structure functions are obtained with the HERAFitter code [237, 245–247].

In the following, we will compare the total (with subscript “*tot*”) and charm-quark contributions (“*c*”) to inclusive F_2 , F_3 , and F_L structure functions, which are defined as in [237]

| Q^2 [GeV ²] | x | y | $F_{2,lt}$ | $F_{2,c}$ | $F_{L,lt}$ | $F_{L,c}$ | $\sigma_{r,NC}^+$ |
|---------------------------|-----------|---------|------------|-----------|------------|-----------|-------------------|
| 2.7 | 0.0000309 | 0.86398 | 0.7768 | 0.1411 | 0.1267 | 0.00844 | 0.8189 |
| 2.7 | 0.00013 | 0.20523 | 0.6275 | 0.09204 | 0.1173 | 0.00592 | 0.7163 |
| 2.7 | 0.02 | 0.00133 | 0.3871 | 0.00723 | 0.0849 | 0.00074 | 0.3943 |
| 4.5 | 0.0000618 | 0.71999 | 0.964 | 0.193 | 0.1866 | 0.01879 | 1.0583 |
| 4.5 | 0.00032 | 0.13896 | 0.7187 | 0.1136 | 0.1547 | 0.01191 | 0.8305 |
| 4.5 | 0.013 | 0.00342 | 0.4317 | 0.02011 | 0.0898 | 0.00259 | 0.4518 |
| 10. | 0.00013 | 0.85281 | 1.192 | 0.31011 | 0.2535 | 0.04618 | 1.2886 |
| 10. | 0.0008 | 0.12352 | 0.8064 | 0.16391 | 0.1758 | 0.0263 | 0.9685 |
| 10. | 0.02 | 0.00494 | 0.4614 | 0.03152 | 0.0766 | 0.00564 | 0.4929 |
| 120. | 0.0016 | 0.74111 | 1.1038 | 0.41841 | 0.179 | 0.08637 | 1.3852 |
| 120. | 0.008 | 0.14822 | 0.6915 | 0.18639 | 0.0905 | 0.03846 | 0.8761 |
| 120. | 0.18 | 0.00659 | 0.3312 | 0.00591 | 0.0128 | 0.00095 | 0.3371 |
| 650. | 0.0085 | 0.84779 | 0.768 | 0.24564 | 0.0791 | 0.04104 | 0.9216 |
| 650. | 0.032 | 0.20072 | 0.5249 | 0.09203 | 0.0364 | 0.01444 | 0.6122 |
| 650. | 0.25 | 0.02569 | 0.252 | 0.00306 | 0.0059 | 0.00032 | 0.2545 |
| 2000. | 0.032 | 0.6929 | 0.5502 | 0.10329 | 0.0328 | 0.01347 | 0.5973 |
| 2000. | 0.13 | 0.15202 | 0.3634 | 0.0164 | 0.011 | 0.00172 | 0.3698 |
| 2000. | 0.25 | 0.07905 | 0.244 | 0.00327 | 0.0049 | 0.00027 | 0.2433 |
| 8000. | 0.13 | 0.68224 | 0.3948 | 0.01837 | 0.01 | 0.00149 | 0.284 |
| 8000. | 0.18 | 0.43917 | 0.3307 | 0.00903 | 0.0069 | 0.00066 | 0.2649 |
| 8000. | 0.25 | 0.31621 | 0.254 | 0.00356 | 0.0043 | 0.00022 | 0.2148 |

Table II.3: Predictions for NC DIS structure functions and reduced cross sections from HERA-1 [237] at NNLO, obtained with the CT10 code [233] and Les Houches toy PDFs [160].

and include all scattering contributions coupled to the photon and Z boson currents. The light quark contributions (“ lt ”) are defined by subtracting the charm-quark contributions from the total structure functions. This means that F_c is defined as the structure function that one would get if only the electromagnetic charge of the charm quark was nonzero [241, 243], and then F_{lt} is implicitly defined by

$$F_{tot} \equiv F_{lt} + F_c = \sum_{l=1}^{N_l} F_l + F_c, \quad (\text{II.1})$$

where F_l is the structure function obtained when only the charge of the l -th quark is nonzero. With this definition, at NNLO F_l receives a contribution from the process with charm in the final state, such as $\gamma^*u \rightarrow uc\bar{c}$, as well as from diagrams containing the charm quark in virtual loops. Note that there is a cancellation of terms with large logs of Q^2/m_c^2 between these two contributions.

The NNLO results for $F_{2,lt(c)}$, $F_{L,lt(c)}$, and the reduced cross sections obtained for a representative subset of the HERA-1 data points, using the four different codes, are collected in Tables II.3-II.6. These tables should be useful for future comparisons, for instance for validation of structure function codes. In the following we compare and discuss these results, both at NLO and at NNLO. Comparisons at LO are not meaningful because of the different perturbative ordering between different codes.

In Fig. II.5 we plot the light structure function $F_{2,lt}$ at NLO and NNLO, normalized to the HERAPDF results. The data point indexing is ordered in increasing Q^2 (starting from $Q^2 = 2.7$ GeV²), then increasing x . We find excellent agreement at NLO among all groups, with small fluctuations at the per mille level at low Q due to numerical precision, and moderate oscillations

| Q^2 [GeV ²] | x | y | $F_{2,lt}$ | $F_{2,c}$ | $F_{L,lt}$ | $F_{L,c}$ | $\sigma_{r,NC}^+$ |
|---------------------------|-----------|---------|------------|-----------|------------|-----------|-------------------|
| 2.7 | 0.0000309 | 0.86398 | 0.7821 | 0.17992 | 0.261 | 0.01067 | 0.7628 |
| 2.7 | 0.00013 | 0.20523 | 0.6318 | 0.10519 | 0.1711 | 0.00669 | 0.7324 |
| 2.7 | 0.02 | 0.00133 | 0.3893 | 0.01013 | 0.0829 | 0.00073 | 0.3995 |
| 4.5 | 0.0000618 | 0.71999 | 0.972 | 0.2175 | 0.2507 | 0.01961 | 1.0596 |
| 4.5 | 0.00032 | 0.13896 | 0.7249 | 0.11996 | 0.1685 | 0.01122 | 0.8429 |
| 4.5 | 0.013 | 0.00342 | 0.435 | 0.02257 | 0.0885 | 0.00244 | 0.4575 |
| 10. | 0.00013 | 0.85281 | 1.2026 | 0.32346 | 0.2759 | 0.04743 | 1.2958 |
| 10. | 0.0008 | 0.12352 | 0.8135 | 0.16653 | 0.1771 | 0.02543 | 0.9783 |
| 10. | 0.02 | 0.00494 | 0.465 | 0.03274 | 0.0797 | 0.00588 | 0.4978 |
| 120. | 0.0016 | 0.74111 | 1.107 | 0.40842 | 0.1824 | 0.08717 | 1.3761 |
| 120. | 0.008 | 0.14822 | 0.693 | 0.18279 | 0.0935 | 0.03914 | 0.8739 |
| 120. | 0.18 | 0.00659 | 0.3317 | 0.00594 | 0.0149 | 0.00113 | 0.3376 |
| 650. | 0.0085 | 0.84779 | 0.7681 | 0.2396 | 0.0817 | 0.04192 | 0.9133 |
| 650. | 0.032 | 0.20072 | 0.5249 | 0.09021 | 0.0385 | 0.01505 | 0.6103 |
| 650. | 0.25 | 0.02569 | 0.252 | 0.00305 | 0.0068 | 0.00022 | 0.2546 |
| 2000. | 0.032 | 0.6929 | 0.5489 | 0.10207 | 0.0345 | 0.01416 | 0.5939 |
| 2000. | 0.13 | 0.15202 | 0.3632 | 0.0163 | 0.0121 | 0.00189 | 0.3695 |
| 2000. | 0.25 | 0.07905 | 0.2439 | 0.00326 | 0.0055 | 0.00019 | 0.2432 |
| 8000. | 0.13 | 0.68224 | 0.3937 | 0.01893 | 0.011 | 0.0017 | 0.2837 |
| 8000. | 0.18 | 0.43917 | 0.3301 | 0.00928 | 0.0077 | 0.00076 | 0.2649 |
| 8000. | 0.25 | 0.31621 | 0.2537 | 0.00365 | 0.0048 | 0.00017 | 0.2148 |

Table II.4: Same as Table II.3, using the HERAFitter code [237, 245–247].

| Q^2 [GeV ²] | x | y | $F_{2,lt}$ | $F_{2,c}$ | $F_{L,lt}$ | $F_{L,c}$ | $\sigma_{r,NC}^+$ |
|---------------------------|-----------|---------|------------|-----------|------------|-----------|-------------------|
| 2.7 | 0.0000309 | 0.86398 | 0.7809 | 0.17478 | 0.2611 | 0.01104 | 0.7604 |
| 2.7 | 0.00013 | 0.20523 | 0.6316 | 0.10218 | 0.1713 | 0.00678 | 0.7292 |
| 2.7 | 0.02 | 0.00133 | 0.3895 | 0.01016 | 0.0835 | 0.00074 | 0.3997 |
| 4.5 | 0.0000618 | 0.71999 | 0.9713 | 0.2174 | 0.2488 | 0.02008 | 1.0623 |
| 4.5 | 0.00032 | 0.13896 | 0.7249 | 0.12013 | 0.1678 | 0.0113 | 0.8431 |
| 4.5 | 0.013 | 0.00342 | 0.4351 | 0.02258 | 0.0888 | 0.00246 | 0.4577 |
| 10. | 0.00013 | 0.85281 | 1.2024 | 0.32374 | 0.2735 | 0.04786 | 1.2991 |
| 10. | 0.0008 | 0.12352 | 0.8134 | 0.16673 | 0.1762 | 0.02555 | 0.9784 |
| 10. | 0.02 | 0.00494 | 0.465 | 0.03268 | 0.0797 | 0.00592 | 0.4977 |
| 120. | 0.0016 | 0.74111 | 1.1067 | 0.40833 | 0.181 | 0.08729 | 1.3784 |
| 120. | 0.008 | 0.14822 | 0.6929 | 0.18255 | 0.0929 | 0.03919 | 0.8736 |
| 120. | 0.18 | 0.00659 | 0.3317 | 0.0059 | 0.0147 | 0.00113 | 0.3376 |
| 650. | 0.0085 | 0.84779 | 0.7669 | 0.23899 | 0.0811 | 0.04189 | 0.9126 |
| 650. | 0.032 | 0.20072 | 0.5243 | 0.08985 | 0.0382 | 0.01503 | 0.6093 |
| 650. | 0.25 | 0.02569 | 0.2519 | 0.00302 | 0.0067 | 0.00037 | 0.2545 |
| 2000. | 0.032 | 0.6929 | 0.5462 | 0.1013 | 0.0341 | 0.01409 | 0.5896 |
| 2000. | 0.13 | 0.15202 | 0.3624 | 0.01615 | 0.0119 | 0.00188 | 0.3682 |
| 2000. | 0.25 | 0.07905 | 0.2437 | 0.00322 | 0.0054 | 0.00031 | 0.2429 |
| 8000. | 0.13 | 0.68224 | 0.3893 | 0.0186 | 0.0107 | 0.00167 | 0.2756 |
| 8000. | 0.18 | 0.43917 | 0.3277 | 0.00914 | 0.0075 | 0.00075 | 0.2607 |
| 8000. | 0.25 | 0.31621 | 0.2525 | 0.0036 | 0.0047 | 0.00026 | 0.2129 |

Table II.5: Same as Table II.3, using the MSTW08 code [235].

| Q^2 [GeV ²] | x | y | $F_{2,lt}$ | $F_{2,c}$ | $F_{L,lt}$ | $F_{L,c}$ | $\sigma_{r,NC}^+$ |
|---------------------------|-----------|---------|------------|-----------|------------|-----------|-------------------|
| 2.7 | 0.0000309 | 0.86398 | 0.7809 | 0.13392 | 0.1035 | 0.0089 | 0.8324 |
| 2.7 | 0.00013 | 0.20523 | 0.6309 | 0.08936 | 0.0981 | 0.00628 | 0.7176 |
| 2.7 | 0.02 | 0.00133 | 0.3884 | 0.0069 | 0.0736 | 0.00073 | 0.3953 |
| 4.5 | 0.0000618 | 0.71999 | 0.9629 | 0.19426 | 0.1706 | 0.01982 | 1.0656 |
| 4.5 | 0.00032 | 0.13896 | 0.7181 | 0.1138 | 0.1425 | 0.01266 | 0.8302 |
| 4.5 | 0.013 | 0.00342 | 0.431 | 0.01932 | 0.0828 | 0.00293 | 0.4503 |
| 10. | 0.00013 | 0.85281 | 1.1897 | 0.31837 | 0.247 | 0.05032 | 1.2962 |
| 10. | 0.0008 | 0.12352 | 0.8046 | 0.16446 | 0.1714 | 0.02859 | 0.9673 |
| 10. | 0.02 | 0.00494 | 0.4601 | 0.03125 | 0.0742 | 0.00642 | 0.4913 |
| 120. | 0.0016 | 0.74111 | 1.1083 | 0.40632 | 0.1794 | 0.08744 | 1.3769 |
| 120. | 0.008 | 0.14822 | 0.6939 | 0.18171 | 0.0907 | 0.03899 | 0.8738 |
| 120. | 0.18 | 0.00659 | 0.3319 | 0.00614 | 0.013 | 0.00098 | 0.338 |
| 650. | 0.0085 | 0.84779 | 0.771 | 0.23832 | 0.0795 | 0.0412 | 0.9169 |
| 650. | 0.032 | 0.20072 | 0.5268 | 0.08994 | 0.0367 | 0.01452 | 0.612 |
| 650. | 0.25 | 0.02569 | 0.2524 | 0.00307 | 0.006 | 0.00032 | 0.255 |
| 2000. | 0.032 | 0.6929 | 0.5519 | 0.10081 | 0.0332 | 0.01354 | 0.5965 |
| 2000. | 0.13 | 0.15202 | 0.3643 | 0.01615 | 0.0112 | 0.00174 | 0.3704 |
| 2000. | 0.25 | 0.07905 | 0.2443 | 0.00324 | 0.005 | 0.00027 | 0.2436 |
| 8000. | 0.13 | 0.68224 | 0.3953 | 0.01807 | 0.0104 | 0.00152 | 0.2847 |
| 8000. | 0.18 | 0.43917 | 0.3311 | 0.0089 | 0.0072 | 0.00067 | 0.2655 |
| 8000. | 0.25 | 0.31621 | 0.2541 | 0.00352 | 0.0044 | 0.00023 | 0.2151 |

Table II.6: Same as Table II.3, using the APFEL code [244] with the FONLL-C scheme. These results agree at the per mille level with those of the N -space `FastKernel` code adopted in the NNPDF fits.

of at most 1.5% at high Q from different treatment of electroweak corrections and Z or γ/Z interference terms. Note that at large Q^2 experimental uncertainties are typically $> 10\%$, so these differences have no impact on the fit results.

At NNLO we observe some systematic shifts of 1% between MSTW/HERAPDF and CTEQ/NNPDF especially around the data point 50, which corresponds to $Q^2 \sim 6$ GeV². However, we have checked that if we use a 3-flavor scheme we find very good agreement, within 0.2%, for $F_{2,lt}$ at NNLO in that Q region. Therefore, we attribute these shifts to the aforementioned contribution from the processes with $\gamma^*q \rightarrow qc\bar{c}$ contributions, or charm quark loops, which first appear at NNLO and are known to be implemented differently in the codes that were compared. As with other flavor scheme differences, there should be convergence at higher orders.

Turning now to the heavy-quark structure function, Fig. II.6 shows the results for $F_{2,c}$. MSTW and HERAPDF agree as they should, since they both use the optimal TR' scheme. We also observe close similarity between CTEQ and NNPDF, which are based on the numerically close schemes S-ACOT- χ , FONLL-A (at NLO) and FONLL-C (at NNLO). In the low- Q region, CTEQ and NNPDF are in very good agreement, and both are smaller than MSTW/HERAPDF. In the intermediate- Q region, all groups agree within a couple of percent. It has been further verified that, if one uses the NNPDF or CTEQ scheme definition in the MSTW code at NNLO, even better agreement is found between the groups. The ‘‘spike’’ structure for NNPDF is due to the use of a different kinematical variable in the GM-VFN scheme definition, i.e. x is used in the FONLL scheme [243], while $\chi = x(1 + 4m_c^2/Q^2)$ is used in the TR' [242] and S-ACOT- χ [241] schemes. This effect is mainly seen at the highest x point in each Q^2 bin, where F_2^c is a small contribution to the total.

The overall trends in $F_{2,c}$ are consistent with the results obtained in the context of the 2010

Les Houches heavy-quark benchmarks [160] (see also the follow-up comparisons with S-ACOT- χ at NNLO in [241]). The differences are reduced when going from NLO and NNLO, in agreement with the general expectation that, at each order in α_s , the GM-VFN heavy-quark schemes are equivalent up to contributions proportional to m_c^2/Q^2 at one higher order. Apart from the residual differences in their heavy-quark schemes, the CTEQ and NNPDF codes evaluate $\mathcal{O}(\alpha_s^2)$ heavy-quark scattering contributions by interpolation of integral tables [248] and direct integration [243], respectively. This contributes to some of the minor differences seen between the CTEQ and NNPDF $F_{2,c}$ values at NNLO.

Fig. II.7 presents comparisons of $F_{2,tot}$, which is impacted by all effects seen in Figs. II.5 and II.6. Again the differences decrease as we go from NLO to NNLO.

We now turn to the other structure functions. Figs. II.8-II.10 show results for F_L . Here different counting of perturbative orders adopted by the groups results in large discrepancies between the MSTW/HERAPDF and CTEQ/NNPDF F_L values of nominally the same orders, e.g., at LO F_L vanishes for CTEQ/NNPDF, while it is of $\mathcal{O}(\alpha_s)$ for MSTW/HERAPDF. We have checked explicitly that, once we use the $\mathcal{O}(\alpha_s)$ ($\mathcal{O}(\alpha_s^2)$) Wilson coefficients for F_L with LO (NLO) toy PDFs both in CTEQ and MSTW codes, the respective CTEQ and MSTW values agree at the 1-2% level. We also find very good agreement on F_3 among all groups.

Finally, in Fig. II.11 we show a comparison of the HERA reduced cross sections constructed from F_2 , F_L , and F_3 [237], which can be directly compared to the data. Again we see excellent agreement between all groups, and significant convergence from NLO to NNLO. Except for the extremely high Q region, where there exist some differences in the implementations of electroweak corrections (and where data points have very large errors), all curves agree within 1% in the moderate- Q region, and 2% in the low- Q region. The MSTW and HERAPDF predictions are essentially identical, as they should be (other than the differences due to electroweak corrections or numerical precision). CTEQ and NNPDF are quite close, too, even at low Q , due to the similarities of the S-ACOT- χ and FONLL-A (FONLL-C) heavy-quark schemes at NLO (NNLO).

We conclude from this benchmark exercise that the differences in theoretical predictions of neutral current DIS cross sections between CT, HERAPDF, MSTW and NNPDF are well understood as mostly arising from the choice of the respective heavy-quark schemes, non-identical counting of perturbative orders, electroweak contributions, and that these theoretical differences are small at NNLO compared to the experimental margin of error. Therefore, we expect that the differences in heavy-quark schemes should not have a large impact on the fits using only HERA-1 data or on the Higgs cross sections predicted from them at the NNLO. This will be investigated in the next section.

Before closing this section, we note that in the following fits, NNPDF uses the truncated solution for the DGLAP evolution equations and the α_s renormalization-group evolution. Modifications resulting from this choice (essentially from a different treatment of higher-order perturbative corrections as compared to the exact solutions used in the CT, MSTW and HERAPDF codes) should be quite small at NNLO. We have verified that it is certainly negligible for the running of α_s . Second, larger differences (of order 10%) are observed between the group's predictions for charged-current DIS cross sections, which are still evaluated at NLO. As the experimental uncertainties on the charged-current DIS cross sections are still rather significant, the current differences between the codes in the charged-current sector are not anticipated to be of the same consequence for the gluon PDF as those in the neutral-current DIS cross sections.

1.4 Benchmark PDF fits to HERA-1 data

1.4.1 Setup

We will first describe the setup used for the fits to the reduced data set based on the combined HERA-1 DIS data only. At this stage we performed the baseline fit based on the default settings, as well as a series of alternative fits designed to assess dependence on the input assumptions. The kinematical ranges of the data sets included in the fits, and the number of points in each measurement, are summarized in Table II.7. The baseline fit includes only the combined inclusive data with $Q^2 > 5\text{GeV}^2$ to minimize the differences due to the heavy-quark schemes. Some alternative fits also include the combined charm quark production data and vary the lower Q^2 cut or other input parameters. We assume the strong coupling constant to be $\alpha_s(M_Z) = 0.118$ and set the pole mass of the charm quark to a common value of 1.4GeV in the baseline fit and to the default values of each group in the variant fits. NNLO QCD theory is used throughout.

In the HERA-1-only fits, the data do not constrain PDFs in the extremely large x region or some of the flavor combinations, e.g., $\bar{u} - \bar{d}$, $(s + \bar{s})/(\bar{u} + \bar{d})$, $s - \bar{s}$. The remaining degrees of freedom are associated mostly with g , u_v , d_v , and $\bar{u} + \bar{d}$ PDFs. Therefore, CTEQ fits use a smaller number of free PDF parameters than in their global fits, as well as updated parametrization forms for some flavors based on Chebyshev polynomials [249,250]. The MSTW HERA1-only fit is done using an updated parametrization based on Chebyshev polynomials for some flavors, which has been shown [250] to lead to a change in the Higgs cross section at the LHC of only a small fraction of a percent compared to the published MSTW'08 parametrizations. The HERAPDF baseline fit uses the same number of free parameters as in HERAPDF1.5, which is smaller than in CTEQ and MSTW global fits. Similarly, the baseline neural-network parametrizations of NNPDF are the same as in their global fits and produce very large uncertainty bands for their unconstrained PDF combinations. The dependence on the PDF parametrization form is further discussed in Sec. 1.4.3.

All PDF analyses utilize the figure-of-merit χ^2 to find the best fit and estimate the PDF uncertainties. In the presence of correlated systematics, χ^2 can be written as a function of the PDF parameters a and nuisance parameters λ ,

$$\chi^2(a, \lambda) = \sum_{k=1}^{N_{pt}} \frac{1}{s_k^2 + \sigma_k^2} \left(D_k - T_k - \sum_{\alpha=1}^{N_\lambda} \beta_{k,\alpha} \lambda_\alpha \right)^2 + \sum_{\alpha=1}^{N_\lambda} \lambda_\alpha^2, \quad (\text{II.2})$$

where N_{pt} and N_λ are the total numbers of data points and correlated systematic errors, respectively [251,252]. T_k are the theoretical predictions, and D_k are the central values of experimental measurement. s_k , σ_k , and $\beta_{k,\alpha}$ are the statistical, uncorrelated systematic, and correlated sys-

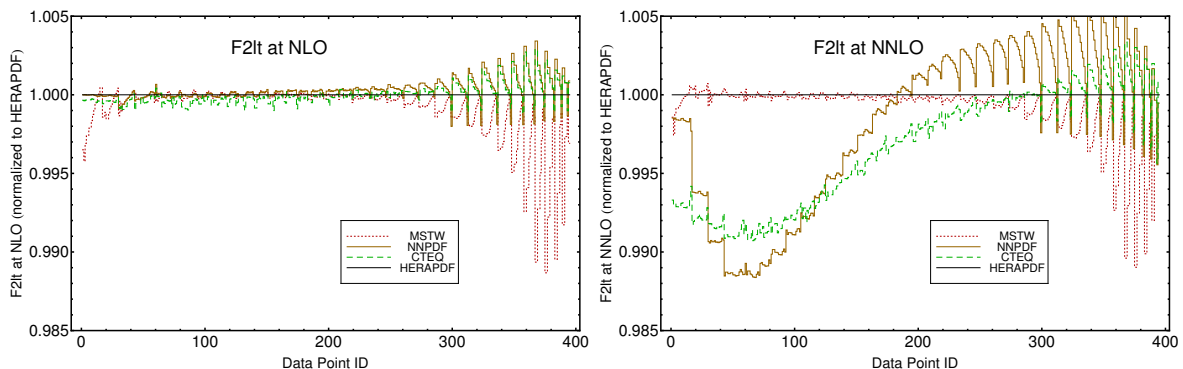


Fig. II.5: Structure function $F_{2,lt}(x, Q)$ at NLO and NNLO from all groups, normalized to the results from the HERAPDF1.5 code.

| | NC (e^+p) | NC (e^-p) | CC (e^+p) | CC (e^-p) | Charm |
|--------------------------------------|------------------------------|---------------|---------------|---------------|--------------------------|
| Q^2 range [GeV ²] | 0.045-30000 | 90-30000 | 300-15000 | 300-30000 | 2.5-1000 |
| x range | 0.621×10^{-6} -0.65 | 0.0013-0.65 | 0.008-0.4 | 0.013-0.4 | 3×10^{-5} -0.05 |
| $N_{pt}, Q^2 \geq 2 \text{ GeV}^2$ | 408 | 145 | 34 | 34 | 52 |
| $N_{pt}, Q^2 \geq 3.5 \text{ GeV}^2$ | 379 | 145 | 34 | 34 | 47 |
| $N_{pt}, Q^2 \geq 5 \text{ GeV}^2$ | 353 | 145 | 34 | 34 | 47 |

Table II.7: Kinematic ranges and number of points in the HERA-1-only fits.

| | s_k (sta.) | σ_k (unc. sys.) | $\beta_{k,NL}$ (cor., not lum.) | $\beta_{k,L}$ (lum.) |
|--------------------|------------------------|------------------------|---------------------------------|----------------------|
| d_1 (exp.) | D_k | D_k | D_k | D_k |
| d_2 (HERAPDF) | $\sqrt{D_k \cdot T_k}$ | T_k | T_k | T_k |
| d_3 (NNPDF/MSTW) | D_k | D_k | D_k | T_k |
| d_4 (CTEQ) | D_k | D_k | T_k | T_k |

Table II.8: Normalization factors in the definitions of experimental errors adopted by the PDF analysis groups.

tematic errors, including luminosity error. The available experimental errors are published in the form of fractional errors. Depending on how they are normalized, there exist several definitions of the χ^2 function [217, 233, 237], some of which are reviewed in Table II.8. The table entries list the variables that multiply the corresponding fractional errors.

The usage of χ^2 with the d_1 definition in the fit would lead to the D’Agostini bias from the luminosity error [253]. The published HERAPDF set adopts the d_2 definition. MSTW and NNPDF use the d_3 definition for their published sets³. The CT10 PDF sets use the d_4 definition by default. The justification for $d_{2,3,4}$ requires one to draw a clear distinction between the additive and multiplicative experimental errors, which has not been done in the combined HERA-1 publications. Instead, in the published combined HERA-1 data set, the uncertainty associated with the χ^2 definition in the combination procedure has been counted as one of the correlated systematics. In the HERA1-only baseline fits, all four groups used the d_4 definition. The effects of using the alternative χ^2 definitions is discussed in Sec. 1.4.3.

1.4.2 Baseline fits

In their baseline fits, each group provides a best-fit candidate set, which yields the lowest χ^2 for the HERA-1 inclusive DIS data. The NNPDF group additionally provides an estimate of the PDF uncertainty, serving as a measure of the agreement between the best fits of the different groups. CTEQ and MSTW have both examined the Higgs cross section variation using the Lagrange Multiplier method [255], each obtaining a 68% c.l. uncertainty of about 0.4 pb on σ_H at 8 TeV (corresponding to $\Delta\chi^2 = 1$), which is a bit bigger than the standard HERAPDF1.5 uncertainty of ≈ 0.25 pb.

In Table II.9 the first three rows show the quality of the best fits from the four groups, including total χ^2 , luminosity shift and maximum systematic shift required. We see that all these best fits describe the HERA-1 inclusive data pretty well, with $\chi^2/d.o.f.$ being less than unity. The systematic shifts are less than 2σ and show similarities among the different groups. The Higgs production cross sections through gluon fusion at the LHC for 8 and 14 TeV are also included in Table II.9 and illustrated in Fig. II.12. Comparing with Table II.2 we find that, for

³NNPDF actually use the $T^{(0)}$ method [254], in which the theoretical values multiplying the correlated systematic errors are held constant in a series of iterations. MSTW2008 apply a quartic penalty to the normalization uncertainty.

| 566 data points | CTEQ | MSTW | NNPDF | HERAPDF |
|-------------------------|-------|-------|------------------|---------|
| χ^2 | 521.8 | 514.8 | 548.5 | 535.0 |
| lum. shift | -0.19 | 0.27 | 0.16 | 0.18 |
| max. shift | 1.64 | 1.51 | 1.82 | 1.81 |
| σ_H [pb], 8 TeV | 17.86 | 18.25 | 18.60 \pm 1.10 | 18.82 |
| σ_H [pb], 14 TeV | 46.37 | 47.38 | 48.76 \pm 2.26 | 48.78 |

Table II.9: Outputs of the best baseline fits, including values of χ^2 as defined in Eq. (II.2), luminosity and maximal systematic shifts, and Higgs cross sections.

all groups except HERAPDF, the cross sections are lowered by a similar amount compared to the public sets: by 0.6 pb at 8 TeV and 1.2 pb at 14 TeV. The cross sections from HERAPDF are increased a little compared to HERAPDF1.5 due to the removal of the preliminary HERA-2 data included in HERAPDF1.5. The trends of relative differences between the groups are very similar to those for the public sets. The spread of the Higgs cross sections is still at the level of 4 – 5 %. The PDF uncertainties in the NNPDF column are larger than those predicted by NNPDF2.3, which has many additional data sets included. All predictions are now within the 1σ error bands of NNPDF.

Fig. II.13 shows a plot for the gluon PDFs that is analogous to Fig. II.2. The hierarchy of CT, MSTW, and NNPDF predictions at the values of x relevant for Higgs production remains similar to that of Fig. II.2. The HERAPDF curve moved above both CT and MSTW curves at these x , in contrast to Fig. II.2, where it is below CT. At large x the relative gluon shapes are very similar to those in the global fits, with the central gluon PDF from NNPDF being lower than those of the other three groups in the $x \gtrsim 0.2$ region, but still within the large gluon uncertainty from all of them. (The HERA DIS data set does not impose a strong constraint on $g(x, Q)$ at high x .) However, for $x \lesssim 10^{-3}$ the shapes and ordering of gluon PDFs change, with the MSTW and CTEQ gluons staying below the NNPDF one in the central Higgs production region. Fig. II.14 presents plots for the gluon-gluon parton luminosity similar to Fig. II.3. All predictions are located inside, or close to the PDF uncertainties predicted by NNPDF for invariant masses above 100 GeV.

Fig. II.15 is a counterpart of Fig. II.4 and shows Higgs rapidity distributions obtained with the HERA-1 baseline PDFs. The spread of the distribution in the central region is a little larger than the spread of the inclusive cross sections. It generally amounts to $\sim 1.5\sigma$ of the uncertainties predicted by NNPDF. While all curves moved somewhat in Fig. 15 as compared to Fig. 4, the HERAPDF curve underwent the most pronounced change between the two sets of figures, mostly as a consequence of the removal of the HERA-2 data set from their fit. The ratio to NNPDF is flatter in the rapidity distribution for the HERA-1-only fit.

1.4.3 Dependence of the fits on input assumptions

In addition to the fits with the baseline settings, we carried out various exploratory fits to understand sensitivity to the input parameters.

Choice of the Q^2 cut. The internal consistency of the HERA-1 inclusive DIS data set was examined by varying the low Q^2 cut for data selection. Fig. II.16 shows the best fits of MSTW and HERAPDF with Q^2 cuts of 2, 3.5, 5, 7.5, and 10 GeV². Fig. II.17 gives similar plots for CT10 and NNPDF fits with Q^2 cuts of 2, 3.5, and 5 GeV. The gluon PDFs can vary by up to 2% around the central region of Higgs production depending on the chosen Q^2 cut. However, the inclusive $gg \rightarrow H$ cross sections are less sensitive to the Q^2 cut due to compensation from the gluon PDFs across the whole range of x which is accessed. For example, Table II.10 shows

the relative variations of the inclusive cross sections. Cross sections from MSTW, CTEQ, and HERAPDF fits are rather stable, with variations of about 1%. The NNPDF cross sections show a larger variation of about 2%.

Inclusion of charm production. Another group of fits included the combined HERA-1 charm quark production data in addition to the inclusive data. Fig. II.18 shows the ratios of the gluon PDFs from fits with and without the charm data for different groups. In the comparison we choose a Q^2 cut of 3.5 GeV^2 and the charm quark mass of the default value of each group as in Table II.1. The charm quark production data generally prefer slightly smaller gluon PDFs around the Higgs mass region, especially in the NNPDF PDFs, which show a reduction of about 1.5%. The relative changes of the predictions for Higgs cross sections when including the charm data are shown in Table II.11. There is little variation, the largest change being a reduction of about 2% for the NNPDF fits.

Parametrization dependence was studied by repeating the fits using alternative PDF parametrization forms and input scales Q_0 .

The requirement of the positivity imposed on the gluon PDF or gluon-mediated cross sections alters the span of allowed gluon PDF shapes at $x < 10^{-3}$ and also may affect very large x via the momentum sum rule. All published PDF sets except for CTEQ allow a negative gluon PDF at very small x and Q . In the alternative series, HERAPDF replaced the second gluon term, introduced to allow small x negativity, by a positive definite form with an additional polynomial. In this case the input scale was set to 1.9 GeV^2 . Similarly MSTW have removed the second term in the original parametrization and included one more Chebyshev polynomial while simultaneously changing the initial scale to 1.3 GeV , the same as for CTEQ, but lower than for HERAPDF. They checked that changing the input scale while maintaining the same parametrization form resulted in a fit quality and PDFs essentially identical to those using the default input scale of 1 GeV .

The NNPDF fits use the same very general parametrization for the HERA-only fit as in their global fit, hence little parametrization dependence is expected. In the public global fit, NNPDF does not require a positive definite gluon (though positivity of observables such as F_L is imposed). NNPDF also examined how their PDFs would change if positivity on their gluon PDFs is imposed.

Fig. II.19a shows the ratios of gluon PDFs with positive-definite and default parametrizations, from HERAPDF, MSTW, and NNPDF. In the case of the HERAPDF or NNPDF fits, the gluon PDFs are only affected by the positivity requirement at small $x \sim 10^{-4}$ and large $x \sim 0.2$, and the Higgs cross sections are reduced or increased by about half percent. The gluon PDF in the MSTW fit could change by 10% at $x \sim 0.1$ and induce a reduction of the Higgs cross sections by 4%. However, the MSTW fit with positive gluon has a χ^2 larger by 15 units and thus is not favored by the HERA-1 data.

The baseline parametrization of HERA-only fits by CTEQ uses a positive-definite gluon and Chebyshev polynomials for some flavors. In addition, we explored three alternative parametrizations: CTEQ-1, a more flexible parametrization with Chebyshev polynomials; CTEQ-2, equivalent to the CT10 NNLO parametrization with fewer free parameters; and CTEQ-3, which is the baseline parametrization in which one Chebyshev polynomial is replaced by a term proportional to $x^p(1-x)^{64}$ to allow a negative gluon. The best-fit χ^2 values are about 521 for the parametrizations with Chebyshev polynomials (baseline, CTEQ-1, and CTEQ3) and 539 (somewhat worse) for CTEQ-2. The shapes of the gluon PDF for the alternative parametrizations, compared to the alternative parametrization, are illustrated in Fig. II.19b. We see some variation in the shape of $g(x, Q)$, especially for $x \sim 0.1$, but the total Higgs production cross sections remain rather stable. The χ^2 vs. σ_H dependence (for the LHC 8 TeV) in a Lagrange multiplier (LM) scan for the baseline, CTEQ-1, and CTEQ-2 parametrizations is illustrated in

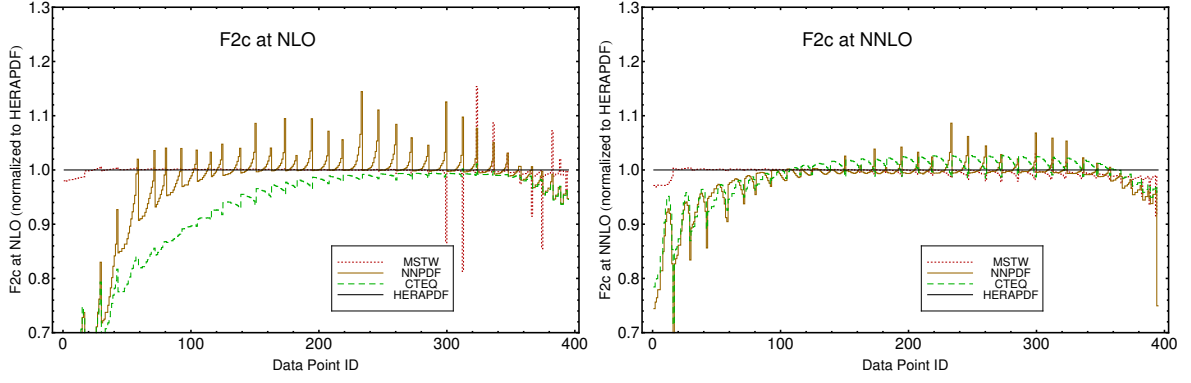


Fig. II.6: Same as Fig. II.5, for the structure function $F_{2,c}$.

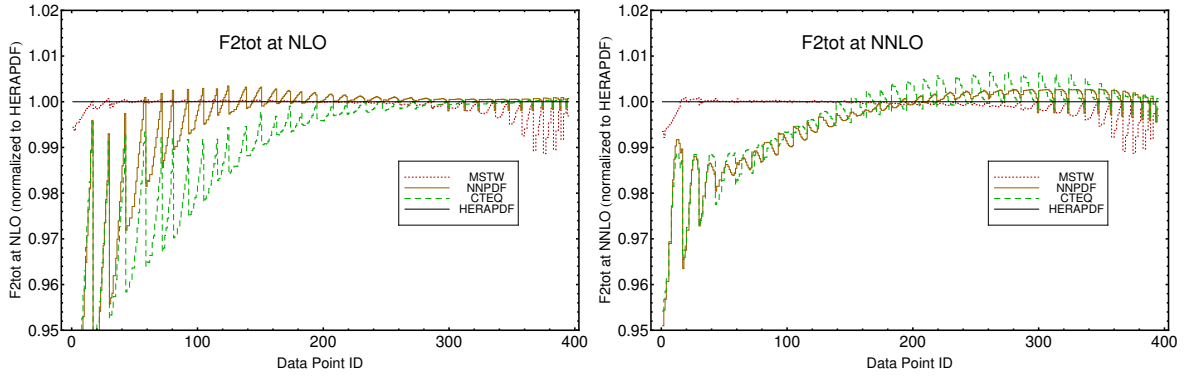


Fig. II.7: Same as Fig. II.5, for the structure function $F_{2,tot}$.

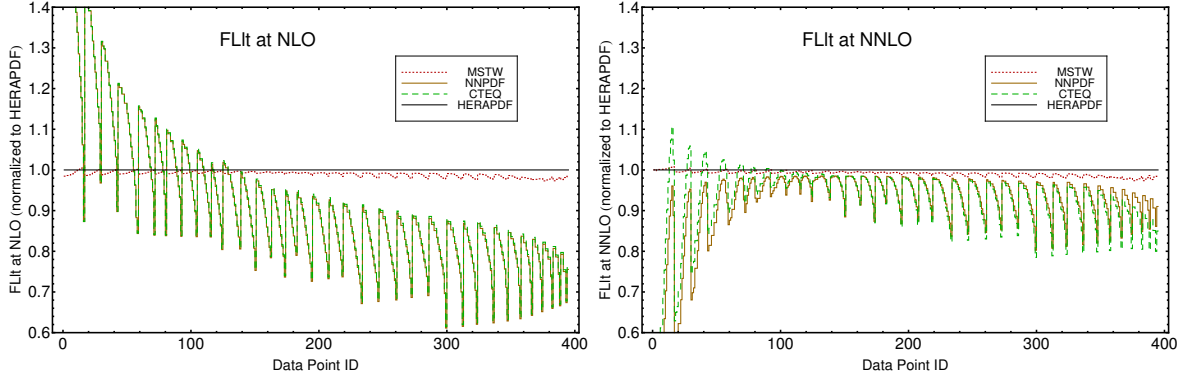


Fig. II.8: Structure function $F_{L,lt}(x, Q)$ at nominal NLO and NNLO from all groups, normalized to the results from the HERAPDF1.5 code. The counting of perturbative orders for $F_L(x, Q)$ differs in the CTEQ/NNPDF and HERAPDF/MSTW conventions, as discussed in the main text.

| | CTEQ | MSTW | NNPDF | HERAPDF |
|--|---------|----------|---------|----------|
| Range of low Q^2 cuts [GeV^2] | 2.0-5.0 | 2.0-10.0 | 2.0-5.0 | 2.0-10.0 |
| $\delta\sigma_H/\sigma_H$ [%], LHC 8 TeV | 1.3 | 0.9 | 2.6 | 1.1 |
| $\delta\sigma_H/\sigma_H$ [%], LHC 14 TeV | 1.2 | 0.8 | 2.2 | 1.4 |

Table II.10: Relative variations in predicted Higgs cross sections when changing the Q^2 cut in selection of the HERA-1 inclusive DIS data.

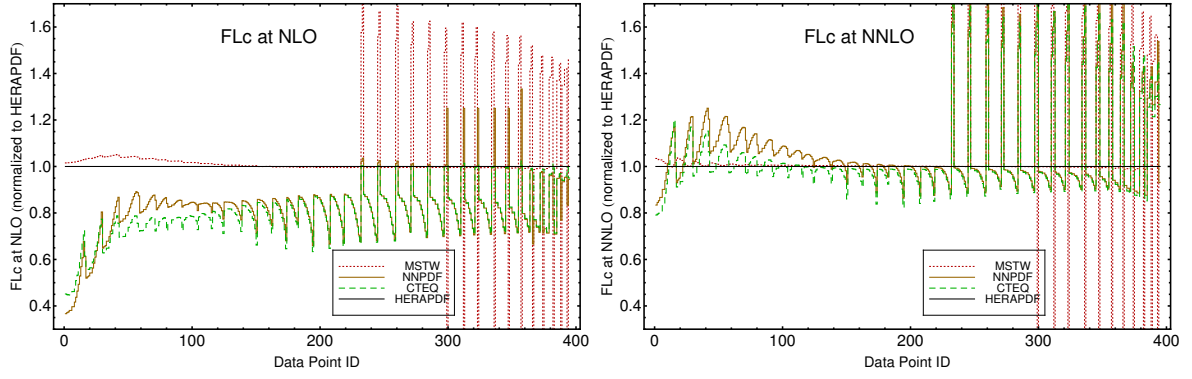


Fig. II.9: Same as Fig. II.8, for the structure function $F_{L,c}$.

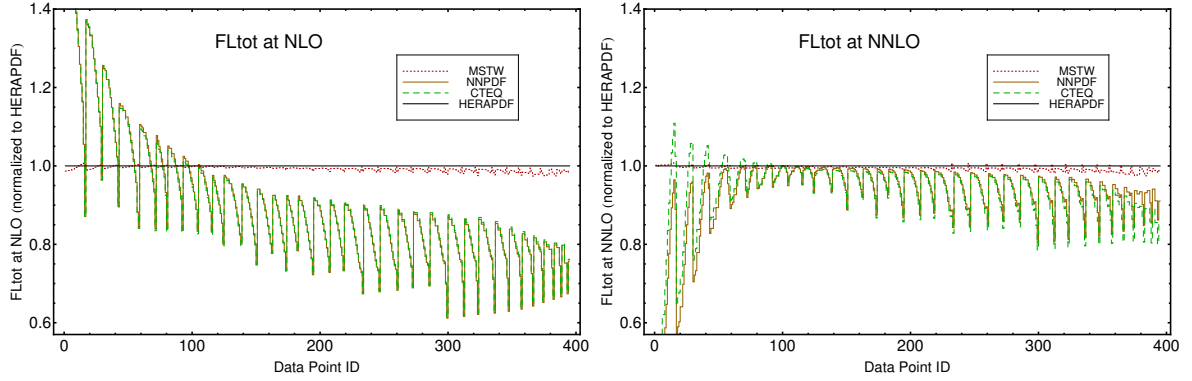


Fig. II.10: Same as Fig. II.8, for the structure function $F_{L,tot}$.

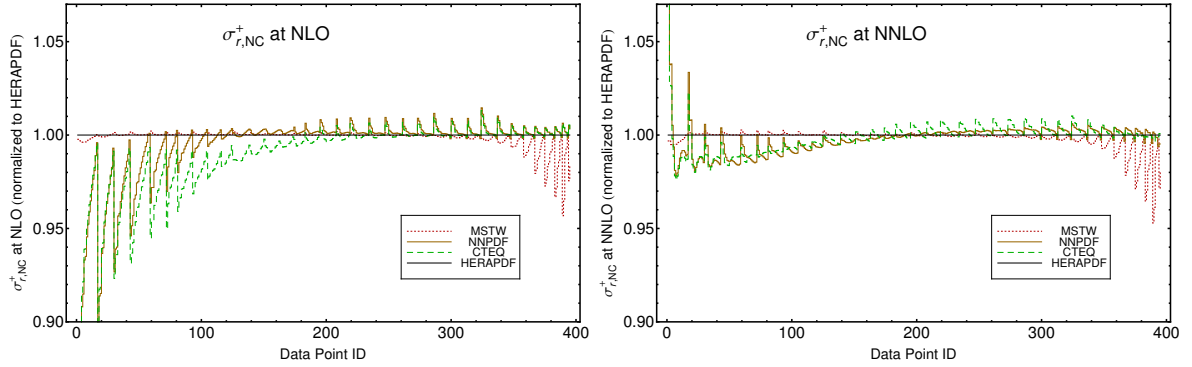


Fig. II.11: Same as Fig. II.5, for the HERA reduced cross section, $\sigma_{r,NC}^+$.

| | CTEQ | MSTW | NNPDF | HERAPDF |
|---|------|------|-------|---------|
| $\delta\sigma_H/\sigma_H$ [%], LHC 8 TeV | -0.7 | -0.4 | -2.0 | -0.2 |
| $\delta\sigma_H/\sigma_H$ [%], LHC 14 TeV | -0.5 | -0.4 | -1.9 | 0.2 |

Table II.11: Relative changes in the predicted Higgs cross sections upon including the HERA-1 charm production data in addition to the inclusive DIS data.

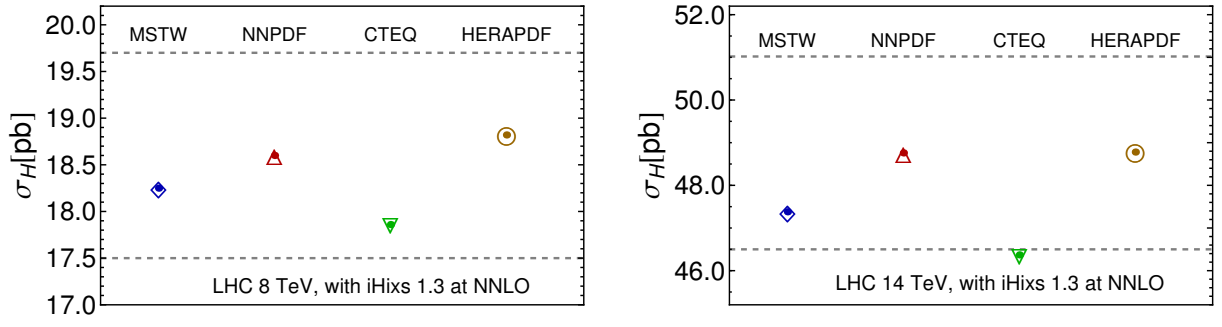


Fig. II.12: Predictions for inclusive cross sections of the SM Higgs boson production through gluon fusion based on the HERA-1-only NNLO PDFs. The settings are the same as in Fig. II.1. The dashed lines are the edges of the 1σ uncertainty band determined using the NNPDF set (and including PDF uncertainties only).

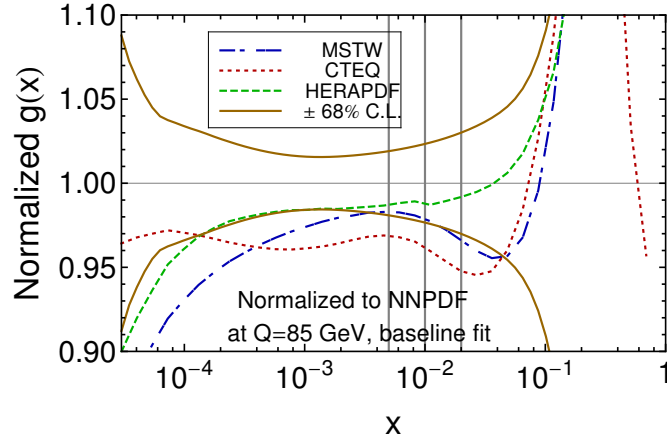


Fig. II.13: Comparison of the gluon PDFs from the baseline HERA-1 NNLO fits at a common scale $Q = 85$ GeV, normalized to the NNPDF central prediction.

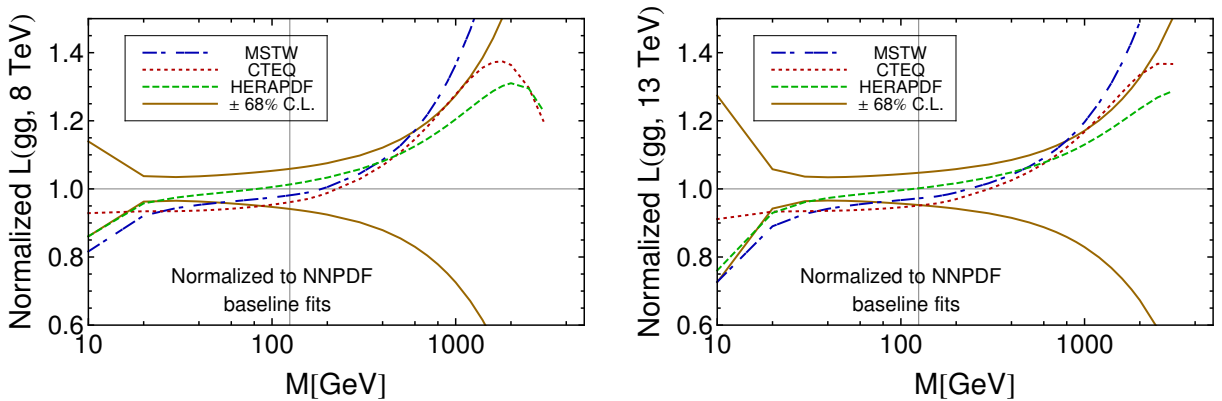


Fig. II.14: Comparison of the gluon-gluon parton luminosity as a function of invariant mass at the LHC 8 and 13 TeV from the HERA-1-only NNLO fits, normalized to the NNPDF central prediction. The factorization scale is set to the invariant mass. The vertical line indicates mass of the SM Higgs boson.

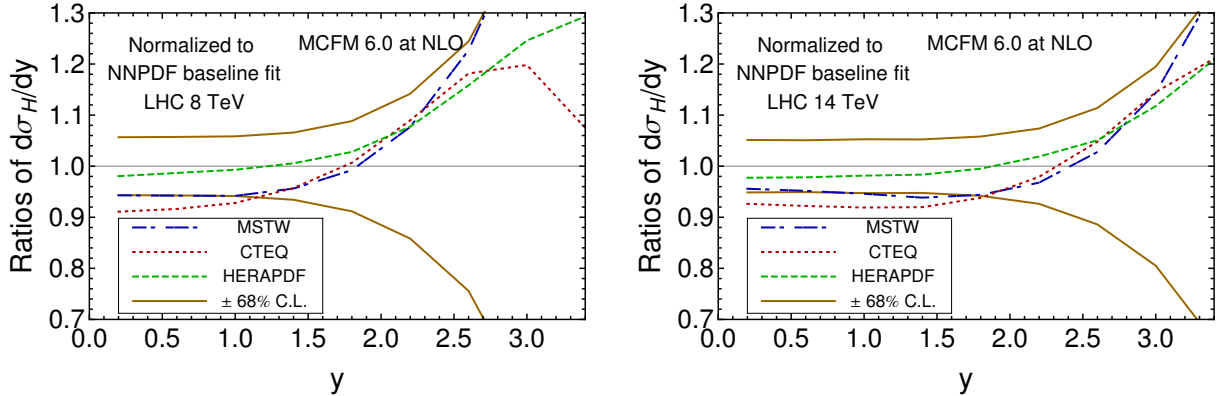


Fig. II.15: Comparison of the rapidity distribution of the SM Higgs boson in production through gluon fusion for baseline HERA-1-only NNLO PDFs, normalized to the NNPDF central prediction. The settings are the same as in Fig. II.3.

| | MSTW | NNPDF | HERAPDF |
|--|------|-------|---------|
| $\delta\sigma_H/\sigma_H[\%]$, LHC 8 TeV | -0.4 | -1.3 | 1.2 |
| $\delta\sigma_H/\sigma_H[\%]$, LHC 14 TeV | 0.4 | -0.6 | 0.2 |

Table II.12: Relative changes in the predicted Higgs cross sections when the default χ^2 definition of each group is replaced by d_4 definition.

Fig. II.20. All three scans show consistent results for the values of the best-fit cross sections and overall dependence of χ^2 on σ_H . For the CTEQ-3 form (allowing for a negative gluon), the convergence of the fit is worse for some values of σ_H in the LM scan. Nevertheless, the best-fit value of σ_H for CTEQ-3 is 17.9 pb, which is close to the baseline result.

Definition of χ^2 . As mentioned in Sec. 1.4.1, several definitions of χ^2 can be implemented in the fits with only HERA-1 data. The dependence on the χ^2 definition may be viewed as an additional systematic uncertainty. In Fig. II.21 we plot ratios of the gluon PDFs from the fit with the d_4 definition of the χ^2 to the gluon PDFs from the fit with the default χ^2 definition of HERA, MSTW, and NNPDF groups. CTEQ fits always use the d_4 definition and are not included in the figure. Other settings, besides the χ^2 definition, are the same in this comparison. We can see that the χ^2 definition can have some impact on the shape of the gluon PDF, and thus on the rapidity distribution of the Higgs boson. For example, when we change from the d_3 definition to the d_4 definition the gluon PDF is enhanced in the small x region (< 0.01) and reduced for $x > 0.1$. An opposite trend is observed when changing from the d_2 definition to d_4 . However, the inclusive cross sections are still stable, with changes less than 1%. This is shown in Table II.12.

Treatment of heavy quarks and other theoretical choices, such as the values of factorization and renormalization scales, may affect the gluon PDFs. Dependence on parameters of the heavy-quark schemes and mass of the charm quark has been studied before [160, 239, 256, 257], and relatively small impact on the gluon PDF at a fixed α_s has been observed. In the context of the current study, we varied some settings of the heavy-quark schemes and observed the changes in the gluon PDFs. In CTEQ fits, the pole charm mass and the λ parameter introduced by the slow rescaling convention in the S-ACOT- χ scheme [241, 258] has been varied to gauge the associated theoretical uncertainty due to the heavy-quark contributions. [The baseline CTEQ fit assumes $\lambda = 0$ and $m_c = 1.4$ GeV.] The dependence on m_c and λ in the CTEQ HERA-1 only

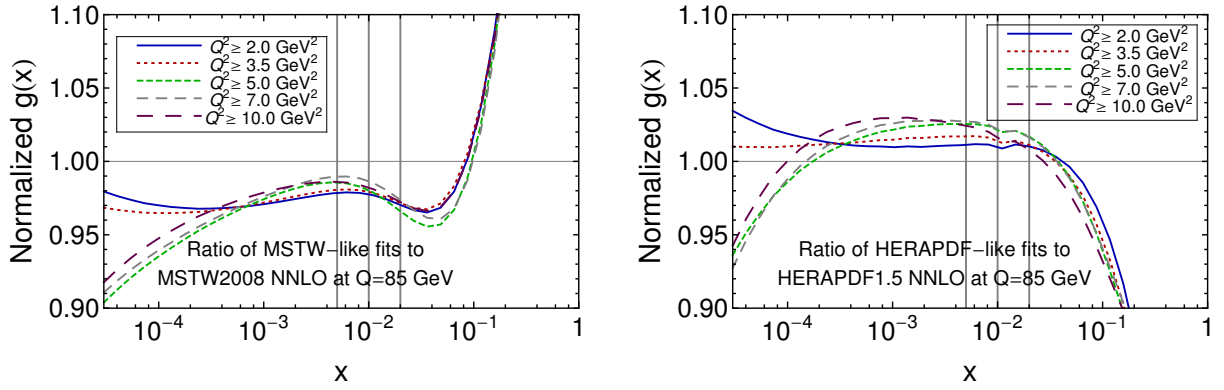


Fig. II.16: Dependence of the gluon PDF on the Q^2 cut in HERA-1 inclusive data selection, from MSTW and HERAPDF fits.

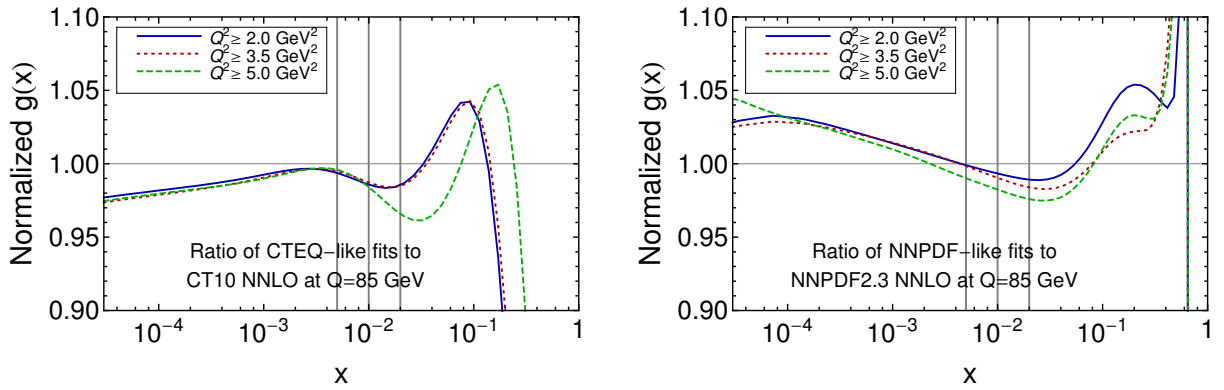


Fig. II.17: Dependence of the gluon PDF on the Q^2 cut in HERA-1 inclusive data selection, for CTEQ and NNPDF fits.

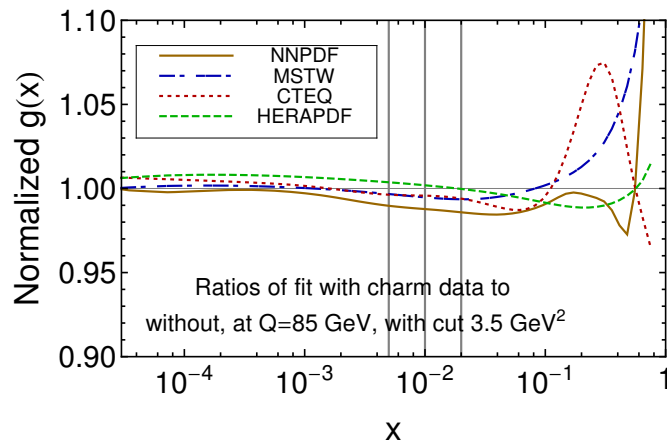


Fig. II.18: Changes of the gluon PDF when including the HERA-1 charm quark production data in addition to the inclusive DIS data.

fit is compatible with the behavior seen in the global fits [257], with the Higgs cross sections changing within 2-3% under variation of m_c and λ before appreciable increase in χ^2 is reached. In the MSTW study the gluon and Higgs cross sections have been obtained from fits which use the FONLL-C scheme used by NNPDF at NNLO, and HERAPDF have performed fits using the full ACOT scheme. In all cases, variations were small, though not totally negligible. Overall, this suggests that higher-order effects beyond NNLO in HERA DIS cross sections compare to a fraction of the current experimental uncertainty.

1.5 Summary and outlook

This work is motivated by the need to understand, and possibly reduce, the discrepancies between different PDF sets related to the predictions for the cross sections for inclusive Higgs boson production via gluon fusion at the LHC, in order to improve the prospects of Higgs boson characterization. In this contribution we have performed a first step in this direction, by comparing in detail the outcomes of the PDF fits by CT, HERAPDF, MSTW and NNPDF groups to the well-understood combined HERA-1 data set. As an important spin-off, we have carried out a benchmark comparison of NNLO neutral-current DIS structure functions, which have shown reasonable agreement between the four fitting codes when using the same toy PDF set. We have acquired good understanding of the remaining differences arising from the use of diverse GM-VFN schemes and counting of perturbative orders, and observed a distinctly improving agreement when going from NLO to NNLO.

We have then completed a series of benchmark fits at NNLO using only HERA-1 data and studied the predictions of the resulting PDFs for the gluon fusion Higgs cross sections. In general the HERA-1 only fits prefer slightly smaller Higgs cross sections than in the global fits, though they are fully consistent within the larger uncertainties of the former. Predictions from different groups for the Higgs cross sections show a spread at a similar level as in the published NNLO PDF sets, and with mostly similar hierarchy. However, since in the HERA-1 only fits the PDF uncertainties are substantially larger than in the global fits, we find that the predictions from all groups agree well within the PDF uncertainty in this case. Various systematic effects on the Higgs cross section predictions have also been studied, leading to effects at the level of a percent or two, well within the PDF uncertainties.

Therefore, the main conclusion of this work is that, in the HERA-1-only fits, the predictions of all four fitting groups are consistent within the PDF uncertainties. There are however some interesting trends, for instance the hierarchy between NNPDF, MSTW and CT seems to be maintained both in the global and HERA1-only fits. This could be related to different methodological choices associated with the selection of the gluon parametrization or alike issues, some of which were investigated in Sec. 1.4.3.

The next natural step will be to continue this exercise by adding additional experimental data sets into the PDF fits sequentially. This will require both benchmarking the theoretical predictions used by each group for the different observables and ensuring that all groups use exactly the same data points, uncertainties and definition of the systematic uncertainties and covariance matrix. The data that could be added to the HERA-1 data include fixed-target neutral current DIS data, charged current neutrino DIS data, vector boson and inclusive jet production data, and future HERA-2 combined data, until a data set similar to that used in the three global fits is reproduced.⁴ Another possible way forward would be to compare the impact of new LHC data that is sensitive to the gluon PDF in the region relevant for Higgs production, like direct photon production [259, 260], vector boson production in association with jets [261], top quark pair production [262] and inclusive jet production [263]. We hope that, by building

⁴ A first exercise in this direction by the NNPDF Collaboration is presented as a separate contribution to these proceedings.

on the results and strategy presented in this contribution, this future work will contribute to reduction of PDF uncertainties at the NNLO level of accuracy that is called for by the LHC physics program.

Acknowledgments

This work at MSU and SMU was supported by the U.S. DOE Early Career Research Award DE-SC0003870, U.S. National Science Foundation under Grant No. PHY-0855561, and by Lightner-Sams Foundation. The work of RST is supported partly by the London Centre for Terauniverse Studies (LCTS), using funding from the European Research Council via the Advanced Investigator Grant 267352 and is also funded by the Science and Technology Research Council (STFC). The work of S.F. is supported by an Italian PRIN 2010 grant and by a European EIBURS grant. This research was supported in part by the European Commission through the ‘‘HiggsTools’’ Initial Training Network PITN-GA-2012-316704.

2 Dataset sensitivity of the $gg \rightarrow H$ cross-section in the NNPDF analysis⁵

2.1 Introduction

Parton distributions provide a dominant source of uncertainty on all Higgs production modes at the LHC: combined PDF+ α_s uncertainties are around $\sim 8\%$ for gluon fusion, the production mode with largest cross section. In a particularly unfortunate situation, for this process, and for the Higgs mass of $m_H = 125$ GeV, differences between the three PDF sets that enter the PDF4LHC recommendation [218] adopted by the Higgs Cross Section Working Group predictions [38], namely CT10 [233], MSTW [235] and NNPDF2.3 [236], are such that their gluon-gluon luminosities differ more than for any other mass value [217]. The reason for this discrepancy could be methodological: this is investigated in a companion contribution to these proceedings, where methodological differences between CTEQ, HERAPDF, NNPDF and MSTW are studied in the controlled setting of fitting to a common and consistent dataset, the combined HERA-I data.

However, the reason could also be that there are tensions, i.e. minor inconsistencies, between data included in a global fit. Results could then differ either because of small differences in the dataset adopted, or because different fits respond differently to data inconsistencies. If this is the case, the discrepancies would eventually be resolved as more and more data become available, specifically from the LHC, but in practice this might take a very long time. It is therefore important to understand whether this might be the case.

With this motivation, in this contribution we explore, in the framework of the NNPDF2.3 global analysis, how the Higgs cross section in the gluon fusion channel is affected by the choice of fitted dataset. First of all we present a correlation study to quantify which of the experiments in the global fit affect more the gluon PDF in the region of x relevant for Higgs production. Then we present the results of a wide variety of NNPDF2.3-like fits with different datasets, and study how the Higgs production cross-section changes as these different choices of fitted dataset are adopted.

As mentioned above, the present study is based on the NNPDF2.3 framework [236], but now varying the fitted dataset. In all the fits that are presented in this contribution, the value of $\alpha_s(M_Z) = 0.119$ is adopted. This value is consistent with the current PDG average [264] and also with a direct determination from the NNPDF2.1NNLO fit [265–267]. Theoretical predictions for the inclusive $gg \rightarrow H$ cross-section at NNLO were computed with the `iHixs` code, v1.3.3 [268]. A similar, more detailed study was presented in the framework of the CT10 global fits in [238], and an earlier related study in the MSTW08 framework can be found in [269].

⁵S. Forte and J. Rojo

2.2 Gluon sensitivity to individual datasets

We first study the sensitivity of the gluon PDF to the different data included in the global fit, with the motivation of quantifying which datasets mostly constrain $g(x, m_H)$ in the region relevant to the $gg \rightarrow H$ cross-section, namely $x \in [0.005, 0.05]$. Note that the total Higgs production cross-section in the gluon fusion channel is dominated by the threshold region, which means that even beyond leading order the result is mostly controlled by the gluon luminosity at $\tau = \frac{m_H^2}{s}$, i.e. the gluon PDF at $x = \sqrt{\frac{m_H^2}{s}} \approx 0.01$.

This sensitivity of the gluon on each individual dataset can be quantified by computing the correlation [223, 225] between the gluon PDF $g(x, m_H)$ and the contribution to the χ^2 from the given experiment. This is given by

$$\rho(x) = \frac{\langle g^{(k)}(x, m_H) \chi^{2(k)} \rangle_{\text{rep}} - \langle g^{(k)}(x, m_H) \rangle_{\text{rep}} \langle \chi^{2(k)} \rangle_{\text{rep}}}{\sigma_{g(x, m_H)} \sigma_{\chi^2}} \quad (\text{II.3})$$

where averages are computed over the sample of $k = 1, \dots, N_{\text{rep}}$ replicas. We normalize the correlation to the number of datapoints, i.e. such that $\rho = N_{\text{dat}}$ means complete correlation, thereby accounting for the fact that datasets with a larger number of points will carry more weight in the global fit. In practice this is done by multiplying by N_{dat} the correlation coefficient defined according to Eq. II.3.

In Fig. II.22 we show the correlation between the gluon PDF $g(x, Q = m_H)$ and the χ^2 for different datasets in the NNPDF2.3 fit. From these correlation profiles, we see that in the region relevant for the Higgs cross-section in the gluon fusion channel, the experiments which carry highest weight in the global fit are some of the DIS fixed target data, in particular BCDMS and CHORUS, as well as the inclusive HERA-I data. Other experiments have a smaller weight in the global fit χ^2 because of the smaller number of points, like ATLAS jets or HERA charm data, but they could still have a non-negligible impact as they may affect PDFs in regions for which experimental information is scarce.

Having established which data have a potential impact on the results of the fit, we now study in detail how the NNPDF2.3 predictions for the Higgs cross section are affected when some of these datasets are added to or removed from the global fit. These results however are indirect, since they do not allow us to quantify how the Higgs $gg \rightarrow H$ cross-section (with the associated PDF uncertainties) vary when only a subset of the data is included, as compared to the reference value from the NNPDF2.3 global fit. To address this issue, in the next section we study the dataset dependence of $\sigma(gg \rightarrow H)$ in the NNPDF2.3 fit

2.3 Dataset dependence of $\sigma(gg \rightarrow H)$ in the NNPDF2.3 fit

We have performed a large number of variants of the NNPDF2.3NNLO fit keeping all the settings unchanged and varying only the fitted dataset. For each of these fits, we have then computed the $gg \rightarrow H$ cross-section with `iHixs`, and compared the results with the reference NNPDF2.3 values, as well as with those of CT10 and MSTW08 NNLO fits. In all cases we use $\alpha_s(M_Z) = 0.119$

In our first two exercises, we start with a fit to HERA data only, and then we build up the dataset of the global fit by adding experiments or groups of experiments one after the other. In the first case, shown in Fig. II.23, we start with experiments which should be subject to relatively smaller systematics, namely deep-inelastic scattering (DIS), starting with the very clean combined HERA-I data (which have minimal systematics), then adding combined HERA F_2^c data, then HERA-2 ZEUS data, and then fixed target DIS data, first with charged lepton beams and then with neutrino beams. We then add first, jet data (Tevatron and LHC) which

are the hadron collider data which should mostly impact the gluon (though at rather larger x), and finally other (Drell-Yan, W and Z production) hadron collider data, which we do not expect to have a big impact, first Tevatron and then LHC. The reader is referred to Ref. [236] and references therein for a detailed list and discussion of the various datasets (including number of datapoints, kinematic cuts, and references). For reference, we also show the corresponding values from CT10 and MSTW, with the same value of $\alpha_s(M_Z) = 0.119$.

When only HERA data is used the PDF uncertainties are large, around 7%, because only indirect constraints on the gluon PDF for $x \sim 0.01$ are provided. Still, it is remarkable that even with a single dataset, PDF uncertainties are already below the 10% range. Furthermore, no manifest inconsistencies appear: each time a dataset is added, the cross-section always moves within the 1-sigma band of the previous result, and PDF uncertainties are reduced. Despite their overall consistency, it is clear that different data pull in different directions. In particular, HERA-II and HERA F_2^c data seem to pull the cross section towards smaller values; charged-lepton fixed-target DIS data then have little impact; however, neutrino DIS data increase the cross-section and reduce the PDF uncertainties substantially. Hadron collider data finally have a minor effect.

This exercise raises several questions: are the charm data also pulling the cross-section down, or only the HERA-2 data? Are neutrino data pulling the cross section up because of the lack of hadron collider data, or would they even if the hadron collider data were not included? Are hadron collider data having little effect only because they were added in the very end?

In order to try to answer some of these questions, we repeat the exercise but now changing the order in which datasets are added. To answer the first question, we add the charm data directly to the HERA-I data. To answer the third question, we then add the LHC data immediately after the HERA-I and charm data. To answer the second question, we only add neutrino data after all hadron collider data have been also added. Results are shown in Fig. II.24.

A tentative conclusion would be that first, the charm data do pull the cross section down, without affecting much the uncertainty. Second, LHC data reduce the PDF errors substantially and also lead to smaller cross-sections (always within 1-sigma). And third, neutrino DIS data increase the cross-section by a factor around 2-sigma (this time without affecting much PDF uncertainties). Again, all other data have a minor effect. This exercise shows that a “collider only” fit leads to a smaller Higgs cross section, something that was already noticed in Ref. [236]. Such a collider-only fit is not subject to uncertainties related to the treatment of lower-scale data, nuclear targets, and neutrino beams, and thus in principle more reliable. It is important to understand, however, that PDF uncertainties for the collider-only fit are significantly larger, and results are consistent at a 90% confidence level with those of the global fit. Therefore, we cannot conclude that there is any clear evidence of inconsistency in the global fit, which remains thus the most reliable result, even though there is some indication that LHC data and neutrino DIS data do pull the fit in opposite directions.

In order to try to elucidate this, we have performed an exercise in which, with the goal of understanding the impact of each individual data set, we remove from the global fit only a single dataset at a time. Results are shown in Fig. II.25. Again, the overall consistency of the global fit is quite remarkable, since no experiment leads to a pull larger than one-sigma, and typically rather less. Results seem consistent with those of the previous exercise: removing neutrino data the cross-section goes down, which confirms that neutrino data tend to increase the cross-section. Removing jet data, the cross-section goes up, which confirms that hadron collider data seem to pull the cross section in the opposite direction as neutrino data, and suggests that it is jet data which have this effect. The remaining datasets seem to have a more moderate impact either in terms of absolute shift of the cross section (such as LHC data) or in terms of their pull, i.e. the amount the cross-section moves in units of the standard deviation (such as HERA data).

Whereas these studies start providing some indications, more detailed investigations would be needed in order to reach a clear-cut conclusion. These include studying multiple correlations: for example, it was shown in Ref. [266] that the impact of a particular set of DIS data on α_s depends on whether jet data are or are not included in the fit: namely, it may turn out that effects (including possible inconsistencies) are only revealed when a pair of data (or more) are simultaneously considered (and included or removed). Also, it might be worth studying more detailed statistical indicators, such as those which can be defined when including new data through Bayesian reweighting [270, 271].

Conclusion

In summary, we have seen that there is no clear sign of inconsistency for any of the data included in the NNPDF2.3 global fit. However, there does seem to be some indication of possible tension between data, with neutrino DIS data pulling the Higgs cross section up, and the prediction from a collider-only fit leading to a rather lower cross-section than that of the global fit, with a rather larger uncertainty and compatible with it at a 90% confidence level. More detailed studies within the NNPDF framework, including investigations of multiple correlations, could shed further light on these issues, but it would be especially interesting if it were possible to compare the behavior of different global fits upon the inclusion of individual datasets.

Of course, future measurements of LHC processes are going to provide significant further constraints, and are likely to eventually resolve all discrepancies. These include isolated photon production [259], the total cross-sections and differential distributions in top quark pair production [262], the transverse momentum distribution of electroweak vector bosons [261], inclusive jet and dijet production data [90] as well as ratios of the above cross-sections between 13 and 8 TeV [272].

Acknowledgments

We would like to acknowledge useful discussions with R. D. Ball, J. Huston, P. Nadolsky, J. Pumplin, and R. Thorne. We thank the organizers of the Les Houches "Physics at TeV colliders 2013" workshop where part of this work was performed. The work of S. F. is supported by an Italian PRIN 2010 and by a European EIBURS grant

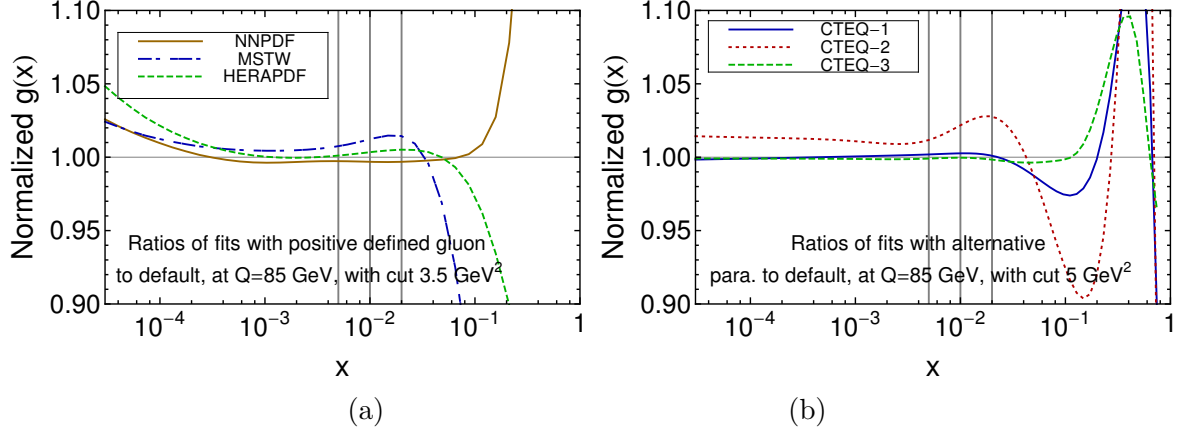


Fig. II.19: Dependence of the gluon PDF on the choice of parametrization forms of the PDFs for (a) MSTW, NNPDF, and HERAPDF fits with HERA-1 inclusive and charm quark production data, and (b) CTEQ fits with only HERA-1 inclusive data.

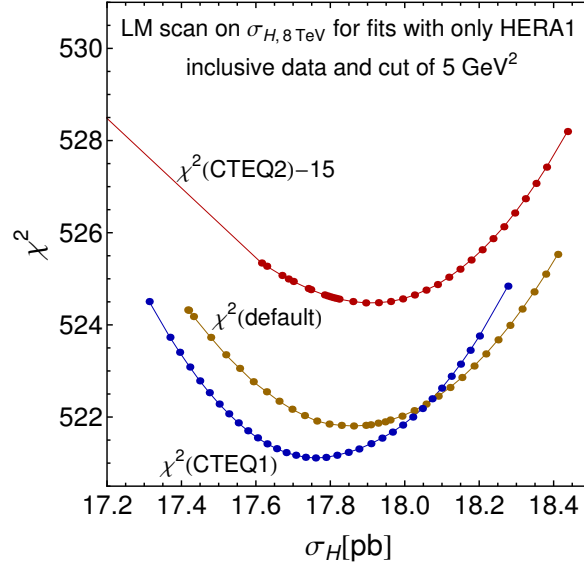


Fig. II.20: LM scan of the Higgs cross section at the LHC 8 TeV for CTEQ fits with different parametrization forms and only HERA-1 inclusive data.

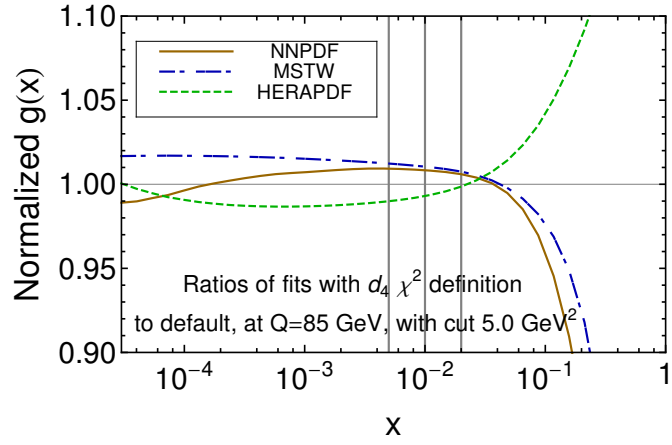


Fig. II.21: Dependence of the gluon PDF on χ^2 definition used, for MSTW, NNPDF, and HERAPDF fits with only HERA-1 inclusive data.

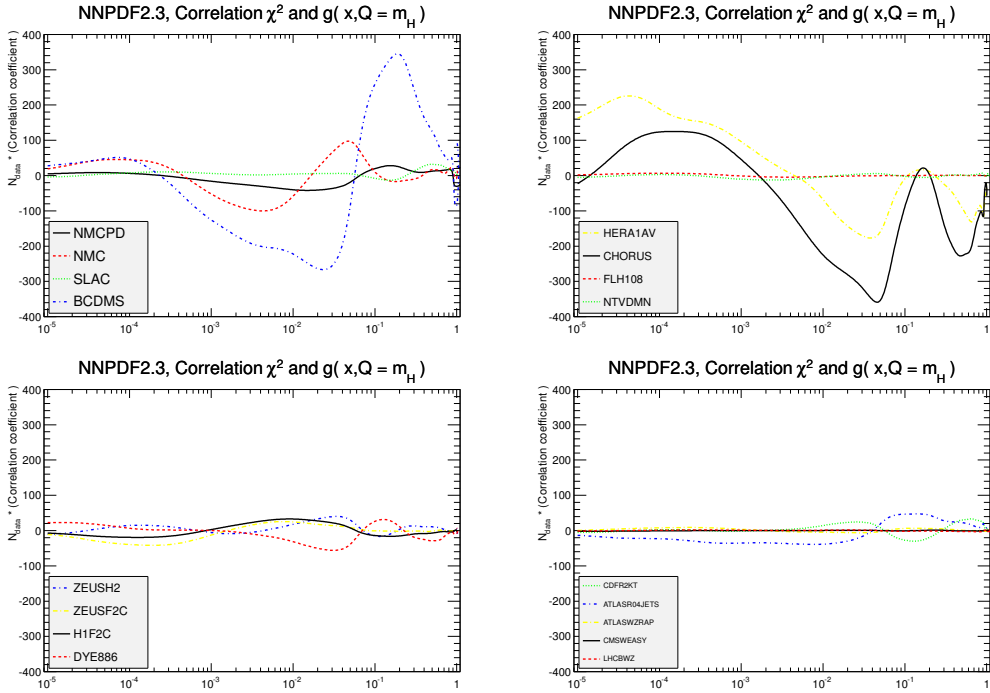


Fig. II.22: The correlation coefficient (normalized to N_{dat}) between the gluon PDF at $Q = m_H$ and the χ^2 for a representative subset of the experiments included in the NNPDF2.3 NNLO fit, as a function of x .

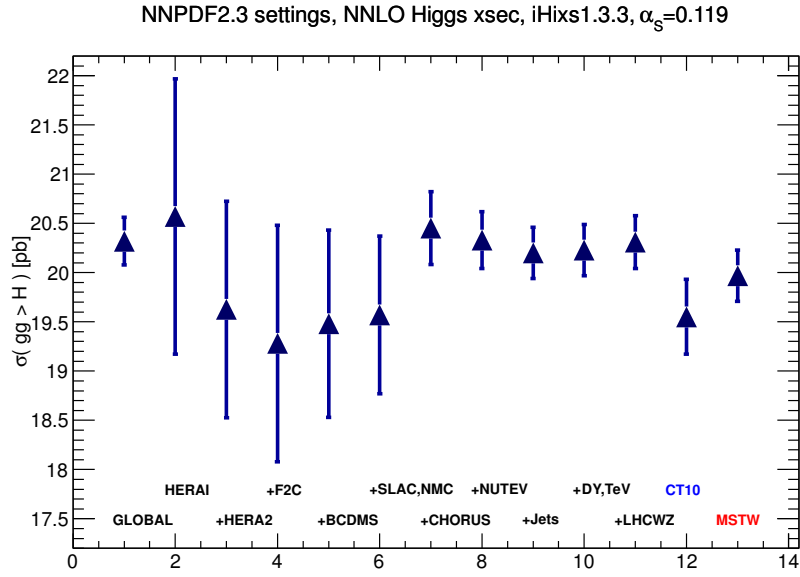


Fig. II.23: NNLO predictions for the Higgs production cross-section in the gluon fusion channel for NNPDF2.3-like fits with different datasets. Starting from the HERA-I dataset (second point from the right), we sequentially add all datasets until the global fit result (first point) is reproduced. For reference, we also show the corresponding values from CT10 and MSTW, with the same value of $\alpha_s(M_Z) = 0.119$.

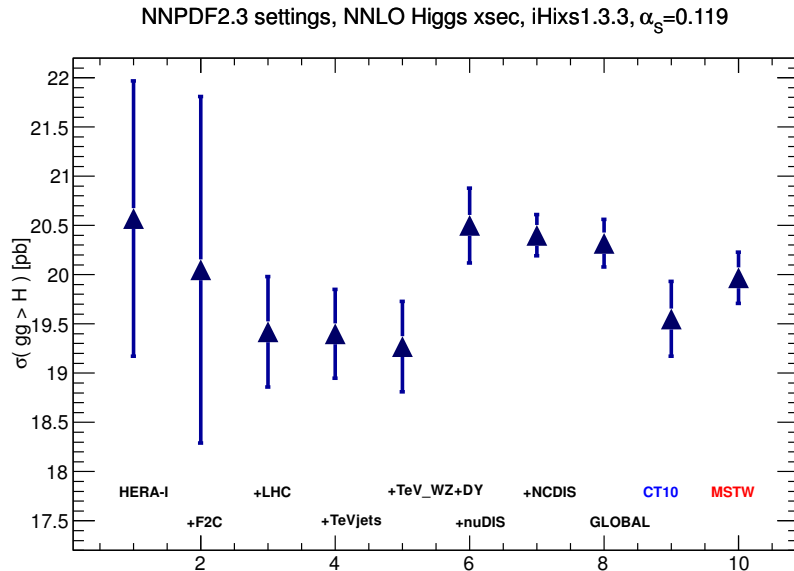


Fig. II.24: Same as Fig. II.23, but changing the order in which datasets are added.

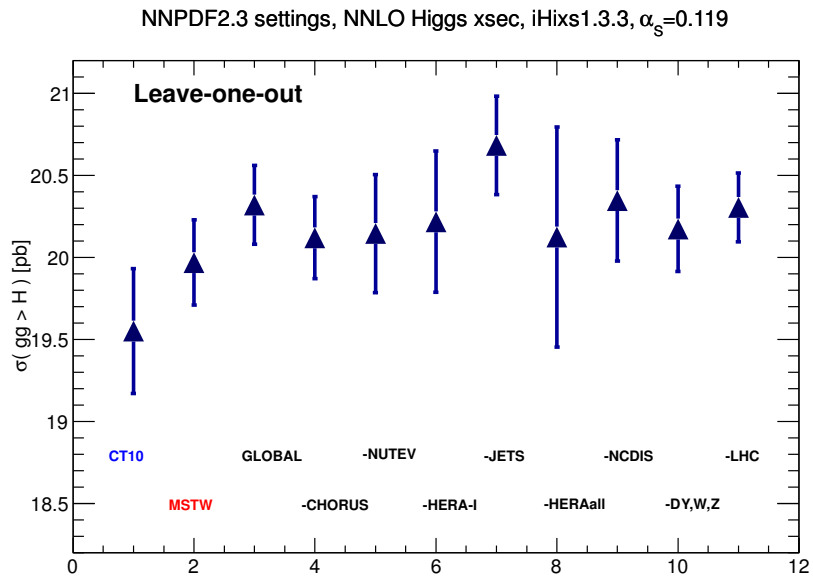


Fig. II.25: Same as Fig. II.23, but with one dataset at a time removed from the global fit.

3 New access to PDF data via LHAPDF⁶

I present an overview of problematic technical issues in the LHAPDF system, and of a complete rewrite of LHAPDF which addresses them, plus prospects for future development of systems for PDF data access in HEP.

3.1 History and evolution of LHAPDF

LHAPDF v5 and earlier themselves arose out of a Les Houches meeting [273], as the need for a scalable system to replace PDFLIB became pressing. The problem with PDFLIB was that the data for interpolating each PDF was stored in the library, and as PDF fitting became something of an industry (particularly with the CTEQ and MRST collaborations producing many sets), this model was no longer viable due to the explosion in the size of the compiled library.

LHAPDF was originally intended to address this problem by instead storing only the parameters of each parton density fit at a fixed low scale and then using standard DGLAP evolution in Q via QCDNUM [246] to evolve this, build a dynamic interpolation grid, and thereafter work as before.

However, by the mid-2000s and version 4 of LHAPDF, this model had also broken down. Each PDF parameterisation required custom code to be included in the LHAPDF library, and the bundled QCDNUM within LHAPDF had itself become significantly outdated: upgrading it was not an option due to the need for consistent behaviour between LHAPDF versions. Additionally PDF fitting groups, concerned that the built-in QCDNUM evolution would not precisely match that used by their own fitting code, had universally chosen to supply full interpolation grid files rather than evolution starting conditions, and LHAPDF had acquired a large collection of set-specific interpolation routines to read and use these files. At the time of writing, of the many actively used PDFs in use for LHC simulation and phenomenology only the CTEQ6L1 [251] PDF uses QCDNUM evolution; all others are interpolation-based.

At the same time as these trends back to interpolation-based PDF provision, user demand resulted in new features for simultaneous use of several PDFs – a so-called “multiset” mode. The implementation of this simply involves multiplying the amount of allocated interpolation space by a factor of `NMXSET`, which defaults to a value of 3. Hence in a default LHAPDF 5 build, it is possible to switch rapidly between up to three PDF sets (although only one of these “slots” can be active at any time).

3.2 Memory/speed and correctness problems with LHAPDF5

Aside from the maintenance issue of requiring new interpolation code in LHAPDF in order to use a new PDF set (an issue ameliorated some time ago by addition of special PDF names for various orders of generic spline interpolation), the major problems with LHAPDF v5 relate to the technical implementation of the various interpolation routines and the multiset mode.

Both these issues are rooted in Fortran’s static memory allocation. As usual, the interpolation routines for various PDFs operate on large arrays of floating point data declared as common blocks. However, in practice they are not used commonly, but rather each PDF “wrapper” code operates on its own array. As the collection of supported PDF sets has become larger, the memory requirements of LHAPDF have continually grown, and with version 5.9.1 (the final version in the v5 series) more than 2 GB is declared as necessary to use it at all. In practice this is not a “real” issue – operating systems are not so foolish as to allocate memory to store uninitialized data for PDFs which are not being used – but on memory managed systems such as the LHC Grid where 2 GB is the maximum level permitted per core/process, it is enough to

⁶A. Buckley

block any LHAPDF 5 jobs from running.

A workaround solution was provided some time ago for this problem: a so-called “low memory mode” in which LHAPDF 5 could be built, reducing the static memory footprint within acceptable limits. This has the effect of only providing interpolation array space for one member in each PDF set, which is usually sufficient for event generation but unworkable for uncertainty studies in which each event must be re-evaluated or reweighted to each member in the PDF error set: unless the user structures their code runs in a rather unnatural way, constant re-initialisation of the single PDF slots from the data file slows operations to a crawl. For this reason, PDF reweighting studies for the LHC have had to be done using special, often private, user builds of LHAPDF rather than the standard versions distributed by the LHC experiments. There is danger here for error and inconsistency.

Notably, low-memory mode is incompatible with the recent trend to compute (in particular NLO) PDF reweightings within an MC generator run rather than post hoc, since every event involves upwards of 40 slow PDF re-initializations which dominate the generation time: large scale experiment MC production with this feature enabled in aMC@NLO [6], Sherpa [166], or POWHEG [26] requires an improved LHAPDF.

Further options exist for selective disabling of LHAPDF support for particular PDF families, as an alternative way to reduce the memory footprint. However, since this highly restricts the parton density fits which can be used, it has not found much favour.

The last set of problems with LHAPDF 5 relate, concerningly, to the *correctness* of the output. For example different generations of PDF fit families share the same interpolation code, although they may have different ranges of validity in x - Q phase space, and wrong ranges are sometimes reported. The reporting of Λ_{QCD} metadata has notoriously been dysfunctional for a long time and cannot be fixed, with the result that shower MC generators which attempt to acquire an appropriate α_s definition from the PDF will fail – indeed PYTHIA 6’s many tunes depend on this behaviour! And since the multiset mode is only implemented as a multiplying factor on the size and indexing offsets, reported values of metadata such as α_s and x, Q boundaries does not match the currently active PDF slot, but rather the last set to be initialized.

All of these problems stem from the combination of the static nature of Fortran memory handling and from the way that evolving user demands on LHAPDF forced retro-fitting of features such as grid interpolation and multiset mode on to a system not designed to incorporate them. These combine with other “emergent” features such as the lack of any versioned connection between the PDF data files and the library, the menagerie of interpolation grid data formats (each group has its own, and sometimes several), and the need for code additions to use new sets, to make LHAPDF 5 difficult both to use and to maintain.

3.3 LHAPDF 6: a new library design and programmatic interface

LHAPDF v6 is a completely new PDF library system, written specifically to address all of the above problems, both technical and maintenance/manpower related. As so many of the problems fundamentally stem from Fortran’s memory handling (at least prior to Fortran 90) and the bulk of new experimental and event generator code is written in C++, we have also chosen to write the new LHAPDF 6 in object oriented C++.

The central code/design object in LHAPDF 6 is the PDF, an interface class representing parton density functions for a variety of parton flavours.⁷ An extra object, `PDFSet` is provided purely for (significant) convenience in accessing PDF set metadata and all the members in the

⁷The nomenclature around “PDFs”, “PDF sets” etc. is historically rather sloppy: we use the LHAPDF tradition of referring to a single multi-flavour fit as a “PDF” or “member”, and several such PDFs as a “set”; single-flavour parton densities do not exist as named entities in the code.

set, e.g. for making systematic variations within a set.

As LHAPDF 5 included special case treatments for PDFs including a photon or gluino constituent, which were rather “hacky”, LHAPDF 6 allows completely general flavours, identified using the standard PDG Monte Carlo ID code [264] scheme. An alias of 0 for 21 = gluon is also supported, for backward compatibility and the convenience of being able to access all QCD partons with a for-loop from -6 to 6. A hypothetical PDF might hence declare, for example, that it only contains explicit up, down and gluino flavours, and all other parton flavours would return $xf(x, Q^2) = 0$ everywhere (this PDF would not be expected to describe data particularly well, but there is no *technical* obstacle to its construction!) $xf(x, Q^2)$ values may be retrieved from the library either for a single flavour at a time, for all flavours simultaneously as a `int → double std::map`, or for the standard QCD partons as a `std::vector of double s`. The latter method can also be used to fill a pre-existing `vector` for improved speed.

A key feature in the LHAPDF 6 design is a powerful “cascading metadata” system, whereby any information (integer, floating point, string, or lists of them) can be attached to a PDF, a PDF set, or the global configuration of the LHAPDF system via a string-valued lookup key. If, for example, $\alpha_s(M_Z)$ is not defined on a PDF, the system will automatically fall back to looking in its containing set and then the LHAPDF configuration for a value before throwing an error. This information is set by default in the PDF/set/configuration data files using the standard YAML [274] syntax. The access to this information is via the general `Info` class, from which `PDFSet` and `PDFInfo` are specialised. The info system is used to compactly implement a multitude of metadata properties, from quark and Z masses to the PDG ID of the parent particle (to allow for identifiable nuclear PDFs), and the error treatment, confidence level, etc. to allow automated error computation. All metadata set from file may also be explicitly overridden in the user code. PDF sets can contain metadata keys expressing the version of LHAPDF required to correctly process it, and an integer data version key to allow for tracking of bugfixes to the data file: these provide a robust way to track PDF data versions, and also to declare that a PDF is unvalidated (with no `DataVersion` key, or a declared negative version).

Following the strong trend towards interpolated PDFs, whereby PDF groups can obtain arbitrarily faithful representations of their fits by increasing the sampling density, and away from internally QCD-evolved PDFs, the only internally provided PDF type in LHAPDF 6 is an interpolation on a rectangular grid in x - Q^2 space. The `PDF` class, however, is abstract in the sense that any means of PDF evolution may be implemented according to the interface that it defines. The built-in grid interpolation is provided in the internal `GridPDF` class and associated helper structures for handling the grid and flavour decomposition. In fact, each PDF may contain many distinct grids in Q^2 , in order to allow for parton density discontinuities (or discontinuous gradients) across quark mass thresholds: however these subgrids, and the x , Q^2 sampling points (interpolation “knots”) within them must be the same for all flavours in the PDF. The interpolation is currently performed using cubic splines in $\log Q$ - $\log x$ space, but as the interpolator algorithm is configurable via a metadata key there is the possibility of evolving better interpolators in a controlled way without changing previous PDF behaviours. Internally, PDF querying is natively done via Q^2 rather than Q , since event generator shower evolution naturally occurs in a squared energy (or p_\perp) variable and it is advisable to minimise expensive calls of `sqrt`. For this log-based interpolation measure, however, the logarithms of (squared) knot positions are also pre-computed in the interpolator construction to avoid excessive `log` calls. Custom extrapolators are also possible, but at present only “freeze” and “throw error” extrapolation handlers are provided for handling PDFs outside their fitted range.

The interpolation PDF data files use a single uniform plain text format. This starts with a YAML-format header section (to provide member-specific metadata overrides), then blocks of numbers for each x - Q^2 subgrid, each started by a header declaring the knot positions and

encoded parton flavours. As opposed to LHAPDF 5, where each PDF set was encoded in a single text data file, the LHAPDF 6 format is that each set is a *directory*, which contains one “info” file of set-wide metadata, plus one “.dat” file for each PDF member in the set. This permits much faster lookup of set-level metadata, and random access to single members in the set. If desired, the member content of a set could be stripped down to save space in special applications. It is possible, using the `zlibc` library [275], to zip the data files in the directory for space-saving and faster data reading. The data parser has internally been optimised for fast reading of ASCII numerical data. As there is no set-specific or family-specific handling code in the library, new PDFs may be made and privately tested (or even released separately from LHAPDF) without needing a new version of the LHAPDF library. The only update required for a new official set is an updated version of the `pdfsets.index` file, which provides a lookup to PDF names and member numbers from the global LHAPDF ID code. The latest version of this file, along with the PDF data itself compressed as one tarball per set, is available for download from the LHAPDF website [276].

Since α_s evolution is key to correct PDF evolution and usage, LHAPDF 6 contains implementations of α_s running via three methods: an analytic approximation, a cubic spline interpolation in $\log Q$, and numerical solution of the ODE – the latter used to dynamically populate an interpolation grid which is used thereafter for performance reasons. These evolvers are specified (cf. grid interpolators and extrapolators) via metadata keys on the PDF member or set, which can be programmatically overridden. Flavour thresholds/masses, orders of QCD running, and fixed points/ Λ_{QCD} are all correctly handled in the analytic and ODE solvers, and subgrids are available in the interpolation.

The most distinctive change in LHAPDF 6 is how the user manages the memory associated with PDF objects, namely they are now fully responsible for it. A user may create as many or as few PDFs at runtime as they wish – there is neither a necessity to create a whole set at a time, nor any need to re-initialise objects, nor a limitation to `MMXSETS` concurrent PDF sets. The flip-side to this flexibility is that the user is also responsible for cleaning up the memory use afterwards, either with manual calls to `delete` or by use of e.g. smart pointers. PDFs or info objects (or interpolators, extrapolators, α_s objects...) are created by the `new` operator in helper functions, via string-valued identifiers or the global LHAPDF ID code, which is still in use and will continue to be allocated for submitted PDFs. Unlike in LHAPDF 5, the different PDF objects exist independently of each other and can be used concurrently, e.g. in multi-threaded programming, although as always with concurrent programming care must be taken to avoid accidentally sharing memory between the threads.

Finally, since uptake of LHAPDF 6 is realistically contingent on the mass of pre-existing code continuing to work (while providing a more friendly and powerful alternative interface) legacy interfaces have been provided to the Fortran LHAPDF and PDFLIB interfaces, and to the LHAPDF 5 C++ interface. C++ preprocessor hooks have been provided to allow smooth migration to v6 based on the version of LHAPDF found on the system at compile time. These legacy interfaces have been successfully tested with a variety of MC generator codes.

3.4 Migration and validation programme

A major task, at least as substantial as writing the new library, has been the migration of PDFs from the multitude of version 5 formats to the new format and interpolator, and then validating their faithfulness to the originals. This has been done in several steps, starting with a Python script which used the LHAPDF 5 interface (with some extensions) to extract the grid knots and dump the PDF data at the original knot points into the new format. This script has undergone extensive iteration, as support was added for subgrids, member-specific metadata, etc. etc., and to allow more automation of the conversion process for hundreds of PDFs. The choice was made

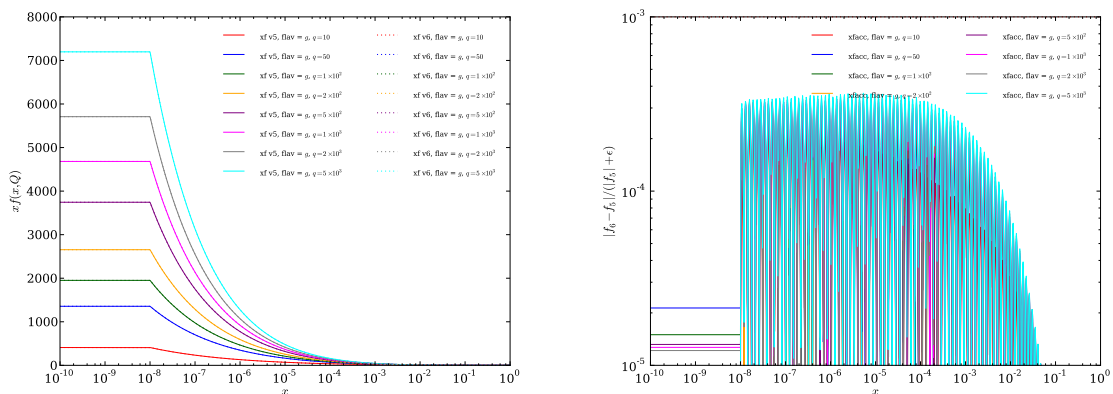


Fig. II.26: Example comparison plots for the validation of the CT10nlo central gluon PDF, showing the raw PDF behaviour as a function of x , and the corresponding v5 vs. v6 regularised accuracy metric. The differences between v5 and v6 cannot be seen in the left-hand plot, since as seen on the right the fractional differences are everywhere below one part in 1000.

to only convert the most recent PDF sets in each family unless there were specific requests for earlier ones: this collection is over 200 PDF sets, and at a conversion rate of approximately one second per member it takes several hours to re-dump the full collection.

After dumping, the set directories are zipped into tarballs and uploaded to the LHAPDF website. PDFs which have been approved by their original authors are available in the “main” download area, while those yet to be blessed are contained in a subsidiary “unvalidated” staging area. Validated PDFs are also made available on CERN AFS, at `/afs/cern.ch/sw/lcg/external/lhapdfsets/current`.

To become validated, a comparison system has been developed which uses the same C++ code to dump PDF xf values in scans across x and Q (as well as α_s values in Q) at a wide range of values in each variable, from both LHAPDF 5 and 6. The corresponding data files from each version are then compared to each other using a difference metric which corresponds to the fractional deviation of the v6 value from the original v5 one in regions where the xf value is large, but which suppresses differences as the PDFs go to zero, to minimise false alarms. An ad hoc difference tolerance of 10^{-3} was chosen on consultation with PDF authors as a level to which no-one would object, despite differences in opinion on e.g. preferred interpolation schemes. This level, as illustrated in Fig. II.26 for the CT10nlo central PDF member validation, has been achieved almost everywhere for the majority of PDFs. Where differences do occur (e.g. on MSTW set flavour thresholds before they were explicitly added to the migration script) they are typically restricted to single points on the extremes of the PDF phase space, or as transient spikes on flavour thresholds: these cases can then be individually examined to determine if there is a genuine problem, which so far has not been the case. This validation and plotting process is much slower than PDF conversion, and generates huge volumes of plots (several x and Q scans of each flavour in each member of each set) and hence we have so far used only the central members of each set for validation. At the time of writing, all NNPDF and MRST/MSTW sets have been approved by their authors, as have several heavily-used CTEQ sets. Approval of the remainder of CTEQ sets, and the HERA, ATLAS, and ABM sets, is pending.

3.5 Status, limitations and prospects

After a lengthy testing period and useful user feedback, the first official LHAPDF 6 version was released in August 2013. Since then several further developments and bugfixes (as well

as increased PDF set support) has occurred and at the time of writing version 6.0.5 may be downloaded, along with data files, from <http://lhapdf.hepforge.org>. An automatic data downloader/manager script is provided with the library to help with PDF data management. Author approval of the remaining unvalidated sets is hoped to happen soon.

At present the scope of LHAPDF 6 is intentionally more LHC-focused than LHAPDF 5: we are mindful of the small amount of development manpower and the interests of those involved. Accordingly, no QCD evolution is planned for the library although we will consider proposals and code patches, and the class interface is available for anyone to plug their own implementations into, should they so wish. Similarly, there is at present no plan to include automatic nuclear corrections or PDFs of the resolved virtual photon: we believe that the former is better done explicitly using one of several nuclear corrections tools, and the latter is not presently of interest at the LHC (although EW constituents of nucleons are fully supported) and can be implemented for fixed values of virtuality and impact parameter using the current interface. Double-parton PDFs and generalised PDFs for CCFM QCD evolution are also considered as special cases and are not directly supported by the LHAPDF 6 interface (after consultation with PDF authors.)

The library is currently considered in a production-ready state, and several generators and LHC experiments have updated their code interfaces to make use of it. The performance has been found to be (of course) vastly better than LHAPDF 5 in terms of memory usage, by explicit design. It has also been pleasing to find that design decisions such as the split member data files lead to a measurably faster start-up time, and that the possibility of evolving single flavours at a time (as opposed to LHAPDF 5, which always evolved all flavours) can produce significant speed-ups (of order a factor of 3) in MC event generation and event reweighting. We have scheduled several developments to get even better performance, such as caching interpolation weights between calls to a PDF interpolator, and optimising the interpolation code to make use of vectorized instructions on modern CPUs. Use of GPGPUs has been suggested, but we advise that anyone wanting that functionality contact the LHAPDF developers with a plan for their implementing at least a proof of concept version. Zipped access to PDF data files is already possible by slightly tricky use of `zlibc`, but this could also become a built-in library feature if it can be implemented without incurring unacceptable dependency and build difficulties.

Some physics improvements have also been suggested, such as use of a $\log(1-x)$ measure for high- x interpolation, a low- Q extrapolation scheme based on computed anomalous scaling dimensions, and (optional) distinction between quark masses and flavour thresholds in α_s evolution.

We are pleased that a year after the project started, LHAPDF 6 is a mature, performant and powerful library for future PDF access at Run 2 of the LHC and beyond, with an active and increasing user base. Our thanks to all who helped us to get here!

Acknowledgements

AB thanks the Les Houches workshop once again for the hospitality and enjoyable/productive working environment in the Chamonix valley, and acknowledges support from a Royal Society University Research Fellowship, a CERN Scientific Associateship, an IPPP Associateship, and the University of Glasgow's Leadership Fellow programme.

Chapter III

Phenomenological studies

1 Inclusive jet cross section at the LHC and the impact of weak radiative corrections¹

1.1 Introduction

Quantum chromodynamics (QCD) describes the strong interaction between quarks and gluons, which are confined within bound states and cannot be observed as free particles. Instead, in high-energetic hadron collisions, collimated streams of particles, known as “jets”, are produced that convey essential information about the hard scattering process between the hadrons’ constituents. The investigation of these jets, technically defined through jet algorithms, allows to compare predictions from perturbation theory with measurements and to look for new phenomena at the highest accessible transverse momenta. In particular, the energy scale dependence of the strong coupling can be determined, and the parton distribution functions (PDFs), notably the gluon PDF, can be constrained.

The high quality and precision of the measurements performed by the experiments at the Large Hadron Collider (LHC) at CERN demand a similar level of accuracy in the theoretical predictions. The QCD corrections to jet production are known up to next-to-leading order (NLO) in perturbation theory [277–279], and a substantial effort is currently put into the computation of the corrections at next-to-next-to-leading order (NNLO), where the purely gluonic channel, retaining the full dependence on the number of colours, was completed recently [15, 16].

Probing the high-energy regime beyond 1 TeV of jet transverse momentum, electroweak (EW) corrections might become large because of the appearance of Sudakov-type and other high-energy logarithmic terms in the calculations. In particular, the leading term is given by $\alpha_w \ln^2(Q^2/MW^2)$, where Q denotes the typical scale of the hard-scattering reaction, MW is the W-boson mass, and $\alpha_w = \alpha/s_w^2 = e^2/(4\pi s_w^2)$ is derived from the $SU(2)$ gauge coupling e/s_w with s_w being the sine of the weak mixing angle θ_w . The potential impact of these EW corrections has to be evaluated in order to accompany the NNLO QCD prediction.

This article is organized as follows: In Section 1.2, the purely weak radiative corrections of $\mathcal{O}(\alpha_s^2\alpha)$ to the inclusive jet production are presented, where the restriction to the weak corrections, denoted by $\alpha_s^2\alpha_w$, is motivated by the aforementioned logarithmic enhancements. In the following section 1.3 the measurement is introduced, to which the theory predictions are compared in Section 1.4. Section 1.5 summarizes the results and gives a short outlook.

1.2 Weak radiative corrections and tree-level electroweak contributions

The weak corrections form a well-defined gauge-invariant subset of the full EW ones and can be supplemented by the photonic contributions at a later time. In case of the photonic corrections to jet production the high-energy logarithmic terms correspond to the well-known infrared singularities, which cancel against bremsstrahlung corrections and therefore do not lead to logarithmically enhanced contributions. The results shown in the following are based on the calculation of the respective corrections to dijet production presented in Ref. [87], which includes a detailed discussion of the numerical results presented in the form of distributions in the dijet invariant mass and the transverse momenta of the leading and sub-leading jets. Corrections at

¹S. Dittmaier, A. Huss and K. Rabbertz

this order have been previously calculated for the single-jet inclusive cross section in Ref. [280], and preliminary results to dijet production were shown in Ref. [281].

The EW interaction does not only affect jet cross sections through radiative corrections, but in case of the four-quark subprocesses the production of jets can also occur via the exchange of EW gauge bosons already at leading order (LO). As a consequence, the Born cross section receives, in addition to the pure QCD contribution of $\mathcal{O}(\alpha_s^2)$, further contributions of $\mathcal{O}(\alpha_s\alpha)$ and $\mathcal{O}(\alpha^2)$ from the interference between QCD and EW diagrams and the squares of the EW amplitudes. The different contributions that need to be considered at tree level are illustrated exemplarily for the case of the partonic subprocess $u + d \rightarrow u + d$ in Fig. III.1. The interference term of $\mathcal{O}(\alpha_s\alpha)$ only contributes to the product between t - and u -channel diagrams due to the colour structure. Note that all EW gauge bosons are accounted for in the LO prediction, i.e. the photonic contributions are included.

As motivated in the introduction, the NLO calculation is restricted to the purely weak corrections defined by the order $\alpha_s^2\alpha_w$. A selection of interference contributions that enter the calculation of the virtual corrections is shown in Fig. III.2. The purely gluonic channel does not receive corrections through this order, and the corrections to the subprocesses with two gluons and two quarks correspond to the weak $\mathcal{O}(\alpha_w)$ corrections to the LO $\mathcal{O}(\alpha_s^2)$ cross section which are shown in Fig. III.2(a). The fact that diagrams of both, $\mathcal{O}(\alpha_s)$ and $\mathcal{O}(\alpha_w)$, occur at LO in case of the four-quark process leads to two different ways to obtain corrections of the order $\alpha_s^2\alpha_w$. Firstly, the one-loop diagrams of $\mathcal{O}(\alpha_s\alpha_w)$ interfered with the LO QCD diagram, similarly to the corrections to the two-gluon–two-quark subprocess, which is illustrated in Fig. III.2(b). Secondly, the one-loop NLO QCD diagrams of $\mathcal{O}(\alpha_s^2)$ interfered with the LO weak diagrams as shown in Fig. III.2(c). Note, however, that a strict separation of the weak and QCD corrections is not possible, which is reflected by the appearance of diagrams such as the third loop diagram in Fig. III.2(b). This box diagram can be obtained in two ways: by considering the weak corrections to the tree-level diagram shown on the right of Fig. III.2(b), and by attaching a virtual gluon to the tree-level diagram in Fig. III.2(c). This signals that all contributions of the defining order $\alpha_s^2\alpha_w$ have to be taken consistently into account and, furthermore, the corresponding real-emission corrections need to be included in the case of the four-quark processes to ensure the proper cancellation of infrared divergences. Further details on the calculation of the corrections can be found in Ref. [87].

1.3 Measurement of the inclusive jet cross section with the CMS detector

The inclusive jet cross section that is compared to theory predictions has been measured with the CMS detector [282] in 2011 from proton–proton collision data at $\sqrt{s} = 7$ TeV. The recorded

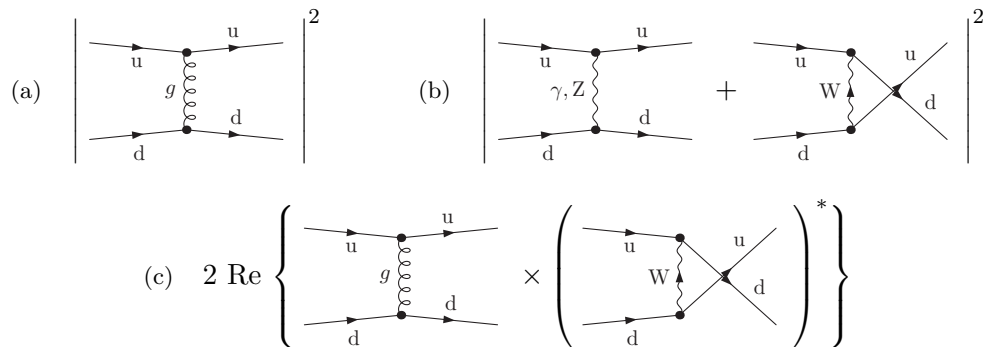


Fig. III.1: The tree-level contributions to the process $u + d \rightarrow u + d$ of the orders (a) α_s^2 , (b) α^2 , and (c) $\alpha_s\alpha$.

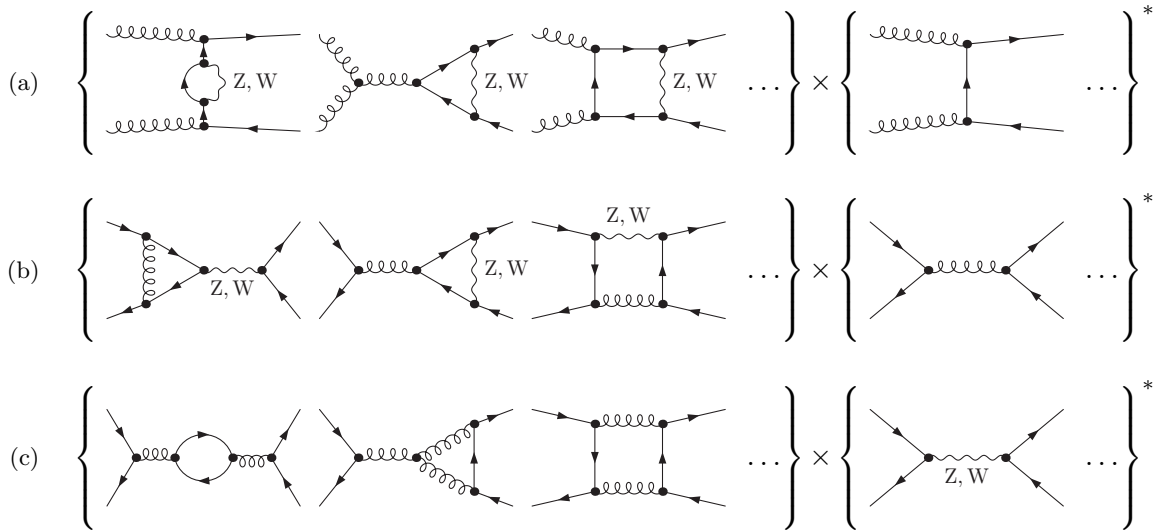


Fig. III.2: The virtual corrections of $\mathcal{O}(\alpha_s^2\alpha_w)$ illustrated in terms of typical interferences for the (a) two-gluon-two-quark and (b), (c) four-quark subprocess.

data correspond to 5.0 fb^{-1} of integrated luminosity and reach up to 2 TeV in jet transverse momentum p_T and 2.5 in absolute jet rapidity $|y|$. The measurement is performed double-differentially with five equally sized bins of $\Delta|y| = 0.5$ up to $|y| = 2.5$ and a binning in jet p_T that follows the jet p_T resolution of the central detector. The minimal p_T imposed on any jet is 114 GeV while the upper reach in p_T is limited by the available amount of data and decreases with $|y|$.

Employing the FASTJET package [283] jets are reconstructed using the collinear- and infrared-safe anti- k_T clustering algorithm [284] with a jet size parameter of $R = 0.7$. The measured cross sections, corrected for detector effects, are published in Ref. [90] and are available via the HEPDATA project [285, 286] including correlations between systematic and statistical experimental uncertainties. Non-perturbative QCD corrections, see Sect. 1.4, that were used in the CMS reference are provided in the HEPDATA files as well.

The measurement is subject to four categories of experimental uncertainties: the jet energy scale, the luminosity, the unfolding, and a residual uncertainty. The jet energy scale as the dominant source of systematic uncertainty affects the jet cross section to about 5–25% of uncertainty. The luminosity, which is known to a precision of 2.2%, corresponds to a global normalization uncertainty. The unfolding corrects for detector effects and is related to the jet energy resolution and the modelling of the detector response in detailed Monte Carlo simulations. It leads to an uncertainty on the cross section of the order of 3–4%. Diverse residual effects are summarized into an uncorrelated uncertainty of 1%.

1.4 Comparison between theory and measurement

The EW corrections studied here consist of the two contributions introduced in Sect. 1.2. They have been evaluated with the renormalization and factorization scales, μ_R and μ_F , set to the maximum jet p_T , $p_{T,\text{max}}$. The results are presented in Fig. III.3 as a function of the transverse momentum p_T for the five rapidity bins in terms of correction factors K :

The weak radiative corrections of $\mathcal{O}(\alpha_s^2\alpha_w)$ denoted by $K_{\text{weak}}^{1\text{-loop}}$ are negligible for small transverse momenta and become increasingly negative towards higher scales. This cor-

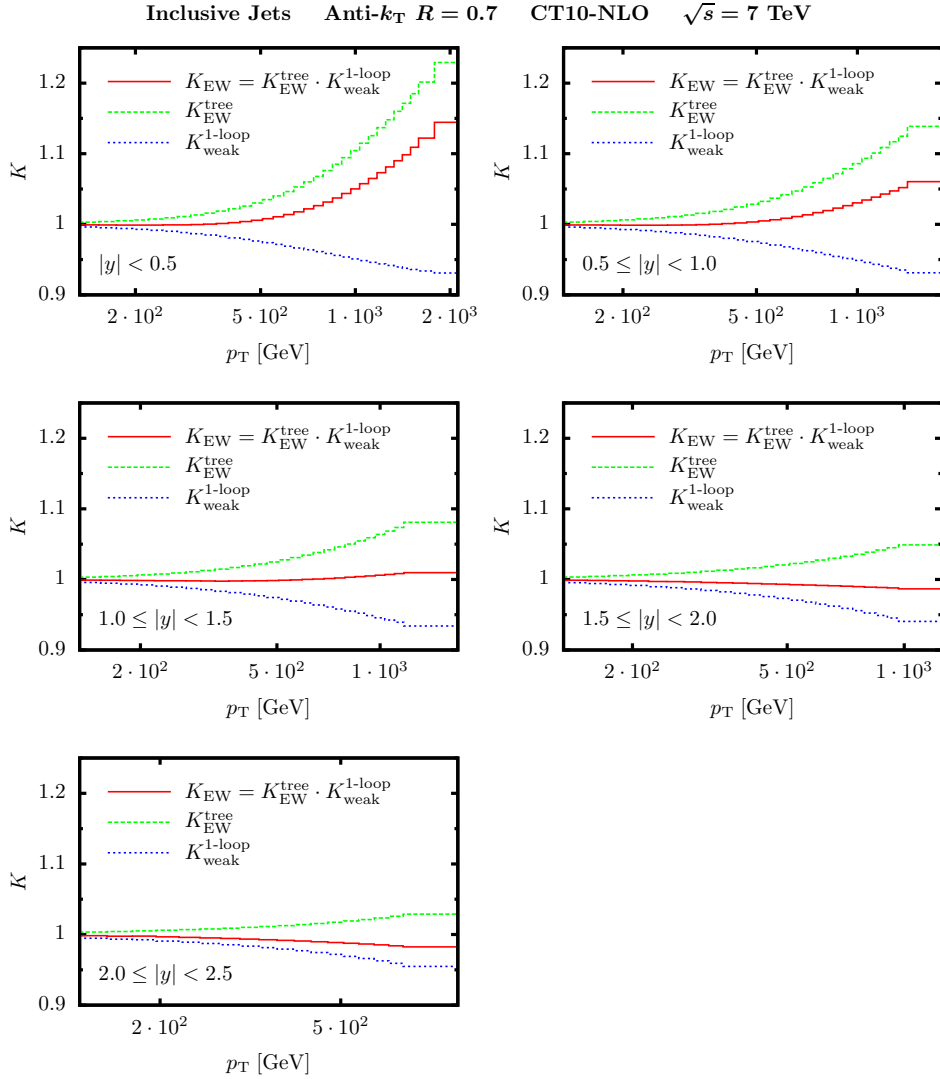


Fig. III.3: The EW correction factors to the transverse-momentum distribution for inclusive jet production for each rapidity bin, divided into the weak radiative corrections of $\mathcal{O}(\alpha_s^2 \alpha_w)$ (dotted blue), the tree-level contributions of $\mathcal{O}(\alpha_s \alpha, \alpha^2)$ (dashed green), and the combination of both contributions (solid red).

responds to the typical behaviour known from the weak high-energy logarithms, which become large in the so-called ‘‘Sudakov regime’’, where all scalar invariants of different momenta in the hard scattering are required to be simultaneously much larger than the weak gauge-boson masses. For instance, as discussed in more detail in Ref. [87], the tails of the dijet invariant-mass distributions do not probe this Sudakov regime, but are dominated by the Regge (forward) region. As a consequence, the weak corrections to the dijet invariant-mass distribution turn out to be much smaller than in the case of the inclusive jet p_T considered here, where the Sudakov regime is probed at high p_T .

The tree-level contributions of $\mathcal{O}(\alpha_s \alpha, \alpha^2)$ with the associated correction factor K_{EW}^{tree} solely appear in the four-quark subprocesses and are negligible at small transverse momenta, where the cross section is dominated by gluon-induced channels. Towards higher transverse momenta, the PDFs are probed at larger values of the momentum fraction x , so that the relative size of the quark–quark luminosity becomes more and more relevant

| $ y < 0.5$ | | | $0.5 \leq y < 1.0$ | | | $1.0 \leq y < 1.5$ | | | $1.5 \leq y < 2.0$ | | | $2.0 \leq y < 2.5$ | | |
|-------------|---|----------|----------------------|---|----------|----------------------|---|----------|----------------------|---|----------|----------------------|---|----------|
| p_T [GeV] | $\frac{K_{EW}^{tree}}{K_{EW}^{1-loop}}$ | K_{EW} | p_T [GeV] | $\frac{K_{EW}^{tree}}{K_{EW}^{1-loop}}$ | K_{EW} | p_T [GeV] | $\frac{K_{EW}^{tree}}{K_{EW}^{1-loop}}$ | K_{EW} | p_T [GeV] | $\frac{K_{EW}^{tree}}{K_{EW}^{1-loop}}$ | K_{EW} | p_T [GeV] | $\frac{K_{EW}^{tree}}{K_{EW}^{1-loop}}$ | K_{EW} |
| 114 – 133 | $\frac{1.002}{0.997}$ | 0.999 | 114 – 133 | $\frac{1.002}{0.997}$ | 0.999 | 114 – 133 | $\frac{1.003}{0.997}$ | 0.999 | 114 – 133 | $\frac{1.003}{0.996}$ | 0.999 | 114 – 133 | $\frac{1.003}{0.996}$ | 0.999 |
| 133 – 153 | $\frac{1.003}{0.996}$ | 0.999 | 133 – 153 | $\frac{1.003}{0.996}$ | 0.999 | 133 – 153 | $\frac{1.003}{0.996}$ | 0.999 | 133 – 153 | $\frac{1.003}{0.995}$ | 0.999 | 133 – 153 | $\frac{1.004}{0.995}$ | 0.998 |
| 153 – 174 | $\frac{1.004}{0.995}$ | 0.999 | 153 – 174 | $\frac{1.004}{0.995}$ | 0.999 | 153 – 174 | $\frac{1.004}{0.995}$ | 0.999 | 153 – 174 | $\frac{1.004}{0.994}$ | 0.999 | 153 – 174 | $\frac{1.004}{0.993}$ | 0.998 |
| 174 – 196 | $\frac{1.005}{0.994}$ | 0.999 | 174 – 196 | $\frac{1.005}{0.994}$ | 0.999 | 174 – 196 | $\frac{1.005}{0.993}$ | 0.999 | 174 – 196 | $\frac{1.005}{0.993}$ | 0.998 | 174 – 196 | $\frac{1.005}{0.993}$ | 0.998 |
| 196 – 220 | $\frac{1.006}{0.993}$ | 0.999 | 196 – 220 | $\frac{1.006}{0.993}$ | 0.999 | 196 – 220 | $\frac{1.006}{0.992}$ | 0.998 | 196 – 220 | $\frac{1.006}{0.991}$ | 0.998 | 196 – 220 | $\frac{1.006}{0.991}$ | 0.997 |
| 220 – 245 | $\frac{1.007}{0.991}$ | 0.999 | 220 – 245 | $\frac{1.008}{0.991}$ | 0.999 | 220 – 245 | $\frac{1.008}{0.989}$ | 0.998 | 220 – 245 | $\frac{1.008}{0.990}$ | 0.997 | 220 – 245 | $\frac{1.008}{0.989}$ | 0.996 |
| 245 – 272 | $\frac{1.009}{0.990}$ | 0.999 | 245 – 272 | $\frac{1.009}{0.990}$ | 0.999 | 245 – 272 | $\frac{1.009}{0.990}$ | 0.998 | 245 – 272 | $\frac{1.009}{0.988}$ | 0.997 | 245 – 272 | $\frac{1.008}{0.987}$ | 0.995 |
| 272 – 300 | $\frac{1.011}{0.988}$ | 0.999 | 272 – 300 | $\frac{1.011}{0.988}$ | 0.999 | 272 – 300 | $\frac{1.011}{0.987}$ | 0.998 | 272 – 300 | $\frac{1.010}{0.986}$ | 0.996 | 272 – 300 | $\frac{1.009}{0.986}$ | 0.994 |
| 300 – 330 | $\frac{1.013}{0.987}$ | 1.000 | 300 – 330 | $\frac{1.013}{0.986}$ | 0.999 | 300 – 330 | $\frac{1.013}{0.985}$ | 0.998 | 300 – 330 | $\frac{1.012}{0.984}$ | 0.996 | 300 – 330 | $\frac{1.010}{0.984}$ | 0.994 |
| 330 – 362 | $\frac{1.019}{0.985}$ | 1.000 | 330 – 362 | $\frac{1.019}{0.984}$ | 1.000 | 330 – 362 | $\frac{1.019}{0.983}$ | 0.998 | 330 – 362 | $\frac{1.018}{0.982}$ | 0.995 | 330 – 362 | $\frac{1.017}{0.982}$ | 0.993 |
| 362 – 395 | $\frac{1.022}{0.981}$ | 1.001 | 362 – 395 | $\frac{1.022}{0.980}$ | 1.000 | 362 – 395 | $\frac{1.022}{0.979}$ | 0.998 | 362 – 395 | $\frac{1.021}{0.978}$ | 0.995 | 362 – 395 | $\frac{1.020}{0.977}$ | 0.992 |
| 395 – 430 | $\frac{1.027}{0.979}$ | 1.002 | 395 – 430 | $\frac{1.027}{0.978}$ | 1.001 | 395 – 430 | $\frac{1.027}{0.977}$ | 0.998 | 395 – 430 | $\frac{1.026}{0.976}$ | 0.994 | 395 – 430 | $\frac{1.025}{0.975}$ | 0.991 |
| 430 – 468 | $\frac{1.030}{0.976}$ | 1.004 | 430 – 468 | $\frac{1.030}{0.975}$ | 1.002 | 430 – 468 | $\frac{1.030}{0.974}$ | 0.998 | 430 – 468 | $\frac{1.029}{0.973}$ | 0.994 | 430 – 468 | $\frac{1.028}{0.972}$ | 0.990 |
| 468 – 507 | $\frac{1.035}{0.974}$ | 1.006 | 468 – 507 | $\frac{1.035}{0.973}$ | 1.003 | 468 – 507 | $\frac{1.035}{0.972}$ | 0.998 | 468 – 507 | $\frac{1.034}{0.971}$ | 0.993 | 468 – 507 | $\frac{1.033}{0.970}$ | 0.989 |
| 507 – 548 | $\frac{1.040}{0.972}$ | 1.008 | 507 – 548 | $\frac{1.040}{0.971}$ | 1.005 | 507 – 548 | $\frac{1.040}{0.970}$ | 0.999 | 507 – 548 | $\frac{1.039}{0.969}$ | 0.993 | 507 – 548 | $\frac{1.038}{0.968}$ | 0.988 |
| 548 – 592 | $\frac{1.046}{0.970}$ | 1.011 | 548 – 592 | $\frac{1.046}{0.969}$ | 1.007 | 548 – 592 | $\frac{1.046}{0.968}$ | 0.999 | 548 – 592 | $\frac{1.045}{0.967}$ | 0.992 | 548 – 592 | $\frac{1.044}{0.966}$ | 0.987 |
| 592 – 638 | $\frac{1.053}{0.969}$ | 1.014 | 592 – 638 | $\frac{1.053}{0.968}$ | 1.009 | 592 – 638 | $\frac{1.053}{0.967}$ | 1.000 | 592 – 638 | $\frac{1.052}{0.966}$ | 0.991 | 592 – 638 | $\frac{1.051}{0.965}$ | 0.985 |
| 638 – 686 | $\frac{1.061}{0.967}$ | 1.018 | 638 – 686 | $\frac{1.061}{0.966}$ | 1.011 | 638 – 686 | $\frac{1.061}{0.965}$ | 1.001 | 638 – 686 | $\frac{1.060}{0.964}$ | 0.991 | 638 – 686 | $\frac{1.059}{0.963}$ | 0.984 |
| 686 – 737 | $\frac{1.070}{0.965}$ | 1.022 | 686 – 737 | $\frac{1.070}{0.964}$ | 1.013 | 686 – 737 | $\frac{1.070}{0.963}$ | 1.001 | 686 – 737 | $\frac{1.069}{0.962}$ | 0.990 | 686 – 737 | $\frac{1.068}{0.961}$ | 0.983 |
| 737 – 790 | $\frac{1.079}{0.963}$ | 1.026 | 737 – 790 | $\frac{1.079}{0.962}$ | 1.017 | 737 – 790 | $\frac{1.079}{0.961}$ | 1.002 | 737 – 790 | $\frac{1.078}{0.960}$ | 0.990 | 737 – 790 | $\frac{1.077}{0.959}$ | 0.983 |
| 790 – 846 | $\frac{1.089}{0.961}$ | 1.032 | 790 – 846 | $\frac{1.089}{0.960}$ | 1.020 | 790 – 846 | $\frac{1.089}{0.959}$ | 1.003 | 790 – 846 | $\frac{1.088}{0.958}$ | 0.989 | 790 – 846 | $\frac{1.087}{0.957}$ | 0.983 |
| 846 – 905 | $\frac{1.101}{0.959}$ | 1.037 | 846 – 905 | $\frac{1.101}{0.958}$ | 1.023 | 846 – 905 | $\frac{1.101}{0.957}$ | 1.004 | 846 – 905 | $\frac{1.100}{0.956}$ | 0.989 | 846 – 905 | $\frac{1.099}{0.955}$ | 0.983 |
| 905 – 967 | $\frac{1.115}{0.957}$ | 1.044 | 905 – 967 | $\frac{1.115}{0.956}$ | 1.026 | 905 – 967 | $\frac{1.115}{0.955}$ | 1.005 | 905 – 967 | $\frac{1.114}{0.954}$ | 0.988 | 905 – 967 | $\frac{1.113}{0.953}$ | 0.983 |
| 967 – 1032 | $\frac{1.131}{0.955}$ | 1.050 | 967 – 1032 | $\frac{1.131}{0.954}$ | 1.030 | 967 – 1032 | $\frac{1.131}{0.953}$ | 1.006 | 967 – 1248 | $\frac{1.130}{0.952}$ | 0.987 | 967 – 1248 | $\frac{1.129}{0.951}$ | 0.987 |
| 1032 – 1101 | $\frac{1.148}{0.953}$ | 1.058 | 1032 – 1101 | $\frac{1.148}{0.952}$ | 1.034 | 1032 – 1101 | $\frac{1.148}{0.951}$ | 1.007 | 1032 – 1101 | $\frac{1.147}{0.950}$ | 1.007 | 1032 – 1101 | $\frac{1.146}{0.949}$ | 1.007 |
| 1101 – 1172 | $\frac{1.166}{0.951}$ | 1.065 | 1101 – 1172 | $\frac{1.166}{0.950}$ | 1.038 | 1101 – 1172 | $\frac{1.166}{0.949}$ | 1.008 | 1101 – 1172 | $\frac{1.165}{0.948}$ | 1.008 | 1101 – 1172 | $\frac{1.164}{0.947}$ | 1.008 |
| 1172 – 1248 | $\frac{1.185}{0.949}$ | 1.073 | 1172 – 1248 | $\frac{1.185}{0.948}$ | 1.043 | 1172 – 1248 | $\frac{1.185}{0.947}$ | 1.009 | 1172 – 1684 | $\frac{1.184}{0.946}$ | 1.010 | 1172 – 1684 | $\frac{1.183}{0.945}$ | 1.010 |
| 1248 – 1327 | $\frac{1.205}{0.947}$ | 1.081 | 1248 – 1327 | $\frac{1.205}{0.946}$ | 1.047 | 1248 – 1327 | $\frac{1.205}{0.945}$ | 1.010 | | | | | | |
| 1327 – 1410 | $\frac{1.225}{0.945}$ | 1.090 | 1327 – 1410 | $\frac{1.225}{0.944}$ | 1.052 | | | | | | | | | |
| 1410 – 1497 | $\frac{1.245}{0.943}$ | 1.098 | 1410 – 1784 | $\frac{1.245}{0.942}$ | 1.060 | | | | | | | | | |
| 1497 – 1588 | $\frac{1.265}{0.941}$ | 1.109 | | | | | | | | | | | | |
| 1588 – 1784 | $\frac{1.285}{0.939}$ | 1.122 | | | | | | | | | | | | |
| 1784 – 2116 | $\frac{1.305}{0.937}$ | 1.144 | | | | | | | | | | | | |

Table III.1: The numerical values of the correction factors for each transverse-momentum p_T and rapidity $|y|$ bin, c.f. Fig. III.3.

compared to the gluon-induced channels. Hence, the tree-level contributions become large at high p_T and are positive at the LHC.

It is observed that these two contributions are of the same generic size, however, with opposite sign, leading to significant cancellations in the combined correction factor Eq. (III.2).² In the central region ($|y| < 1.0$) the tree-level contributions exceed the weak radiative ones, leading to a net correction that is positive and increases towards higher jet p_T up to 15% for $p_T = 2$ TeV and $|y| < 0.5$. In the more forward region with $2.0 \leq |y| < 2.5$, on the other hand, the weak corrections slightly surpass the tree-level contributions leading to negative corrections that amount to -2% for transverse momenta of $p_T \approx 800$ GeV. The numerical values of the respective correction factors are given in Table III.1 separately for each bin in p_T and $|y|$.

The different corrections that enter the comparison between theory and measurement are shown in Fig. III.4 and comprise the pure QCD corrections at NLO, the EW corrections discussed above, and non-perturbative corrections.

The NLO QCD predictions are obtained using NLOJET++ [92, 93] within the framework of FASTNLO [287] and represent the dominant corrections, which are typically of the order of 20%. They have been derived for renormalization and factorization scales of $\mu_R = \mu_F = p_{T,\text{jet}}$ for each jet, which differs from the scale choice $\mu_R = \mu_F = p_{T,\text{max}}$ in the EW corrections. However, differences in the QCD corrections induced by the two scale settings are negligible at high p_T and amount to at most $+4\%$ at lowest jet p_T .

²At the Tevatron proton–anti-proton collider, the tree-level contribution is dominated by the quark–anti-quark induced channels. They turn out to be negative at high p_T , so that they further enhance the negative weak corrections.

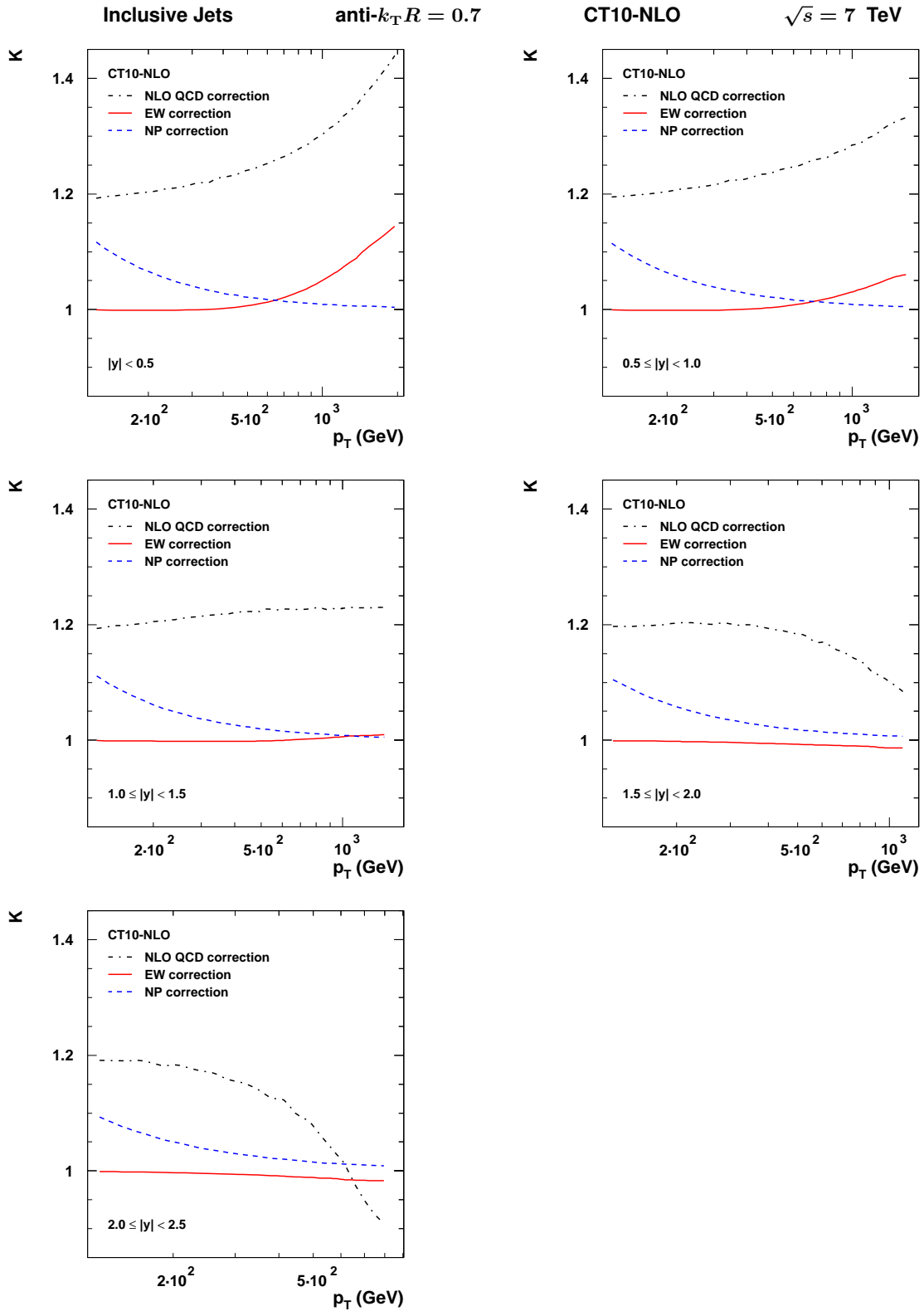


Fig. III.4: The three correction factors that enter the theory–data comparison as given by the NLO QCD corrections (“NLO QCD” dash-dotted black), the EW corrections (“EW” solid red), and the non-perturbative effects (“NP” dashed blue).

The NP corrections account for the underlying event, typically described in terms of multiple-parton interactions, and the hadronization process. Both cannot be described within perturbative QCD, but are modelled by Monte Carlo (MC) event generators, which introduce additional free parameters that have to be tuned to measurements. In Ref. [90] the CMS Collaboration compared the two MC event generators PYTHIA6 [288] and HERWIG++ [164], which offer different models and implementations of the NP effects. The NP correction is defined as the relative difference between the relevant cross sections predicted with and without multiple-parton interactions and hadronization. The central value of this correction is estimated as the average of the predictions by PYTHIA6 and HERWIG++ and the uncertainty as \pm half of their difference. The exact numbers are available from the HEPDATA record of the CMS data and amount to about +10% at low p_T decreasing steadily towards higher jet p_T 's. Beyond about 800 GeV they become negligible.

The total correction factor to be applied to a leading-order QCD prediction is then given by

$$K_{\text{tot}} = K_{\text{QCD}} \cdot K_{\text{NP}} \cdot K_{\text{EW}}, \quad (\text{III.1})$$

where

$$K_{\text{EW}} = K_{\text{weak}}^{1\text{-loop}} \cdot K_{\text{EW}}^{\text{tree}} \equiv (1 + \delta_{\text{weak}}^{1\text{-loop}}) \cdot (1 + \delta_{\text{EW}}^{\text{tree}}). \quad (\text{III.2})$$

More details on the definition of the relative correction factors $\delta_{\text{weak}}^{1\text{-loop}}$ and $\delta_{\text{EW}}^{\text{tree}}$ can be found in Ref. [87], where an alternative approach was employed in combining the two contributions, namely $K_{\text{EW}} = (1 + \delta_{\text{weak}}^{1\text{-loop}} + \delta_{\text{EW}}^{\text{tree}})$, which differs, however, only through higher-order terms. Figures III.5 and III.6 summarize the comparison between theory and experiment separately for each rapidity bin in terms of ratios with respect to the NLO QCD prediction obtained with the CT10-NLO PDF set [289]. In order to examine the impact of the choice of different PDF sets, the plots further include the ratios of the NLO QCD predictions derived with various other PDF sets [227, 235, 237, 290].³ The dependence on the PDF set almost perfectly cancels in the relative correction factor of the weak radiative corrections $K_{\text{weak}}^{1\text{-loop}}$. The tree-level part $K_{\text{EW}}^{\text{tree}}$, on the other hand, exhibits a small dependence on the choice for the PDFs, which is expected since these contributions are sensitive to the relative size of the quark PDFs to the gluon PDF. For each rapidity bin the left plot displays the data points that have been divided by the NP correction factor, whereas in the right plot they are further divided by the EW corrections. Differences are visible in particular at central rapidity with $|y| < 1.0$. Because of the large statistical uncertainty of the measurement in the relevant region no significant impact on fits of PDFs and/or the strong coupling constant are expected. This will be different, once larger amounts of data become available at 8 or even 13 TeV centre-of-mass energy.

1.5 Summary and Outlook

Electroweak corrections to the inclusive jet cross section have been derived double-differentially in the jet transverse momentum p_T and absolute rapidity $|y|$. They comprise corrections of the order $\alpha_s^2 \alpha_w$ as well as contributions of $\mathcal{O}(\alpha_s \alpha, \alpha^2)$ to the LO QCD prediction. This calculation complements the previously published results of Ref. [87], where the dijet production process was studied in detail. The Sudakov-type logarithms present in the weak corrections become sizeable in the high- p_T tail of the transverse-momentum distribution. They are negative throughout and can amount to a -7% correction for $|y| < 0.5$ and $p_T \approx 2$ TeV at the LHC for 7 TeV centre-of-mass energy. The tree-level EW contributions are of the same generic size and positive

³Since photonic NLO corrections, which require a PDF redefinition via the factorization of photonic collinear singularities, are not yet included, $\mathcal{O}(\alpha)$ -corrected PDF sets such as NNPDF2.3QED should not be used in combination with these EW corrections.

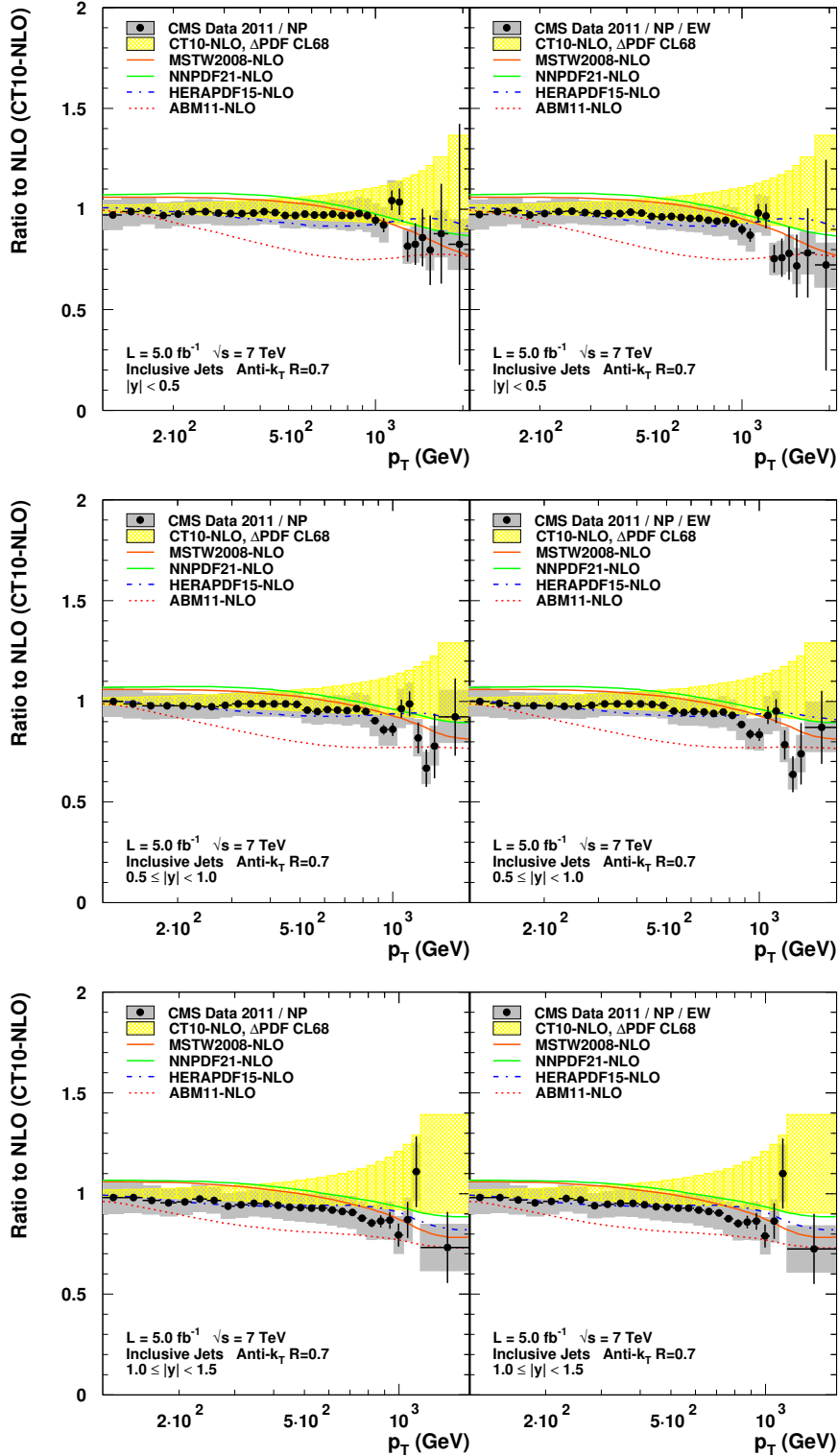


Fig. III.5: The theory–data comparison for the rapidity bins $|y| < 0.5$, $0.5 \leq |y| < 1.0$, and $1.0 \leq |y| < 1.5$, illustrated in terms of ratios with respect to the NLO QCD prediction obtained with the CT10-NLO PDF set. On the left, only NP correction factors are taken into account in this ratio, and on the right also the EW corrections.

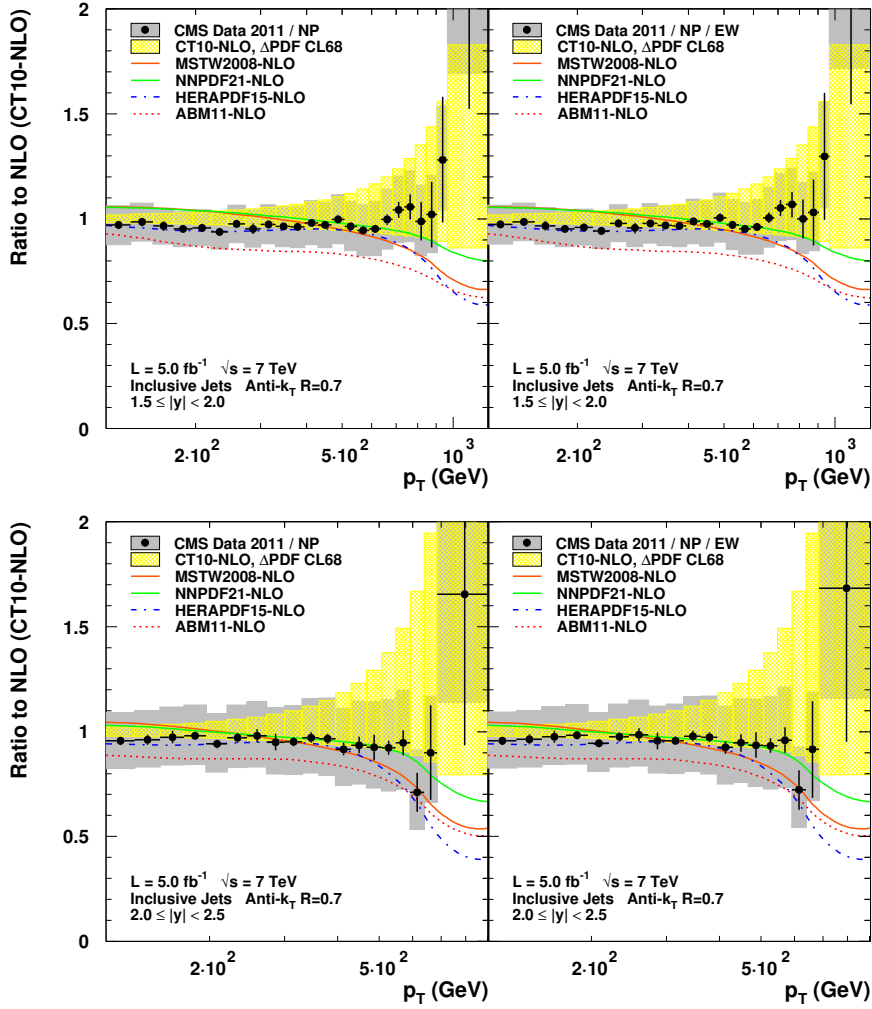


Fig. III.6: The theory–data comparison for the rapidity bins $1.5 \leq |y| < 2.0$, and $2.0 \leq |y| < 2.5$, illustrated in terms of ratios with respect to the NLO QCD prediction obtained with the CT10-NLO PDF set. On the left, only NP correction factors are taken into account in this ratio, and on the right also the EW corrections.

at the LHC, which induces large cancellations between the two, so that the impact of the EW corrections to the inclusive jet cross section turns out to be of moderate size.

Accounting for the sizeable QCD corrections at NLO and estimating non-perturbative effects, which are small at high p_T , the presented theory predictions have been compared to data published by the CMS experiment at the LHC for a centre-of-mass energy of 7 TeV [90]. For the given amount of 5 fb^{-1} of integrated luminosity the statistical uncertainties of the measurement are too large at jet transverse momenta beyond 1 TeV to detect a significant impact of the EW corrections. However, it will be most interesting to repeat this comparison with data collected at higher centre-of-mass energies and with more data. At 8 TeV for example, the LHC delivered roughly four times the luminosity of the 7 TeV running period.

Furthermore, the two contributions that enter the EW corrections behave differently with respect to an increase of the collider energy [87], which can strongly affect the accidental cancellations observed here. For a fixed value of the jet transverse momentum, the scales appearing in the large logarithms that are responsible for the bulk of the weak corrections will remain mostly unchanged. This in turn means that for a given value of the transverse momentum, the weak

radiative corrections will not be affected much by the collider energy. The tree-level contributions, on the other hand, are strongly dependent on the parton luminosities, in particular, the q and \bar{q} PDFs. For fixed values of the transverse momentum, an increase in the collider energy corresponds to probing smaller values of the momentum fractions x in the PDFs. Therefore, the tree-level contributions will decrease for higher collision energies and the impact of the weak one-loop corrections are expected to become more strongly pronounced.

2 NNLO QCD and NLO EW Drell Yan background predictions for new gauge boson searches⁴

2.1 Introduction

New gauge boson searches belong to the flagship measurements at the high energy frontier. In particular, searches for Z' and W' bosons are 'golden channels' due to their clean final state signatures and rather high rates. However, they require a precise modelling of the large neutral current (NC) and charged current (CC) Drell Yan backgrounds, which have the same final state signatures. For this kind of searches, very high invariant masses could and will be explored with the available LHC c.m.s. energies of 8 TeV in Run I and of anticipated 14 TeV in Run II, respectively. High invariant masses challenge the understanding of a kinematic region where NNLO QCD corrections $\mathcal{O}(\alpha_s^2)$ and NLO electroweak corrections $\mathcal{O}(\alpha)$ become of similar size (c.f. discussion at this workshop). In the following a few observations and practical, novel methods related to the modelling of NNLO QCD and NLO EW high mass Drell Yan cross sections are summarised. Part of the methodologies have been developed in the context of a recent Z' search analysis [291].

2.2 Framework and tools

Drell Yan production in proton-proton collisions can be calculated with high precision and over a wide kinematic range up to next-to-next-to-leading-order (NNLO) in the strong coupling constant using recent versions of the programs FEWZ [292–294] and DYNNLO [295, 296]. Both programs calculate vector boson production and decays with full spin correlations and finite width effects. They are used widely by LHC experimentalist since they allow the application of important kinematic phase space requirements. In addition, powerful and fast programs like ZWPROD [297] and VRAP [298] are used for total cross section calculations and estimates of e.g. factorisation and renormalisation scale uncertainties as well as to cross check the predictions of the various programs for high invariant masses. Such a cross check revealed that the total NNLO

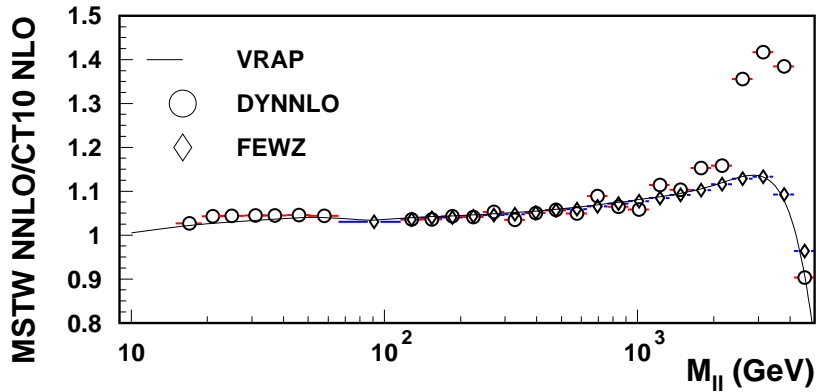


Fig. III.7: NNLO-to-NLO QCD k-factors for total NC Drell Yan cross sections at $\sqrt{s} = 8$ TeV using VRAP 0.9, FEWZ 3.1.b2 and DYNNLO 1.3. See text and Ref. [276] for the details of the PDFs.

QCD cross section predictions by FEWZ 3.1.b2 and VRAP 0.9 are in excellent agreement for invariant dilepton masses from 10 to 5000 GeV, whereas the DYNNLO 1.3 version appears not to be suitable for off-resonant cross section calculations. This observation is illustrated in Fig. III.7 for NC DY channel using an LHC c.m.s. energy of $\sqrt{s} = 8$ TeV. The calculation of the QCD

⁴U. Klein

NNLO-to-NLO k-factors shown uses the proton parton distribution functions MSTW2008nnlo at NNLO QCD and CT10 at NLO QCD (a similar observation was obtained for CC DY but is not shown here) [299]. An updated version of DYNNLO 1.4 is now available which shows for total LO QCD NC DY cross sections in the mass range 60 to 5000 GeV an excellent agreement [299], however, more detailed cross checks are worthwhile also for CC DY production and specific phase space cuts also for the resonant region where the experimental precision is very high (less than a few percent). For example, the fiducial resonant W cross section predictions varied within 1% between FEWZ and DYNNLO (using the same SM and electroweak parameters for both programs) as reported by ATLAS [94] already in 2012.

The QCD NNLO-to-NLO k-factor for LHC Run II at $\sqrt{s} = 14$ TeV are illustrated for NC Drell Yan production in Fig. III.8 (right). The QCD k-factors show a wide spread for invariant masses larger than about 4 TeV reflecting the lack of knowledge in the proton parton distribution functions at high Bjorken- x values. The corresponding spread in the predictions at NNLO QCD using modern PDFs with respect to the CT10nnlo PDF is shown in Fig. III.8 (left).

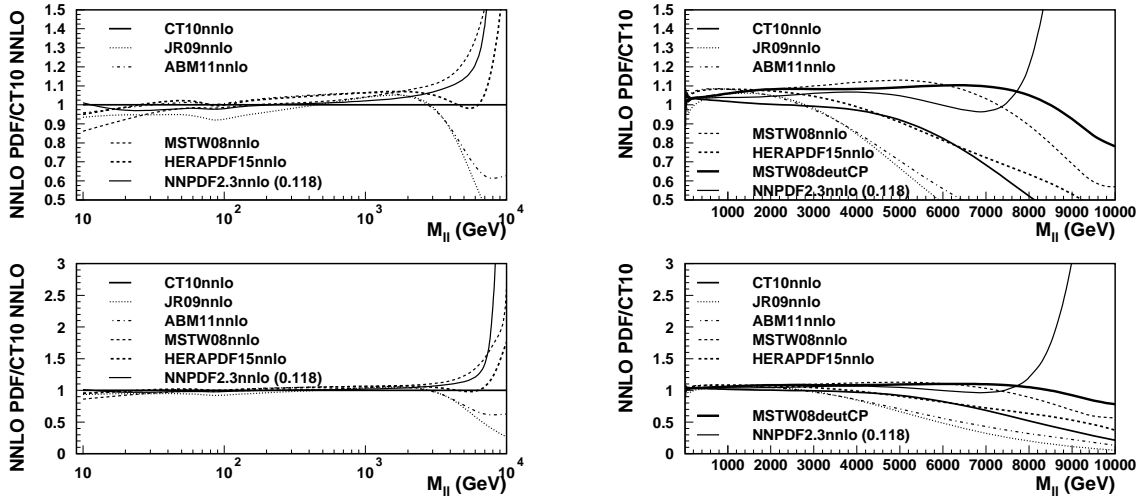


Fig. III.8: Invariant mass dependence of the total NC Drell Yan production cross section predictions for modern NNLO PDFs w.r.t. the CT10nnlo PDF (left plots) and the QCD NNLO-to-NLO QCD k-factors w.r.t. to CT10 NLO QCD (right plots). The lower and upper panels show the same quantities but with different y -axis ranges from 0 to 3 and 0.5 to 1.5), respectively. The LHC energy is $\sqrt{s} = 14$ TeV. Calculations are based on VRAP 0.9 and the NNLO (NLO) PDFs [276] as indicated in the legend.

While the QCD k-factors are rather insensitive to the choice of the SM model inputs and the electroweak parameter scheme, care has to be taken for the absolute cross section predictions including those NLO electroweak corrections which are not addressed already in the unfolding of the experimental data. It is well known from the literature, see e.g. [126] for a brief introduction into the most commonly used electroweak schemes, that the G_μ electroweak scheme is well suited for Drell Yan production.

In the calculations presented here, the electroweak scheme is set to the G_μ scheme according to the details outlined in [126] and calculated by SANC [300]. A summary of the values is given in Tab. III.2.

The CKM values are taken from electroweak fits based on all precision observables as reported in [301]. Here the values of the CKM fit [301] are used. The pseudo-rapidity η_ℓ distribution of resonant single W^\pm production is sensitive to the choice of the value of V_{cs} . Fig.III.9 illustrates the effect of changing the fitted V_{cs} to the currently best experimentally

| | | | |
|------------------------------|---|----------|----------|
| M_Z | 91.1876 GeV | V_{ud} | 0.97427 |
| Γ_Z | 2.4949 GeV | V_{us} | 0.22534 |
| $\Gamma(Z \rightarrow ll)$ | 0.084 GeV | V_{ub} | 0.00351 |
| M_W | 80.385 GeV | V_{cd} | 0.22520 |
| Γ_W | 2.0906 GeV | V_{cs} | 0.97344 |
| $\Gamma(W \rightarrow l\nu)$ | 0.22727 GeV | V_{cb} | 0.0412 |
| M_H | 125 GeV | V_{td} | 0.00867 |
| m_t | 173.5 GeV | V_{ts} | 0.0404 |
| G_F | $1.1663787 \times 10^{-5} \text{ GeV}^{-2}$ | V_{tb} | 0.999146 |
| $\sin^2 \theta_W$ | 0.22289722252391828 | | |
| α_G | $7.56239563669733848 \times 10^{-3}$ | | |
| vec_{up} | 0.40560740660288463 | | |
| vec_{dn} | -0.70280370330144226 | | |
| vec_{le} | -0.10841110990432690 | | |

Table III.2: Electroweak input parameters in the G_μ scheme for the NC and CC Drell Yan cross section calculations.

known value of $V_{cs} = 1.006 \pm 0.023$ [301] on the fiducial pseudo-rapidity η_ℓ distributions of resonant single W^+ and W^- production. Since all other CKM matrix elements relevant for CC Drell Yan production are determined with high precision, the use of either the fitted or the measured values (except the above described V_{cs} features) give the same results otherwise.

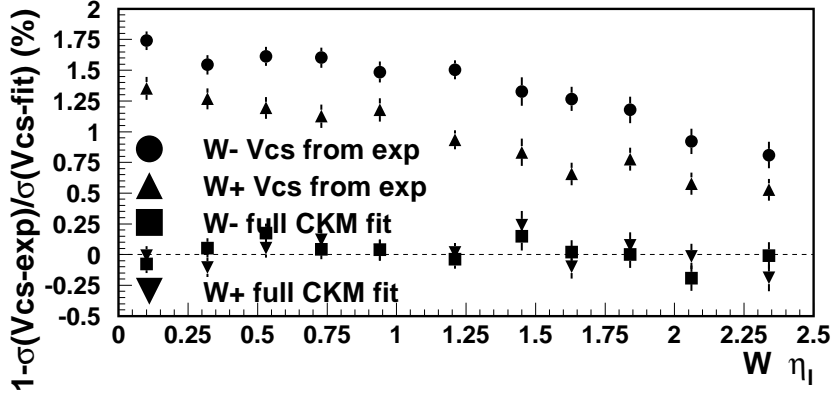


Fig. III.9: Effect of the choice of V_{cs} on the fiducial pseudo-rapidity η_ℓ distributions of resonant W cross sections at $\sqrt{s} = 7$ TeV. Calculations are performed with DYNLO 1.3 NLO QCD and the CT10 NLO PDF.

The free Standard Model input parameters are chosen from the 2012 PDG [301], except the partial leptonic decay width, $\Gamma(W \rightarrow l\nu)$. The PDG value of $\Gamma(W \rightarrow l\nu) = 226.36$ MeV includes already higher order QCD and more importantly higher order electroweak effects and the use of this value would be then inconsistent with the set-up of higher order electroweak programs like e.g. SANC [300, 302]. To get a consistent evaluation of higher order electroweak effects (except QED FSR) also on the W decay kinematics, thus the LO partial width $\Gamma(W \rightarrow l\nu) = 227.27$ MeV has to be used in the QCD and EW calculations.

2.3 Combining NNLO QCD with NLO EW corrections

In Drell Yan production, the by far dominant part of the higher order electroweak corrections is the final state QED radiation (QED FSR) from the final state leptons. The LHC Drell Yan Monte Carlo simulations often use PHOTOS [303] as an "afterburner" for the modelling of QED FSR, and the experimental data are usually unfolded for QED FSR effects. PHOTOS and SANC QED FSR agree quantitatively very well [304]. The SANC program can be thus used to calculate the electroweak corrections excluding QED FSR for both NC and CC Drell Yan. Those missing HO EW terms include contributions from initial state photon radiation (ISR QED), electroweak loop corrections and initial and final state photon interferences. The recent FEWZ 3.1 versions allow for the NC Drell Yan channel to select the G_μ electroweak scheme and the simultaneous calculation of NLO electroweak corrections [294]. To enable the calculation of NLO EW effects except QED FSR and to match thus QCD and EW predictions to experimental data the following EW control flags had been introduced into FEWZ 3.1.a3 (and maintained in the updated versions), where FEWZ reads the control flag (EWflag) and uses it as a binary number [305]:

- EWflag = 0 = (0000)_2 means nothing off (Weak, ISR*FSR, ISR, FSR all on)
- EWflag = 1 = (0001)_2 means FSR off
- EWflag = 2 = (0010)_2 means ISR off
- EWflag = 4 = (0100)_2 means ISR*FSR off
- EWflag = 8 = (1000)_2 means Weak off
- EWflag = 7 = (0111)_2 means ISR*FSR, ISR and FSR all off (only Weak is on)

Various NLO QCD and NLO EW calculations have been performed for NC Drell Yan over a wide invariant mass range, where each mass bin has been calculated separately to avoid biases in the calculations, using the CT10 NLO PDF and the EWflag options as described above in FEWZ 3.1.b2. The HO EW corrections show a strong invariant mass dependence as illustrated in Fig. III.10 for the NC Drell Yan production at $\sqrt{s} = 8$ TeV and the expected large QED FSR contributions. The significant reduction of the QED FSR contributions using a recombination of the FSR photon and lepton within a cone of 0.1 ($w_{R(\gamma, l)} < 0.1$), usually called "dressed leptons" by experimenters, is shown in Fig. III.10 as well. The ATLAS strategy of dressing leptons has been widely discussed within the LPCC EW working group initiated by Ref. [306]. It is important to note that any lepton dressing can be performed on Monte Carlo generator level only, i.e. experimental measurements can be unfolded to various levels of QED FSR corrections based on the QED FSR code and EW parameter settings as implemented in the used Monte Carlos.

FEWZ LO QCD based HO EW correction calculations, except QED FSR (FEWZ EWflag=1), and corresponding SANC calculations, performed in the G_μ scheme, agree very well for NC Drell Yan process. Hence in the following the FEWZ results are used to demonstrate an improved understanding of the application of HO EW corrections to (N)NLO QCD predictions relevant for an estimate of an EW (except QED FSR) systematic uncertainty for very high invariant masses. The method developed here has been transferred successfully to CC Drell Yan production where no combined NNLO QCD and NLO EW code is available yet, and the results of various external programs need to be combined in a consistent way.

Various methodologies of combining HO QCD and HO EW effects for DY production have been discussed over the past decade, see e.g. also this and other Les Houches workshop contributions and references therein. From the viewpoint of an experimenter performing new gauge boson searches and SM DY measurements, the practical question needed an answer how mass dependent EW systematic uncertainties could be estimated when further mixed $\mathcal{O}(\alpha\alpha_s)$ contributions are not calculated yet.

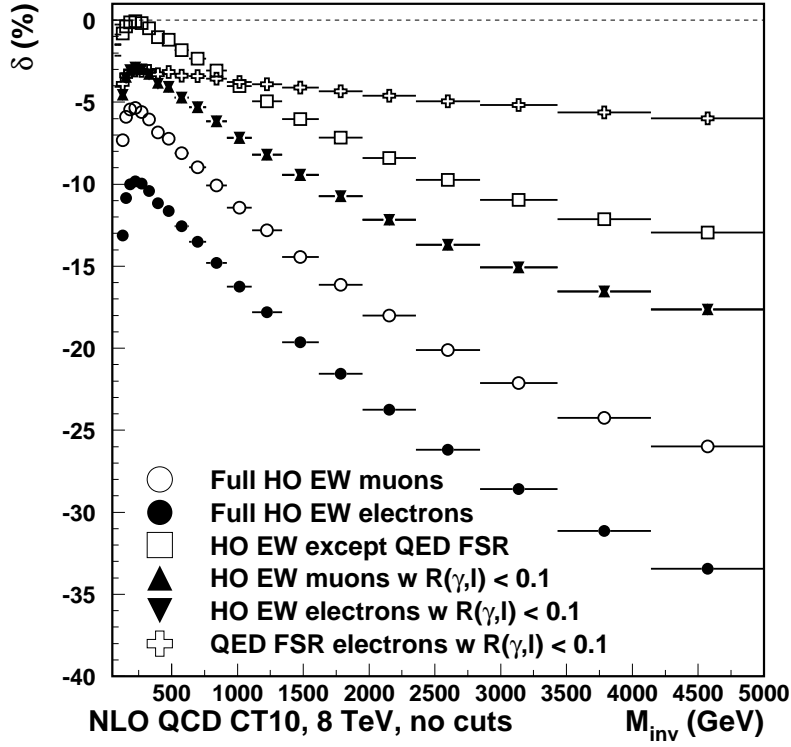


Fig. III.10: Invariant mass dependence of various higher order EW contributions (δ in %) for NC Drell Yan production at $\sqrt{s} = 8$ TeV. Shown are the full NLO EW corrections for electrons (full circles) and muons (open circles), the full NLO EW corrections using a recombination of the FSR photon and lepton with in a cone of 0.1 ($w R(\gamma, l) < 0.1$) for electrons (full triangles top down) and muons (full triangles top up), the NLO EW corrections except QED FSR (open squares), the QED FSR corrections using a recombination of the FSR photon and electron (open crosses) with in a cone of 0.1 ($w R(\gamma, l) < 0.1$). Calculations are based on FEWZ 3.1.b2 NLO QCD and NLO EW using the CT10 NLO PDF.

Using fixed order LO QCD calculations for a given EW parameter scheme as the baseline, σ_{LO_QCD} , there are mainly two methodologies which are called here in short "factorised approach", Eq. III.3, and "additive approach", Eq. III.6 to construct a combined NNLO QCD and NLO EW DY cross section, $\sigma_{NNLO_QCD+NLO_EW}$. In the context of the here discussed new gauge boson searches, "EW" refers here always to the HO EW corrections except QED FSR (also sometimes called "missing HO EW corrections", δ_{miss} , since those corrections are missing in the experimental Monte Carlos while QED FSR is included already).

Factorised approach:

$$\sigma_{NNLO_QCD+NLO_EW} = k_{QCD} \times k_{EW} \times \sigma_{LO_QCD} \quad (\text{III.3})$$

$$k_{QCD} = \frac{\sigma_{NNLO_QCD}}{\sigma_{LO_QCD}} \quad (\text{III.4})$$

$$k_{EW} = \frac{\sigma_{NLO_EW, LO_QCD}}{\sigma_{LO_QCD}}. \quad (\text{III.5})$$

Additive approach:

$$\sigma_{NNLO_QCD+NLO_EW} = \sigma_{NNLO_QCD} + \Delta\sigma_{LO_QCD+NLO_EW} \quad (\text{III.6})$$

$$= \sigma_{NNLO_QCD} \left(1 + \frac{\Delta\sigma_{LO_QCD+NLO_EW}}{\sigma_{NNLO_QCD}} \right). \quad (\text{III.7})$$

The factorised approach, Eq. III.3, assumes that the HO EW corrections are the same for all orders of QCD, and thus can be determined based on LO QCD and then transferred to any higher order in QCD. The additive approach, Eq. III.6, is e.g. followed in the NC DY FEWZ code [294] for the combination of HO QCD and EW corrections. This approach assumes that the EW except QED FSR corrections are mainly additive in their nature and the same term needs to be added for all orders of QCD, thus the relative fraction of HO EW corrections for each order of QCD is changing. Here a careful analysis has been performed to understand the

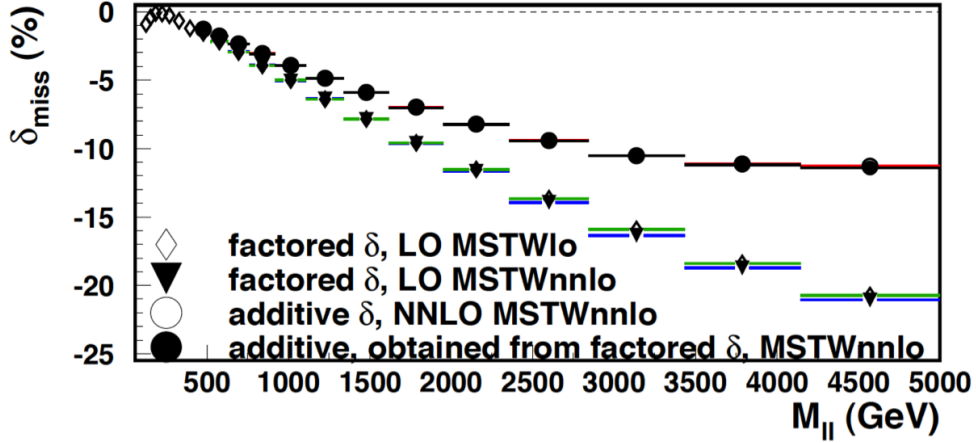


Fig. III.11: HO EW except QED FSR (δ_{miss} in %) corrections for NC Drell Yan production. The results of the factorised approach based on LO QCD and the MST2008lo LO PDF (open diamonds) and MSTW2008nnlo NNLO PDF (full triangles on top) are shown. Using the MSTW2008nnlo PNNLO PDF, the results of a full, one-step NNLO QCD and NLO EW (open circles) and the additive approach according to Eq. III.6 (full circles) are shown. Calculations are based on FEWZ 3.1.b2 and $\sqrt{s} = 8$ TeV.

transfer of the additive EW term to all orders of QCD. It has been found that consistent results can only be achieved if the term

$$\Delta\sigma_{LO_QCD+NLO_EW} = \sigma_{LO_QCD+NLO_EW} - \sigma_{LO_QCD} \quad (\text{III.8})$$

is calculated at LO QCD with exactly the same PDF as the wanted highest order QCD result. For example, if a NNLO QCD prediction using the MSTW2008nnlo PDF is aimed for, then the additive EW corrections term can be calculated with high precision based on LO QCD but using the MSTW2008nnlo PDF. Similarly e.g. for a NLO QCD prediction using the CT10 PDF, this would require the HO EW calculation done based on LO QCD using CT10. The results of this study are shown in Fig. III.11 where the mass dependence of the HO EW except QED FSR corrections are shown for the factorised and the additive approach, and the excellent agreement of the resulting NNLO QCD and NLO EW except QED FSR predictions using either directly FEWZ 3.1.b2 or the strategy according to Eq. III.6. The formalism described above is robust and gives a prescription also applicable for CC DY processes where the NNLO QCD and NLO EW calculation rely on different external programs for the QCD and the EW part. Also indicated in Fig. III.11 is the expected weak PDF dependence of the HO EW corrections. For higher invariant masses the discrepancies between the additive and factorised approaches are significant, and the results of the two approaches are used to get an estimate of the mass dependent systematic uncertainty for the HO EW except QED FSR corrections for NC and CC Drell Yan processes. Since roughly speaking, the factorised approach maximises potential mixed $\mathcal{O}(\alpha\alpha_s)$ contributions but with its sign is unknown, the following strategy has been suggested for

each invariant mass bin: The central value of the combined NNLO QCD and NLO EW except QED FSR prediction is taken from the additive approach while the difference to the factorised approach results is taken as a double sided systematic uncertainty estimate. The resulting mean HO EW except QED FSR corrections with those symmetric uncertainties are shown in Fig.III.12 (lower plot) for the expected LHC Run II at $\sqrt{s} = 14$ TeV. Also illustrated in Fig. III.12 (upper plot) is the rather weak energy dependence for the HO EW except QED FSR corrections.

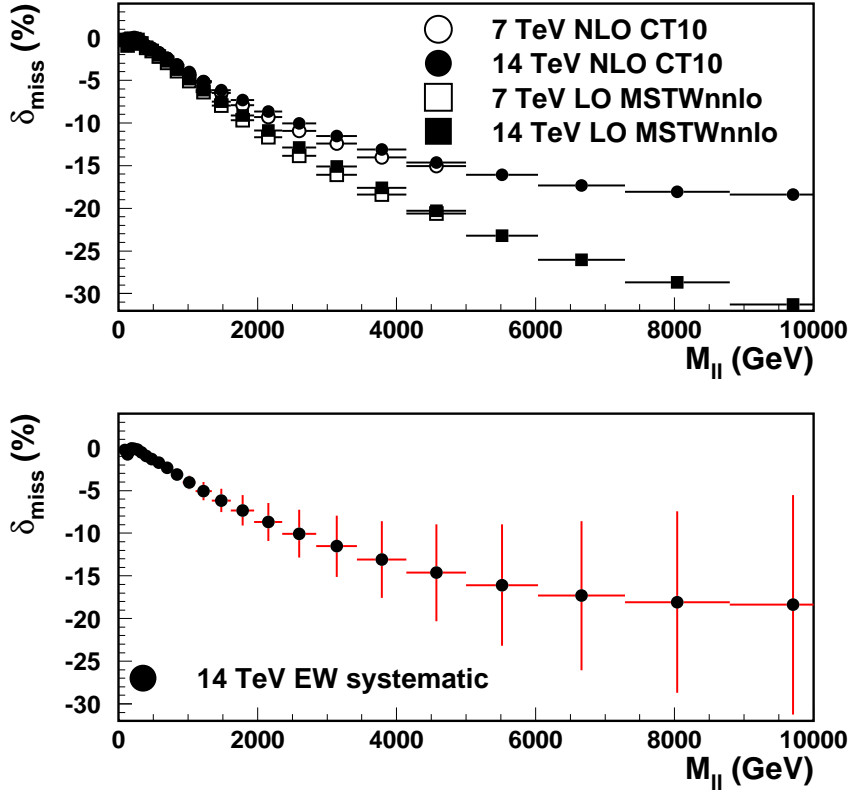


Fig. III.12: HO EW except QED FSR (δ_{miss} in %) corrections for NC Drell Yan production. The results of the factorised (additive) approach based on LO QCD (NLO QCD) for $\sqrt{s} = 7$ TeV are shown in the upper plot with empty squares (empty circles) and for 14 TeV with full squares (full circles). An estimate of the EW except QED FSR systematic uncertainty, see text, is shown in the lower plots for $\sqrt{s} = 14$ TeV. All calculations are based on FEWZ 3.1.b2 and the PDFs as indicated in the legend.

2.4 Matching Monte Carlo programs and external calculations

The methodologies discussed in the previous chapter work reliably for total cross sections and well defined variables like the invariant mass or the pseudo-rapidity of the final state leptons, but fail e.g for variables like the $p_T(\ell)$ or $p_T(Z, W)$ which rely on a modelling of soft gluon resummation and parton shower effects usually taken care of in Monte Carlo programs. While the LHC Monte Carlo programs are powerful tools for the description of complex QCD processes, they are not very well defined w.r.t. the electroweak part and the EW parameter scheme used. Here, a study has been performed to understand the matching of a well-defined external QCD calculation using the G_μ scheme with parameters according to Tab. III.2 and currently PDG guided EW parameter settings as used in LHC Monte Carlo generations. Fig. III.13 shows the deviations between external NLO (LO) QCD predictions using FEWZ 3.1.b2 with

the well-defined G_μ scheme and currently used NLO (POWHEG) and LO (PYTHIA) Monte Carlo generators for NC Drell Yan production at $\sqrt{s} = 8$ TeV. The observations in Fig. III.13 illustrates that depending on the Monte Carlo generation used an additional "matching" could be needed to normalise the Monte Carlo to the best theoretical available cross section prediction. It also is apparent from Fig. III.13 that this could be an issue relevant for high invariant masses specifically.

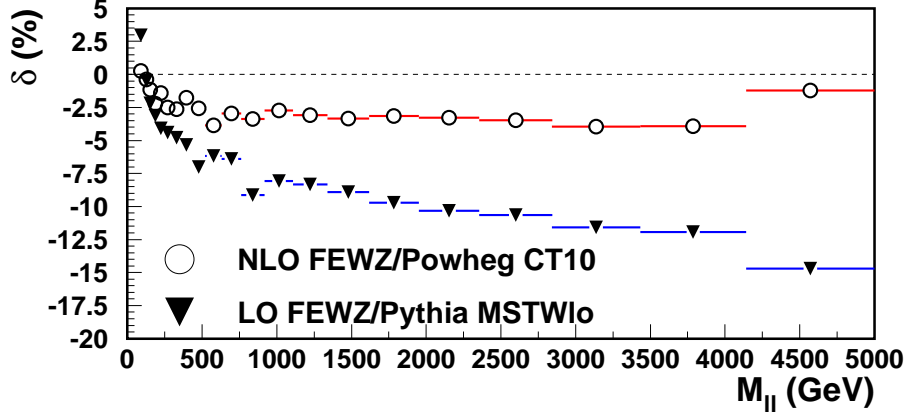


Fig. III.13: Deviation (δ in %) between external NLO (open circles) and LO (full triangles on top) QCD predictions using FEWZ 3.1.b2 with the well-defined G_μ scheme and currently used NLO (POWHEG) and LO (PYTHIA) Monte Carlo generators for NC Drell Yan production at $\sqrt{s} = 8$ TeV and over a wide kinematic range in the invariant mass.

For high mass new gauge boson searches thus the following novel methodology has been developed to transfer the best external NNLO QCD and NLO EW except QED FSR knowledge to LHC Drell Yan Monte Carlo samples interfaced to PHOTOS for QED FSR (and using SANC for the HO EW except QED FSR corrections in a consistent way; other QED FSR models may require other HO EW except QED FSR calculations for high invariant masses to maintain overall consistency of the full HO EW corrections) :

$$\sigma_{NNLO_QCD+NLO_EW} = k_{\text{fit}} \times \sigma_{MC} \quad (\text{III.9})$$

$$k_{\text{fit}} = \frac{\sigma_{NNLO_QCD+NLO_EW}}{\sigma_{MC}}. \quad (\text{III.10})$$

The factor k_{fit} is obtained by a mass-dependent fit of the ratios of total cross sections per invariant mass bin as described in in Eq. III.10. Thus this factor automatically corrects for any possible mismatches in the EW parameter scheme and "forces" the mass-dependent Monte Carlo Drell Yan cross section to the "best" NNLO QCD and NLO EW knowledge. Further systematic uncertainties due to the knowledge of the PDFs and the EW except QED FSR corrections can be then assigned. The fit function of $k_{\text{fit}}(M_{inv})$ and its uncertainties can be conveniently applied as weights to each Monte Carlo event and the "best" NNLO QCD and NLO EW knowledge could be propagated to more complex variables with kinematic cuts.

2.5 Photon-induced background contributions

The subject of photon-induced dilepton contributions has been discussed in the theory community since a decade (c.f. other contributions to this workshop). Recently this subject has been revived from the experimenter's point of view [307] showing the potentially large size of such

contributions for off-peak (low and high mass) NC Drell Yan production at the LHC. Furthermore, indications are found in a recent Standard Model high mass Drell Yan analysis performed by ATLAS that LHC data may include such backgrounds [308]. In Ref. [308] also the radiation of real (on-shell) W and Z bosons has been quantified for the experimental conditions following the procedure outlined in Ref. [140]. Using the same technique, the contributions due to real W and Z boson radiation have been also calculated for the 2012 Z' analysis [291], but those background contributions are much smaller than the photon-induced background contributions and hence not discussed here further. Since our knowledge of photon-induced processes is very poor,

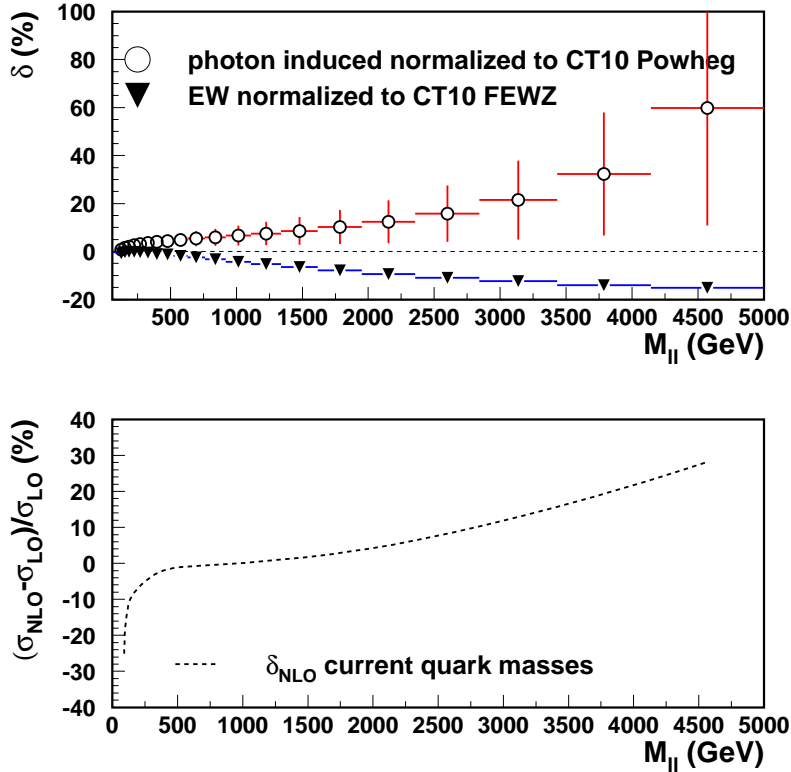


Fig. III.14: Photon induced background contributions calculated with $p_{T,\ell} > 25$ GeV and $\eta_\ell < 2.5$ MRST2004QED photon PDF and $\sqrt{s} = 8$ TeV over a wide invariant mass range. Shown are the leading order photon induced dilepton contribution using the mean of the two available MRST2004qed predictions as the central values and the deviations between the two predictions and the central value as an uncertainty estimate (upper plot). The LO photon induced contribution is displayed as a fraction of a NLO POWHEG NC DY prediction. Overlaid is also the HO EW except QED FSR correction including its systematic uncertainty estimate as described in the text. Next-to-leading order photon induced dilepton production contribution w.r.t. to the dominant LO photon-induced cross sections over a wide invariant mass range (lower plot). Calculations are performed with MCSANC [302]. using the nominal MRST2004qed PDF.

only rough estimates are possible using the MRST2004QED PDF [151]. Here a modified version of the MRST2004qed PDF is used which offers two parameterisations [309], i.e. reflecting the sensitivity to the choice of the quark mass, either current quark masses as used for the nominal parameterisation or constituent quark masses as used for an alternative parameterisation.

First estimates of the size of photon-induced contributions have been performed at parton level only due to the lack of full Monte Carlo simulations at that time. Since dilepton production $\gamma\gamma \rightarrow \ell\ell$ is an additional background which can be significant at high invariant masses, it is

important that the fiducial phase space requirements are applied. The general strategy is then that this background contribution is quantified separately and added to the theory prediction including its model uncertainty in data-theory comparisons, see e.g. Ref. [308]. This strategy allows for a re-analysis of the data in the future if the knowledge about this background may have been improved.

The photon induced background contributions for kinematic requirements of $p_{T,\ell} > 25$ GeV and $\eta_\ell < 2.5$ are shown in Fig. III.14 (upper plot) for a LHC c.m.s. energy of $\sqrt{s} = 8$ TeV over a wide invariant mass range. The potential contributions could sizeable and may reach up to 50% - 100 % of the fiducial NC DY cross section at invariant masses of 4 to 5 TeV. Such background contributions may then also significantly reduced expected HO EW effects (also shown in Fig. III.14 upper plot). NLO, quark-photon initiated dilepton production contributions are expected to be negative at lower invariant masses but may add even more backgrounds at higher masses, see Fig. III.14 (lower plot). The current procedure to estimate an uncertainty due this background relies on a simple mean between the two available MRST2004qed predictions at LO to avoid single-sided systematic uncertainties. It was also lively discussed at this workshop that LHC experiments should aim for a measurement of this background employing specific phase space regions.

2.6 NNLO QCD scale uncertainties

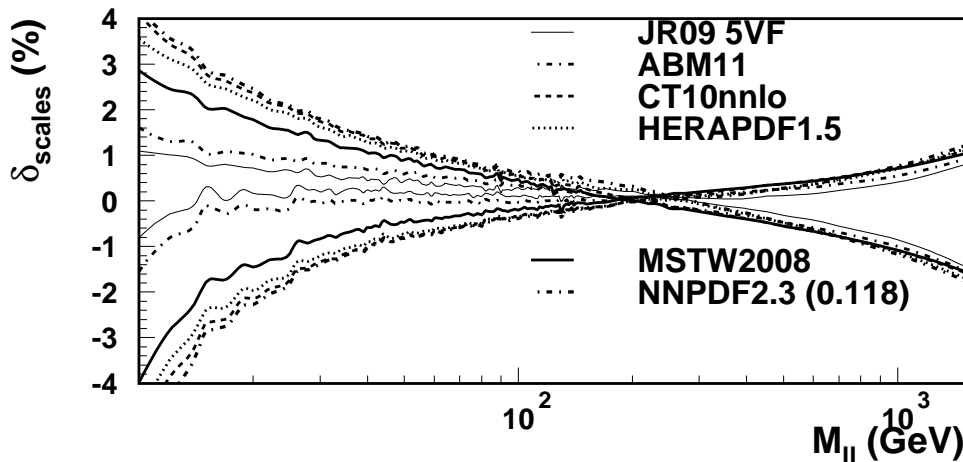


Fig. III.15: Effect on the total NC Drell Yan NNLO QCD cross section predictions due to the change of the renormalisation and factorisation scales simultaneously by a factor 2 or 1/2 for an invariant mass range of 10 to 2000 GeV. See Ref. [276] for the details of the NNLO QCD PDFs; the NNPDF calculations is obtained for $\alpha_s = 0.118$. Calculations are based on VRAP 0.9 and $\sqrt{s} = 7$ TeV.

The nominal renormalisation and factorisation scales for the calculation of DY cross sections are set to either directly to the invariant mass in VRAP or to the mean of an invariant mass bin in FEWZ (DYNLO). The variation of the renormalisation and factorisation scales simultaneously by a factor of 2 or 1/2 can be conveniently calculated in NNLO QCD for the total Drell Yan production cross section using the program VRAP. Fig.III.15 and Fig.III.16 show the resulting effects for NC and CC Drell Yan, respectively, for all modern NNLO parton distribution functions. The mass-dependencies of the scale variations are observed to very similar for NC and CC Drell Yan, and also to show very similar and significant dependencies on the PDF choice. For low and high invariant masses the scale uncertainties are rising, even at NNLO

QCD, and deserve further detailed studies.

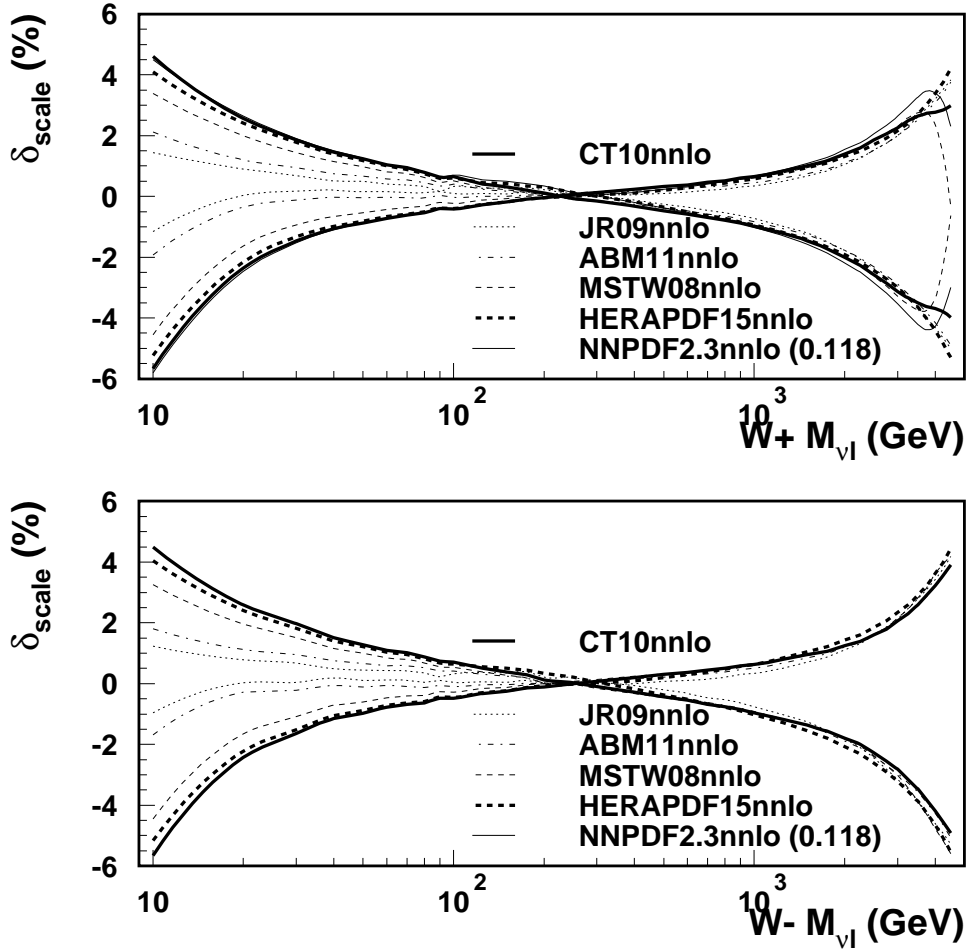


Fig. III.16: Effect on the total CC Drell Yan NNLO QCD cross section predictions due to the change of the renormalisation and factorisation scales simultaneously by a factor 2 or 1/2 for an invariant mass range of 10 to 5000 GeV. See Ref. [276] for the details of the NNLO QCD PDFs; the NNPDF calculations is obtained for $\alpha_s = 0.118$. Calculations are based on VRAP 0.9 and $\sqrt{s} = 8$ TeV.

Acknowledgements

The electroweak and photon-induced background studies of this work have been done together with Dmitry Bardin, Serge Bondarenko, and Lidia Kalinovskaya with the support of the grant CERN-RFBR-Scientific-Cooperation 12-02-91526-CERN_a, and I am very thankful for this exceptional and fruitful collaboration. I also like to thank Lance Dixon, Frank Petriello, Ye Li, Seth Quackenbush and Massimiliano Grazzini for many useful discussions over the past years. Part of this work were supported by my PPSC20 grant "Precision modelling of hadron structure at highest energies". Thanks to my ATLAS and LPCC WG colleagues for the co-operation. Last but not least it is my pleasure to thank warmly the Les Houches workshop for the hospitality and perfect organisation.

3 Electroweak Sudakov corrections to Z/γ + jets at the LHC⁵

3.1 Introduction

Important searches for new phenomena beyond the Standard Model (SM) at the proton-proton (pp) collider LHC are based on the analysis of events with jets and missing transverse momentum (\cancel{p}_T). Typical examples of such studies are searches for squarks and gluinos in all-hadronic reactions containing high- p_T jets, missing transverse momentum and no electrons or muons, as predicted in many supersymmetric extensions of the SM. These final states can appear in a number of R-parity conserving models where squarks and gluinos can be produced in pairs and subsequently decay to standard strongly interacting particles plus neutralinos that escape detection, thus giving rise to a large amount of \cancel{p}_T . Typically, the event selections adopted at run I of the LHC, at center of mass energies of 7 and 8 TeV, require the leading jet p_T larger than 130 GeV or the single jets p_T 's larger than 50 GeV. Moreover, the signal region is defined by $m_{\text{eff}} > 1000$ GeV, where $m_{\text{eff}} = \sum_i p_{T_i} + \cancel{E}_T$, or $H_T > 500$ GeV and $|\vec{H}_T| > 200$ GeV, where $H_T = \sum_i p_{T_i}$ and $\vec{H}_T = -\sum_i \vec{p}_{T_i}$ [310–312].

The main SM backgrounds to the above mentioned signal(s) are given by the production of weak bosons accompanied by jets ($W/Z+n$ jets), pure QCD multiple jet events and $t\bar{t}$ production. Among these processes only $Z+n$ jets (in particular with $Z \rightarrow \nu\bar{\nu}$) constitutes an irreducible background, particularly relevant for final states with 2 and 3 jets. Because new physics signals could manifest themselves as a mild deviation with respect to the large SM background, precise theoretical predictions for the processes under consideration are needed. In order to reduce the theoretical systematic uncertainties, the experimental procedure for the irreducible background determination relies on data driven methods. For instance, a measurement of the cross section for $Z(\rightarrow \nu\bar{\nu})+n$ jets could be done through the measured cross section for $Z(\rightarrow l^+l^-)+n$ jets times the ratio $\frac{\mathcal{B}(Z\rightarrow\nu\bar{\nu})}{\mathcal{B}(Z\rightarrow l^+l^-)}$, which is known with high precision from LEP1 data. With the exception of the ratio of branching ratios, the method is free of theoretical systematics. However, due to the low production rate of $Z(\rightarrow l^+l^-)+n$ jets, in particular in the signal regions, this method results to be affected by large statistical uncertainty. Other possible choices of reference processes are $W+n$ jets and $\gamma+n$ jets. In both cases the statistics is not a limitation and the required theoretical input is the ratio

$$R_V^n = \left[\frac{d\sigma(Z(\rightarrow \nu\bar{\nu})+n \text{ jets})}{dX} \right] / \left[\frac{d\sigma(V+n \text{ jets})}{dX} \right], \quad (\text{III.11})$$

where X is the observable under consideration and $V = W, \gamma$. Additional sources of uncertainties, specific for each channel, are the contamination of other processes, such as $t\bar{t}$ events (for the case of $W+n$ jets) and photon isolation (for the case of $\gamma+n$ jets). Recent theoretical work has been devoted to the study of the theoretical uncertainties related to the ratio of Eq. (III.11). In particular, in Ref. [261] a study of the cancellation in R_W^n of systematic theoretical uncertainties originating from higher-order QCD corrections, including scale variations and choice of PDF's, has been presented. A first detailed analysis of the impact of higher-order QCD corrections, PDF's and scale choice to $R_\gamma^{1,2,3}$ has been shown in Ref. [313]. More recently, the level of theoretical uncertainty induced by QCD higher-order corrections in the knowledge of R_γ^2 and R_γ^3 , relying on the comparison of full NLO QCD calculations with parton shower simulations matched to LO matrix elements, has been discussed in Refs. [314] and [315], respectively. All these studies point out that many theoretical systematics related to pQCD and PDF's largely cancel in the ratio and the corresponding theoretical uncertainty in the ratio R_γ^i can be safely estimated to be within 10%.

What is not expected to cancel in the ratio is the contribution of higher-order electroweak (EW) corrections, which are different for the processes $Z(\rightarrow \nu\bar{\nu})+n$ jets and $\gamma+n$ jets. Moreover

⁵M. Chiesa, L. Barzè, G. Montagna, M. Moretti, O. Nicosini, F. Piccinini, F. Tramontano

these effects can be enhanced by Sudakov logarithms. For R_γ^1 the higher-order EW corrections have been calculated in Refs. [316–318], where it is shown that for a vector boson transverse momentum of 2 TeV they are of the order of 20%. In view of the forthcoming run II of the LHC, it is therefore necessary to quantitatively estimate the effects of EW corrections to R_γ^n , in particular for $n \geq 2$.

In this contribution we present first numerical results on the impact of EW Sudakov corrections to R_γ^2 and R_γ^3 , for two realistic event selections at the LHC, at a center of mass energy of 14 TeV. These results have been obtained by means of the algorithmic implementation of EW Sudakov corrections discussed in Ref. [142], which we describe below.

3.2 Implementation of EW Sudakov corrections in ALPGEN

For energy scales well above the EW scale, EW radiative corrections are dominated by double and single logarithmic contributions (DL and SL, respectively) whose argument involves the ratio of the energy scale to the mass of the weak bosons. These logs are generated by diagrams in which virtual and real gauge bosons are radiated by external leg particles, and correspond to the soft and collinear singularities appearing in QED and QCD, i.e. when massless gauge bosons are involved. At variance with this latter case, the weak bosons masses put a physical cutoff on these “singularities”, so that virtual and real weak bosons corrections can be considered separately. Moreover, as the radiation of real weak bosons is in principle detectable, for those event selections where one does not include real weak bosons radiation, the physical effect of (negative) virtual corrections is singled out, and can amount to tens of per cent. Since these corrections originate from the infrared structure of the EW theory, they are “process independent” in the sense that they depend only on the external on-shell legs [127, 129, 131, 133, 134, 316, 319–327]. As shown by Denner and Pozzorini in Refs. [131, 322], DL corrections can be accounted for by factorizing a proper correction which depends on flavour and kinematics of all possible pairs of electroweak charged external legs. SL corrections can be accounted for by factorizing an appropriate radiator function associated with each individual external leg. Notice that our implementation includes correctly all single logarithmic terms of $\mathcal{O}(\alpha^2\alpha_s^n)$ of both UV and infrared origin, as detailed in Ref. [328]. The above algorithm has been implemented in ALPGEN v2.14 [329], where all the contributing tree-level amplitudes are automatically provided. Since the matrix elements in ALPGEN are calculated within the unitary gauge, for the time being we do not implement the corrections for the amplitudes involving longitudinal vector bosons, which, according to Refs. [131, 322], are calculated by means of the Goldstone Boson Equivalence Theorem. For the processes $Z + 2$ jets and $Z + 3$ jets, this approximation affects part of the $\mathcal{O}(\alpha^3)$ and $\mathcal{O}(\alpha^3\alpha_s)$ contributions, respectively, and we checked that in view of our target precision of few percent it can be accepted ⁶.

3.3 Numerical results

Our numerical results have been obtained by using the code ALPGEN v2.14 with default input parameters/PDF set. The algorithm has been validated with results available in the literature. In Fig. III.17 we show our predictions for the jet p_t distribution for $\gamma + 1$ jet, $Z(\rightarrow \nu\bar{\nu}) + 1$ jet and for the ratio R_γ^1 at $\sqrt{s} = 14$ TeV in the region

$$p_t^j > 100 \text{ GeV}, \quad |y(j)| < 2.5, \quad |y(V)| < 2.5 \quad (V = \gamma, Z) \quad (\text{III.12})$$

⁶The logarithms of photonic origin have not been considered in this realization since they can be treated separately together with their real counterpart for the processes under investigation. At any rate, these gauge invariant contributions (at the leading order $\alpha_s^{n_{jets}}\alpha$) for sufficiently inclusive experimental setup give rise to rather moderate corrections.

and we compare our results with the ones obtained from Refs. [316, 324, 325] by including also the terms proportional to $\log(\frac{M_W}{M_Z})$: the level of agreement we find is well within the percent level. Moreover, we estimated the corrections to p_T^Z and to the leading jet p_T distributions

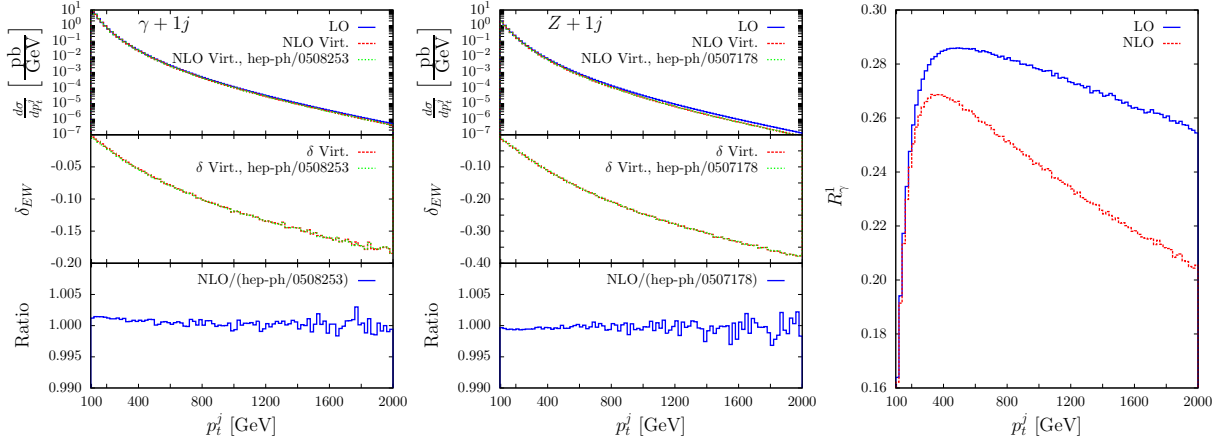


Fig. III.17: p_T^j distribution at $\sqrt{s} = 14$ TeV for $\gamma + 1$ jet and $Z(\rightarrow \nu\bar{\nu}) + 1$ jet and their ratio R_γ^1 at the LO (solid blue lines) and at approximated NLO (dashed red lines). Green dotted lines are the results of Refs. [316, 324, 325] when the difference between the W and the Z masses is not neglected. The ratio of our predictions with the ones of Refs. [316, 324, 325] is shown in the lower panels of the first two plots for $\gamma + 1$ jet and $Z(\rightarrow \nu\bar{\nu}) + 1$ jet, respectively.

in the large tails for the process $Z + 2$ jets with only one fermionic current, as discussed in Ref. [8], finding good agreement. Finally, for $Z + 2$ jets we cross-checked our results with the automatic package **GOSAM v1.0** [4], with the event selection adopted in the present study. Since the electroweak renormalization is not yet available in the present version of **GOSAM**, we subtracted the logarithmic terms due to the renormalization counterterms from the formulae of Refs. [131, 322] and tested the asymptotic behaviour of all relevant distributions. Since the relative weight of two-quark and four-quark subprocesses is about 75% and 25% for total cross sections, while for the observables under consideration and in the high tails is about 50% each at the LO, respectively, we performed this analysis for different subprocesses involving both one and two fermionic currents such as $q\bar{q} \rightarrow Zgg$, $q\bar{q} \rightarrow Zq''\bar{q}''$, $qq \rightarrow Zqq$ and $qq' \rightarrow Zqq'$ (with q and q' belonging to the same isodoublet). For all the above cases we found that the shape of the distributions predicted by the two calculations is in good agreement.

We present our results on $R_\gamma^{2,3}$ for two sets of cuts that mimic the real experimental event selections used by ATLAS and CMS in run I analysis. For the $Z(\rightarrow \nu\bar{\nu}) + 2$ jets and $\gamma + 2$ jets final states we consider the observable/cuts adopted by ATLAS, namely

$$\begin{aligned}
m_{\text{eff}} &> 1 \text{ TeV} & E_T/m_{\text{eff}} &> 0.3 \\
p_T^{j_1} &> 130 \text{ GeV} & p_T^{j_2} &> 40 \text{ GeV} & |\eta_j| &< 2.8 \\
\Delta\phi(\vec{p}_T^j, \vec{H}_T) &> 0.4 & \Delta R_{(j_1, j_2)} &> 0.4
\end{aligned} \tag{III.13}$$

where j_1 (j_2) are the leading (next-to-leading) p_T jets, the missing momentum \vec{p}_T^j is defined as minus the sum of the jet transverse momenta and H_T is the magnitude of \vec{p}_T^j . For the $Z(\rightarrow \nu\bar{\nu}) + 3$ jets and $\gamma + 3$ jets final states we consider the observables/cuts used by CMS, namely

$$\begin{aligned}
H_T &> 500 \text{ GeV} & |\vec{H}_T| &> 200 \text{ GeV} \\
p_T^j &> 50 \text{ GeV} & |\eta_j| &< 2.5 & \Delta R_{(j_i, j_k)} &> 0.5
\end{aligned}$$

$$\Delta\phi(\vec{p}_T^{j_1, j_2}, \vec{H}_T) > 0.5 \quad \Delta\phi(\vec{p}_T^{j_3}, \vec{H}_T) > 0.3 \quad (\text{III.14})$$

Fig. III.18 shows the m_{eff} distribution for $\gamma + 2$ jets and $Z(\rightarrow \nu\bar{\nu}) + 2$ jets, with the ATLAS cuts of Eq. (III.13). In the tails of the distributions the effect of EW Sudakov corrections is of the order of -20% and -40% for the processes $\gamma + 2$ jets and $Z(\rightarrow \nu\bar{\nu}) + 2$ jets, respectively. As a result, the ratio R_γ^2 of the two distributions, which is almost flat at the LO, decreases at the NLO of about 8% for $m_{\text{eff}} \simeq 1$ TeV up to 20% for $m_{\text{eff}} \simeq 4.5$ TeV. Fig. III.19 is the

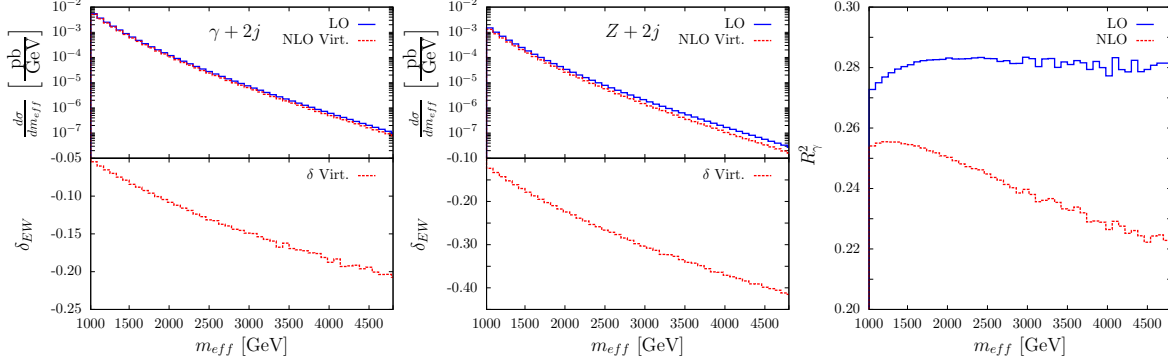


Fig. III.18: m_{eff} distribution at $\sqrt{s} = 14$ TeV for $\gamma + 2$ jets and $Z(\rightarrow \nu\bar{\nu}) + 2$ jets and their ratio R_γ^2 under the ATLAS event selection (same notation of Fig. III.17).

analogous of Fig. III.18 for the observable $|\vec{H}_T|$ under CMS conditions of Eq. (III.14) for the processes $Z(\rightarrow \nu\bar{\nu}) + 3$ jets and $\gamma + 3$ jets at $\sqrt{s} = 14$ TeV. As in the two jets case, EW Sudakov corrections are larger for $Z(\rightarrow \nu\bar{\nu}) + 3$ jets (where they are of the order of -45% for $|\vec{H}_T| \simeq 2$ TeV), while for $\gamma + 3$ jets the size of the corrections is of the order of -20% in the high $|\vec{H}_T|$ tail. Due to the different impact of EW corrections to $\gamma + 3j$ and $Z(\rightarrow \nu\bar{\nu}) + 3j$, the shape of their ratio R_γ^3 changes at the NLO w.r.t. LO and decreases of about 20% for $|\vec{H}_T| \simeq 2$ TeV.

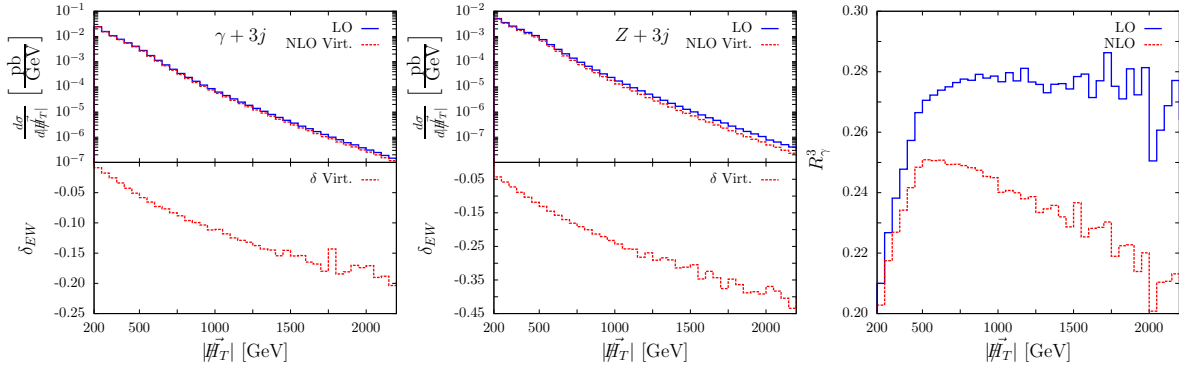


Fig. III.19: $|\vec{H}_T|$ distribution at $\sqrt{s} = 14$ TeV for $\gamma + 3$ jets and $Z(\rightarrow \nu\bar{\nu}) + 3$ jets and their ratio R_γ^3 under the CMS event selection (same notation of Fig. III.17).

To summarize, the theoretical accuracy on the quantity R_γ^n is relevant in the calibration of the process $Z(\rightarrow \nu\bar{\nu}) + n$ jets, an important irreducible background to New Physics searches at the LHC. Contrary to higher-order QCD corrections, which largely cancel in the ratio, as shown in the literature, EW NLO corrections are sizeable, in particular in the phase space regions interesting for New Physics searches. We computed the NLO EW Sudakov corrections to $Z(\rightarrow \nu\bar{\nu}) + n$ jets, $\gamma + n$ jets and to the ratio $R_\gamma^n = \frac{d\sigma(Z(\rightarrow \nu\bar{\nu}) + n \text{ jets})}{d\sigma(\gamma + n \text{ jets})}$ (where $n = 1, 2, 3$) and we showed our results for the LHC at $\sqrt{s} = 14$ TeV. In the typical event selections used for New Physics searches based on the signature $\vec{H}_T + n$ jets, electroweak Sudakov corrections to

$Z(\rightarrow \nu\bar{\nu})+n$ jets and $\gamma+n$ jets in the tails of the distributions considered are of the order of -40% and -20% , respectively. Since the impact of EW corrections to $\gamma+n$ jets and $Z(\rightarrow \nu\bar{\nu})+n$ jets is different, the shape of the ratio R_γ^n changes at NLO accuracy w.r.t. LO, decreasing of about 20% (slightly depending on the observable considered) in the regions where the corrections are larger. Thus EW Sudakov corrections are important in view of a target uncertainty on the ratio R_γ^n of the order of 10%. In this contribution we do not address the issue of real weak corrections, which is left to a future study. While the results presented in Ref. [142] suggest a non-negligible contribution to the signatures $Z(\rightarrow \nu\bar{\nu})+2$ jets and $Z(\rightarrow \nu\bar{\nu})+3$ jets, preliminary investigations of Ref. [315] on R_γ^3 show modest effects, at the % level at most.

Acknowledgments

This work was supported in part by the Research Executive Agency (REA) of the European Union under the Grant Agreement number PITN-GA-2010-264564 (LHCPhenoNet), and by the Italian Ministry of University and Research under the PRIN project 2010YJ2NYW. The work of L.B. is supported by the ERC grant 291377, "LHCtheory - Theoretical predictions and analyses of LHC physics: advancing the precision frontier". F.P. and M.M. would like to thank the CERN PH-TH Department for partial support and hospitality during several stages of the work. F.P. and G.M. thank the organizers of the LH13 Workshop for their kind invitation.

4 Jet rates from recursion relations⁷

We present an improved recursive construction for analytic jet rates of arbitrary flavor at next-to-double-leading-logarithmic accuracy. There are significant computational improvements in this formulation of the recursive algorithm as the explicit sum over integer partitions is avoided at each step in the recursion. We discuss this property and comment on future improvements.

4.1 Introduction

There has been recent interest in analytic all-orders jet rates [215, 330, 331] for the purpose of a meaningful analytic comparison to parton shower Monte Carlo [28, 164, 166, 332, 333]. For example, the distribution of shower paths in the parton shower arriving at a particular phase space point is only known *a posteriori*, after generating a potentially large amount of data. As hadron collider physics turns to more QCD intensive observables, one would like to know this probability distribution *a priori* [334, 335]. In this note we present progress on enumerating the spitting histories in observable, one would like to know this probability distribution *a priori* [334, 335]. In this note we present progress on enumerating the splitting histories in a final state parton cascade based on an analytically solvable recursive evolution equation.

4.2 Recursive Formula

We begin by setting forth our notation. In general, we will be dealing with analytic expressions for n -jet rates containing leading and sub-leading logarithms. To this end, we define the $\mathcal{O}(\alpha_s^n)$ NDLL accurate contribution to jet production

$$\Gamma_n(\mu^2, q^2) = a_s^n \left[\sum_k \sum_{i=0}^{n-1} \sum_{l=0}^n \left(c_{ik}^{(l,n)} \log \left(\frac{q^2}{\mu^2} \right)^{2n} + \tilde{c}_{ik}^{(l,n)} \log \left(\frac{q^2}{\mu^2} \right)^{2n-1} \right) \right]. \quad (\text{III.15})$$

The sum on l is over emitted partons in the event classified as either real or virtual, while the sum over i is over the number of primary emissions in a particular splitting history. The sum on k is over all splitting histories of the same order in l and i which becomes non-trivial starting only at $\mathcal{O}(\alpha_s^4)$ with respect to the core process. Also we have defined $a_s = \alpha_s/\pi$ and for concreteness q is the initiating scale and μ the IR cut-off associated with the resolution scale for jets. Below this scale there is complete real virtual cancellation.

Relating the expansion in (III.15) to the terms of the all-orders expression for the m -jet fraction we have

$$f_m = \sum_{n=m}^{\infty} \Gamma_n^{(l=m)} \quad (\text{III.16})$$

where the superscript indicates that we pick out only the terms with $l = m$ in the first sum of (III.15). The virtue of the 3 sums in (III.15) is that all coefficients stand in one-to-one relation with a diagrammatic splitting history (c at LL and \tilde{c} at NDLL). Note that the definition of $c_{ik}^{(l,n)}$ differs from that in Ref. [330] by including the color factor. In effect, (III.16) tells us that by computing Γ_n we may always recover the rates.

The recursive formula derived in Ref. [330] for the LL coefficients can now be rewritten as a recursion relation for γ itself. We found there

$$\Gamma_n = \left(a_s L^2 \right) \sum_{l=0}^{n-1} b_{n-l}^p (-1)^{n-l} \left(\Gamma_{n-1} d^{(n)} + \sum_{p(n)} \frac{1}{S} \prod_{\sigma_i = \{\sigma_1, \dots, \sigma_r\}} \Gamma_{\sigma_{i-1}}^{(\sigma_i)} \right). \quad (\text{III.17})$$

⁷E. Gerwick, S. Plätzer

Now we insert the general expression (III.18) into the previous evolution equation (III.19) and expand the respective coefficients. We find

$$\begin{aligned}
\Gamma_{nk}(\mu^2, Q^2) = & \left(\frac{\alpha_s}{2\pi}\right)^n \sum_{m=0}^{n-1} \sum_{i,j} \int_{4\mu^2}^{Q^2} \frac{dq^2}{q^2} \times \\
& \left[C_{i,m}^{\text{LL}} C_{i,n-m-1}^{\text{LL}} \sum_{\alpha=0}^{2m} \sum_{\beta=0}^{2(n-m)-2} b_\alpha^{2m} b_\beta^{2(n-m)-2} L^{2n-2-\alpha-\beta} \gamma_{k \rightarrow ij}^{\alpha,\beta} + \right. \\
& C_{i,m}^{\text{NLL}} C_{i,n-m-1}^{\text{LL}} \sum_{\alpha=0}^{2m-1} \sum_{\beta=0}^{2(n-m)-2} b_\alpha^{2m-1} b_\beta^{2(n-m)-2} L^{2n-3-\alpha-\beta} \gamma_{k \rightarrow ij}^{\alpha,\beta} + \\
& C_{i,m}^{\text{LL}} C_{i,n-m-1}^{\text{NLL}} \sum_{\alpha=0}^{2m} \sum_{\beta=0}^{2(n-m)-3} b_\alpha^{2m} b_\beta^{2(n-m)-3} L^{2n-3-\alpha-\beta} \gamma_{k \rightarrow ij}^{\alpha,\beta} + \\
& \left. C_{i,m}^{\text{NLL}} C_{i,n-m-1}^{\text{NLL}} \sum_{\alpha=0}^{2m-1} \sum_{\beta=0}^{2(n-m)-3} b_\alpha^{2m-1} b_\beta^{2(n-m)-3} L^{2n-4-\alpha-\beta} \gamma_{k \rightarrow ij}^{\alpha,\beta} \right], \quad (\text{III.21})
\end{aligned}$$

where

$$\gamma_{k \rightarrow ij}^{\alpha,\beta} \equiv \int_{\mu/q}^{1-\mu/q} dz P_{k \rightarrow ij}(z) \ln^\alpha z^2 \ln^\beta (1-z)^2. \quad (\text{III.22})$$

As is already evident from (III.18), the splitting function $P(z)$, with singular pieces in both $z \rightarrow 0$ and $(1-z) \rightarrow 0$, picks out the logarithmically enhanced coefficients of the corresponding Γ . To this end, we decompose the splitting function as

$$P_{k \rightarrow ij}(z) = \frac{P_{k \rightarrow ij}^{(-)}}{1-z} + \frac{P_{k \rightarrow ij}^{(+)}}{z} + P_{k \rightarrow ij}^{(0)}(z), \quad (\text{III.23})$$

where $P_{k \rightarrow ij}^{(0)}(z)$ is regular at both $z \rightarrow 0$, $z \rightarrow 1$ and we let $\langle P_{k \rightarrow ij}^{(0)} \rangle$ denote its average over $z \in (0, 1)$. This allows us to extract the logarithmic pieces from (III.22). The relevant contributions are

$$\gamma_{k \rightarrow ij}^{\alpha,\beta} = P_{k \rightarrow ij}^{(-)} \frac{(-1)^\beta}{2(\beta+1)} L^{\beta+1} \delta_{\alpha,0} + P_{k \rightarrow ij}^{(+)} \frac{(-1)^\alpha}{2(\alpha+1)} L^{\alpha+1} \delta_{\beta,0} + \langle P_{k \rightarrow ij}^{(0)} \rangle \delta_{\alpha,0} \delta_{\beta,0} + \mathcal{O}(\mu). \quad (\text{III.24})$$

The leading and next-to-leading logarithmic coefficients, defined in (III.18), are given by sums of coefficients from lower n , with pre-factors assigned by the integrated splitting functions. We find

$$\begin{aligned}
C_{k,n}^{\text{LL}} &= \frac{1}{4n} \sum_{m=0}^{n-1} \sum_{i,j} C_{i,m}^{\text{LL}} C_{j,n-m-1}^{\text{LL}} \left(P_{k \rightarrow ij}^{(-)} \xi_{2n-2m-2} + P_{k \rightarrow ij}^{(+)} \xi_{2m} \right) \\
C_{k,n}^{\text{NLL}} &= \frac{1}{2(2n-1)} \times \sum_{m=0}^{n-1} \sum_{i,j} \left[P_{k \rightarrow ij}^{(-)} \left(C_{i,m}^{\text{NLL}} C_{j,n-m-1}^{\text{LL}} \xi_{2n-2m-2} + C_{i,m}^{\text{LL}} C_{j,n-m-1}^{\text{NLL}} \xi_{2n-2m-3} \right) + \right. \\
& \left. P_{k \rightarrow ij}^{(+)} \left(C_{i,m}^{\text{NLL}} C_{j,n-m-1}^{\text{LL}} \xi_{2m-1} + C_{i,m}^{\text{LL}} C_{j,n-m-1}^{\text{NLL}} \xi_{2m} \right) + 2 \langle P_{k \rightarrow ij}^{(0)} \rangle C_{i,m}^{\text{LL}} C_{j,n-m-1}^{\text{LL}} \right]. \quad (\text{III.25})
\end{aligned}$$

with initial condition $C_{k,0}^{\text{LL}} = 1$, $C_{k,0}^{\text{NLL}} = 0$. We define here

$$\xi_n = \sum_{k=0}^n \frac{(-1)^k}{k+1} b_k^n = \begin{cases} \frac{1}{n+1} & n \geq 0 \\ 0 & \text{else} \end{cases}. \quad (\text{III.26})$$

4.3 Discussion

Partitions of integers:

We clarify here the relation between the two recursive constructions, (III.17) and (III.25). In (III.25) there is no sum over integer partitions of the number of partons n . This dramatically reduces the (potentially prohibitive at high multiplicity) computational expense. It is useful to inductively analyze precisely how the second construction (III.25) avoids this complication.

The coefficients $C_{k,n}^{\text{LL}}$ contain information on all splitting histories up to n , including the partitions (and sub-partitions) of n . Now consider the partition $\{\sigma_1, \sigma_2, \dots, \sigma_q\}$ of length q of n so that $\sigma_1 + \sigma_2 + \dots + \sigma_q = n$. We take the term included in Γ_n which is proportional to $c_{\sigma_1} c_{\sigma_2} \dots c_{\sigma_q}$. Now we will display how all partitions of length q of $n + 1$ are generated.

Consider the partition $\{\sigma_2, \dots, \sigma_q\}$ of length $q - 1$ in $\Gamma_{n-\sigma_1}$ which we label $\Gamma_{n-\sigma_1}^{q-1}$. The $z \rightarrow 0$ region of the integral

$$P(z) \Gamma_{\sigma_1}(\mu^2, z^2 q^2) \Gamma_{n-\sigma_1}^q(\mu^2, (1-z)^2 q^2) \quad (\text{III.27})$$

gives the contribution corresponding to the partition $\{\sigma_1 + 1, \sigma_2, \dots, \sigma_q\}$. Similarly, the term $\Gamma_{\sigma_2} \Gamma_{n-\sigma_2}$ generates $\{\sigma_1, \sigma_2 + 1, \dots, \sigma_q\}$. It is clear that this procedure exhausts all partitions of $n + 1$ of length q , which are now contained in Γ_{n+1} . The only partition not included here is of length $n + 1$, which clearly originates from the non-singular regions of $P(z) \Gamma_0 \Gamma_n$.

Systematic improvements:

As presented the recursive construction only includes the resolved coefficient which are leading order in α_s . Including the virtual coefficients along with the NDLL terms, one should have enough information to include the leading effects of the running coupling which formally start at one power higher in the coupling together with sub-leading logarithms. At this stage a direct comparison with parton shower Monte Carlo is possible.

Validation:

We have compared results from the recursion relation presented here (at LL), with the recursion relation discussed previously. The NDLC calculation has been verified for the coefficients quoted in [336]

Outlook:

Both the original recursion proposed in [330], and the new approach with the inclusion of NDLC terms are available as symbolic Mathematica code, while we have also developed a highly efficient numerical implementation in C++. Work is ongoing on including the unresolved components in the new approach, as well. We foresee providing the results in both in the analytic and numeric tools which will in turn enable us to perform more realistic cross checks of the jet rate coefficients against parton shower implementations.

Conclusions

Our prescription for computing analytic jet rate coefficients is relevant a more complete understanding of the probability distributions of exclusive final states. These are typically only accessed via parton shower Monte Carlo, although there are recent attempts to put these on more solid analytic footing [215, 334, 335].

Acknowledgements

We would like to thank the Les Houches workshop for hospitality offered during which some of the work contained herein was performed, and the stimulating environment to foster collaboration on comparing and developing two different approaches to the same problem. SP acknowledges partial support from the Helmholtz Alliance ‘Physics at the Terascale’.

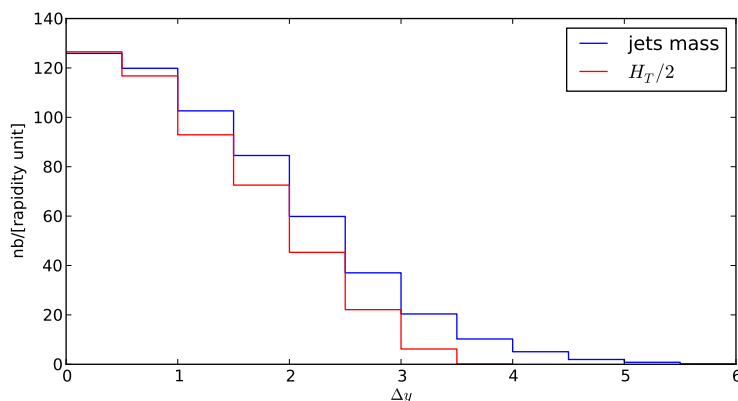


Fig. III.20: Distribution of inclusive 2-jet events with no jets in the region of rapidity between the two jets of highest transverse momentum, for two choices of factorisation and renormalisation scale.

=====

5 Study of the average number of hard jets⁸

5.1 Introduction

Jet vetos are an important ingredient in many analysis, in particular for analysis involving a Higgs boson produced through vector boson fusion. It is necessary to understand the impact of the jet vetos on theoretical predictions and their uncertainties. For this purpose it is useful to test the description offered by different tools in a process offering more available and precise data. In this contribution we investigate the extent to which pure perturbative tools (no underlying event, no hadronisation) can describe dijet events when vetos on further jets are imposed.

We compare theoretical predictions obtained using HEJ [337–339] and NLO predictions obtained by BlackHat+Sherpa [340–345]. We base the analysis on the observables measured by the Atlas collaboration described in [346].

For the NLO predictions we used the invariant mass of all jets as the scale and not the usual $H_T/2$ variable since in configurations with two widely separated jets with moderate transverse momenta (the type of configuration dominant for most observables in this study) H_T is not a good scale to represent the scale of the process, as it is much lower than the partonic center of mass energy. The fact that this scale is too low in these configurations is evidenced by the fact that distributions turn negative for the corresponding observables, as can be seen in Figure III.20, illustrating the cross section for dijet production with no further jets in the region of rapidity between the two hardest jets, as obtained with two different choices for the scale in the calculation of dijets@NLO.

There are different ways of defining the gap fraction at NLO given the ambiguity in the inclusion of higher order terms. In this contribution we will follow two approaches, equivalent up to higher order terms, trying to identify whether one agrees with the data better than the other.

⁸J.R. Andersen, D. Maître

5.2 Gap fractions for a fixed p_t -threshold

In this section we use Q_0 to denote the minimum transverse momentum for the jets. The gap fraction is given by:

$$g = \frac{\sigma_{Y/pt}(Q_0)}{\sigma_{tot}}, \quad (\text{III.28})$$

where $\sigma_{Y/pt}(Q_0)$ is the cross section with the constraint that there are no additional jets with p_T above Q_0 between (in rapidity) the two leading p_T jets (pt) or the forward/backward jets (Y). We use the notation $g = i$ to specify how many jets are in the region of rapidity between the tagging dijets (the condition for this to happen depend on the context, e.g. whether the tagging dijet system is defined by the most energetic jets or the most forward and backward). $j = i$ is used to specify the number of jets. In both cases the equal sign correspond to an exclusive final state, for example $j = 2$ means exactly two jets, while inequalities mean inclusive final state $g \geq 1$ means one or more jets in the gap.

We investigate two different approximations for the gap fraction, which are both equivalent up to α_s^3 . These are

$$\begin{aligned} g &= \frac{\sigma_{g=0}}{\sigma_{tot}} = 1 - \frac{\sigma_{g \geq 1}}{\sigma_{tot}} \\ &= 1 - \frac{\sigma_{g \geq 1}^{\text{NLO}, j \geq 3}}{\sigma_{\text{NLO}, j \leq 2}} = 1 - \frac{\sigma_{\text{NLO}, j >= 3} - \sigma_{g=0}^{\text{NLO}, j=3} - \sigma_{g=0}^{LO, j=4}}{\sigma_{\text{NLO}, j \leq 2}} \end{aligned} \quad (\text{III.29})$$

and

$$g = \frac{\sigma_{g=0}}{\sigma_{tot}} = \frac{\sigma_{g=0}^{\text{NLO}, j=2} + \sigma_{g=0}^{\text{NLO}, j=3} + \sigma_{g=0}^{\text{NLO}, j \geq 4}}{\sigma_{\text{NLO}, j=2} + \sigma_{\text{NLO}, j=3} + \sigma_{\text{NLO}, j \geq 4}} \quad (\text{III.30})$$

In the case where the jets defining the dijet system are the forward/backward ones, the formulae simplify to

$$g_Y = \frac{\sigma_{g=0}}{\sigma_{tot}} = \frac{\sigma_{\text{NLO}, j=2}}{\sigma_{\text{NLO}, j \geq 2}} \quad (\text{III.31})$$

and

$$g_Y = \frac{\sigma_{g=0}}{\sigma_{tot}} = \frac{\sigma_{\text{NLO}, j=2}}{\sigma_{\text{NLO}, j=2} + \sigma_{\text{NLO}, j=3} + \sigma_{\text{NLO}, j \leq 4}}. \quad (\text{III.32})$$

Figure III.21 shows the gap fraction as a function of the the rapidity difference between the two highest transverse momentum jet. The curves corresponds to different slices of the average transverse momentum of the jets

$$\bar{p}_T = \frac{1}{2} (p_T^{j_1} + p_T^{j_2}).$$

From the top to the bottom the slices are:

$$\begin{aligned} 240 \text{ GeV} &< \bar{p}_T < 270 \text{ GeV} \\ 210 \text{ GeV} &< \bar{p}_T < 240 \text{ GeV} \\ 180 \text{ GeV} &< \bar{p}_T < 210 \text{ GeV} \\ 150 \text{ GeV} &< \bar{p}_T < 180 \text{ GeV} \\ 120 \text{ GeV} &< \bar{p}_T < 150 \text{ GeV} \\ 90 \text{ GeV} &< \bar{p}_T < 120 \text{ GeV} \\ 70 \text{ GeV} &< \bar{p}_T < 90 \text{ GeV} \end{aligned} \quad (\text{III.33})$$

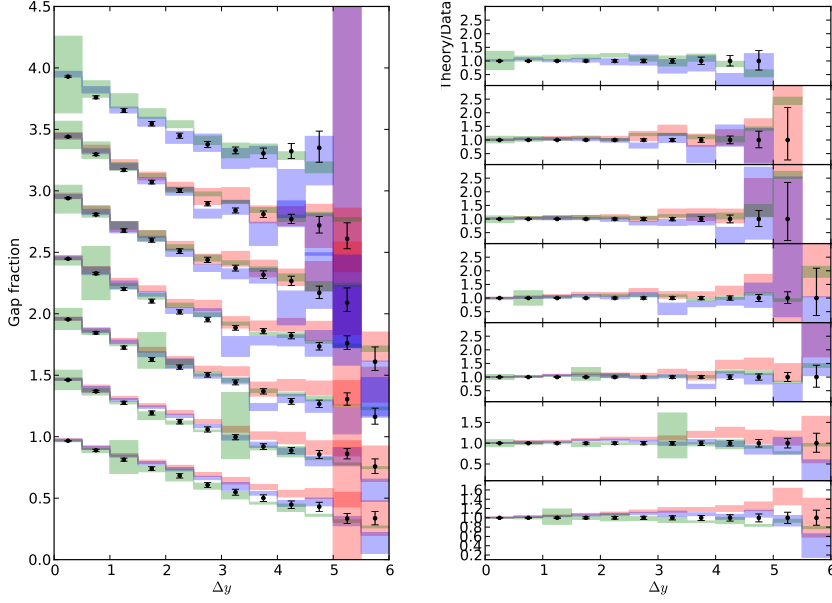


Fig. III.21: Gap fraction as a function of Δy for various slices of \bar{p}_T . The jets defining \bar{p}_T and Δy are the two jets with the largest p_T .

The green curve corresponds to the HEJ prediction, while the blue and red curves correspond to the NLO predictions of formulae (III.29) and (III.30), respectively. The band represent the statistical Monte Carlo integration only. For this observable, the NLO-based prediction fares marginally better compared to ATLAS data [346] when using Eq. (III.30) rather than Eq. (III.29).

In Figure III.22 we present the gap fraction as a function of the average transverse momentum of the highest transverse momentum jets for different slices of rapidity difference between them. The slices are give, from top to bottom by

$$\begin{aligned}
 &5 < \Delta y < 6 \\
 &4 < \Delta y < 5 \\
 &3 < \Delta y < 4 \\
 &2 < \Delta y < 3 \\
 &1 < \Delta y < 2.
 \end{aligned}
 \tag{III.34}$$

The green curve corresponds to the HEJ prediction, while the blue and red curves correspond to the NLO predictions of formulae (III.29) and (III.30), respectively. The band represent the statistical Monte Carlo integration only. For this observable the NLO-based predictions are again better using the gap formula (III.30) rather than that of (III.29); the former overshooting the data less than the latter. The difference between the two formulae becomes larger as the rapidity separation between the jets increases, which is fully understood from the increased of yet higher order terms for increasing rapidity spans.

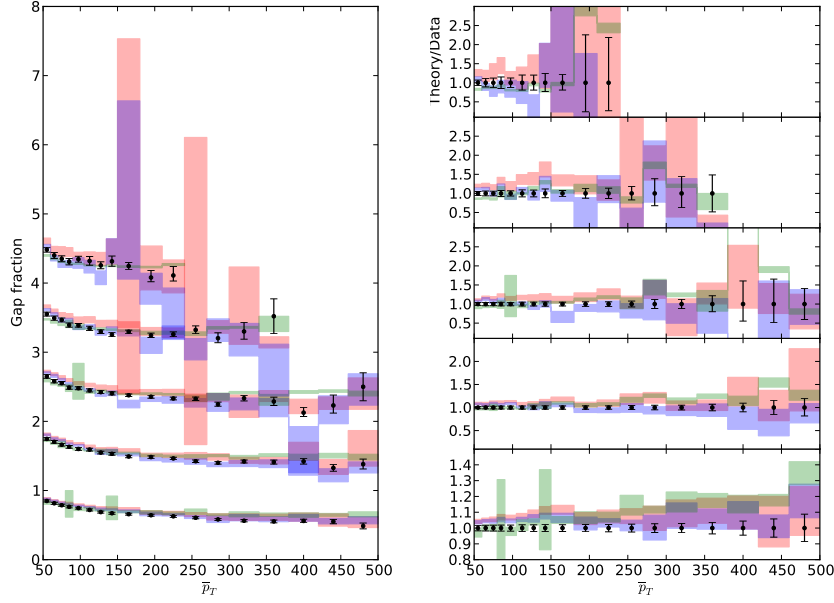


Fig. III.22: Gap fraction as a function of \bar{p}_T for various slices of Δy . The jets defining \bar{p}_T and Δy are the two jets with the largest p_T .

5.3 Mean number of jets

The mean number of jets in the relevant region of rapidity is obviously defined as

$$\langle N_{gap} \rangle = \frac{\sigma_{g=1} + 2\sigma_{g=2} + 3\sigma_{g=3} + \dots}{\sigma_{tot}}. \quad (\text{III.35})$$

Based on NLO-calculations, we can construct equivalent predictions for the average number of jets as

$$\langle N_{gap} \rangle = \frac{1(\sigma_{g=1}^{j=3} + \sigma_{g=1}^{j \geq 4}) + 2\sigma_{g=2}^{j \geq 4} + 3\sigma_{g=3}^{j=5}}{\sigma_{\text{NLO},j=2} + \sigma_{\text{NLO},j=3} + \sigma_{\text{NLO},j \leq 4}} \quad (\text{III.36})$$

and

$$\langle N_{gap} \rangle = \frac{1(\sigma_{g=1}^{j=3} + \sigma_{g=1}^{j=4,LO}) + 2(\sigma_{g=2}^{j=4,LO})}{\sigma_{j \leq 2, \text{NLO}}} \quad (\text{III.37})$$

In the case where the jets defining the dijet system are the forward/backward ones, the formulae simplify to

$$\langle N_{gap} \rangle = \frac{1\sigma_{g=1}^{j=3} + 2\sigma_{g=2}^{j=4} + 3\sigma_{g=3}^{j=5}}{\sigma_{\text{NLO},j=2} + \sigma_{\text{NLO},j=3} + \sigma_{\text{NLO},j=4}} \quad (\text{III.38})$$

and

$$\langle N_{gap} \rangle = \frac{1(\sigma_{g=1}^{j=3}) + 2(\sigma_{g=2}^{j=4,LO})}{\sigma_{\text{NLO},j \leq 2}} \quad (\text{III.39})$$

In Figure III.23 we show the average number of jets in the gap as a function of the average transverse momentum for the last four Δy slices in Eq. III.34. Both the HEJ and the NLO prediction undershoot the data with an increasing difference at large average transverse momentum. The ratio looks similar for the all slices for the HEJ prediction while the disagreement gets worse for increasing rapidity difference for the NLO predictions.

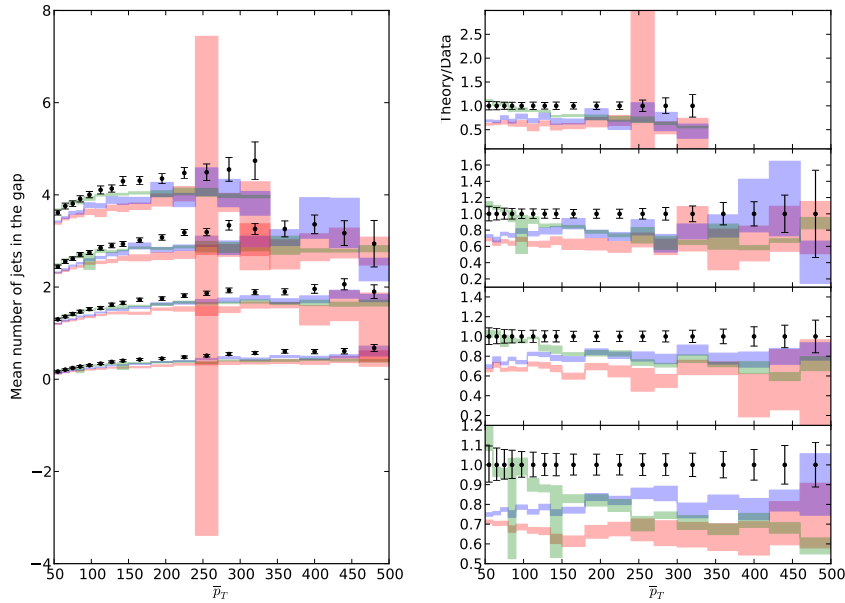


Fig. III.23: Mean number of jets in the gap as a function of \bar{p}_T for various slices of Δy . The jets defining \bar{p}_T and Δy are the two jets with the largest p_T .

5.4 Conclusions

In this contribution we have compared predictions for gap probabilities and related observables from HEJ and BlackHat+Sherpa with experimental data from the ATLAS collaboration. Our analysis shows that both HEJ and NLO can provide a very good (and fully perturbative) description of e.g. the gap fraction in the full range of rapidities and all slices of \bar{p}_T (Fig. III.21).

However, neither HEJ nor the NLO combination provide a perfect description of the data when it comes to e.g. the average number of soft (20GeV) jets in events with two much harder jets (Figure III.23. This is perhaps not surprising, since this is the region where the systematic resummation provided by a parton shower is necessary.

Furthermore, there is no clear preference for one or the other NLO 'strategies' to define the gap fraction. In future work we hope to understand to which extent perturbative methods can describe the gap fraction and extend the study to all distributions in [346]. The statistical samples used for this analysis leaves us with quite large uncertainties, for further studies more statistics will be needed.

6 Uncertainties in $pp \rightarrow h + 2$ jets production through gluon fusion⁹

6.1 INTRODUCTION

The process of Higgs boson production in association with dijets is of interest for several reasons. The interference between the two production channels of Weak-boson fusion (WBF) and gluon fusion (GF) is insignificant [347–349], so it is justified to discuss the processes separately. This study is concerned with the description of the gluon fusion contribution to Higgs boson production in association with dijets.

The gluon fusion channel is of interest not just as a background to the direct study through WBF of the couplings between the weak bosons and the Higgs boson, but also because the structure of the heavy-quark-mediated coupling of the Higgs boson to gluons can be studied beyond the question of normalisation. The structure of the higgs-couplings means that for a CP -specific coupling the cross section displays a striking dependence on the azimuthal angle between rapidity-separated jets. In contrast, the weak-boson-fusion component is relatively flat [350, 351].

In this region of phase space of large rapidity spans of the jets, the component of gluon fusion and weak-boson fusion exhibit very different patterns of radiative corrections. This is caused by a dominant colour octet exchange between the dijets in the case of gluon-fusion, whereas the weak-boson fusion component has no colour exchange between the jets [352, 353]. For the gluon fusion sample, this enhances the contribution from jet multiplicities beyond the two required, and necessitates a generalisation of the Born-level jet analysis to stabilise the extraction of the azimuthal dependence [354]. Furthermore, the enhanced contribution from further hard radiation severely tests the current limits of the perturbative description.

With a satisfactory description of each component, the very different radiation patterns in WBF and GF can be utilised to study each contribution separately (for extraction and verification of the CP -structure of the couplings).

The purpose of the current study is to investigate the variation in the current description of the gluon-fusion contribution, in particular in the testing region of the cuts employed to enhance the weak-boson fusion contribution to Higgs boson production in association with dijets.

6.2 GENERATORS

In this section all generators employed in this study, including their settings and methods of determining the uncertainties, are briefly reviewed.

6.2.1 *aMC@NLO*

Events were generated using MADGRAPH5_aMC@NLO 2.0 [355] for exclusive jet multiplicities ($pp \rightarrow h + 0j$, $pp \rightarrow h + 1j$, $pp \rightarrow h + 2j$), each at NLO accuracy. The virtual corrections were taken from MCFM [44, 356]. Jet multiplicities are then merged using the FxFx merging prescription [357]. Events are then showered with HERWIG++ [164], where events are matched to the hard process. To avoid double counting, the jet multiplicity after showering must match the jet multiplicity of the hard process for which NLO accuracy is desired. This means that only events with 0 jets after showering are kept if they were generated with 0 partons in the matrix element. Because NLO is only desired for Higgs in association with up to two jets, events which have more than two jets after showering are kept if the hard process was generated with two jets. In addition, jets after showering must be matched with the hard partons of the generated event by imposing a $\Delta R = 1$ requirement between jets before and after showering. All matched

⁹J.R. Andersen, F.U. Bernlochner, D. Gillberg, K. Hamilton, T. Hapola, J. Huston, A. Kruse, L. Lönnblad, P. Nason, S. Prestel, M. Schönherr, J.M. Smillie, K. Zapp

| $(\mu_R/m_h, \mu_F/m_h)$ | (0.5,0.5) | (0.5,1) | (1,0.5) | (1,1) | (1,2) | (2,1) | (2,2) |
|--------------------------|-----------|---------|---------|-------|-------|-------|-------|
| POWHEG ggF | 15.83 | 15.90 | 13.20 | 13.29 | 13.34 | 11.27 | 11.31 |
| MinLO-HJ | 16.58 | 16.68 | 12.32 | 12.58 | 12.74 | 10.76 | 10.90 |
| MinLO-HJJ | 22.36 | 23.58 | 16.89 | 17.74 | 18.19 | 13.14 | 13.35 |

Table III.3: Inclusive $pp \rightarrow h$ cross sections in pb for POWHEG ggF, MinLO-HJ and MinLO-HJJ for various scale choices.

jets after showering must have p_\perp larger than the merging scale.

Events were produced using the CT10 parton distribution function [289] throughout. The renormalisation and factorisation scales, μ_R and μ_F , are set following the MinLO procedure [32]. The merging scale was chosen to be 30 GeV for the nominal sample. Scale variations were found by varying μ_R and μ_F up and down by factors of two.

6.2.2 Hej

High Energy Jets (HEJ) describes hard, wide angle (high energy-) emissions to all orders and to all multiplicities. The predictions are based on events generated according to an all-order resummation, merged with high-multiplicity full tree-level matrix-elements. The explicit resummation is built on an approximation to the n-parton hard scattering matrix element [337–339] which becomes exact in the limit of wide-angle emissions, ensuring leading logarithmic accuracy for both real and virtual corrections. These logarithmic terms are important when the partonic invariant mass is large compared to the typical transverse momentum in the event. This is precisely the situation which arises in typical “VBF” cuts, including those used in this study. Matching to the full tree level accuracy for up to three jets is obtained by supplementing the resummation with a merging procedure [358, 359].

The implementation of this framework in a fully-flexible Monte Carlo event generator is available at <http://hej.web.cern.ch>, and produces exclusive samples for events with at least two jets. The predictions include resummation also for events with up to two un-ordered emissions, i.e. contributions from the first sub-leading configurations [360].

The factorisation and renormalisation scales can be chosen arbitrarily, just as in a standard fixed-order calculation. Here, we have chosen to evaluate two powers of the strong coupling at a scale given by the Higgs mass, and for the central predictions the remaining scales are evaluated at $\mu_R = H_T/2$. Thus, for the n -jet tree-level evaluation,

$$\alpha_s^{n+2} = \alpha_s^2(m_h) \cdot \alpha_s^n(\mu_R). \quad (\text{III.40})$$

The scale variation bands shown in the plots here correspond to varying μ_F and μ_R independently by a factor of two in either direction, but discarding evaluations where any ratio is bigger than two. The CT10nlo [233, 289] parton distribution functions were used in the predictions.

6.2.3 PowhegBox

Samples were generated using the latest version of POWHEGBOX (SVN revision 2550). The produced Les Houches files were passed through PYTHIA 8 [333] (v8.1.6) for parton showering (ISR+FSR). This was done for default POWHEG ggF, MinLO-HJ and MinLO-HJJ for each of the scale variation settings. CT10 [289] was used both for the matrix element and hardest emission calculation in POWHEGBOX and parton showering in PYTHIA 8 [361, 362]. The total cross section of these samples are summarised in Tab. 6.2.3.

The PYTHIA 8 default parton showering interface to the POWHEGBOX was used that picks up the SCALUP parameter from the LesHouches file and restricts parton shower emissions to this scale (aka “wimpy showers”). Parton showering/resummation uncertainties were evaluated by producing separate samples with the SCALUP parameter varied by factors of 0.75 and 1.5. A cross check was performed replacing the SCALUP restriction by the “power shower”+“ p_T veto” approach¹⁰. The difference between the two approaches is (well) within the SCALUP variation.

Additional results switching off ISR and/or FSR and including hadronisation and/or MPI are provided at https://dgillber.web.cern.ch/dgillber/Rivet/Powheg_ggF.html.

For the study presented in Sec. 6.3 the MiNLO-HJJ setup was used throughout as it gives the highest formal accuracy for most observables under scrutiny. Please note: for the sake of consistency in describing correlations inbetween the different observable classes the MiNLO-HJJ setup was also used for zero- and one-jet inclusive observables where its formal accuracy falls below the MiNLO-HJ setup.

6.2.4 Pythia 8

The UNLOPS method [35] allows to incorporate multiple next-to-leading order calculations into a parton shower event generator. The implementation of this NLO merging scheme in PYTHIA 8 [333] uses external next-to-leading order matrix element generators to produce events distributed according to inclusive NLO cross sections. Higher-order terms (of the UMEPS merging scheme [31]) are supplied by reweighting additional tree-level input samples. In the UNLOPS approach, the merged prediction for an observable is

$$\begin{aligned}
\langle \mathcal{O} \rangle = & \sum_{m=0}^{M-1} \int d\phi_0 \int \cdots \int \mathcal{O}(S_{+mj}) \left\{ \bar{B}_m + [\hat{B}_m]_{-m,m+1} \right. \\
& \left. - \sum_{i=m+1}^M \int_s \bar{B}_{i \rightarrow m} - \sum_{i=m+1}^M \left[\int_s \hat{B}_{i \rightarrow m} \right]_{-i,i+1} - \sum_{i=M+1}^N \int_s \hat{B}_{i \rightarrow m} \right\} \\
& + \int d\phi_0 \int \cdots \int \mathcal{O}(S_{+Mj}) \left\{ \bar{B}_M + [\hat{B}_M]_{-M,M+1} - \sum_{i=M+1}^N \int_s \hat{B}_{i \rightarrow M} \right\} \\
& + \sum_{n=M+1}^N \int d\phi_0 \int \cdots \int \mathcal{O}(S_{+nj}) \left\{ \hat{B}_n - \sum_{i=n+1}^N \int_s \hat{B}_{i \rightarrow n} \right\}. \quad (\text{III.41})
\end{aligned}$$

The notation is defined in [35]. For this study, $M = 2$ and $N = 3$. The POWHEGBOX generator [26] is used to produce the inclusive NLO samples \bar{B}_0 [363], \bar{B}_1 and \bar{B}_2 [364], while additional tree-level inputs are taken from MADGRAPH/MADEVENT [355,365]. The merging scale criterion (see Appendix A.1 of [35]) is used to remove infrared divergences due to additional jets at Born level. This cut is applied internally in PYTHIA 8, so that no user interference with e.g. the POWHEGBOX source code becomes necessary. All input samples are computed with fixed scales μ_F and μ_R . Terms of $\mathcal{O}(\alpha_s^{n+2})$ and higher due to running scales are included, in a controlled way, by reweighting tree-level samples with factors to produce the CKKW-L [366–368] scale setting prescription.

This NLO merging scheme replaces the approximate α_s^{n+1} -terms of the UMEPS tree-level merging method with the desired full fixed-order expressions, but otherwise leaves higher-order corrections untouched. Particularly, no higher-order terms are introduced by reweighting virtual corrections. Note further that the method keeps the inclusive cross section fixed to the zero-jet

¹⁰ See `Pythia8/examples/main31`.

NLO cross section, without producing spurious logarithmic artifacts of the merging procedure, and without introducing additional finite terms.

To produce results, we generate fixed-order input events with POWHEGBOX and MADEVENT at $E_{\text{CM}} = 8$ TeV, using CT10nlo [233, 289] parton distributions, massless b-quarks, vanishing coupling between b-quarks and Higgs-boson and a stable Higgs-boson of mass $m_h = 125$ GeV. We define the merging scale as the minimal relative shower $p_{\perp\text{evol}}$ and use a merging scale value of $\rho_{\text{ms}} = 15$ GeV. The samples are merged within PYTHIA 8.180. PYTHIA 8 is run with Tune AU2-CTEQ6L1 [362], which uses CTEQ6L1 [251] parton distributions. Masses and widths are, naturally, set equal in POWHEGBOX, MADEVENT and PYTHIA 8. We assess uncertainties by producing two sets of variations:

- Parton shower variation: Use POWHEGBOX and MADEVENT inputs generated with $\mu_F = \mu_R = m_h$, and choose the PYTHIA 8 starting scale μ_Q for adding emissions to zero-parton events as $\mu_{Q,\text{low}} = \frac{1}{2} m_h$, $\mu_{Q,\text{central}} = m_h$ or $\mu_{Q,\text{high}} = 2 m_h$. Construct an envelope from the results of these variations. Only the starting scale for adding emissions to zero-parton events can be varied, as the starting scale for showering $n \geq 1$ -parton events is locked by the CKKW-L prescription.
- Matrix element variation: Vary the renormalisation and factorisation scales in POWHEGBOX and MADEVENT as $\mu_{F,\text{low}} = \mu_{R,\text{low}} = \frac{1}{2} m_h$, $\mu_{F,\text{central}} = \mu_{R,\text{central}} = m_h$ or $\mu_{F,\text{high}} = \mu_{R,\text{high}} = 2 m_h$, keep the PYTHIA 8 starting scale μ_Q for adding emissions to zero-parton events fixed at $\mu_Q = m_h$. Construct an envelope from the results of the variations.

We do not attempt a more complete uncertainty study including variation of renormalisation and factorisation scales in the parton shower, mainly because we have not decided on a strategy of how to deal with such uncertainties, and other fixed-order uncertainties, in the context of parton shower resummation and tuning. However, the envelope of the uncertainty bands presented here should, for most cases, yield a reasonably conservative estimate. Also, for this perturbative-physics driven study, we do not address the (potentially important) uncertainties due to non-perturbative modelling in the event generator.

6.2.5 Sherpa

The SHERPA event generator implements the MEPS@NLO [30, 369] technique to merge multiple NLOPS matched [29] samples of successive jet multiplicities into an inclusive calculation that retains both the NLO accuracy for every individual jet multiplicity and the parton shower’s resummation properties in resumming emission scale hierarchies wrt. inclusive process. This implementation has already been successfully applied to various background processes to Higgs production channels [370, 371]. Also Higgs production through gluon fusion has been studied in detail with this approach recently [372].

For the contribution to this comparative study the subprocesses $pp \rightarrow h+0$ jets, $pp \rightarrow h+1$ jet and $pp \rightarrow h+2$ jets are calculated at next-to-leading order and $pp \rightarrow h+3$ jets at leading order accuracy. The one-loop matrix elements are taken from [373, 374], [375, 376] and [44, 356], respectively. The LO $pp \rightarrow h+3$ jets process, as it is merged on top of the NLO $pp \rightarrow h+2$ jets process by the MENLOPS method [369], receives a local K -factor in dependence of the $pp \rightarrow h+2$ jets composition in terms of \mathbb{S} - and \mathbb{H} -events. For the central prediction, the individual jet multiplicities were separated by $Q_{\text{cut}} = 20$ GeV. The renormalisation and factorisation scales were set according to the CKKW prescription, i.e. $\alpha_s^{2+n}(\mu_R) = \alpha_s(m_h^2) \alpha_s(t_1) \cdots \alpha_s(t_n)$ and $\mu_F = m_h$ for the core process. The parton shower starting scale μ_Q was set to m_h . Throughout, the CT10nlo [233, 289] PDF set was used.

The uncertainties on the central prediction were estimated by varying μ_R and μ_F independently by the customary factor of two and the parton shower starting scale by a factor $\sqrt{2}$.

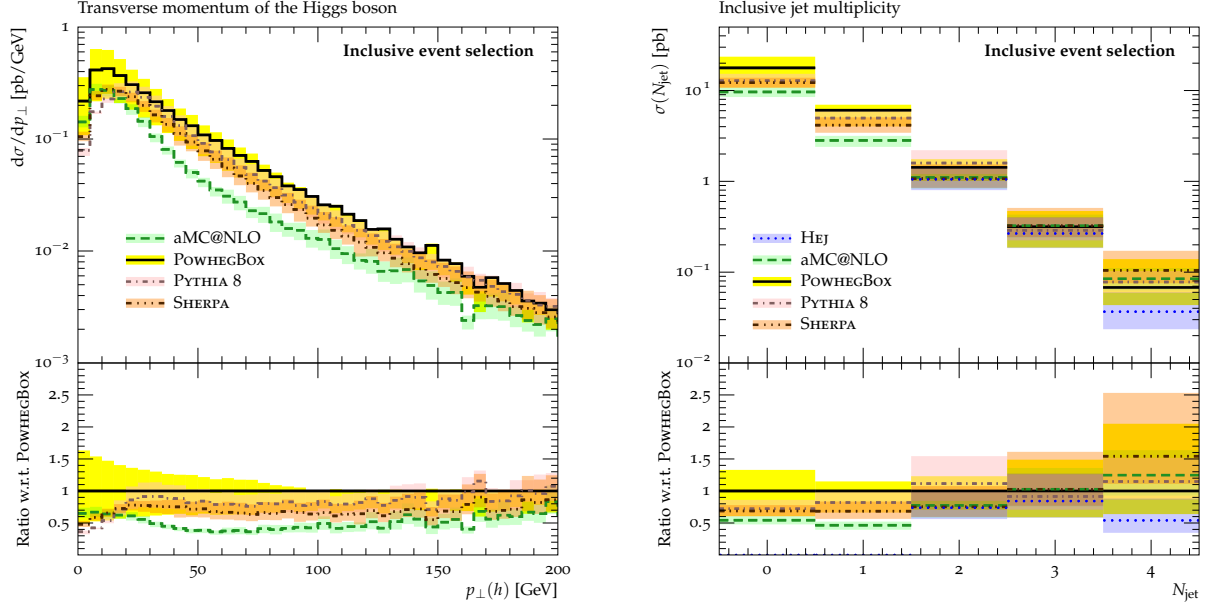


Fig. III.24: Transverse momentum of the Higgs boson (left) and inclusive jet multiplicity (right) as predicted by the different generators. The individual sources of uncertainties used to generate the respective bands are described in Sec. 6.2. Note that for POWHEGBOX the MiNLO-HJJ prediction has been used throughout, despite its lowered accuracy for inclusive and one-jet observables, for consistencies sake.

The merging scale was varied in the range $\{15, 20, 30\}$ GeV. Further, the intrinsic parton shower uncertainties were estimated by varying the evolution variable and the recoil scheme according to [372]. Non-perturbative uncertainties which may very well play a role in analyses looking into hadronic activity within jets widely separated in rapidity [377, 378] are not assessed in this study.

6.3 RESULTS

This study aims at quantifying the gluon fusion contribution and its perturbative uncertainty to typical VBF Higgs plus two jets event selections at the LHC at a centre-of-mass energy of 8 TeV. To summarise Sec. 6.2, the following parameters were then varied to estimate the respective generator’s uncertainty:

$$\begin{aligned}
 \text{HEJ:} & \quad \mu_R, \mu_F \in [\tfrac{1}{2}, 2] \text{ separately} \\
 \text{aMC@NLO:} & \quad \mu_R, \mu_F \in [\tfrac{1}{2}, 2] \\
 \text{POWHEGBOX:} & \quad \mu_R, \mu_F \in [\tfrac{1}{2}, 2] \text{ separately, SCALEUP} \in [0.75, 1.5] \\
 \text{PYTHIA 8:} & \quad \mu_R, \mu_F \in [\tfrac{1}{2}, 2], \mu_Q \in [\tfrac{1}{\sqrt{2}}, \sqrt{2}] \\
 \text{SHERPA:} & \quad \mu_R, \mu_F \in [\tfrac{1}{2}, 2] \text{ separately, } \mu_Q \in [\tfrac{1}{\sqrt{2}}, \sqrt{2}], Q_{\text{cut}} \in [15, 20, 30]
 \end{aligned}$$

A common RIVET [379, 380] analysis implementing the observables for the event selections described below has been used. This analysis is inclusive with respect to the Higgs, i.e. there are no phase space cuts on the Higgs and all decay channels are included. Concerning the presence of additional jets the analysis defines several stages of cuts.

First we study the transverse momentum of the Higgs boson for inclusive Higgs production as obtained in the shower based approaches to study the overall consistency of their fixed-order and resummation properties. The results are shown in Fig. III.24 on the left hand side. POWHEGBOX, PYTHIA 8 and SHERPA are compatible within uncertainties, where POWHEGBOX

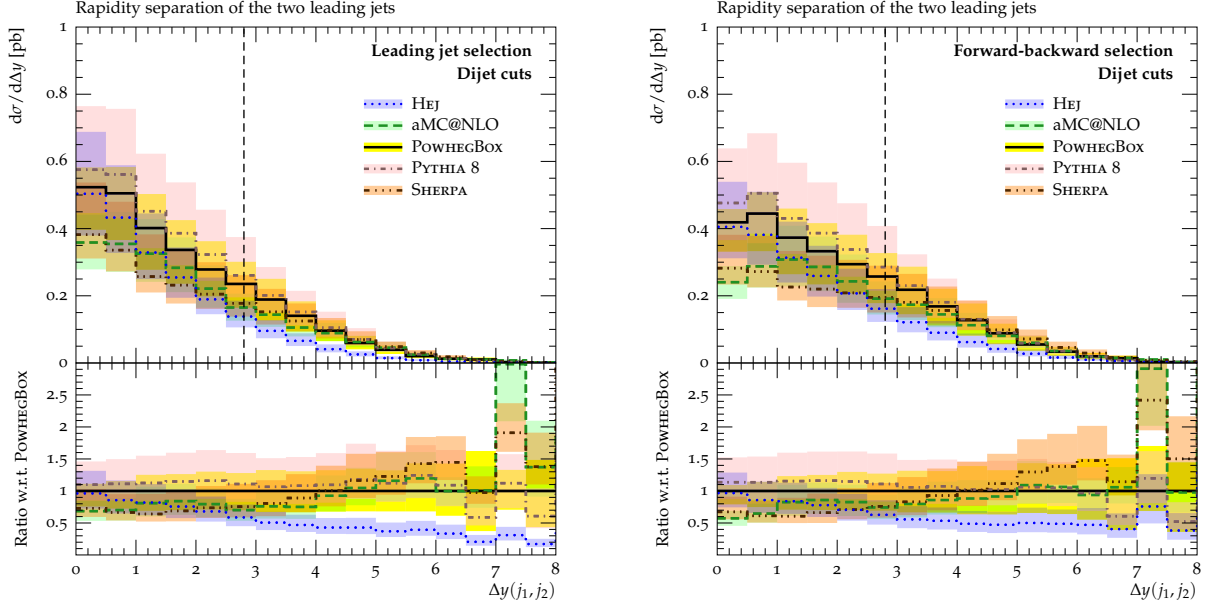


Fig. III.25: Rapidity difference of both tagging jets in the leading jet selection (left) and the forward-backward selection (right) as predicted by the different generators. The individual sources of uncertainties used to generate the respective bands are described in Sec. 6.2. The location of the VBF cut is indicated.

reports somewhat larger central values and uncertainties due to the usage of the `MinLO-HJJ`¹¹, cf. Tab. III.3. `aMC@NLO` has a similar description of the Sudakov region but its predictions fall below those of the other generators for larger transverse momenta. `HEJ` generates at least two jets and thus is not included in the comparison for this observable.

The following observables all depend on the presence of at least one jet. Jets are reconstructed using the anti- k_t algorithm provided by `FASTJET` [283] with radius parameter $R = 0.4$ within the pseudo-rapidity range $|\eta| < 5$ and are required to have a minimal transverse momentum of $p_{\perp} > 30$ GeV. The predictions for the number of jets, shown in Fig. III.24 on the right hand side, are largely consistent, only `aMC@NLO` has somewhat less cross section in the zero- and one-jet inclusive bins. The inclusive dijet cross section is consistent within uncertainties for all generators. From here on, as a minimum of two jets accompanying the Higgs are always required, the `HEJ` prediction is included and it is found to be in good agreement with the shower based approaches. For the higher inclusive jet multiplicities the spread and also the uncertainties are significantly larger. This is expected, as the theoretical accuracy decreases there for all generators. This is especially true for the inclusive four jet rate since – with the exception of `HEJ` – the fourth jet comes from the parton shower only.

For the Higgs+dijet selection two alternatives are considered: In the *leading jet selection* the two hardest jets in the event constitute the tagging jets, while in the *forward-backward selection* the most forward and the most backward (in rapidity) jet are defined as tagging jets. For events with exactly two jets the two selections are obviously identical, for events with more than two jets they can differ. This general dijet selection defines the second level of cuts. The third level is a VBF-like selection in which the two tagging jets are required to have a rapidity separation $\Delta y(j_1, j_2) > 2.8$ and a large invariant mass $m_{jj} > 400$ GeV. The invariant mass and rapidity separation of the tagging jets are shown in Figs. III.25 and III.26, respectively, for

¹¹ As this study focusses on $pp \rightarrow h + 2$ jets topologies `MinLO-HJJ` is used throughout despite its reduced uncertainty for more inclusive observables for consistencies sake.

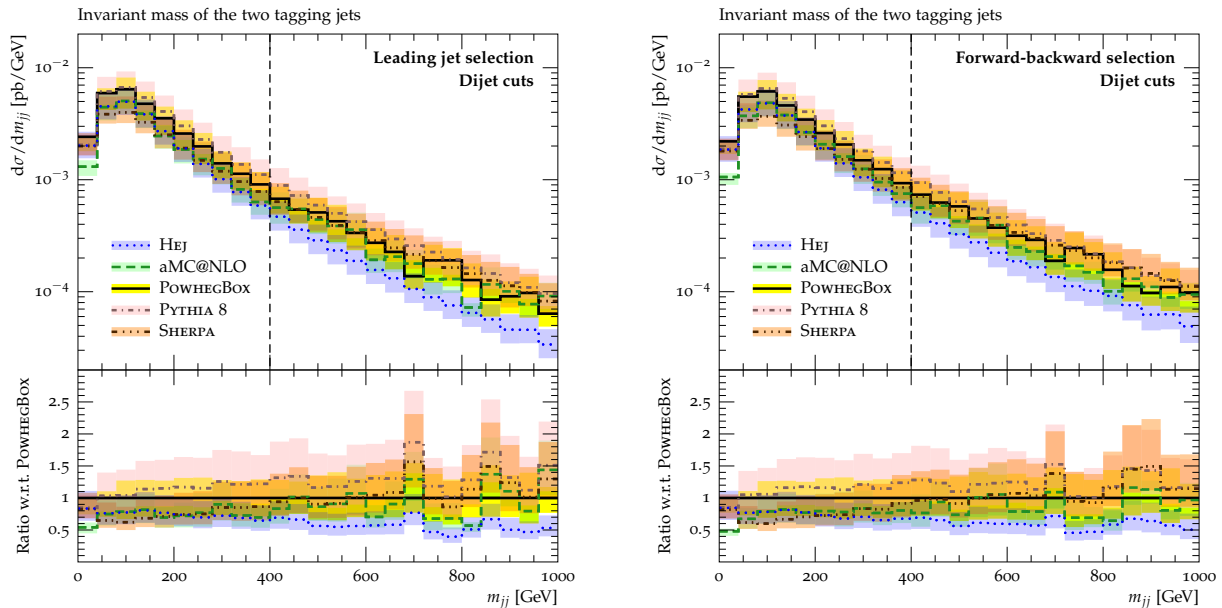


Fig. III.26: Invariant mass of both tagging jets in the leading jet selection (left) and the forward-backward selection (right) as predicted by the different generators. The individual sources of uncertainties used to generate the respective bands are described in Sec. 6.2. The location of the VBF cut is indicated.

both dijet selections before the VBF cuts. As expected, the rapidity separation between the two tagging jets, Fig. III.25, is larger in the forward-backward than in the leading jet selection. In this observable differences between the generators become visible: While POWHEGBOX and PYTHIA 8 are consistent in shape but differ slightly in normalisation, SHERPA and aMC@NLO predict significantly more cross section at large Δy but also differ in normalisation. A possible origin of such differences within the parton shower based event generators is the behaviour of their respective parton shower, which affects distributions both explicitly by radiating additional partons and (for some approaches) through the computation of Sudakov form factors. The slightly higher cross section in the PYTHIA 8 prediction can, for example, be traced to the high value of α_s in Tune AU2-CTEQ6L1. HEJ, on the contrary, falls off faster at large Δy . This can be understood from the systematic resummation of virtual correction in $\log \frac{s}{t}$ which become important at large Δy . In the leading jet selection there is the additional effect that when jets are produced at large rapidity differences the void in between them tends to be filled with additional hard jets unordered in p_\perp . These differences are, however, partially covered by the uncertainties.

The invariant mass distribution is almost identical in the two dijet selections. The predictions are all consistent in shape but differ somewhat in normalisation with PYTHIA 8 at the upper and HEJ on the lower end of the normalisation spectrum. Noteworthy is that SHERPA, and to some extent also PYTHIA 8, predicts more cross section at larger m_{jj} than the other generators, while HEJ predicts slightly less. Here a discussion of how the aMC@NLO, POWHEGBOX, PYTHIA 8 and SHERPA treat configurations with at least three jets which make up a large fraction of the events in the high invariant mass as well as the large Δy regions, seems expedient. Treating three jet configurations as a separate contribution, as is the case in PYTHIA 8 and SHERPA, leads to assigning them a renormalisation scale defined through $\alpha_s^{2+3}(\mu_R) = \alpha_s^2(m_h) \alpha_s(t_1) \alpha_s(t_2) \alpha_s(t_3)$ for ordered jet emissions in the CKKW approach (t_i being the reconstructed emission/clustering scales of the respective approach) whereas treating three jet configurations as real emission corrections to the underlying two jet configuration

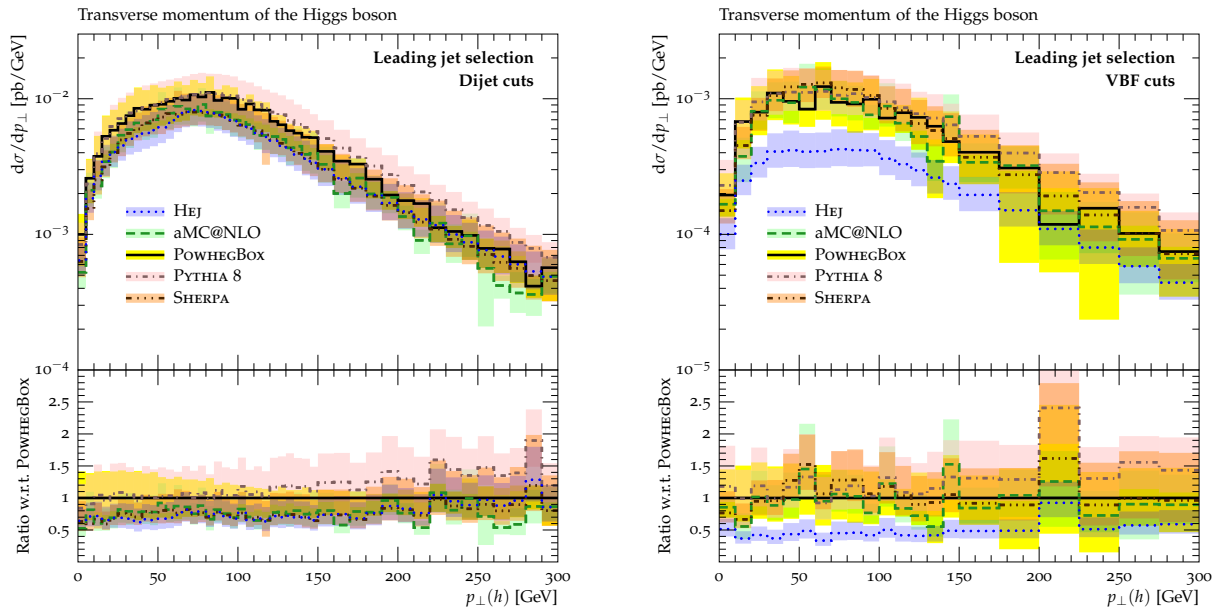


Fig. III.27: Transverse momentum of the Higgs boson produced in association with two jets before (left) and after (right) the application of the VBF selection cuts in the leading jet selection as predicted by the different generators. The individual sources of uncertainties used to generate the respective bands are described in Sec. 6.2.

would result in assigning them a coupling $\alpha_s^{2+3}(\mu_R)$ where the renormalisation scale is defined through that underlying two jet configuration as $\alpha_s^{2+2}(\mu_R) = \alpha_s^2(m_h) \alpha_s(t_1) \alpha_s(t_2)$. Though the difference is of higher order, the latter definition clearly leads to higher values of μ_R in most cases, and therefore lower cross sections. However, note that this simple picture is significantly muddled and partly remedied by the treatment of the real emission configuration in POWHEG-like approaches and the interplay of \mathbb{S} - and \mathbb{H} -events in MC@NLO-like calculations. In case of HEJ, the slight depletion of the cross section at large m_{jj} is also closely related to that at large Δy : instigated by the filling of large rapidity intervals through emissions unordered in transverse momentum leads to a potentially different selection of tagging jets. In conclusion, however, despite all differences in the respective calculations, the resulting predictions are largely covered by the uncertainties. Still, the differences seen for Δy and m_{jj} have a non-negligible effect on the efficiency of the VBF cuts, as seen in the following.

The Higgs transverse momentum in the leading jet selection before and after VBF cuts is displayed in Fig. III.27. It comes out to be very similar in between the different generators, again except for small differences in the normalisation. Only the predictions of POWHEGBOX seem to have a slight tilt as compared to the other generators before and after VBF cuts. Noteworthy is also that while the cross sections after VBF cuts are largely in agreement among aMC@NLO, POWHEGBOX, PYTHIA 8 and SHERPA the cross section predicted by HEJ now drops outside the uncertainties of the parton shower based approaches. This is a result of a trend already seen on Fig. III.25.

Fig. III.28 shows the transverse momentum distribution of the system consisting of the Higgs boson and the two tagging jets in the leading jet selection, again before and after VBF cuts. The results are largely compatible within the uncertainties, with PYTHIA 8 and SHERPA predicting a harder spectrum than aMC@NLO, POWHEGBOX or HEJ. Again, as this distribution is dominated by three jet topologies, this can be understood by the same reasoning as for Fig. III.26. HEJ does not exhibit the typical Sudakov shape with a maximum around 25 GeV as it

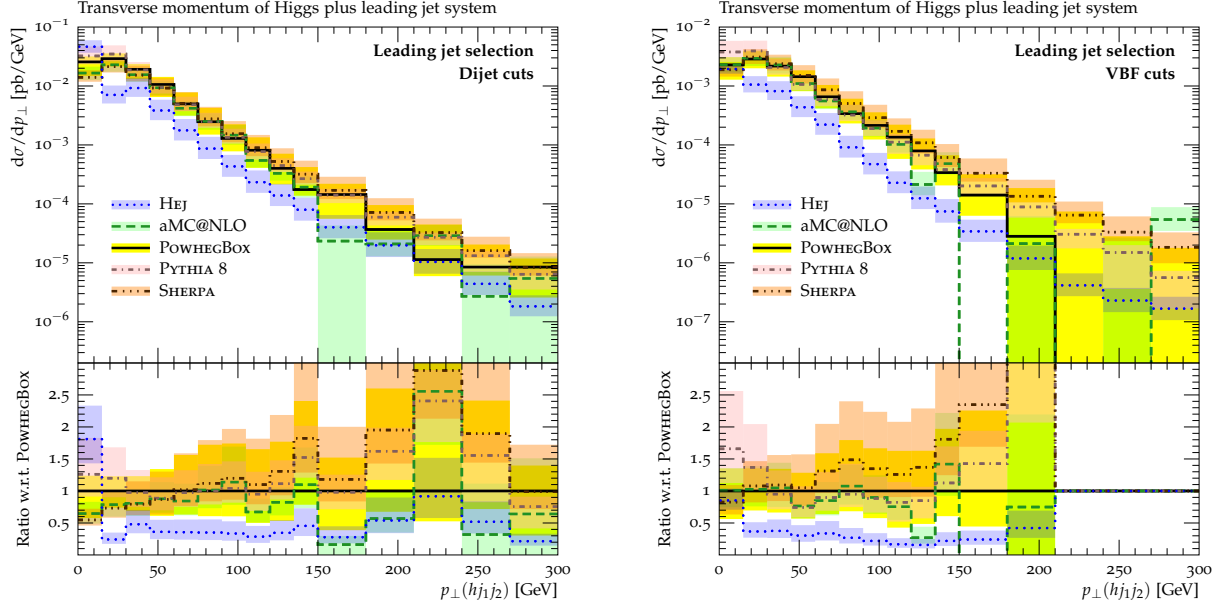


Fig. III.28: Transverse momentum of the Higgs boson plus tagging jets system before (left) and after (right) the application of the VBF selection cuts in the leading jet selection as predicted by the different generators. The individual sources of uncertainties used to generate the respective bands are described in Sec. 6.2.

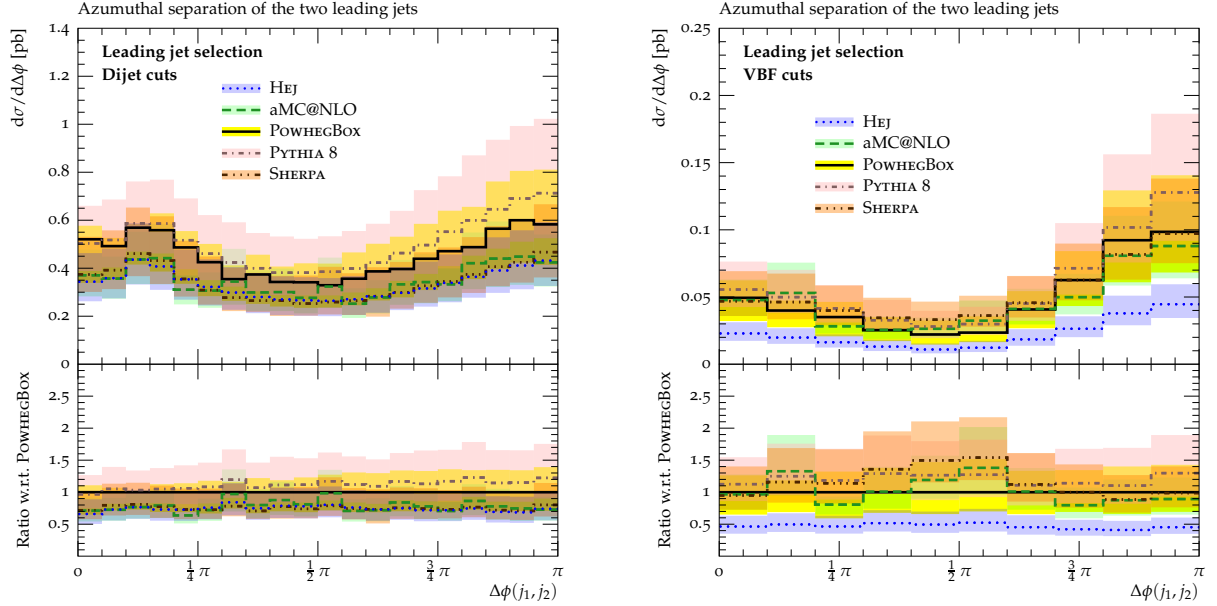


Fig. III.29: Azimuthal separation of the tagging jets before (left) and after (right) the application of the VBF selection cuts in the leading jet selection as predicted by the different generators. The individual sources of uncertainties used to generate the respective bands are described in Sec. 6.2.

is not matched to a parton shower and, therefore, does not contain DGLAP resummation.

In the case of the azimuthal separation between the tagging jets, shown again for the leading jet selection before and after VBF cuts in Fig. III.29, the shapes are very similar before the VBF cuts. But after VBF cuts SHERPA, and to a lesser extent aMC@NLO, predict slightly more cross section in the region $\Delta\phi(j_1, j_2) \sim \pi/2$, whereas PYTHIA 8 predicts slightly more

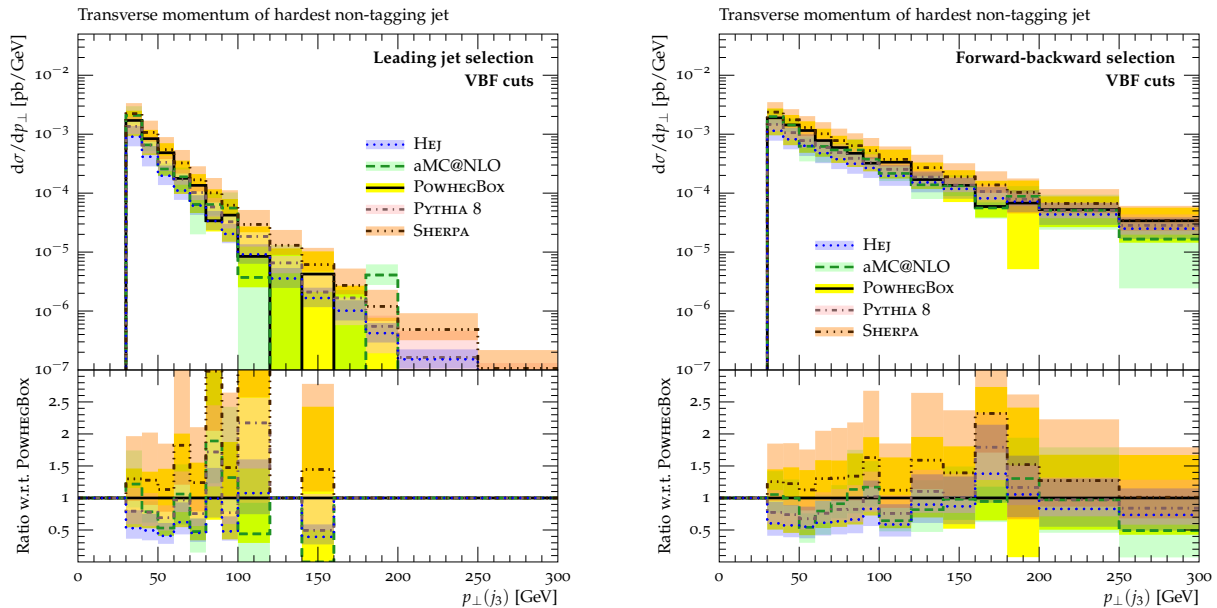


Fig. III.30: Transverse momentum of the hardest non-tagging jet in the leading jet selection (left) and the forward-backward selection (right) after VBF cuts as predicted by the different generators. The individual sources of uncertainties used to generate the respective bands are described in Sec. 6.2.

events in the back-to-back region than the other generators. The PYTHIA 8 result can to some extent again be attributed to the usage of CTEQ6L1 PDFs and its rather high α_s -value in Tune AU2-CTEQ6L1 used for its parton showering.

Fig. III.30 displays the transverse momentum of the hardest non-tagging jets after VBF cuts for both the leading jet and the forward-backward selection. Naturally, in the forward-backward selection, not necessarily taking the two hardest jets as tagging jets, the p_\perp of this third jet is much higher than in the leading jet selection. All generators predict roughly similar shapes for both distributions, but at very different rates. SHERPA predicts the largest cross-section for such events containing at least three jets, followed by aMC@NLO and POWHEGBOX, while PYTHIA 8 and HEJ predict the lowest rates.

Finally, the cross sections at the different selection levels are summarised in Tabs. III.4 and III.5. While good agreement is found for inclusive $pp \rightarrow h + 2$ jets production, as already seen in the distributions, the cross sections in HEJ are generally smaller than those predicted by the other generators once VBF cuts are applied. This can be understood by the difference in the description of additional hard radiation from an underlying configuration. While all generators largely agree for the observables before VBF cuts within their respective uncertainties, both POWHEGBOX and PYTHIA 8 are significantly higher than either aMC@NLO, SHERPA or HEJ. The differences to HEJ are larger for the additional requirement of having the Higgs boson produced within the tagging jets (in rapidity).

After VBF cuts the picture is slightly changed, emphasising their different efficiencies across the generators. The effect of the cuts on predictions of HEJ is larger by a factor of 1.5-2 as compared to the parton shower based generators. This is again understood from the effects seen in Fig. III.25. The cross sections predicted by the parton shower based approaches are in somewhat better agreement than before this set of additional cuts, though their respective uncertainties have increased in some cases, especially in the forward-backward selection. The probability to also find the Higgs boson in between both tagging jets now is substantially increased. This nicely illustrates the effect of the VBF cuts shaping the $pp \rightarrow h + 2$ jets events

Cross sections in the leading jet selection

| Generator | σ_{dijet} [pb] | σ_{dijet} [pb] | σ_{VBF} [pb] | σ_{VBF} [pb] | σ_{VBF} [pb] |
|-----------|------------------------------|---|----------------------------|---|---|
| | | $y_{j_{\text{bw}}} < y_h < y_{j_{\text{fw}}}$ | | $y_{j_{\text{bw}}} < y_h < y_{j_{\text{fw}}}$ | $y_{j_{\text{bw}}} < y_{j_3} < y_{j_{\text{fw}}}$ |
| HEJ | $1.053^{+0.374}_{-0.253}$ | $0.337^{+0.107}_{-0.075}$ | $0.070^{+0.025}_{-0.017}$ | $0.057^{+0.019}_{-0.013}$ | $0.0177^{+0.0092}_{-0.0055}$ |
| aMC@NLO | $1.106^{+0.316}_{-0.272}$ | $0.440^{+0.125}_{-0.109}$ | $0.149^{+0.051}_{-0.039}$ | $0.131^{+0.044}_{-0.035}$ | $0.0338^{+0.0114}_{-0.0088}$ |
| POWHEGBOX | $1.426^{+0.328}_{-0.415}$ | $0.583^{+0.178}_{-0.181}$ | $0.154^{+0.050}_{-0.048}$ | $0.135^{+0.043}_{-0.042}$ | $0.0345^{+0.0165}_{-0.0167}$ |
| PYTHIA 8 | $1.590^{+0.612}_{-0.385}$ | $0.650^{+0.262}_{-0.162}$ | $0.183^{+0.083}_{-0.049}$ | $0.160^{+0.072}_{-0.043}$ | $0.0277^{+0.0110}_{-0.0071}$ |
| SHERPA | $1.073^{+0.462}_{-0.225}$ | $0.422^{+0.185}_{-0.082}$ | $0.165^{+0.071}_{-0.039}$ | $0.138^{+0.061}_{-0.033}$ | $0.0461^{+0.0265}_{-0.0126}$ |

Table III.4: Cross section for $pp \rightarrow h + 2$ jet production within the dijet and VBF cuts as predicted by the different generators in the *leading jet* selection. Additionally the cross sections with the additional requirement that the Higgs boson is produced in between both tagging jets or that a third jet is present and between both tagging jets are given. $y_{j_{\text{fw}}}$ and $y_{j_{\text{bw}}}$ are the rapidities of the forward and the backward tagging jet. The individual sources of uncertainties used to generate the respective bands are described in Sec. 6.2.

Cross sections in the forward-backward selection

| Generator | σ_{dijet} [pb] | σ_{dijet} [pb] | σ_{VBF} [pb] | σ_{VBF} [pb] | σ_{VBF} [pb] |
|-----------|------------------------------|---|----------------------------|---|---|
| | | $y_{j_{\text{bw}}} < y_h < y_{j_{\text{fw}}}$ | | $y_{j_{\text{bw}}} < y_h < y_{j_{\text{fw}}}$ | $y_{j_{\text{bw}}} < y_{j_3} < y_{j_{\text{fw}}}$ |
| HEJ | $1.053^{+0.374}_{-0.253}$ | $0.384^{+0.130}_{-0.089}$ | $0.103^{+0.044}_{-0.028}$ | $0.086^{+0.035}_{-0.022}$ | $0.0585^{+0.0323}_{-0.0190}$ |
| aMC@NLO | $1.106^{+0.316}_{-0.272}$ | $0.512^{+0.147}_{-0.127}$ | $0.183^{+0.058}_{-0.047}$ | $0.163^{+0.050}_{-0.041}$ | $0.0796^{+0.0237}_{-0.0198}$ |
| POWHEGBOX | $1.426^{+0.328}_{-0.415}$ | $0.658^{+0.199}_{-0.214}$ | $0.197^{+0.068}_{-0.068}$ | $0.177^{+0.060}_{-0.061}$ | $0.0878^{+0.0472}_{-0.0394}$ |
| PYTHIA 8 | $1.590^{+0.612}_{-0.385}$ | $0.716^{+0.282}_{-0.175}$ | $0.220^{+0.093}_{-0.055}$ | $0.195^{+0.082}_{-0.049}$ | $0.0726^{+0.0288}_{-0.0173}$ |
| SHERPA | $1.073^{+0.462}_{-0.225}$ | $0.499^{+0.229}_{-0.099}$ | $0.218^{+0.102}_{-0.052}$ | $0.189^{+0.091}_{-0.045}$ | $0.1129^{+0.0656}_{-0.0296}$ |

Table III.5: Cross section for $pp \rightarrow h + 2$ jet production within the dijet and VBF cuts as predicted by the different generators in the *forward-backward* selection. Additionally the cross sections with the additional requirement that the Higgs boson is produced in between both tagging jets or that a third jet is present and between both tagging jets are given. $y_{j_{\text{fw}}}$ and $y_{j_{\text{bw}}}$ are the rapidities of the forward and the backward tagging jet. The individual sources of uncertainties used to generate the respective bands are described in Sec. 6.2.

into a VBF-like topology with a large rapidity span that is very likely to contain the Higgs. The probability to find another jet in between the tagging jets again shows larger variability among the generators, as was already observed in Fig. III.30. Here in both selections SHERPA predicts the largest rates whereas those of HEJ and PYTHIA 8 are the smallest.

It is interesting to observe that as, by construction, the rapidity span is larger in the forward-backward selection than in the dijet selection, not only is the cross section after VBF cuts enlarged, but also have both the probability to find the Higgs and to find an additional jet

in between the two tagging jets increased. In particular the latter is interesting in the context of using jet vetoes to suppress the gluon fusion contribution to VBF-like signatures. This possibility is not studied here, as it also requires careful treatment of the underlying event, which can also produce additional jets.

The full set of observables studied can be found at <http://phystev.in2p3.fr/wiki/2013:groups:sm:higgs:hdijetsresults>.

6.4 CONCLUSIONS

The aim of this study was to quantify the gluon fusion contribution to $h + 2$ jets with a VBF-like signature and its uncertainties. The strategy was to obtain state-of-the-art NLO or multi-jet merged NLO predictions from the event generators HEJ, aMC@NLO, POWHEGBOX, PYTHIA 8 and SHERPA including perturbative uncertainties and do a detailed comparison of both rates and distributions. The events were analysed with a common, generic Higgs analysis. Distributions are plotted at different levels of cuts going from inclusive Higgs via Higgs+dijet to a VBF-like selection.

The gluon fusion contribution to Higgs events with a VBF-like signature turns out to be of the order of 0.1-0.2 pb and is thus non-negligible. This is especially relevant as observables such as $\Delta\phi(j_1, j_2)$ exhibit different shapes in Higgs production through gluon fusion as opposed to production through weak-boson fusion, diluting characteristic patterns used to measure Higgs properties. The predictions by the NLO event generators are in good agreement with one-another within their respective uncertainty estimates. In all cases (except for aMC@NLO) all sources of perturbative uncertainties, stemming from the fixed-order cross-section input, the matched parton shower resummation (in the form of its starting scale), and, where applicable, also the unphysical multijet merging parameter, were accounted for. Additional uncertainties originating in the parton shower splitting functions (evolution variables, choice of the scales of the strong coupling, recoil schemes) are current topics of investigation.

The differences in cross section are reflected in the normalisation of the distributions. The shapes are largely consistent. PYTHIA 8 and SHERPA have been observed to have a tendency to predict slightly harder transverse momentum spectra, but these differences are mostly covered by the reported uncertainties.

Although it is reassuring that the predictions by different generators are generally consistent, the uncertainties remain rather large. Taking the perturbative uncertainties reported by the generators and the spread of the predictions seriously, one arrives at an uncertainty estimate on the cross section that is roughly a factor 2. One possible avenue for the reduction of these uncertainties is the experimental study of the VBF phase space on various signal processes, e.g. [381], to constrain the models. It is further important to note that this study only investigated perturbative uncertainties. Nonperturbative uncertainties stemming from the modelling of the parton-to-hadron fragmentation and especially multiple parton interaction, however, may also play an important role in analyses with gap fractions [377].

Acknowledgements

We would like to thank the organisers of Les Houches 2013 for repeatedly hosting such a fantastic and fruitful workshop. We would also like to thank all participants for a lively and stimulating atmosphere and lots of inspiring discussions.

KH gratefully acknowledges support from Durham University IPPP through their associateship program. TH's and MS's work was supported by the Research Executive Agency (REA) of the European Union under the Grant Agreement number PITN-GA-2010-264564 (LHCPhenoNet). MS further acknowledges support by PITN-GA-2012-315877 (MCnet). JMS is funded

by a Royal Society University Research Fellowship.

7 Higgs boson plus di- and tri-jet production at NLO in QCD¹²

7.1 Introduction

Among the different production mechanisms of a Higgs boson (H) within the Standard Model, Gluon-Gluon Fusion (GGF) via a virtual top-quark loop is the one with the largest cross section at the Large Hadron Collider (LHC). Although direct measurements of the Higgs boson properties in this channel, without applying any vetoes on additional jets, are difficult due to the large QCD background, precise theoretical predictions for the associate production of a Higgs boson and jets in GGF are important for several aspects. On the one hand the possibility to reliably estimate the theoretical uncertainty when a jet veto is applied heavily relies on the knowledge of inclusive and exclusive cross sections for Higgs boson production and additional jets, on the other hand the production of a Higgs boson together two jets in GGF is one of the main irreducible backgrounds to the production of a Higgs boson in Vector Boson Fusion (VBF), which allows to directly probe the coupling of the Higgs boson to other electroweak bosons.

The leading order (LO) contribution to the production of a Higgs boson in association with two jets ($H+2$ -jets) and three jets ($H+3$ -jets), retaining the full top-mass (m_t) dependence, have been computed respectively in Refs. [382, 383], and Ref. [384]. These calculations showed that large top-mass approximation ($m_t \rightarrow \infty$) is valid whenever the mass of the Higgs particle and the p_T of the jets are not much larger than the mass of the top quark. In the results presented here we adopt this approximation and introduce a set of effective vertices, which directly couple the Higgs particle to two, three and four gluons [373, 374]. Feynman rules for these vertices can be found e.g. in Ref. [385]. The next-to-leading order (NLO) corrections for $H+2$ -jets in GGF at LHC were first computed in Ref. [44, 356] using amplitudes computed in Refs. [349, 386–396]. These amplitudes have been also used to obtain matched NLO plus shower predictions [364, 372]. More recently they have been recomputed using for the first time an automated tool for the evaluation of both tree-level and loop amplitudes in Ref. [385]. A similar setup was also used to compute the first NLO results for $H+3$ -jets in GGF [3].

In these proceedings we present some new results for $H+3$ -jets at NLO to which we applied a set of ATLAS-like cuts, and compare it with predictions for $H+2$ -jets at NLO. In Section 7.2 the computational setup used to obtain the various predictions is presented. Compared to the original setup used in Ref. [3], here the newest developments regarding the evaluation of loop amplitudes with integrand reduction techniques based on Laurent expansion were used [397]. In Section 7.3 we present our results and discuss them. They include predictions for the total cross sections and for several relevant distributions, together with scale uncertainty bands.

7.2 Computational details

All parton-level predictions, which we present in these proceedings, have been produced by combined generator packages. The $H+2$ -jets samples were obtained with the GOSAM+SHERPA package while those describing $H+3$ -jets production required the combination of contributions from GOSAM+SHERPA and the MADGRAPH/DIPOLE/EVENT framework. More specifically, the $H+3$ -jets samples were built from the Born plus virtual (BV) terms as provided by GOSAM+SHERPA and the dipole-subtracted real emission (RS) contribution as well as the integrated subtraction terms (I) as produced by MADGRAPH/DIPOLE/EVENT. We checked the consistency of our hybrid MC integration for $H+3$ -jets on $H+2$ -jets, verifying that the full cross section at NLO agrees with the corresponding result for the integration of all contributions

¹²G. Cullen, H. van Deurzen, N. Greiner, J. Huston, G. Luisoni, P. Mastrolia, E. Mirabella, G. Ossola, T. Peraro, F. Tramontano, J. Winter and V. Yundin

(BVIRS) obtained with GOSAM+SHERPA alone. Moreover, for $H+3$ -jets we found excellent agreement between MADGRAPH and SHERPA for the LO cross section.

7.2.1 *Virtual amplitudes*

The virtual 1-loop amplitudes are generated and computed using the GOSAM framework [4], which combines the algebraic generation of d -dimensional integrands via Feynman diagrams [398–401], with the numerical evaluation based upon integrand-reduction [397, 402–407], as implemented in SAMURAI [397, 408–410] and NINJA [397, 411–413] and tensor integral calculus, as implemented in GOLEM95 [414, 415].

The virtual amplitudes for the production of Higgs plus two- and three-jets presented in Ref. [385] and Ref. [3] respectively, were obtained by using the SAMURAI reduction library. For the results presented here, instead, GOSAM was used to generate the input for the new library NINJA [411], which computes the loop amplitude using a novel technique based on the interplay of the reduction at the integrand level and the Laurent expansion of the numerator [397], and proved to be in general faster and more stable compared to the standard integrand reduction method [412]. In fact, by employing NINJA, the evaluation time per phase-space point reduced by a factor of 50%, and the fraction of unstable point dropped below the permille level. The scalar loop integrals are computed using ONELOOP [416].

In order to deal with the complexity of the amplitudes of the processes computed here, several improvements were introduced into GOSAM. They will become public with the release of the new version of the program, whose final development is currently in progress. Among the improvements, there is the possibility to exploit the optimized manipulation of polynomial expressions available in FORM 4.0 [417].

The one-loop amplitudes for Higgs production in GGF containing the effective ggH coupling lead to integrands that may exhibit numerators with rank larger than the number of the denominators. More details about the treatment of these so-called higher-rank integrals can be found in Refs. [3, 385, 410, 415].

7.2.2 *GoSam+Sherpa specifics*

Within SHERPA [166] the tree amplitudes for the Born contributions and real corrections were obtained using the automatic amplitude generator AMEGIC [418], which also automatically generates the subtraction terms and their integrated counterpart using an implementation [419] of the Catani-Seymour dipoles subtraction [200]. The integration of the virtual amplitudes was also performed using SHERPA. The amplitudes generated with GOSAM were interfaced to SHERPA via the Binot-Les-Houches Accord (BLHA) [198, 199], which sets the standards for the communication between a Monte Carlo program and a One Loop Program, and allows to generate and link the two codes fully automatically. The integration of the $H+3$ -jets amplitudes is carried out by generating $\mathcal{O}(10^6)$ events, sampled on a MC grid trained on the Born matrix element, and weighted with the sum of the Born and the virtual amplitudes.

7.2.3 *MadGraph/Dipole/Event specifics*

In the MADGRAPH setup the tree-level amplitudes are obtained using MADGRAPH 4 [420, 421] and the subtraction terms are provided by MADDIPOLE [422, 423], which also implements Catani-Seymour dipole subtraction. The numerical integration is done using MADEVENT [365]. We verified the independence of our result under the variation of the so called α -parameter that fixes the amount of subtractions around the divergences of the real corrections.

7.2.4 Parameter settings and scale variations

The various H +jets calculations are performed for proton-proton collisions at 8 TeV center-of-mass energy using the five-flavour scheme, massless b quarks and a vanishing Yukawa bbH coupling. We only consider the effective coupling of gluons to the Higgs boson evaluated in the infinite top-mass limit. The Higgs boson is stable with a mass of $m_H = 126$ GeV. To guarantee consistent setups, we use the `cteq611` ($\alpha_s(M_Z) = 0.1298$) and `CT10n1o` ($\alpha_s(M_Z) = 0.118$) parton density functions (PDFs) to produce our main results at leading and next-to leading orders in QCD, respectively.

Scale uncertainties were determined following the common procedure applied in fixed-order calculations. Accordingly, we vary the renormalization and factorization scales, μ_R and μ_F , by factors of 2.0 and 0.5.

Everywhere, but in the effective coupling of the Higgs to the gluons, the renormalization and factorization scales are set to

$$\mu_F = \mu_R = \frac{\hat{H}_T}{2} = \frac{1}{2} \left(\sqrt{m_H^2 + p_{T,H}^2} + \sum_i |p_{T,i}| \right), \quad (\text{III.42})$$

where the sum runs over the final state jets. The strong coupling is therefore evaluated at different scales according to $\alpha_s^2 \rightarrow \alpha_s^2(m_H)\alpha_s^2(\hat{H}_T/2)$ for H +2-jets, and $\alpha_s^5 \rightarrow \alpha_s^2(m_H)\alpha_s^3(\hat{H}_T/2)$ for H +3-jets.

7.2.5 Kinematic requirements

In a 2-jets analysis, there are several ways of defining the two tagging jets accompanying the production of the Higgs boson. For this study, we apply a leading jet selection where the two highest p_T jets are specified to be the tagged ones. The third jet therefore is defined as the hardest untagged jet of each event. Jets are constructed utilizing the anti- k_T jet finding algorithm implemented in FASTJET [283, 284, 424] and a separation of $R = 0.4$, $p_t^{(\text{jet})} > 30$ GeV and $|\eta^{(\text{jet})}| < 4.4$. Of course, our inclusive H +jets samples fulfill the tagging jet requirements by definition; in the 3-jets case, we provide predictions where even the first untagged jet is described at NLO accuracy.

7.3 Next-to-leading order results

We divide our result section into two parts: first, we will discuss the cross sections, which we obtain in the different jet multiplicity bins and at different orders of α_s . Then we present a selection of transverse momentum and rapidity observables to better quantify the effects of higher-order corrections and scale variations on the H +jets differential final states.

7.3.1 Inclusive cross sections and multiplicity ratios

Table III.6 lists the inclusive jet cross sections σ_n of all our parton-level calculations using the parameters and constraints as given in Secs. 7.2.4 and 7.2.5. Three jet multiplicity bins, $n = 2, 3, 4$, are relevant to this study and given by requiring at least n jets. We employ two of these to compare the results of the H plus two-jet and three-jet calculations with each other. Except for the down-scale variation ($\mu = \mu_{R,F}/2$), we find the NLO rate effect to be substantial as indicated by the large K -factors. Interestingly, in all cases, they are rather similar in size for both jet bins $n = 2$ and $n = 3$. While the LO cross sections show a strong dependence on joint renormalization and factorization scale variations, the NLO cross section uncertainties due to these $\mu_{R,F}$ variations are considerably reduced to approximately 15%.

Another interesting indicator that we consider at LO and NLO is the three-to-two jet cross section ratio, generally defined as $r_{(n+1)/n} = \sigma_{n+1}/\sigma_n$. Owing to the similar K -factors, it

| Sample K -factor | Cross sections for Higgs boson plus | | | |
|------------------------------|---------------------------------------|-------|---------------------------------------|---|
| | ≥ 2 jets | f_3 | ≥ 3 jets | $r_{3/2}$ |
| LO | | | | |
| $H+2$ -jet2 (LO PDFs) | 1.23 ^{+37%} _{-24%} | | | |
| $H+3$ -jets (LO PDFs) | (0.381) | 1.0 | 0.381 ^{+53%} _{-32%} | 0.310 ^{0.347} _{0.278} |
| ----- | | | | |
| $H+2$ -jets (NLO PDFs) | 0.970 ^{+33%} _{-23%} | | | |
| $H+3$ -jets (NLO PDFs) | (0.286) | 1.0 | 0.286 ^{+50%} _{-31%} | 0.295 ^{0.332} _{0.265} |
| NLO | | | | |
| $H+2$ -jets | 1.590 ^{-4%} _{-7%} | 0.182 | 0.289 ^{+49%} _{-31%} | |
| $H+3$ -jets | (0.485) | 1.0 | 0.485 ^{-3%} _{-13%} | 0.305 ^{0.307} _{0.284} |
| K_2, K_3 (LO PDFs for LO) | 1.29 ^{0.911} _{1.59} | | 1.27 ^{0.806} _{1.63} | |
| K_2, K_3 (NLO PDFs for LO) | 1.64 ^{1.19} _{1.98} | | 1.70 ^{1.10} _{2.13} | |

Table III.6: Cross sections in pb for the various parton-level Higgs boson plus jet samples used in this study. The upper and lower parts of the table show the LO and NLO results, respectively, together with their uncertainties (in percent) from varying scales by factors of two, up (subscript position) and down (superscript position). NLO-to-LO K -factors, K_n , for both the inclusive 2-jets ($n = 2$) and 3-jets ($n = 3$) bin, the cross section ratio $r_{3/2}$ and m -jet fractions, f_m , are given in addition.

remains fairly stable at $\sim 30\%$, roughly a factor 3 times higher than a sole α_s effect. Just for completeness, we have also listed the inclusive three-jet fraction, f_3 , belonging to each sample.

7.3.2 Differential observables

The set of observables we want to present here includes Higgs boson and single-jet transverse momenta, $p_{T,x}$, as well as their respective rapidities, y_x ($x \in \{H, j_{1,2,3}\}$). As an example of a multi-object observable, we also discuss the p_T distribution of the Hj_1j_2 system.

We start our discussion by presenting several predictions for the Higgs boson rapidity distribution in Fig. III.31. In all three panels of this figure, we show the same NLO prediction for $H+3$ -jets production (red lines), and compare it, in the left two panels, with two different $H+3$ -jets predictions of LO accuracy (blue lines). We observe large, $\mathcal{O}(50\%)$, positive corrections that are spread almost uniformly over the entire H rapidity range; they increase in the forward/backward region. In the leftmost panel, both the LO and NLO predictions were obtained from the same NLO PDF set, that is CT10nlo. As seen in the middle panel, the corrections decrease by $\sim 20\%$ if one uses an order α_s treatment that is consistent between the PDFs and the parton-level calculations. Half of the effect can then simply be attributed to the larger $\alpha_s(M_Z)$ value of the cteq611 parametrization that we used to compute the middle panel's LO result. The scale uncertainties of the central predictions are shown by the respective envelopes of same colour. Enhancing the description to NLO accuracy, we find a reduction of these errors from $\pm 50\%$ to less than modulus 30%, which also means that the scale variation bands turn from being fairly symmetric to rather one-sided. This is a consequence of fixing the central/default

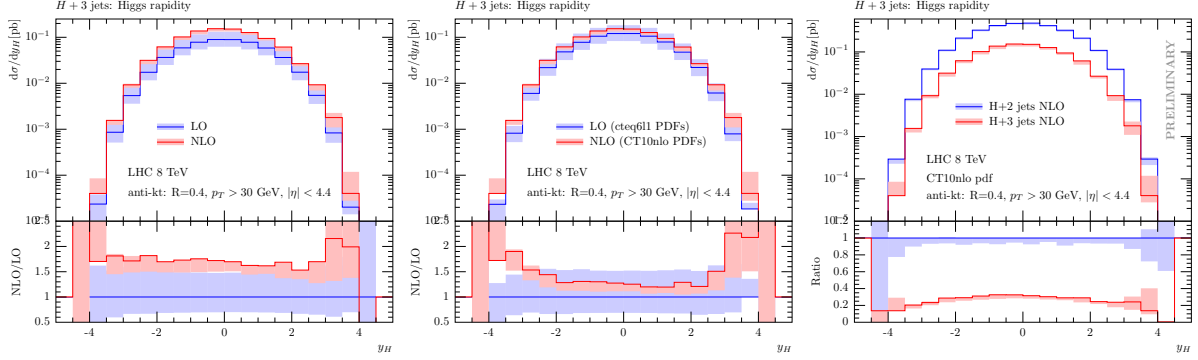


Fig. III.31: Higgs boson rapidity distributions and their $\mu_{R,F}$ scale uncertainties (depicted by pastel-coloured bands) in $H+3$ -jets production at the $E_{\text{cm}} = 8$ TeV LHC. The two plots to the left show a comparison of the NLO (red) to LO (blue) predictions where the left panel’s LO result has been obtained using the same PDF as for the NLO computation. The ratio plots at the bottom visualize the K -factor variation over the Higgs boson’s rapidity range. In the rightmost panel, the y_H distributions of the 3-jets (red) and 2-jets (blue) NLO samples (requiring two tagging jets only) are compared to each other, and their differential cross section ratio is shown in the lower part.

scales right where the NLO cross section plateaus.

The plot to the right of Fig. III.31 is a direct comparison of the y_H distributions given by the 2-jets (blue) and 3-jets (red) NLO samples. Scale variations lead to $\mathcal{O}(20\%)$ uncertainties over a fairly broad y_H range. Although the two NLO samples differ by one order of α_s , the associated scale uncertainties are comparable in size, and only somewhat smaller for the $H+2$ -jets case. Since we do not require more than the two tagging jets, the $H+3$ -jets line in the lower plot actually visualizes the $r_{3/2}$ quantity differentially in dependence on y_H . It varies only mildly around the inclusive, ~ 0.3 value given in the table above. The differential ratio also shows that the production of Higgs bosons in the 3-jets sample is slightly more central than in the 2-jets sample.

We now turn to discuss our results, which we obtained for the single jet observables and the H -system p_t spectra. Figs. III.32, III.34 and Figs. III.33, III.35 follow the same plotting styles/layouts and colour code as chosen for the center and rightmost subfigures of Fig. III.31, respectively. The former set of figures is therefore used to give a broader comparison between NLO and LO predictions as generated by the Higgs boson plus 3-jets final state. In the latter set, we then display how the $H+3$ -jets and $H+2$ -jets NLO results compare to each other for exactly the same selection of observables.

Focusing on the jet transverse momenta and rapidities, p_{t,j_i} (left columns) and y_{j_i} (right columns), as depicted for the three hardest jets in Figs. III.32 and III.33, we notice that they show very similar scale variation characteristics and reduction of errors as discussed for the y_H spectra presented in Fig. III.31. Similarly for the NLO corrections on the jet rapidities, we again find these to be rather well described by constant positive shifts, which here are of the order of 20%, see Fig. III.32. In contrast to this, all differential K -factors associated with the jet p_t distributions in this figure show a decline towards larger p_t values. In other words, even that the rate of Higgs associated jet production gets enhanced at NLO, the p_t tails loose hardness when taking relative measures. This is due to the extra radiation carried away from the system by the fourth jet, which shifts the spectra of all the other jets to lower values. Note that the soft jet K -factors can take values as large as 1.4.

Turning to Fig. III.33, the very same set of $H+3$ -jets NLO predictions is plotted against the corresponding $H+2$ -jets predictions such that the differential $r_{3/2}$ ratios can be read off

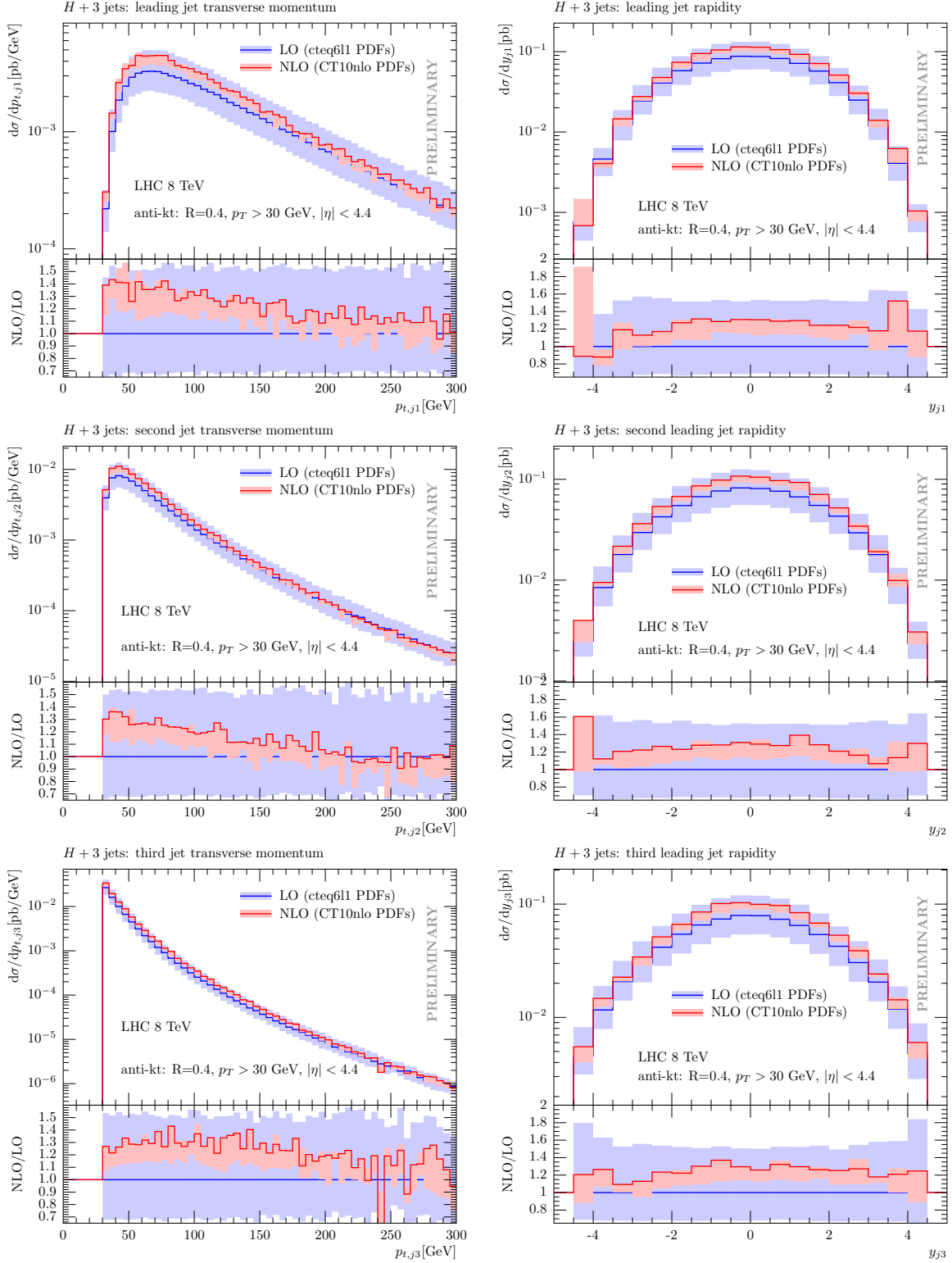


Fig. III.32: Higgs boson plus three-jet production at leading (blue) and next-to leading (red) order for proton–proton collisions at $E_{\text{cm}} = 8$ TeV. The transverse momenta and rapidities of the three hardest jets are shown in the left and right column, respectively. The size of the scale uncertainties has been indicated by the lightly coloured bands occurring around each central prediction. The lower plots show the K -factor variations for each of these single jet observables.

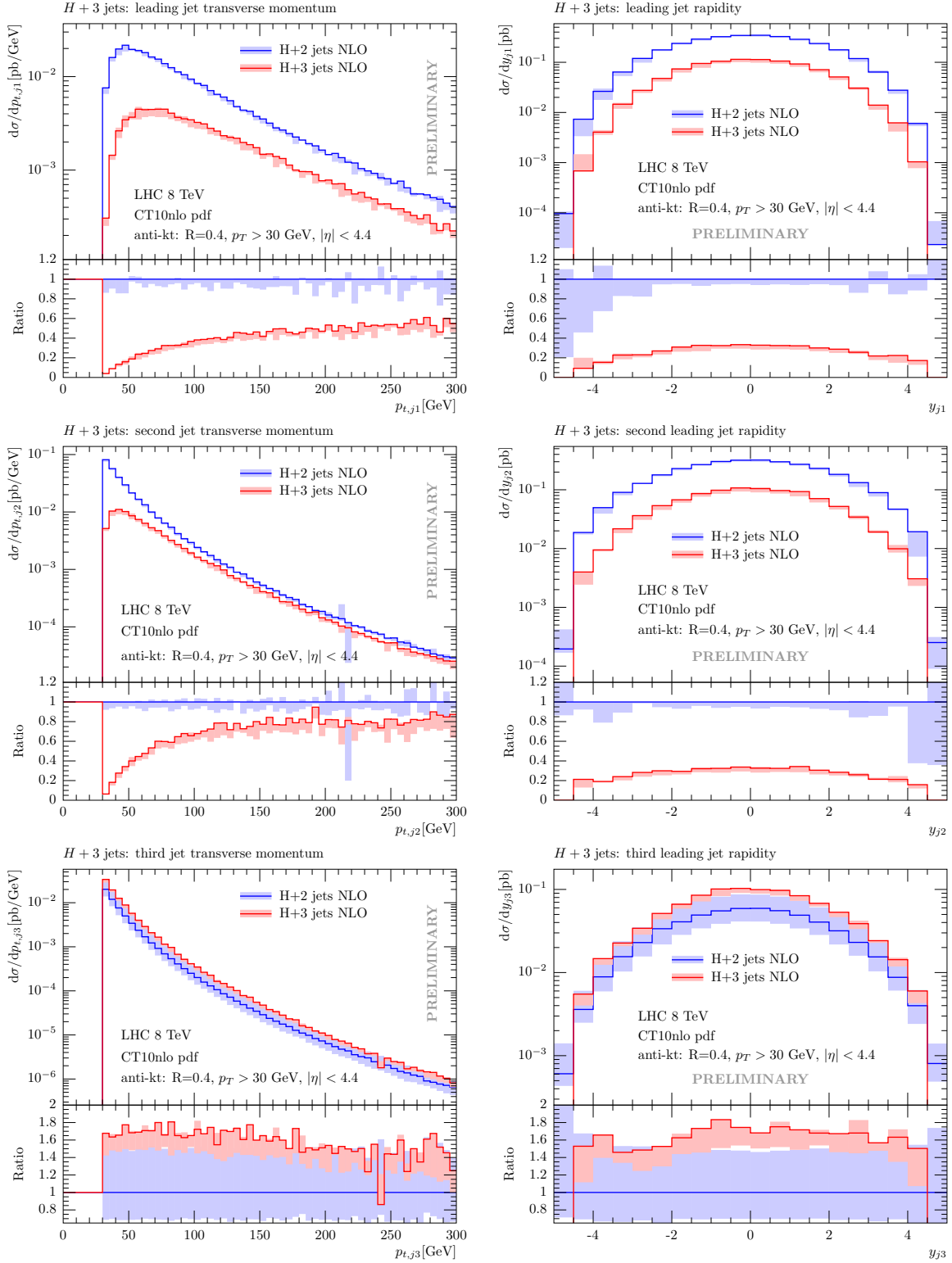


Fig. III.33: Comparison of QCD NLO predictions for inclusive 2-jets (blue) and 3-jets (red) final states in Higgs boson plus jets production at the $E_{\text{cm}} = 8$ TeV LHC. The transverse momenta and rapidities of the three hardest jets are shown in the left and right column, respectively. The colourful envelops around the central predictions depict the size of their scale uncertainties. Each lower plot is used to indicate the cross section ratio between the three-jet and two-jet samples in dependence on the respective single jet observable. Note that in the $H+2$ -jet calculation, the third-jet spectra are only described with LO accuracy.

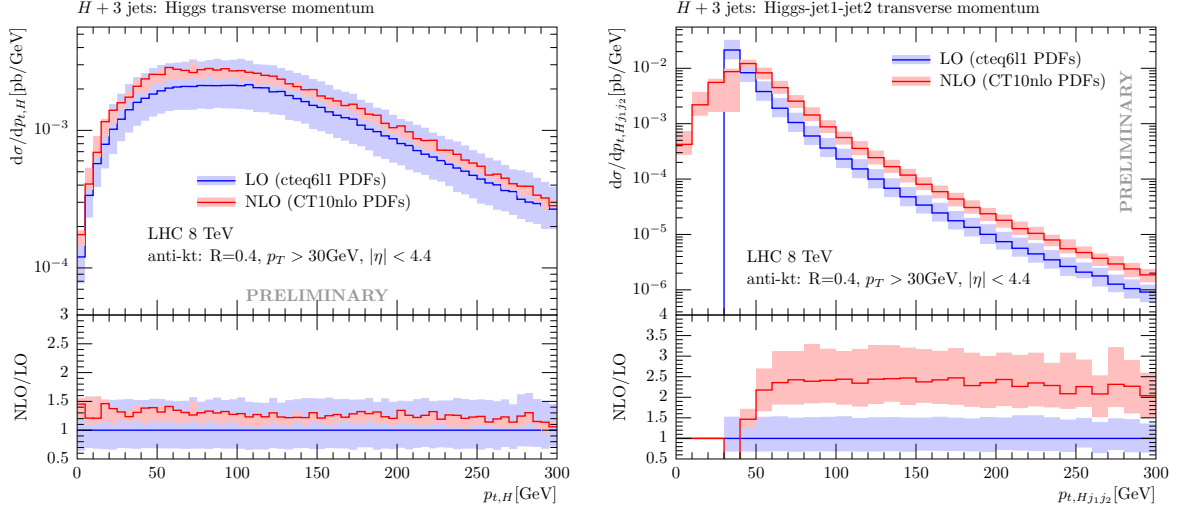


Fig. III.34: Higgs boson plus three-jet production at leading (blue) and next-to leading (red) order for proton-proton collisions at $E_{\text{cm}} = 8$ TeV. Transverse momentum distributions of the Higgs boson (left) and the H plus tagging jet system (right) are shown together with their scale uncertainties indicated by the lightly coloured bands surrounding each central prediction. The lower plots show the K -factor variations as functions of $p_{T,H}$ and p_{T,Hj_1j_2} .

easily. As before, they are rather flat for the y_{j_i} predictions, and do not exceed values larger than 35% owing to the two-tagging-jet requirement. Only if a third jet has to be resolved (cf. the last row of Fig. III.33), we find this ratio to be as large as 1.6, which is no surprise, since it now denotes a K -factor based on a LO third-jet description obtained with NLO PDFs. For the transverse momenta of the first two jets, the $r_{3/2}$ variables show a strong dependence on the hardness of the jets. They rise quickly from very low values of $\mathcal{O}(0.1)$ at the jet threshold to over 50% for $p_t \sim 100$ GeV. This emphasizes the importance of higher jet multiplicity contributions if one targets a complete description of H +jets final states.

Lastly we discuss, in the same manner as before, our findings regarding the p_t distributions of the Higgs bosons and the Hj_1j_2 three-body objects. The NLO corrections to the Higgs boson p_t in three-jet final states (Fig. III.34 to the left) are of the order of +30% and decrease very slowly over the p_t range plotted here. The behaviour under scale variations is as before. Comparing to the $p_{t,H}$ spectrum extracted from the corresponding 2-jets sample, we observe an $r_{3/2}$ ratio that is rising as those for the tagging jet p_t , but on a slower rate; see the left panel in Fig. III.35. In particular, for $p_{t,H}$ values below 100 GeV, it remains locked around 0.2. For transverse momenta above $2M_H$, the 3-jet contributions are again as large as 50%, with similar implications regarding an inclusive multi-jet description of H +jets final states as pointed out in the case of the single jet p_t .

We round off by discussing our three different predictions for the transverse momentum distribution of the Hj_1j_2 systems. Each of the right panels in Figs. III.34 and III.35 shows the p_t spectrum computed from the H +3-jets NLO samples. First we compare it to corresponding LO predictions (Fig. III.34), then to the ones of the H +2-jets NLO samples (Fig. III.35). The p_{t,Hj_1j_2} is an interesting variable for our study since it is sensitive to the description of any additional parton radiation beyond the two tagging jets. It is out of question that a fixed-order description of the low p_t region cannot be achieved reliably without supplementing the necessary resummation contributions. Nevertheless we can use this variable to point out important features of the three different calculations as well as discuss the formal accuracy of the tails of these p_{t,Hj_1j_2} spectra. The prediction taken from the H +3-jets LO sample is just given by the

third-jet p_t distribution of lowest order, with a clear indication of the jet p_t threshold at 30 GeV, cf. Fig. III.34. The hardness of the third jet simply determines the recoil of the $H_{j_1 j_2}$ system. Above threshold, we therefore have a LO accurate description of the $p_{t,H_{j_1 j_2}}$ spectrum. The situation cannot be improved by an $H+2$ -jets NLO computation (Fig. III.35): the difference in the tails is caused by the replacement of LO with NLO PDFs, again pointing to a 20% effect as discussed earlier. The region below the jet threshold gets filled by real emission contributions that are too soft to be resolved as a jet. However, the resulting low- p_t spectrum is highly unphysical due to the missing contributions from multiparton emissions.¹³ Turning to the NLO accurate evaluation of $H+3$ jets, we finally improve the precision to which we describe the $p_{t,H_{j_1 j_2}}$ tail. For transverse momenta larger than 60 GeV, we have achieved NLO precision. Besides neglecting Sudakov corrections, below this value we are missing contributions only a full NNLO $H+2$ -jet calculation can provide (contributions such as double unresolved and virtual plus unresolved emissions). However, contributions with two more jets beyond the tagged ones or three jets and unresolved extra emission already lead to p_t balancing as well as p_t enhancing effects such that we find large, $\mathcal{O}(3)$, fairly constant corrections for higher $p_{t,H_{j_1 j_2}}$ and a depletion towards zero $p_{t,H_{j_1 j_2}}$. A last few comments are in order concerning the scale variation characteristics of the $p_{t,H_{j_1 j_2}}$ predictions: firstly, a reduction from $\pm 50\%$ to $\pm 30\%$ is only found for the prediction from the $H+3$ -jets NLO calculation (red envelopes). As discussed the other evaluations only give LO accurate results. Secondly, in contrast to other $H+3$ -jets NLO predictions, the much more symmetric band found here is a consequence of the dominance of the four-jet contributions that feature a LO scale variation behaviour.¹⁴

Conclusions

Taking advantage of the recent developments in the automated computation of NLO predictions we reported on NLO QCD results in an ATLAS-like analysis of inclusive Higgs boson plus 2-jets and 3-jets final states.

The loop amplitudes were generated with GOSAM and computed using a new development in integrand reduction techniques, based on a Laurent expansion, and implemented in the code NINJA. For tree-level amplitudes and phase space integration we used SHERPA and the MADGRAPH/DIPOLE/EVENT framework.

We find that NLO corrections are important and result in a substantial change of rate and jet hardness. At the level of the total inclusive cross section we find an increase of almost 30% for both $H+2$ -jets and $H+3$ -jets, whereas the scale variation reduces to approximately 15%. Considering differential distributions, we observe that rapidity distributions for the Higgs boson and the first three hardest jets obtain a positive shift of about 20%, which is rather constant over the full kinematical range. For the transverse momentum distributions of the jets instead, we observe a decrease in the K-factor towards larger p_t values, whereas in the transverse momentum distribution of the Higgs boson, this decrease is only very slow. The differential $r_{3/2}$ ratios for the rapidities are rather flat and never exceed 35%, however in the case of the transverse momentum distributions they reach up to 50% for the leading jet and the Higgs boson. This shows that $H+3$ -jets contributions cannot be neglected in an inclusive two-jet sensitive analysis. Another observable, where NLO corrections to $H+3$ -jets play an important role is the p_t distribution of

¹³Known as the Sudakov effect, the very same discussion occurs, for example, for the $p_{t,H}$ distribution in Higgs boson production at NLO. The reduction seen here for the very first $p_{t,H_{j_1 j_2}}$ bin of the $H+2$ -jets NLO computation is caused by those events satisfying $p_{t,H_{j_1 j_2}} \equiv 0$, i.e. Born, virtual and integrated subtraction contributions as well as those from counter events fall into the first bin diminishing the large effect from (unresolved) real emissions.

¹⁴On a more quantitative level, we note that the ‘BVI’ contributions of the $p_{t,H_{j_1 j_2}}$ and p_{t,j_3} distributions are exactly the same while the ‘RS’ ones of the former are considerably harder than those of the latter. This leads to a different cancellation pattern when combining the scale varied ‘BVI’ and ‘RS’ predictions (they work in opposite directions). For the $p_{t,H_{j_1 j_2}}$, we then find the ‘RS’ uncertainties to be the dominating ones for $p_{t,H_{j_1 j_2}} \gtrsim 60$ GeV.

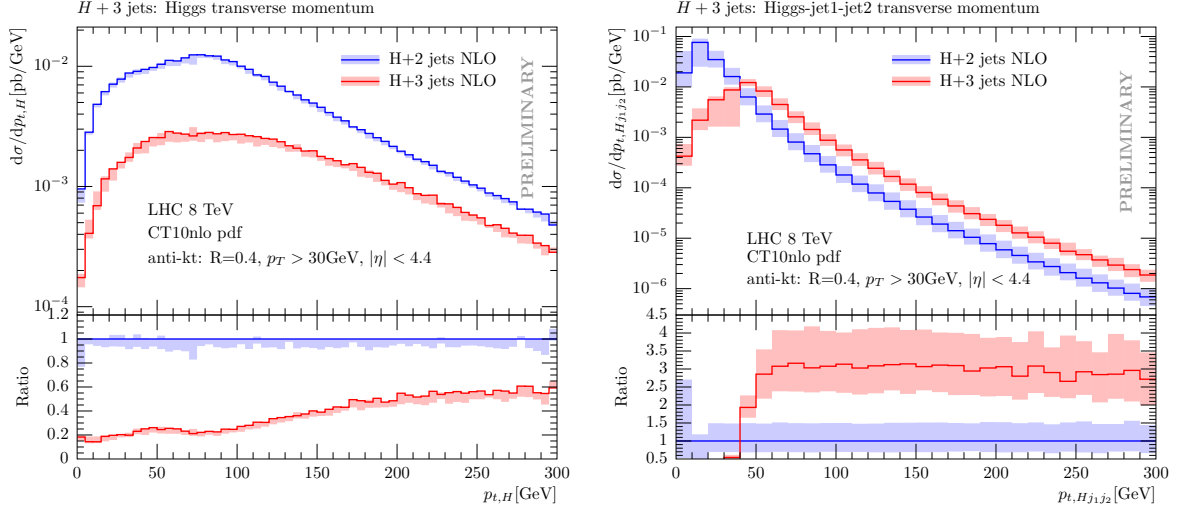


Fig. III.35: Comparison of QCD NLO predictions for inclusive 2-jets (blue) and 3-jets (red) final states in Higgs boson plus jets production at the $E_{\text{cm}} = 8$ TeV LHC. The transverse momenta of the Higgs boson and Higgs boson plus $j_1 j_2$ system are shown in the left and right panel, respectively. Colourful envelopes are used to depict the size of scale uncertainties. The lower plots indicate the cross section ratios between the three-jet and two-jet samples in dependence on the p_T value. Note that in the $H+2$ -jets case, the $p_{T,Hjj}$ distribution has LO accuracy only.

the $Hj_1 j_2$ system. In fact, for the first time, the distribution is described at NLO accuracy for $p_t > 2p_{t,\text{min}}^{(\text{jet})} = 60$ GeV.

It would be interesting to study the impact of the NLO corrections presented here when typical VBF cuts are applied. Modern Monte Carlo tools allow furthermore to study these correction in a matched NLO plus parton shower framework merged with lower multiplicity predictions. We postpone these studies to future publication.

Acknowledgements

We would like to thank the organizers of the Les Houches "Physics at TeV colliders 2013" workshop for the stimulating environment.

The work of G.C. was supported by DFG SFB-TR-9 and the EU TMR Network LHCPHENOnet. The work of H.v.D., G.L., P.M., T.P., and V.Y. was supported by the Alexander von Humboldt Foundation, in the framework of the Sofja Kovaleskaja Award 2010, endowed by the German Federal Ministry of Education and Research. G.O. was supported in part by the National Science Foundation under Grant PHY-1068550. F.T. acknowledges partial support by MIUR under project 2010YJ2NYW. This research used computing resources from the Rechenzentrum Garching.

8 Jet-bin uncertainties estimate through jet efficiencies¹⁵

8.1 Introduction

In order to fully establish whether the new particle recently discovered at the LHC [425, 426] is the SM Higgs boson, precise measurements of its properties, in particular its couplings, are essential. Establishing a significant departure from the simple SM-like pattern could be a first manifestation of New Physics. In fact, the new particle lies in a region of parameter space where

¹⁵P. F. Monni (Work in collaboration with A. Banfi, G.P. Salam, and G. Zanderighi)

many decay modes have an appreciable branching fraction, leading to a very rich phenomenology. On the other hand, many decay channels (*e.g.* $H \rightarrow b\bar{b}$, $H \rightarrow W^+W^-$) are very difficult to measure because of the large QCD background. Most Higgs-boson events involve either none or one jet, since higher multiplicity events are suppressed by powers of the strong coupling constant, and hence more rare. It is natural then to impose a veto on additional jets so as to significantly reduce the dominant background, while reducing only modestly the signal. Therefore, it is essential to know how much these tight kinematical cuts reduce the signal cross section, and what the uncertainties in the resulting signal are. However, a precise assessment of the theory error in the presence of a jet veto is a challenging task.

Tight kinematical cuts applied to QCD radiation give rise to large Sudakov logarithms of the form $\alpha_s^n \ln^{2n}(m_H/p_{t,\text{veto}})$ in the perturbative series. When scale variation is used to estimate the theory uncertainty, the K-factor effects nearly cancel against the large logarithms leading to an underestimate of the actual perturbative error. Such logarithmic terms spoil the convergence of the perturbative series in the region where the logarithms are very large, and they must be resummed to all orders in the strong coupling. Not only does resummation allow for a more precise theory prediction, but it also gives a direct handle to estimate the size of higher-order Sudakov logarithms, which is necessary for a reliable assessment of uncertainties.

Resummed predictions for the Higgs+0 jet cross section and efficiencies have been obtained both in the context of the CAESAR method [427,428], and in an effective theory framework [429] up to next-to-next-to-leading logarithmic level. Some terms beyond this accuracy have been recently obtained in [430,431]. The impact of heavy quark masses on the resummed predictions has been also studied for both the $p_{t,\text{veto}}$ [432] and $p_{t,H}$ [432,433] cross sections. When more than a tagged jet is present in the process, the infrared structure of the perturbative series becomes more complex and new logarithms of the non-global type [434,435] appear. For the H+1 jet cross section, NLL resummation for the global class in the regime $p_{t,\text{veto}} \ll p_{t,\text{jet}} \sim m_H$ was obtained in [436].

In order to optimize the sensitivity, some experimental analyses (*e.g.* $gg \rightarrow H \rightarrow W^+W^-$, VBF) combine data with different jet multiplicities. Since resummed predictions are currently only available for 0- and 1-jet bins, it is of primary importance to have a robust prescription to estimate reliably the uncertainties associated with a fixed-order calculation. Moreover, a good method should allow one to incorporate any resummed predictions whenever available.

A first approach based on the combination of inclusive jet bin uncertainties was proposed by Stewart and Tackmann in [437]. Uncertainties in the exclusive jet-bin cross sections are obtained by treating the errors in the inclusive jet-bins as uncorrelated. An alternative prescription was presented in [427,428], and it is referred to as the jet-veto efficiency (JVE) method. It is based on the assumption that the uncertainties in the jet-fractions (efficiencies) with different multiplicities are uncorrelated with each other and with the uncertainty in the total cross section. This is physically motivated by the fact that uncertainties in jet fractions are dominated by Sudakov suppression effects, whilst K-factor effects (which rule the uncertainty in the total cross section) largely cancel in the definition of the jet fractions themselves. The latter method allows one to treat resummed predictions for different jet bins on the same footing as fixed-order ones. For the resummed 0-jet cross section, the error obtained with the JVE method is consistent with the direct estimate obtained from scale variations in the resummed calculation. More recently, a recipe to combine uncertainties for different resummed jet-bin cross sections in the context of SCET resummation was presented in [438]. When resummed predictions are not available, the latter method reduces to the standard scale variation which underestimates the theoretical error. In the following sections, we briefly recall the JVE method, and present a generalisation to any jet multiplicity.

8.2 The JVE method

The uncertainties in jet-bin cross sections are due to a combination of K-factor effects which rule the uncertainty in the total cross section, and Sudakov suppression effects due to the presence of severe cuts on the real QCD radiation. The idea behind the JVE approach is to disentangle these two effects and treat them separately. Therefore, we define n -jet efficiencies ϵ_n as

$$\epsilon_n = \frac{\sigma_{n\text{-jet}}}{\sigma_{\geq n\text{-jet}}}, \quad (\text{III.43})$$

where $\sigma_{n\text{-jet}}$ is the exclusive n -jet cross section.

To a large extent, K-factor effects cancel in the ratio (III.43), since the uncertainty in the n -jet efficiency is largely ruled by Sudakov suppression. Therefore, one can treat the uncertainties in the n -jet efficiency and in the inclusive n -jet cross section as uncorrelated. The uncertainties in the two quantities are computed separately and then combined according to the latter assumption.

The theory error in the inclusive n -jet cross section is obtained by standard scale variation, which is not affected by cancellations in the inclusive case. Threshold resummation effects can be also included [40]. To obtain the uncertainty in the n -jet efficiency, we start by noticing that $m+1$ different schemes for the jet fractions can be defined at $N^m\text{LO}$. As an example we consider the 0-jet efficiency ϵ_0 . Using the current state-of-the-art calculations at NNLO for both the 0-jet and the total cross sections, the following three equivalent schemes can be defined to this perturbative accuracy

$$\epsilon_0^{(a)}(p_{t,\text{veto}}) = \frac{\Sigma_0(p_{t,\text{veto}}) + \Sigma_1(p_{t,\text{veto}}) + \Sigma_2(p_{t,\text{veto}})}{\sigma_0 + \sigma_1 + \sigma_2}, \quad (\text{III.44})$$

$$\epsilon_0^{(b)}(p_{t,\text{veto}}) = \frac{\Sigma_0(p_{t,\text{veto}}) + \Sigma_1(p_{t,\text{veto}}) + \bar{\Sigma}_2(p_{t,\text{veto}})}{\sigma_0 + \sigma_1}, \quad (\text{III.45})$$

$$\epsilon_0^{(c)}(p_{t,\text{veto}}) = 1 + \frac{\bar{\Sigma}_1(p_{t,\text{veto}})}{\sigma_0} + \left(\frac{\bar{\Sigma}_2(p_{t,\text{veto}})}{\sigma_0} - \frac{\sigma_1}{\sigma_0^2} \bar{\Sigma}_1(p_{t,\text{veto}}) \right), \quad (\text{III.46})$$

where

$$\Sigma_{0\text{-jet}}(p_{t,\text{veto}}) = \Sigma_0(p_{t,\text{veto}}) + \Sigma_1(p_{t,\text{veto}}) + \Sigma_2(p_{t,\text{veto}}) + \dots \quad (\text{III.47})$$

$$\sigma_{\geq 0\text{-jet}} = \sigma_{\text{tot}} = \sigma_0 + \sigma_1 + \sigma_2 + \dots, \quad (\text{III.48})$$

and

$$\Sigma_i(p_{t,\text{veto}}) = \bar{\Sigma}_i(p_{t,\text{veto}}) + \sigma_i, \quad \bar{\Sigma}_i(p_{t,\text{veto}}) = - \int_{p_{t,\text{veto}}}^{\infty} dp_t \frac{d\Sigma_i(p_t)}{dp_t}. \quad (\text{III.49})$$

Schemes (III.45) and (III.46) differ from Eq. (III.44) only by terms $\mathcal{O}(\alpha_s^3)$, which are not under control. The uncertainty in the 0-jet efficiency is obtained as the envelope of all scale variations for the central scheme (III.44) and the central values relative to the remaining two schemes (III.45) and (III.46). The spread between different schemes is associated with the Sudakov suppression effects and it increases for lower efficiencies, *i.e.* when more radiation is suppressed. When resummation of large Sudakov logarithms is available, it can be included as shown in [427, 428], and the variation of the corresponding resummation scale is included in the envelope. Resummed and fixed-order calculations for different jet bins are treated in the same way, and can be straightforwardly combined. Below we discuss the JVE method for an arbitrary number of exclusive jet bins, and we explicitly work out the case of only two jet bins.

8.2.1 Formulation for any jet multiplicity

In the general case with n exclusive jet bins and one inclusive bin, we define the n exclusive cross sections as

$$\sigma_{0\text{-jet}} = \epsilon_0 \sigma_{\text{tot}}, \quad (\text{III.50})$$

$$\sigma_{1\text{-jet}} = \epsilon_1 (1 - \epsilon_0) \sigma_{\text{tot}}, \quad (\text{III.51})$$

$$\sigma_{2\text{-jet}} = \epsilon_2 (1 - \epsilon_1) (1 - \epsilon_0) \sigma_{\text{tot}}, \quad (\text{III.52})$$

...

$$\sigma_{n\text{-jet}} = \epsilon_n (1 - \epsilon_{n-1}) \dots (1 - \epsilon_0) \sigma_{\text{tot}}, \quad (\text{III.53})$$

and the inclusive one as

$$\sigma_{>n\text{-jet}} = (1 - \epsilon_n) (1 - \epsilon_{n-1}) \dots (1 - \epsilon_0) \sigma_{\text{tot}}. \quad (\text{III.54})$$

To express the uncertainty in the jet-bin cross sections, we define the following $n + 1$ vectors in the $(n + 1)$ -dimensional euclidean space

$$\Delta\sigma_i = \left(\frac{\partial\sigma_i}{\partial\epsilon_n} \delta\epsilon_n, \frac{\partial\sigma_i}{\partial\epsilon_{n-1}} \delta\epsilon_{n-1}, \dots, \frac{\partial\sigma_i}{\partial\epsilon_0} \delta\epsilon_0, \frac{\partial\sigma_i}{\partial\sigma_{\text{tot}}} \delta\sigma_{\text{tot}} \right), \quad (\text{III.55})$$

where σ_i denotes either any of the n exclusive or the inclusive jet-bin cross sections, $\delta\epsilon_i$ denotes the uncertainty in the i -jet efficiency, computed as described above, and $\delta\sigma_{\text{tot}}$ is the uncertainty in the total cross section. They fulfill the following conditions

$$\delta\epsilon_i \cdot \delta\epsilon_j = \delta^2\epsilon_i \delta_{ij}, \quad (\text{III.56})$$

$$\delta\epsilon_i \cdot \delta\sigma_{\text{tot}} = 0. \quad (\text{III.57})$$

The vectors corresponding to the exclusive cross sections read

$$\Delta\sigma_{0\text{-jet}} = (0, \dots, \sigma_{\text{tot}} \delta\epsilon_0, \epsilon_0 \delta\sigma_{\text{tot}}), \quad (\text{III.58})$$

$$\Delta\sigma_{1\text{-jet}} = (0, \dots, (1 - \epsilon_0) \sigma_{\text{tot}} \delta\epsilon_1, -\epsilon_1 \sigma_{\text{tot}} \delta\epsilon_0, \epsilon_1 (1 - \epsilon_0) \delta\sigma_{\text{tot}}), \quad (\text{III.59})$$

$$\begin{aligned} \Delta\sigma_{2\text{-jet}} = & (0, \dots, (1 - \epsilon_1) (1 - \epsilon_0) \sigma_{\text{tot}} \delta\epsilon_2, -\epsilon_2 (1 - \epsilon_0) \sigma_{\text{tot}} \delta\epsilon_1, \\ & -\epsilon_2 (1 - \epsilon_1) \sigma_{\text{tot}} \delta\epsilon_0, \epsilon_2 (1 - \epsilon_1) (1 - \epsilon_0) \delta\sigma_{\text{tot}}), \end{aligned} \quad (\text{III.60})$$

...

while for the inclusive one we find

$$\begin{aligned} \Delta\sigma_{>n\text{-jet}} = & - \left(\prod_{i=0; i \neq n}^{i=n} (1 - \epsilon_i) \sigma_{\text{tot}} \delta\epsilon_n, \prod_{i=0; i \neq n-1}^{i=n} (1 - \epsilon_i) \sigma_{\text{tot}} \delta\epsilon_{n-1}, \dots, \right. \\ & \left. \prod_{i=0; i \neq 0}^{i=n} (1 - \epsilon_i) \sigma_{\text{tot}} \delta\epsilon_0, - \prod_{i=0}^{i=n} (1 - \epsilon_i) \delta\sigma_{\text{tot}} \right), \end{aligned} \quad (\text{III.61})$$

where we define

$$\prod_{i=0; i \neq 0}^{i=0} (1 - \epsilon_i) = 1. \quad (\text{III.62})$$

The resulting symmetric covariance matrix reads

$$\text{Cov}[\sigma_{0\text{-jet}}, \sigma_{1\text{-jet}}, \dots, \sigma_{>n\text{-jet}}] = \begin{pmatrix} \Delta\sigma_{0\text{-jet}} \cdot \Delta\sigma_{0\text{-jet}} & \Delta\sigma_{0\text{-jet}} \cdot \Delta\sigma_{1\text{-jet}} & \dots & \Delta\sigma_{0\text{-jet}} \cdot \Delta\sigma_{>n\text{-jet}} \\ & \Delta\sigma_{1\text{-jet}} \cdot \Delta\sigma_{1\text{-jet}} & \dots & \Delta\sigma_{1\text{-jet}} \cdot \Delta\sigma_{>n\text{-jet}} \\ & & & \Delta\sigma_{>n\text{-jet}} \cdot \Delta\sigma_{>n\text{-jet}} \end{pmatrix}. \quad (\text{III.63})$$

8.2.2 Case with two jet bins

As a case of study we analyse the case of a 0–jet bin and an inclusive 1–jet bin. Resummed predictions for the 0–jet efficiency ϵ_0 were obtained in [427, 428] up to NNLO+NNLL. The inclusive 1–jet cross section can be written in terms of ϵ_0 as

$$\sigma_{\geq 1\text{-jet}}(p_{t,\text{veto}}) = (1 - \epsilon_0)\sigma_{\text{tot}}, \quad (\text{III.64})$$

where σ_{tot} is the total cross section for Higgs boson production in gluon fusion, currently known to NNLO. Since we only have two jet bins, we can define the following two 2-dimensional vectors (III.55)

$$\Delta\sigma_{0\text{-jet}} = (\sigma_{\text{tot}}\delta\epsilon_0, \epsilon_0\delta\sigma_{\text{tot}}), \quad (\text{III.65})$$

$$\Delta\sigma_{\geq 1\text{-jet}} = (-\sigma_{\text{tot}}\delta\epsilon_0, (1 - \epsilon_0)\delta\sigma_{\text{tot}}). \quad (\text{III.66})$$

The covariance matrix between the exclusive 0–jet and the inclusive 1–jet cross sections can be easily obtained as shown in Eq. (III.63) and it can be written as a sum of a totally correlated and a totally anti-correlated terms

$$\text{Cov}[\sigma_{0\text{-jet}}, \sigma_{\geq 1\text{-jet}}] = \begin{pmatrix} \epsilon_0^2\delta^2\sigma_{\text{tot}} & \epsilon_0(1 - \epsilon_0)\delta^2\sigma_{\text{tot}} \\ \epsilon_0(1 - \epsilon_0)\delta^2\sigma_{\text{tot}} & (1 - \epsilon_0)^2\delta^2\sigma_{\text{tot}} \end{pmatrix} + \begin{pmatrix} \sigma_{\text{tot}}^2\delta^2\epsilon_0 & -\sigma_{\text{tot}}^2\delta^2\epsilon_0 \\ -\sigma_{\text{tot}}^2\delta^2\epsilon_0 & \sigma_{\text{tot}}^2\delta^2\epsilon_0 \end{pmatrix} \quad (\text{III.67})$$

The two matrices in the right hand side of Eq. (III.67) are uncorrelated. The first term corresponds to the K-factor contribution and it is proportional to the uncertainty in the total cross section. This gives rise to a totally correlated uncertainty between the two jet bins. The second term in Eq. (III.67) encodes Sudakov effects, and thus it is proportional to the uncertainty in the 0–jet efficiency, yielding a totally anti-correlated uncertainty between the two jet bins.

8.2.2.1 Numerical results for LHC

Below we provide tables with numerical results for cross sections and efficiencies for the values of veto scales and jet radii, as used in current LHC analyses. The predictions for the 0–jet efficiency are computed to NNLO+NNLL and top- and bottom-quark mass effects are included as described in [432]. All uncertainties have been made symmetric with respect to the central value.

Exact m_t and m_b corrections

| R | $p_{t,\text{veto}}$ [GeV] | $\sigma_{\text{tot}}^{8\text{TeV}}$ [pb] | $\epsilon_0^{(8\text{TeV})}$ | $\sigma_{0\text{-jet}}^{(8\text{TeV})}$ [pb] | $\sigma_{\geq 1\text{-jet}}^{(8\text{TeV})}$ [pb] |
|-----|---------------------------|--|------------------------------|--|---|
| 0.4 | 25 | 19.24 ± 1.78 | 0.602 ± 0.070 | 11.59 ± 1.72 | 7.66 ± 1.52 |
| 0.5 | 30 | 19.24 ± 1.78 | 0.657 ± 0.070 | 12.64 ± 1.79 | 6.60 ± 1.48 |

Table III.7: Total inclusive cross section, jet-veto efficiency and zero-jet cross section for Higgs production at the 8 TeV LHC for two different values of the jet radius R and $p_{t,\text{veto}}$. Results include exact top and bottom mass dependence. The quoted total cross section and the corresponding errors have been computed with the `hnnlo` 2.0 code [433].

In the first two tables the total cross section is computed at NNLO QCD. Quark-mass effects lead to a modest decrease of about half a percent in the zero-jet cross section with respect to the large- m_t result. The uncertainties in the cross section increase by about 2% (and amount to about 14%) when top and bottom masses are taken into account. In tab. III.9 we report

Large- m_t approximation

| R | $p_{t,\text{veto}}$ [GeV] | $\sigma_{\text{tot}}^{8\text{TeV}}$ [pb] | $\epsilon_0^{(8\text{TeV})}$ | $\sigma_{0\text{-jet}}^{(8\text{TeV})}$ [pb] | $\sigma_{\geq 1\text{-jet}}^{(8\text{TeV})}$ [pb] |
|-----|---------------------------|--|------------------------------|--|---|
| 0.4 | 25 | 19.03 ± 1.76 | 0.613 ± 0.064 | 11.66 ± 1.62 | 7.36 ± 1.39 |
| 0.5 | 30 | 19.03 ± 1.76 | 0.667 ± 0.058 | 12.70 ± 1.61 | 6.34 ± 1.25 |

Table III.8: As table III.7 but in the large m_t approximation.

Large- m_t approximation ($\sigma_{\text{tot}}^{8\text{TeV}}$ from HXSWG)

| R | $p_{t,\text{veto}}$ [GeV] | $\sigma_{\text{tot}}^{8\text{TeV}}$ [pb] | $\epsilon_0^{(8\text{TeV})}$ | $\sigma_{0\text{-jet}}^{(8\text{TeV})}$ [pb] | $\sigma_{\geq 1\text{-jet}}^{(8\text{TeV})}$ [pb] |
|-----|---------------------------|--|------------------------------|--|---|
| 0.4 | 25 | 19.27 ± 1.45 | 0.613 ± 0.064 | 11.81 ± 1.51 | 7.46 ± 1.35 |
| 0.5 | 30 | 19.27 ± 1.45 | 0.667 ± 0.058 | 12.86 ± 1.47 | 6.42 ± 1.22 |

Table III.9: As table III.7 but in the large m_t approximation. Unlike in table III.8 the total cross section is taken from the HXSWG [40] and includes finite-width, electro-weak and threshold resummation effects.

the jet-veto efficiency and cross section using the improved total cross section recommended by the Higgs Cross Section Working Group (HXSWG) [40] instead of the pure NNLO value. Improvements include the treatment of the Higgs width, NNLL threshold effects and NLO electro-weak corrections. To figure out only the size of mass effects one has to compare results including mass corrections to tab. III.8, rather than tab. III.9, since the improved predictions for the total cross section included in tab. III.9 are not available when finite-mass effects are included.

8.2.3 Case with three jet bins

Current LHC analyses for $H \rightarrow W^+W^-$ use exclusive 0- and 1- jet bins, and an inclusive 2-jet bin. In addition to the 0-jet efficiency ϵ_0 defined in Eqs. (III.44), (III.45), (III.46), we introduce the three schemes for the 1-jet efficiency ϵ_1 available at NNLO

$$\epsilon_1^{(a)} = 1 - \frac{\sigma_{\geq 2\text{-jet}}^{\text{NLO}}}{\sigma_{\geq 1\text{-jet}}^{\text{NNLO}}}, \quad (\text{III.68})$$

$$\epsilon_1^{(b)} = 1 - \frac{\sigma_{\geq 2\text{-jet}}^{\text{NLO}}}{\sigma_{\geq 1\text{-jet}}^{\text{NLO}}}, \quad (\text{III.69})$$

$$\epsilon_1^{(c)} = 1 - \frac{\sigma_{\geq 2\text{-jet}}^{\text{NLO}}}{\sigma_{\geq 1\text{-jet}}^{\text{LO}}} + \left(\frac{\sigma_{\geq 1\text{-jet}}^{\text{NLO}}}{\sigma_{\geq 1\text{-jet}}^{\text{LO}}} - 1 \right) \frac{\sigma_{\geq 2\text{-jet}}^{\text{LO}}}{\sigma_{\geq 1\text{-jet}}^{\text{LO}}}. \quad (\text{III.70})$$

These three schemes differ by NNNLO terms. Notice that scheme (III.68) is currently not available yet, but the NNLO QCD corrections to $H + 1\text{-jet}$ production is being computed. The three 3-dimensional vectors (III.55) are

$$\Delta\sigma_{0\text{-jet}} = (0, \sigma_{\text{tot}}\delta\epsilon_0, \epsilon_0\delta\sigma_{\text{tot}}), \quad (\text{III.71})$$

$$\Delta\sigma_{1\text{-jet}} = ((1 - \epsilon_0)\sigma_{\text{tot}}\delta\epsilon_1, -\epsilon_1\sigma_{\text{tot}}\delta\epsilon_0, \epsilon_1(1 - \epsilon_0)\delta\sigma_{\text{tot}}), \quad (\text{III.72})$$

$$\Delta\sigma_{\geq 2\text{-jet}} = (-(1 - \epsilon_0)\sigma_{\text{tot}}\delta\epsilon_1, -(1 - \epsilon_1)\sigma_{\text{tot}}\delta\epsilon_0, (1 - \epsilon_1)(1 - \epsilon_0)\delta\sigma_{\text{tot}}). \quad (\text{III.73})$$

The covariance matrix reads

$$\text{Cov}[\sigma_{0\text{-jet}}, \sigma_{1\text{-jet}}, \sigma_{\geq 2\text{-jet}}] = \begin{pmatrix} \Delta\sigma_{0\text{-jet}} \cdot \Delta\sigma_{0\text{-jet}} & \Delta\sigma_{0\text{-jet}} \cdot \Delta\sigma_{1\text{-jet}} & \Delta\sigma_{0\text{-jet}} \cdot \Delta\sigma_{\geq 2\text{-jet}} \\ \Delta\sigma_{1\text{-jet}} \cdot \Delta\sigma_{1\text{-jet}} & \Delta\sigma_{1\text{-jet}} \cdot \Delta\sigma_{\geq 2\text{-jet}} & \\ \Delta\sigma_{\geq 2\text{-jet}} \cdot \Delta\sigma_{\geq 2\text{-jet}} & & \end{pmatrix}, \quad (\text{III.74})$$

with the following scalar products

$$\begin{aligned}
\Delta\sigma_{0\text{-jet}} \cdot \Delta\sigma_{0\text{-jet}} &= \sigma_{\text{tot}}^2 \delta^2 \epsilon_0 + \epsilon_0^2 \delta^2 \sigma_{\text{tot}}, \\
\Delta\sigma_{0\text{-jet}} \cdot \Delta\sigma_{1\text{-jet}} &= -\epsilon_1 \sigma_{\text{tot}}^2 \delta^2 \epsilon_0 + \epsilon_0 \epsilon_1 (1 - \epsilon_0) \delta^2 \sigma_{\text{tot}}, \\
\Delta\sigma_{0\text{-jet}} \cdot \Delta\sigma_{\geq 2\text{-jet}} &= -(1 - \epsilon_1) \sigma_{\text{tot}}^2 \delta^2 \epsilon_0 + \epsilon_0 (1 - \epsilon_1) (1 - \epsilon_0) \delta^2 \sigma_{\text{tot}}, \\
\Delta\sigma_{1\text{-jet}} \cdot \Delta\sigma_{1\text{-jet}} &= (1 - \epsilon_0)^2 \sigma_{\text{tot}}^2 \delta^2 \epsilon_1 + \epsilon_1^2 \sigma_{\text{tot}}^2 \delta^2 \epsilon_0 + \epsilon_1^2 (1 - \epsilon_0)^2 \delta^2 \sigma_{\text{tot}}, \\
\Delta\sigma_{1\text{-jet}} \cdot \Delta\sigma_{\geq 2\text{-jet}} &= -(1 - \epsilon_0)^2 \sigma_{\text{tot}}^2 \delta^2 \epsilon_1 + \epsilon_1 (1 - \epsilon_1) \sigma_{\text{tot}}^2 \delta^2 \epsilon_0 + \epsilon_1 (1 - \epsilon_1) (1 - \epsilon_0)^2 \delta^2 \sigma_{\text{tot}}, \\
\Delta\sigma_{\geq 2\text{-jet}} \cdot \Delta\sigma_{\geq 2\text{-jet}} &= (1 - \epsilon_0)^2 \sigma_{\text{tot}}^2 \delta^2 \epsilon_1 + (1 - \epsilon_1)^2 \sigma_{\text{tot}}^2 \delta^2 \epsilon_0 + (1 - \epsilon_1)^2 (1 - \epsilon_0)^2 \delta^2 \sigma_{\text{tot}} \text{(III.75)}
\end{aligned}$$

Conclusions

The jet-veto-efficiency (JVE) method is generalised to an arbitrary jet multiplicity, and a general parametrization for the covariance matrix is provided. The method presented here can be applied to any exclusive production of a color singlet accompanied by jets.

9 Higgs production in association with top quarks at the LHC: comparison of different approaches for NLO QCD simulations matched with parton shower¹⁶

Research focus

We present a comparison of the predictions for $t\bar{t}H$ production at the Large Hadron Collider (LHC) including NLO QCD corrections matched to parton shower as obtained by different approaches: i) PowHel, that uses HELAC-NLO to compute NLO matrix-elements and the POWHEG-Box for the matching, ii) the POWHEG-Box combined with a routine that provides the analytic virtual matrix elements as calculated in [439–442], iii) SHERPA combined with the same aforementioned routine. Predictions from these different approaches at NLO QCD / LHE level show very good agreement among each other, with an uncertainty on the inclusive cross section of less than 1%, whereas the differential distributions at the hadron level computed by i) and ii) agree within a few percents, i.e. within the uncertainty due to the renormalization- and factorization-scale variation.

9.1 Introduction

Among the main single-Higgs-boson production mechanisms at the LHC, the associated production of a Higgs boson with a pair of top quarks, i.e. $pp \rightarrow t\bar{t}H$, has the smallest cross section at both $\sqrt{s} = 8$ and 14 TeV. However, the experimental discovery of a Higgs boson with a mass around 125–126 GeV has cast new light on the role played by $t\bar{t}H$ production. Detailed studies of the properties of the discovered particle will be used to confirm or exclude the Higgs mechanism of electroweak symmetry breaking as minimally implemented in the Standard Model. In this context, the measurement of the $t\bar{t}H$ production rate can provide a clean direct access to the top-Higgs Yukawa coupling, probably the most crucial coupling to fermions, on which the present SM uncertainties are still very large. Thus, both the ATLAS and CMS experimental collaborations at LHC have provided analyses trying to isolate $t\bar{t}H$ events, exploiting the full amount of data available at both $\sqrt{s} = 7$ and 8 TeV [443–446], and even more dedicated studies are part of the Higgs precision program for Run II of the LHC.

First analyses of $t\bar{t}H$ events mainly considered the $H \rightarrow b\bar{b}$ decay channel [443, 444], since it offers the highest branching ratio for a Higgs boson with a mass around 125 GeV. However, due to the high uncertainties on the background for this channel, also related to the difficulties

¹⁶M.V. Garzelli, H.B. Hartanto, B. Jäger, A. Kardos, L. Reina, Z. Trócsányi, D. Wackerroth

in reconstructing heavy-flavor jets and distinguishing them from light jets, more recent analyses have tried to exploit different decay channels, like $H \rightarrow \tau^+ \tau^-$ and $H \rightarrow \gamma \gamma$ [445, 446].

For most of the analyses published so far, the shapes of the expected differential distributions used during the experimental studies are still produced on the basis of LO results, provided by PYTHIA, although fully differential theoretical predictions and events including QCD NLO corrections matched with parton shower are already publicly available since 2011. In particular, NLO QCD corrections to $t\bar{t}H$ have first been computed in Refs. [439–442, 447, 448] and specified to the case of both the Tevatron and the LHC with $\sqrt{s} = 14$ TeV. These predictions have further been extended to the case of the LHC with $\sqrt{s} = 7$ TeV and 8 TeV in Ref. [38] and Ref. [40], respectively, whereas matchings with parton shower have been presented both in Ref. [449] by means of the `aMC@NLO` approach and in Ref. [450] by means of the `PowHel` approach. Furthermore, a comparison between the last two approaches, specified to the case of the LHC with $\sqrt{s} = 7$ TeV, appeared in Ref. [39] and showed very good agreement at least at the level of the residual uncertainties due to variations of the renormalization and factorization scales, of the parton distribution function (PDF), and of the shower Monte Carlo (SMC) (`PYTHIA` [288, 333] vs. `HERWIG++` [161]) used.

In this contribution we present a study of theoretical predictions for $t\bar{t}H$ at $\sqrt{s} = 8$ TeV by comparing three different methods: the already existing `PowHel` approach and two new implementations, both relying on virtual matrix elements analytically computed on the basis of Refs. [439–442], interfaced with the `POWHEG-Box` [26] and `SHERPA` [166, 451], respectively.

9.2 Short review of the implementations

9.2.1 *PowHel*

The `PowHel` implementation of $t\bar{t}H$ relies on the interface between the publicly available event generators `HELAC-NLO` [5] and the `POWHEG-Box` [26]. In particular, the `HELAC-NLO` components (`HELAC-Phegas` [452], `HELAC-1LOOP` [453], `HELAC-Dipole` [204]) are used to compute all matrix elements required as input by the `POWHEG-Box`, that performs the matching to parton shower according to the `POWHEG` [37, 170] formalism. Working in a general multiparticle framework, 1-loop matrix elements are computed automatically, by using the `OPP` method [402] complemented by analytical formulas for calculating the contributions of the R_2 rational terms [454], all implemented in `HELAC-1LOOP` [455]. On the other hand, the subtraction terms necessary to factor out the infrared NLO singularities in dimensional regularization are computed automatically by the `POWHEG-Box`, on the basis of the `FKS` subtraction formalism [456]. The `PowHel` implementation of $t\bar{t}H$ was described in detail and extensively tested in the original paper [450] and cross-checked with respect to the `aMC@NLO` one at both partonic and hadronic level in Refs. [39, 450]. The output of `PowHel` are events stored in files in Les Houches format (LHE) [457], including up to first radiation emission, publicly available on the web [458] at the address: <http://grid.kfki.hu/twiki/bin/view/DbTheory/TthProd>. These events can be further showered by means of standard SMC event generators (so far, both the interfaces with the fortran version of `PYTHIA` and `HERWIG++` have been tested and used to produce theoretical predictions). Several millions of $t\bar{t}H$ events provided by `PowHel` at different energies ($\sqrt{s} = 7, 8$ and 14 TeV) and in different configurations, have already been made available and used by the experimental collaborations at LHC for their preliminary studies aiming at optimizing their $t\bar{t}H$ analysis setup.

9.2.2 *One-loop matrix elements matched with the POWHEG-Box and SHERPA*

In this study we have implemented the one-loop QCD matrix elements for $q\bar{q} \rightarrow t\bar{t}H$ and $gg \rightarrow t\bar{t}H$ calculated in Refs. [439–442] in both the `POWHEG-Box` and `SHERPA`. Both implemen-

tations have been tested at the NLO QCD parton level comparing total and differential cross sections against the original calculation, where the $O(\alpha_s)$ real-radiation emission is calculated using phase-space-slicing techniques. They are in the form of a library of routines that contains all the analytical building blocks needed to calculate the $\mathcal{O}(\alpha_s)$ one-loop QCD corrections to the partonic channels mentioned above and have been thoroughly tested against the analogous calculation presented in Refs. [447, 448]. These routines are already publicly available in `SHERPA` and will soon be made available as part of the `POWHEG-Box` repository. The tools and algorithms that have been used in the calculation are thoroughly explained in the original publications to which we refer for all details.

9.3 Checks and predictions

The NLO predictions discussed in this section were obtained by considering proton-proton collisions at $\sqrt{s} = 8$ TeV, using the CT10 NLO set of parton distribution functions with five active flavours [289] as provided by the LHAPDF interface [273] and a running strong coupling computed accordingly. We fixed masses and couplings using $m_t = 172.5$ GeV, $m_H = 125$ GeV, $m_W = 80.385$ GeV, $m_Z = 91.1876$ GeV, and the Fermi constant $G_F = 1.16639 \cdot 10^{-5}$ GeV⁻². The electromagnetic coupling was derived from G_F , m_Z and m_W in the G_μ scheme. Factorization and renormalization scales were varied around the central value $\mu_0 = \mu_R = \mu_F = m_t + m_H/2$ by a factor of two, in order to compute scale-uncertainty. Top quarks, as well as the Higgs boson, were produced on shell, whereas their subsequent decays were handled by the SMC code used, according to its default implementation. In this study recent fortran versions of `PYTHIA` (`PYTHIA 6.4.25` - `6.4.28`) were interfaced to both the `PowHe1` and the `POWHEG-Box` implementations, whereas `SHERPA` includes its own parton-shower implementation.

For each of the implementations described in the previous section, we generated several millions of events and stored them in the Les Houches Event (LHE) file format, including up to first radiation emission (LHE level). This first emission is computed internally according to the matching scheme of the respective program, i.e. the `POWHEG` scheme in the `POWHEG-Box` and the `MC@NLO` scheme in `SHERPA`. Subsequent emissions are always computed by the SMC.

We first compare inclusive results, without applying any selection cuts. The total NLO QCD cross sections from the three implementations at the central-scale value turned out to be respectively $\sigma_{\text{PowHe1}} = 126.8 \pm 0.1$ fb, $\sigma_{\text{POWHEG-Box}} = 126.7 \pm 0.1$ and $\sigma_{\text{SHERPA}} = 126.8 \pm 0.1$ fb, showing agreement within the statistical uncertainty. Uncertainties related to scale variation in the interval $[\mu_0/2, 2\mu_0]$, as computed by `PowHe1` amount to + 5.2 - 11.8 fb, corresponding to + 4.1% - 9.3% with respect to the central value quoted above.

Differential distributions of the transverse momentum of the top quark, the antitop quark and the Higgs boson, as well as their rapidities, are shown in Fig. III.36. The ratio of the predictions of the `POWHEG-Box` and `PYTHIA` with respect to those by `PowHe1` is also shown in each panel. The slightly larger fluctuations shown by `SHERPA` predictions with respect to those from `PowHe1` and `POWHEG-Box` have a statistical origin (the number of events we generated so far using `SHERPA` is slightly lower than those using the other two implementations). Agreement within 10% is found for the three different implementations considered in this paper, in the p_\perp region below 450 GeV.

In the pre-showered events, a resolved first radiation emission may emerge, leading to a light jet. The predictions for the transverse momentum and rapidity of this emission, shown in Fig. III.37, are very sensitive to the matching. A further zoom in the Sudakov region is presented in Fig. III.38. From these plots we can conclude that the matching implementations in `PowHe1` and the `POWHEG-Box` are fully consistent among each other. On the other hand, a consistent comparison with the first radiation emission from `SHERPA` is more delicate due to the differences in the matching algorithm, which accounts for the respective different way to solve

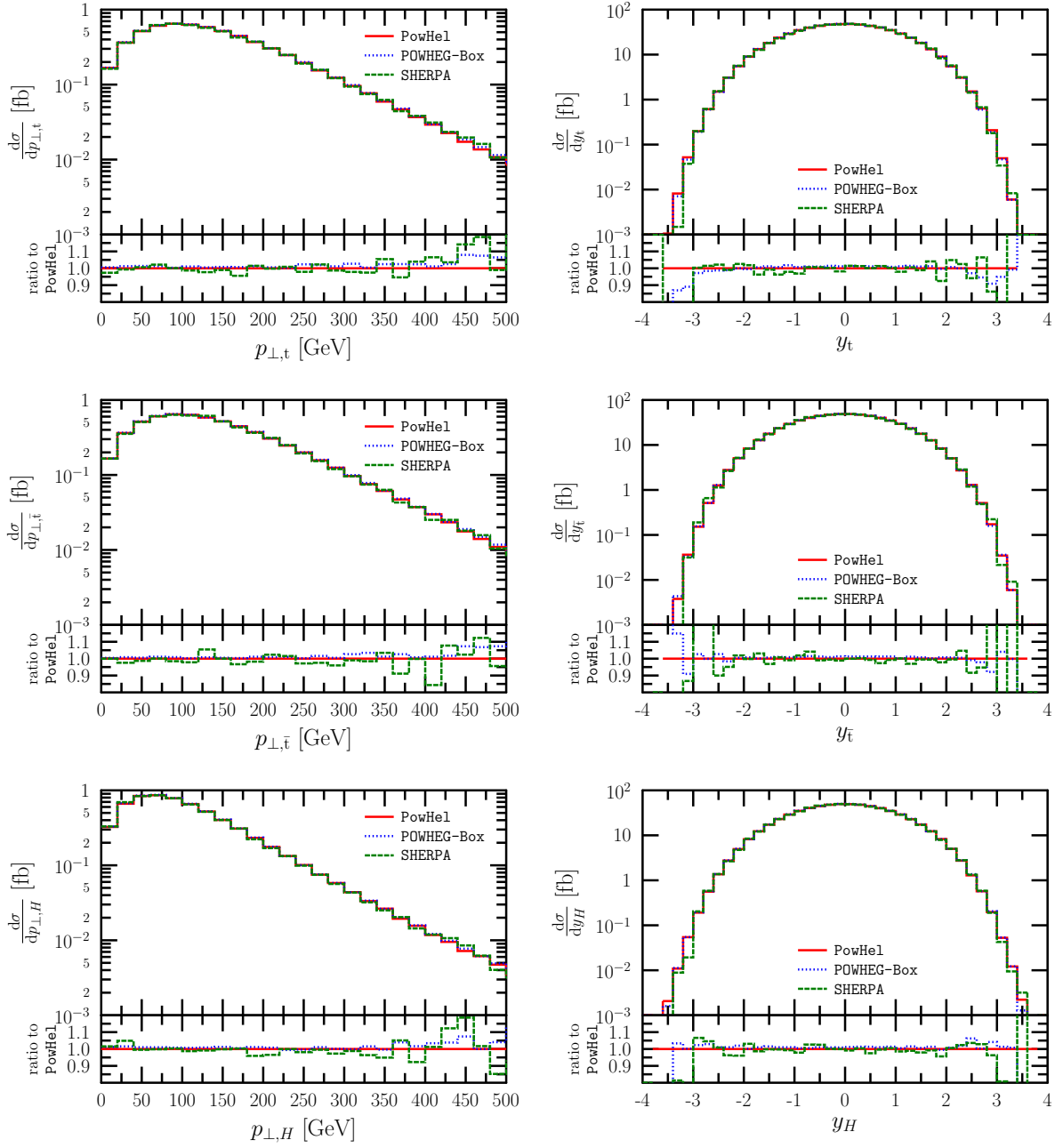


Fig. III.36: Transverse momentum and rapidity of the top (upper panel), the anti-top (intermediate panel), and the Higgs boson (lower panel), as obtained at LHE level by the three NLO QCD + PS implementations [PowHel (red solid line), the POWHEG-Box (blue dotted line), and SHERPA (green dashed line)]. The ratio of the POWHEG-Box and SHERPA predictions with respect to those from PowHel is shown in the lower inset of each panel.

the double-counting problem.

In order to further explore the kinematic properties of the produced particles the separations in the rapidity – azimuthal-angle plane between different pairs of heavy particles are shown in Fig. III.39. Predictions from PowHel and the POWHEG-Box agree within 3% in the $[0, \sim 3.5]$ ΔR interval for all considered pairs, whereas, for larger ΔR , PowHel produces a small

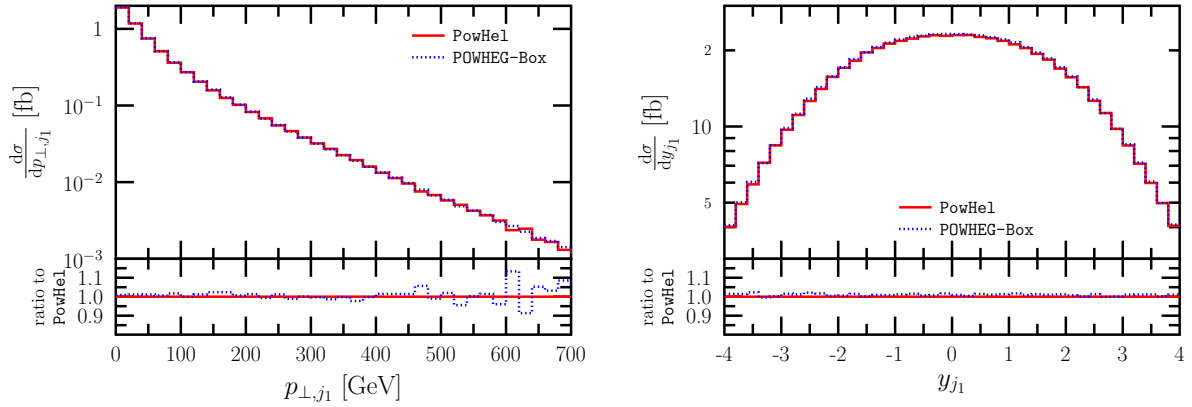


Fig. III.37: Transverse momentum and rapidity of the hardest resolved jet, as obtained at LHE level by the two POWHEG-based NLO QCD + PS implementations [PowHel (red solid line), and the POWHEG-Box (blue dotted line)]. The ratio of the POWHEG-Box and SHERPA predictions with respect to those from PowHel is shown in the lower inset of each panel.

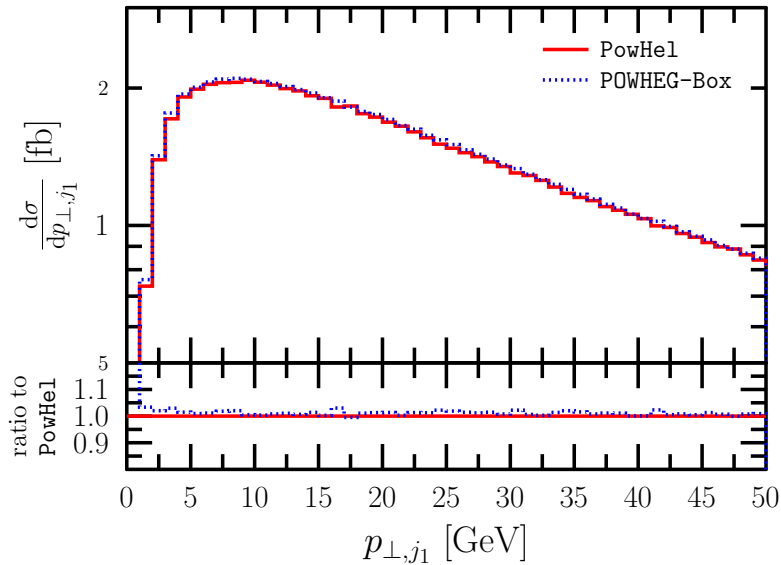


Fig. III.38: Zoom of the transverse momentum of the hardest resolved jet in the low p_{\perp} region, as obtained at LHE level by the two POWHEG-based NLO QCD + PS implementations [PowHel (red solid line), and the POWHEG-Box (blue dotted line)]. The ratio of the POWHEG-Box predictions with respect to those from PowHel is shown in the lower inset.

excess of events with respect to the POWHEG-Box. SHERPA predictions for $\Delta R(t, \bar{t})$, $\Delta R(t, \bar{H})$ and $\Delta R(\bar{t}, H)$, agree within 10% with those from the other two implementations up to $\Delta R \sim 3.5$, although the distributions show some shape distortion with a steeper slope with respect to those from the other two implementations, which are characterized by a similar stable shape.

After checking the predictions at the NLO accuracy and from pre-showered events, as a next step we compare predictions after full SMC simulation, i.e. after parton shower, hadronization, and hadron decay. We showered the events produced by PowHel and the POWHEG-Box by means of PYTHIA, by using the Perugia-0 tune [459], providing a p_{\perp} -ordered shower. Shower

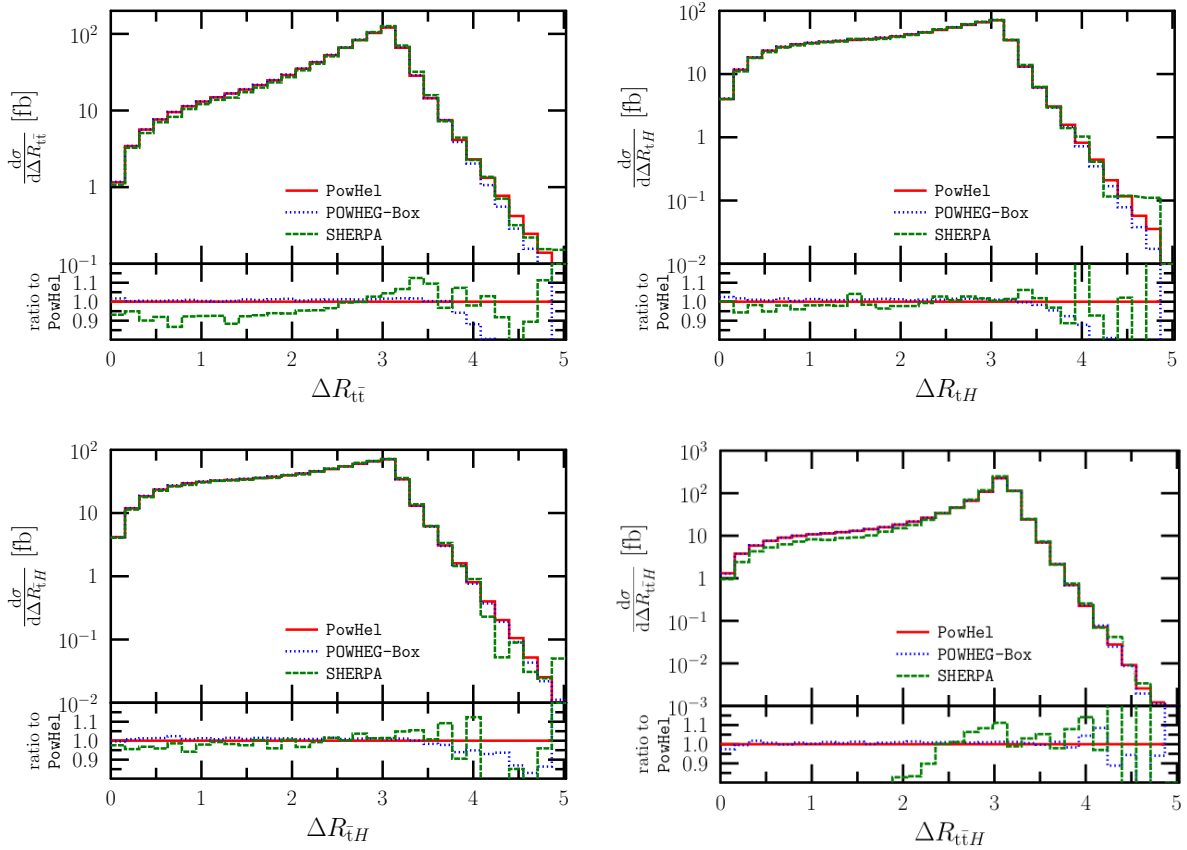


Fig. III.39: Separation in the rapidity – azimuthal-angle plane of different pairs of heavy particles $[(t, \bar{t}), (t, H), (\bar{t}, H), (t\bar{t}, H)]$, as obtained at LHE level by the three NLO QCD + PS implementations [PowHel (red solid line), the POWHEG-Box (blue dotted line), and SHERPA (green dashed line)]. The ratio of the POWHEG-Box and SHERPA predictions with respect to those from PowHel is shown in the lower inset of each panel.

emissions beyond the leading one were forced to occur with a p_{\perp} smaller than the first one, already computed by the POWHEG matching. In order to limit jet activity, we forced the Higgs to decay in the $H \rightarrow \gamma\gamma$ channel. All other particles and hadrons were treated according to the PYTHIA default implementation.

In order to investigate the effect of the parton shower on experimentally accessible distributions, we consider differential cross-sections involving hard jets and leptons at the SMC level. We reconstruct jets out of all hadronic tracks with rapidity $|y| < 5$ by the anti- k_T algorithm [284] as implemented in the Fastjet package [283], with a resolution parameter of $R = 0.4$. Jets that do not exhibit a transverse momentum $p_{\perp}^{\text{jet}} > 20$ GeV and a rapidity $|y^{\text{jet}}| < 4.5$ are discarded. Similarly, we consider only leptons with a transverse momentum $p_{\perp}^{\ell} > 20$ GeV and rapidity $|y^{\ell}| < 2.5$ that are well-separated from all hard jets in the rapidity – azimuthal-angle plane, i.e. such that $\Delta R_{\ell, \text{jet}} > 0.4$.

Distributions concerning the total number of jets per event and the number of jets per event with a $p_{\perp} > 50$ GeV are shown in Fig. III.40, and are peaked around 4 and 2 jets, respectively, for both implementations. These peaks correspond to the semileptonic decay of the top quarks, taking into account that in these simulations the Higgs boson was not allowed to decay hadronically. The agreement between PowHel and the POWHEG-Box is within a very few

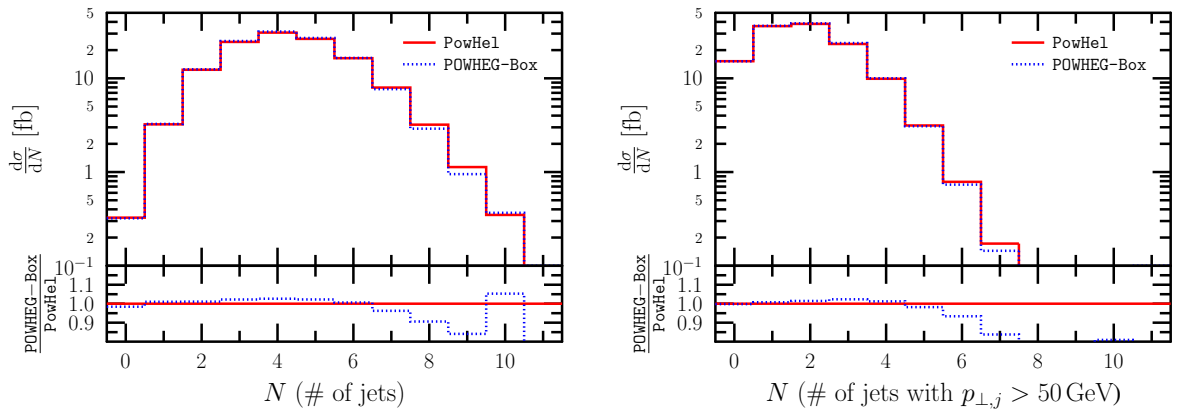


Fig. III.40: Number of jets per event and number of jets per event with $p_{\perp,j} > 50$ GeV, as obtained at the hadron level by the two NLO QCD + PS implementations [PowHel (red solid line), and the POWHEG-Box (blue dotted line)] interfaced to PYTHIA. The ratio of the POWHEG-Box predictions with respect to those from PowHel is shown in the lower inset of each panel.

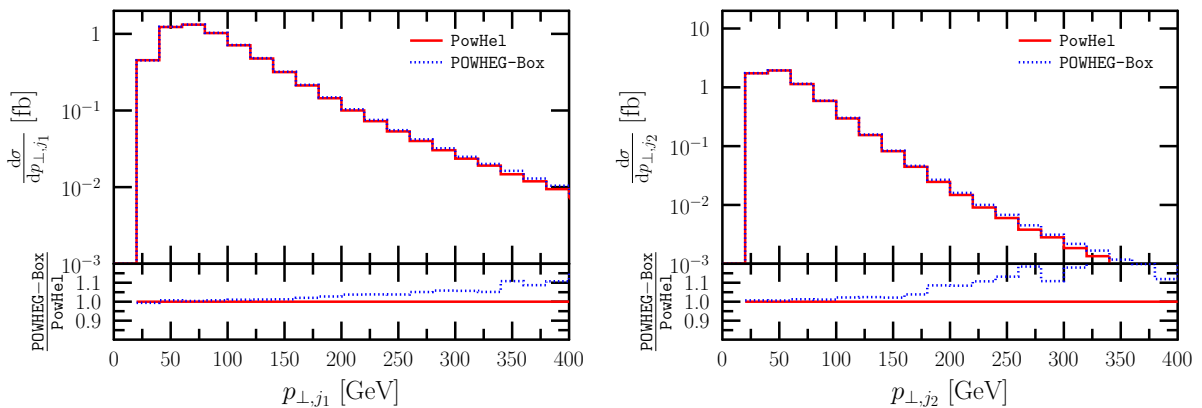


Fig. III.41: Transverse momenta of the hardest and next-to-hardest jets, as obtained at the hadron level by the two NLO QCD + PS implementations [PowHel (red solid line), and the POWHEG-Box (blue dotted line)] interfaced to PYTHIA. The ratio of the POWHEG-Box predictions with respect to those from PowHel is shown in the lower inset of each panel.

percents from 0 up to 6 jets, whereas, for higher jet multiplicities, PowHel leads to slightly more events with a larger number of (slightly softer) jets than the POWHEG-Box.

The distributions of the transverse momentum of the hardest and next-to-hardest jets are shown in Fig. III.41, from where it is clear that PowHel and the POWHEG-Box predictions agree up to about 200 GeV. The small differences at higher transverse momentum reflect the slight deviation found in the distributions of $p_{\perp,t}$ and $p_{\perp,\bar{t}}$ in the pre-showered events.

The rapidities of these same jets are presented in Fig. III.42 showing very good agreement between the two implementations in the whole phase-space region plotted.

Predictions concerning the ΔR separation between these two jets, presented in Fig. III.43, show again an almost perfect agreement between PowHel and the POWHEG-Box, whereas those concerning their invariant mass show agreement within 10%, with the POWHEG-Box distribution slightly harder than the PowHel one.

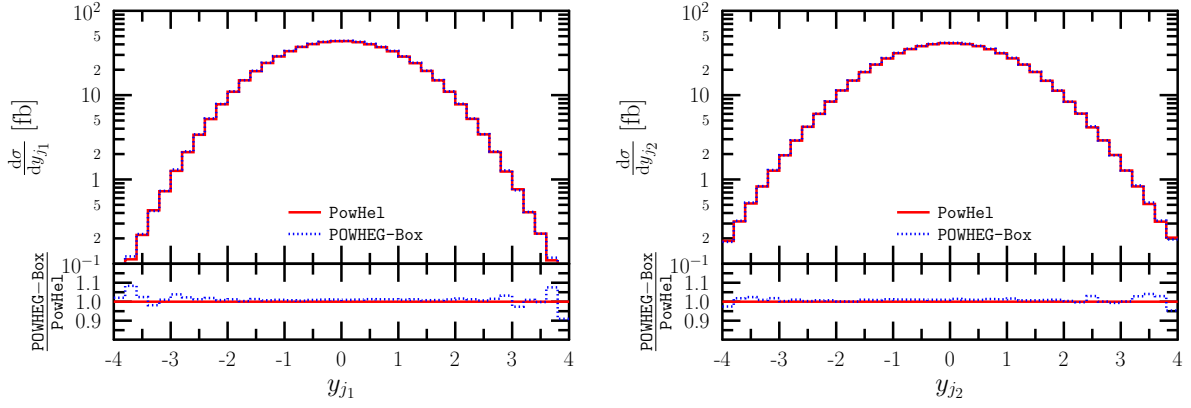


Fig. III.42: Rapidities of the hardest and next-to-hardest jets, as obtained at the hadron level by the two NLO QCD + PS implementations [PowHel (red solid line), and the POWHEG-Box (blue dotted line)] interfaced to PYTHIA. The ratio of the POWHEG-Box predictions with respect to those from PowHel is shown in the lower inset of each panel.

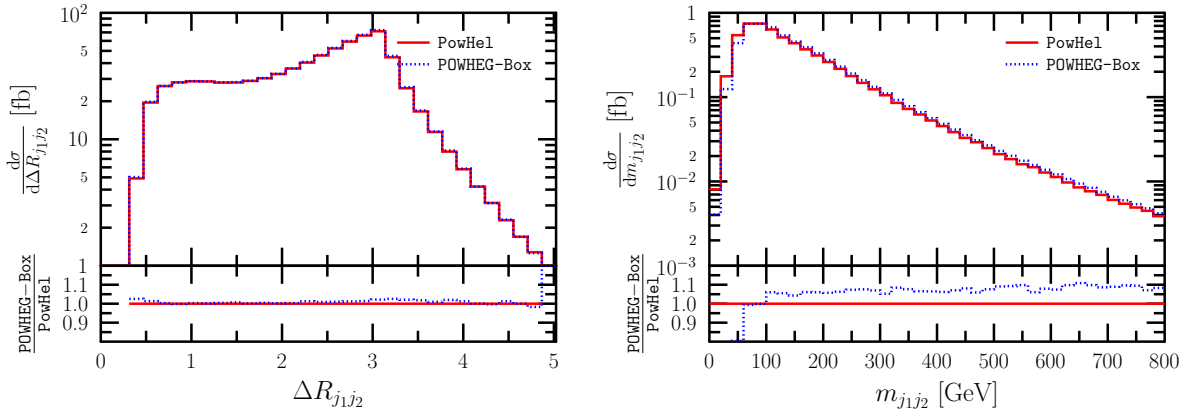


Fig. III.43: Separation between the two hardest jets in the rapidity – azimuthal-angle plane and their invariant mass, as obtained at the hadron level by the two NLO QCD + PS implementations [PowHel (red solid line), and the POWHEG-Box (blue dotted line)] interfaced to PYTHIA. The ratio of the POWHEG-Box predictions with respect to those from PowHel is shown in the lower inset of each panel.

Finally, distributions related to the hardest isolated lepton and antilepton of each event are shown in Fig. III.44 and III.45. As for transverse momentum distributions, shown in Fig. III.44, the agreement between PowHel and the POWHEG-Box predictions decreases with increasing p_{\perp} , staying within 10% up to ~ 200 GeV, with the POWHEG-Box predictions increasingly harder than those from PowHel in the tails. As for rapidities, shown in Fig. III.45, the agreement between PowHel and the POWHEG-Box predictions is within 5% over the whole range under study and no shape distortion occurs.

The comparison of the predictions by PowHel + PYTHIA and the POWHEG-Box + PYTHIA shown in Figs. III.40 - III.45 with those from SHERPA after its whole internal SMC evolution is still under way.

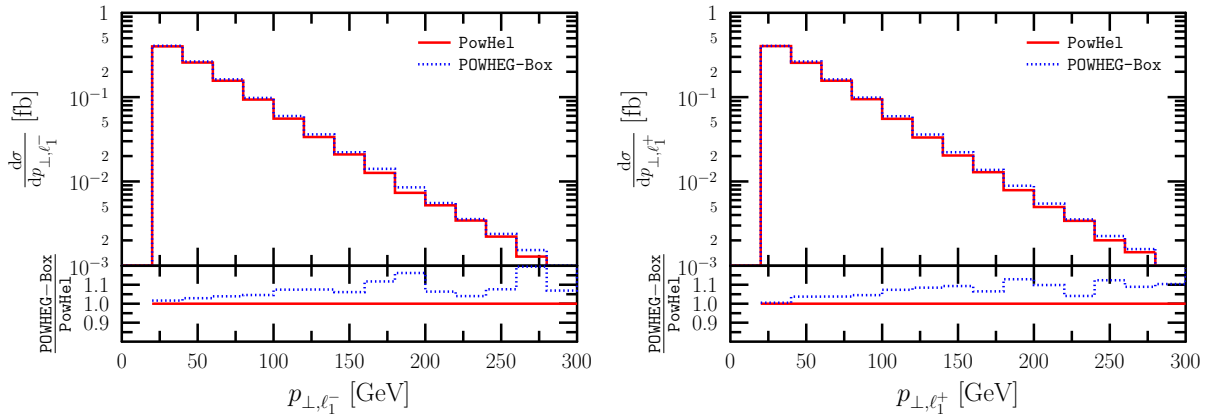


Fig. III.44: Transverse momenta of the hardest isolated lepton and the hardest isolated antilepton, as obtained at the hadron level by the two NLO QCD + PS implementations [PowHel (red solid line), and the POWHEG-Box (blue dotted line)] interfaced to PYTHIA. The ratio of the POWHEG-Box predictions with respect to those from PowHel is shown in the lower inset of each panel.

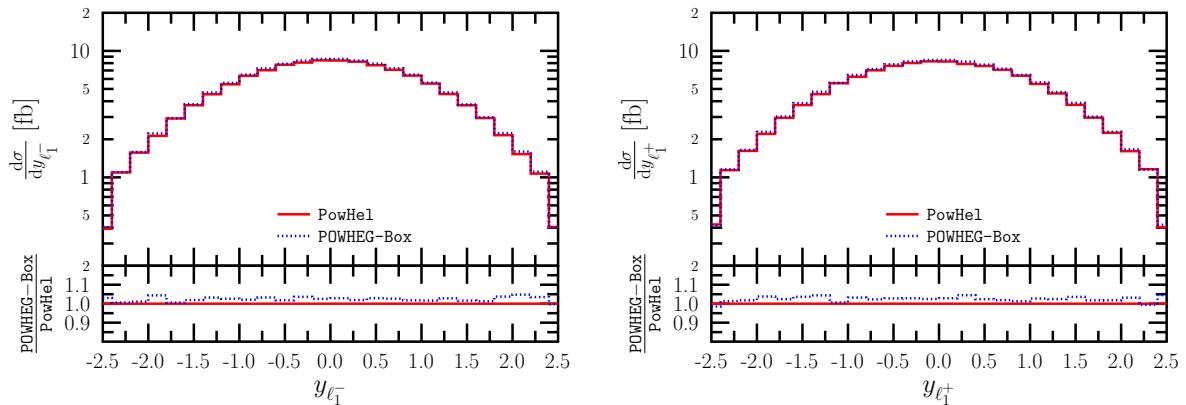


Fig. III.45: Rapidities of the hardest isolated lepton and the hardest isolated antilepton, as obtained at the hadron level by the two NLO QCD + PS implementations [PowHel (red solid line), and the POWHEG-Box (blue dotted line)] interfaced to PYTHIA. The ratio of the POWHEG-Box predictions with respect to those from PowHel is shown in the lower inset of each panel.

9.4 Conclusions

We have compared three different implementations of $t\bar{t}H$ production at the LHC, including NLO QCD corrections matched to parton showers. One of these implementations (PowHel) can be considered mature, and was already extensively checked in the past, whereas the other two (POWHEG-Box and SHERPA) are new and introduced in this paper for the first time. Distributions at the inclusive level are in agreement within a few percent, i.e. within renormalization and factorization scale uncertainties, over a large fraction of the phase-space. The regions where distributions from different implementations show the largest disagreement turned out to be the high transverse momentum tails. Thus, in view of experimental studies in boosted regions, the comparison of different implementations is particularly important. The PowHel and POWHEG-Box matching implementations turned out to be fully consistent among each other, as shown by the very good agreement on the properties of first radiation emission in the Sudakov region. A more

detailed comparison will be presented elsewhere.

Acknowledgements

M. V. G., B. J., A. K., L. R., and D. W. would like to thank the Aspen Center for Physics where preliminary work on the comparison presented in this study was initiated, after initial discussions in Les Houches. Their work in Aspen was supported in part by the National Science Foundation under Grant No. PHYS-1066293. B. J. would like to thank the AHRP alliance for support. A. K. and Z. T. would like to thank the LHCPHenoNet network PITN-GA-2010-264564 for support, the Hungarian Scientific Research Fund grant K-101482, and the Supercomputer, the national virtual lab TAMOP-4.2.2.C-11/1/KONV-2012-0010 project. The work of L.R. is partially supported by the U.S. Department of Energy under grant DE-FG02-13ER41942, and by the European Research Council under the European Union's Seventh Framework Programme (FP/2007-2013) ERC Grant Agreement n. 279972 "NPFlavour". The work of D.W. is supported in part by the U.S. National Science Foundation under grant no. PHY-1118138.

10 Next-to-next-to-leading order corrections to Higgs boson pair production at the LHC¹⁷

10.1 Introduction

Recently, both ATLAS [425] and CMS [426] collaborations discovered a new boson at the Large Hadron Collider (LHC), whose properties are so far compatible with the long sought standard model (SM) Higgs boson [460–462]. In order to decide whether this particle is indeed responsible for the electroweak symmetry breaking, a precise measurement of its couplings to fermions, gauge bosons and its self-interactions is needed. In particular, the knowledge of the Higgs self-couplings is the only way to reconstruct the scalar potential.

The possibility of observing Higgs pair production at the LHC have been discussed in Refs. [55, 463–470]. In general, it has been shown that despite the smallness of the signal and the large background its measurement can be achieved at a luminosity-upgraded LHC.

The dominant mechanism for SM Higgs pair production at hadron colliders is gluon fusion, mediated by a heavy-quark loop. The leading-order (LO) cross section has been calculated in Refs. [471–473]. The next-to-leading order (NLO) QCD corrections have been evaluated in Ref. [52] within the large top-mass approximation and found to be large, with an inclusive K factor close to 2. The finite top-mass effects were analysed at this order in Ref. [53], finding that a precision of $\mathcal{O}(10\%)$ can be achieved if the exact top-mass leading-order cross section is used to normalize the corrections.

Given the size of the NLO corrections, it is necessary to reach higher orders to provide accurate theoretical predictions. In this proceeding we present the next-to-next-to-leading order (NNLO) corrections for the inclusive Higgs boson pair production cross section [54].

10.2 Description of the calculation

The effective single and double-Higgs coupling to gluons is given, within the large top-mass approximation, by the following Lagrangian

$$\mathcal{L}_{\text{eff}} = -\frac{1}{4}G_{\mu\nu}G^{\mu\nu} \left(C_H \frac{H}{v} - C_{HH} \frac{H^2}{v^2} \right). \quad (\text{III.76})$$

Here $G_{\mu\nu}$ stands for the gluonic field strength tensor and $v \simeq 246$ GeV is the Higgs vacuum expectation value. While the $\mathcal{O}(\alpha_S^3)$ of the C_H expansion is known [474, 475], the QCD corrections of C_{HH} are only known up to $\mathcal{O}(\alpha_S^2)$ [374]. Up to that order, both expansions yield the same result.

The NNLO contributions to the SM Higgs boson pair production squared matrix element can be separated into two different classes: (a) those containing two gluon-gluon-Higgs vertices (either ggH or $ggHH$) and (b) those containing three or four effective vertices. Given the similarity between ggH and $ggHH$ vertices, the contributions to the class (a) are equal to those of single Higgs production, except for an overall LO normalization (assuming that $C_H = C_{HH}$ up to $\mathcal{O}(\alpha_S^3)$). These results can be obtained from Refs. [476–478].

Contributions to the class (b) first appear at NLO as a tree-level contribution to the subprocess $gg \rightarrow HH$, given that each ggH and $ggHH$ vertex is proportional to α_S . Then, at NNLO we have one-loop corrections and single real emission corrections. The former have been calculated in Ref. [479]. The remaining contributions involve the partonic subprocesses $gg \rightarrow HH + g$ and $qg \rightarrow HH + q$ (with the corresponding crossings). Examples of the Feynman diagrams involved in the calculation are shown in Figure III.46.

¹⁷D. de Florian and J. Mazzitelli

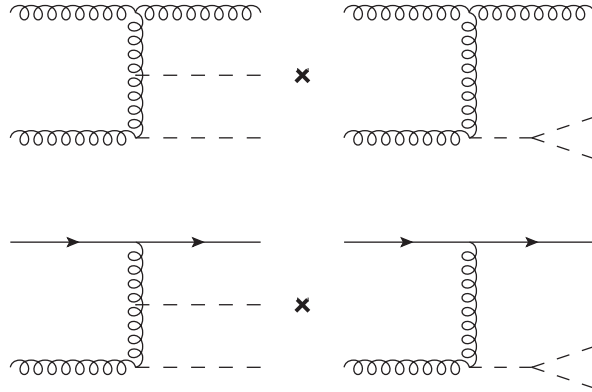


Fig. III.46: Example of Feynman diagrams needed for the NNLO calculation for $gg \rightarrow HHg$ (top) and $gg \rightarrow HHq$ (bottom) subprocesses. Other parton subprocesses can be obtained from crossings.

To compute this contribution we used the Mathematica packages FeynArts [480] and FeynCalc [481] in order to generate the Feynman diagrams and evaluate the corresponding amplitudes. The calculation was performed using nonphysical polarizations, which we cancel by including ghosts in the initial and final states. In order to subtract the soft and collinear divergencies, we used the Frixione, Kunszt, and Signer subtraction method [456]. Further details of the calculation, together with the explicit expressions for the NNLO results, can be found in Ref. [54].

10.3 Phenomenology

Here we present the numerical results for the LHC. At each order, we use the corresponding MSTW2008 [235] set of parton distributions and QCD coupling. We recall that we always normalize our results using the exact top- and bottom-mass dependence at LO. For this analysis we use $M_H = 126$ GeV, $M_t = 173.18$ GeV and $M_b = 4.75$ GeV. The bands of all the plots are obtained by varying independently the factorization and renormalization scales in the range $0.5 Q \leq \mu_F, \mu_R \leq 2 Q$, with the constraint $0.5 \leq \mu_F/\mu_R \leq 2$, being Q the invariant mass of the Higgs pair system.

We assume for the phenomenological results that the two-loop corrections to the effective vertex $ggHH$ are the same than those of ggH (that is $C_{HH}^{(2)} = C_H^{(2)}$, following the notation of Ref. [479]), as it happens at one-loop order. We change its value in the range $0 \leq C_{HH}^{(2)} \leq 2C_H^{(2)}$ in order to evaluate the impact of this unknown coefficient and find a variation in the total cross section of less than 2.5%.

In Figure III.47 we present the LO, NLO and NNLO predictions for the hadronic cross section at the LHC as a function of the Higgs pair invariant mass, for a c.m. energy $E_{cm} = 14$ TeV. As can be noticed from the plot, only at this order the first sign of convergence of the perturbative series appears, finding a nonzero overlap between the NLO and NNLO bands. Second order corrections are sizeable, this is noticeable already at the level of the total inclusive cross sections, where the increase with respect to the NLO result is of $\mathcal{O}(20\%)$, and the K factor with respect to the LO prediction is about $K_{\text{NNLO}} = 2.3$. The scale dependence is clearly reduced at this order, resulting in a variation of about $\pm 8\%$ around the central value, compared to a total variation of $\mathcal{O}(\pm 20\%)$ at NLO.

In Figure III.48 we show the total cross section as a function of the c.m. energy E_{cm} , in the range from 8 TeV to 100 TeV. We can observe that the size of the NLO and NNLO corrections

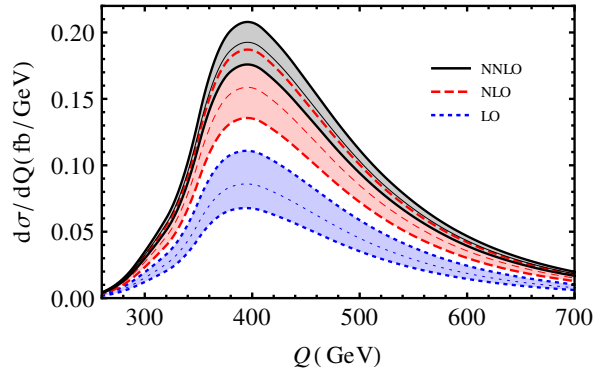


Fig. III.47: Higgs pair invariant mass distribution at LO (dotted blue), NLO (dashed red) and NNLO (solid black) for the LHC at c.m. energy $E_{cm} = 14$ TeV. The bands are obtained by varying μ_F and μ_R in the range $0.5Q \leq \mu_F, \mu_R \leq 2Q$ with the constraint $0.5 \leq \mu_F/\mu_R \leq 2$.

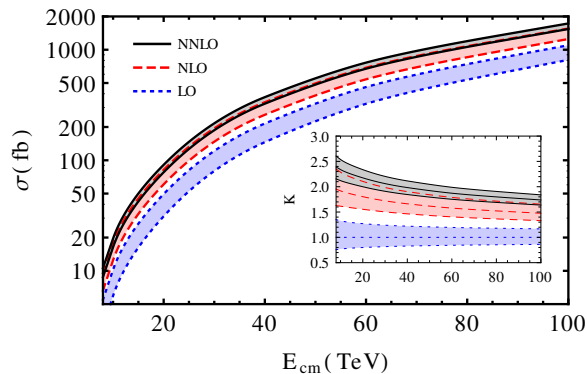


Fig. III.48: Total cross section as a function of the c.m. energy E_{cm} for the LO (dotted blue), NLO (dashed red) and NNLO (solid black) prediction. The bands are obtained by varying μ_F and μ_R as indicated in the main text. The inset plot shows the corresponding K factors.

is smaller as the c.m. energy increases. We can also notice that the scale dependence is substantially reduced in the whole range of energies when we include the second order corrections. The ratio between NNLO and NLO predictions as a function of the c.m. energy is quite flat, running from 1.22 at 8 TeV to 1.18 at 100 TeV. On the other hand, the ratio between NNLO and LO runs from 2.39 to 1.74 in the same range of energies.

Finally, we present in Table III.10 the value of the NNLO cross section for $E_{cm} = 8, 14, 33$ and 100 TeV. We have taken into account three sources of theoretical uncertainties: missing higher orders in the QCD perturbative expansion, which are estimated by the scale variation, and uncertainties in the determination of the parton flux and strong coupling. To estimate the parton distributions and coupling constant uncertainties we used the MSTW2008 90% C.L. error PDF sets [482], which are known to provide very close results to the PDF4LHC working group recommendation for the envelope prescription [218]. As we can observe from Table III.10, nonperturbative and perturbative uncertainties are of the same order.

It is worth noticing that the soft-virtual approximation, which was presented in Ref. [479], gives an extremely accurate prediction for the NNLO cross section, overestimating for example the $E_{cm} = 14$ TeV result by less than 2%. As expected, this approximation works even better

| E_{cm} | 8 TeV | 14 TeV | 33 TeV | 100 TeV |
|------------------------|------------|------------|------------|------------|
| σ_{NNLO} | 9.76 fb | 40.2 fb | 243 fb | 1638 fb |
| Scale [%] | +9.0 – 9.8 | +8.0 – 8.7 | +7.0 – 7.4 | +5.9 – 5.8 |
| PDF [%] | +6.0 – 6.1 | +4.0 – 4.0 | +2.5 – 2.6 | +2.3 – 2.6 |
| PDF+ α_S [%] | +9.3 – 8.8 | +7.2 – 7.1 | +6.0 – 6.0 | +5.8 – 6.0 |

Table III.10: Total cross section as a function of the c.m. energy at NNLO accuracy. We use the exact LO prediction to normalize our results. The different sources of theoretical uncertainties are discussed in the main text.

than for single Higgs production, due to the larger invariant mass of the final state.

Acknowledgements

This work was supported in part by UBACYT, CONICET, ANPCyT and the Research Executive Agency (REA) of the European Union under the Grant Agreement number PITN-GA-2010-264564 (LHCPhenoNet).

11 Photon isolation studies¹⁸

11.1 Introduction

Many interesting physics signatures at the LHC involve the presence of single or multiple photons in the final state. These photons may either be produced directly, through the fragmentation of a quark or gluon, or else through the decay of a resonance – such as e.g. the Higgs boson.

The production of prompt photons is the subject of this analysis. The expression ‘prompt photons’ refers to photons produced at large transverse momenta which do not arise from the decay of hadrons, such as π^0 , η , etc. Prompt photons can be produced according to two possible mechanisms, one of them being fragmentation.

To be precise, the collider experiments at the Tevatron and the LHC do not perform *inclusive* photon measurements. The background of secondary photons coming from the decays of π^0 , η , etc., overwhelms the signal by several orders of magnitude. To reject this background, the experimental selection of prompt diphotons requires *isolation* cuts. In addition to the rejection of the background of secondary photons, the isolation cuts (or criteria) also affect the prompt-diphoton cross section itself, in particular by reducing the effect of fragmentation.

The standard cone isolation and the “smooth” cone isolation proposed by Frixione [158] are two of these criteria. The standard cone isolation is easily implemented in experiments, but it only suppresses a fraction of the fragmentation contribution. The smooth cone isolation (formally) eliminates the entire fragmentation contribution, but its experimental implementation (at least in its original form) is complicated¹⁹ by the finite granularity of the LHC and Tevatron detectors.

On the theoretical side, including fragmentation contributions to photon production can greatly increase the complexity of the calculations, while the application of appropriate isolation cuts can effectively remove those fragmentation contributions. How to apply these isolation criteria to the theoretical tools and how to deal with the fragmentation contributions consistently by the theory side is one of the subjects of this note.

¹⁸L. Cieri and D. de Florian

¹⁹There is activity in the experimental implementation [160, 483, 484] of the discretized version of the smooth isolation criterion. An experimental implementation of the smooth isolation criterion was done by the OPAL collaboration [485].

Besides the differences between these two isolation criteria, it is possible (*i.e.* it has physical meaning) to compare theoretical descriptions obtained using the smooth cone isolation criterion and data taken with the standard criterion, because a cross section obtained using the smooth cone isolation criterion provides always a lower bound for a cross section in which the standard criterion was implemented, if one uses the same isolation parameters for both criteria. Furthermore, as we show in this note, this bound turns out to be an excellent approximation to the standard criterion result with an accuracy of the order of the 1% if tight cuts are imposed.

Given these results, and the fact that in general it is not possible to exactly match the experimental isolation conditions to the theoretical implementation and viceversa, we propose a pragmatic accord to perform a more precise comparison between the data and the fixed order calculations, that allows to extend the TH computation up to NNLO in some cases. That is the major motivation for this note.

The following studies concern Monte Carlo integrators (as DIPHOX [486], JetFOX [487] or 2γ NNLO [488], etc) for which the fragmentation component is a purely collinear phenomenon. For Monte Carlo generators (parton–shower Monte Carlo), in which the fragmentation photons are emitted off quarks at non–zero angle during the showering process, we recommend reference [378].

11.2 Isolation criteria

In this section we summarize the standard and “smooth” isolation criteria, including their advantages and problems concerning the theoretical and experimental implementations.

11.2.1 The standard cone isolation criterion

The isolation criterion used by collider experiments is schematically as follows. A photon is said to be isolated if, in a cone of radius R in rapidity and azimuthal angle around the photon direction, the amount of deposited hadronic transverse energy $\sum E_T^{had}$ is smaller than some value E_{Tmax} chosen by the experiment:

$$\sum E_T^{had} \leq E_{Tmax} \quad \text{inside} \quad (y - y_\gamma)^2 + (\phi - \phi_\gamma)^2 \leq R^2, \quad (\text{III.77})$$

where E_{Tmax} can be either, a fixed value²⁰ or a fraction of the transverse momentum of the photon ($p_T^\gamma \epsilon$, where typically $0 < \epsilon \leq 1$). This is the so-called standard cone isolation criterion. In addition to the rejection of the background of secondary photons, these isolation cuts also affect the prompt-diphoton cross section itself, in particular by reducing the effect of fragmentation, but should be structured so as to have a high efficiency for the retention of real, isolated photons.

A theoretical description of isolated photons is complicated because of the occurrence of collinear singularities between photons and final-state quarks. A finite cross section is only obtained when these singularities are absorbed into the fragmentation functions. As a result the only theoretically well-defined quantity (if we don’t use the smooth cone criterion) is the sum of the direct and fragmentation contributions. Once these two contributions are included one can isolate the photon using the cuts of Eq. (III.77) in an infrared safe way [489].

In addition, a tight isolation cut also has the undesirable effect of making the theoretical prediction unstable [489], due to the restriction of the available phase-space for parton emission. When the size of the cone used is in the limit of the narrow cone ($R|^{+1}-1$, $R \sim 0.1$) earlier studies reveal potential problems. This leads to a collinear sensitivity in the form of a fairly large

²⁰This requirement was typically used at the Tevatron and was motivated by the fact that most of the energy in the isolation cone results from the underlying event (and pile-up), and so is independent of the photon energy [160].

dependence on $\ln(1/R)$, which could make the prediction unreliable²¹. In a recent calculation [490] these large logarithmic terms were resummed restoring the reliability of the calculation.

11.2.2 The “smooth” isolation criterion

There exist an alternative to the standard criterion: the criterion proposed by Frixione in Ref. [158] (see also Ref. [491, 492]). This criterion modifies Eq. (III.77) in the following way

$$\sum E_T^{had} \leq E_{Tmax} \chi(r), \quad \text{inside any } r^2 = (y - y_\gamma)^2 + (\phi - \phi_\gamma)^2 \leq R^2. \quad (\text{III.78})$$

with a suitable choice for the function $\chi(r)$. This function has to vanish smoothly when its argument goes to zero ($\chi(r) \rightarrow 0$, if $r \rightarrow 0$), and has to verify $0 < \chi(r) < 1$, if $0 < r < R$. One possible election is,

$$\chi(r) = \left(\frac{1 - \cos(r)}{1 - \cos R} \right)^n, \quad (\text{III.79})$$

where n is typically chosen as $n = 1$ (unless otherwise stated we rely on this value for the phenomenological results presented in this note). This means that, closer to the photon, less hadronic activity is permitted inside the cone. At $r = 0$, when the parton and the photon are exactly collinear, the energy deposited inside the cone is required to be exactly equal to zero, and the fragmentation component (which is a purely collinear phenomenon in perturbative QCD) vanishes completely. Since no region of the phase space is forbidden, the cancellation of soft gluon effects takes place as in ordinary infrared-safe cross sections. This is the advantage of this criterion: it eliminates all the fragmentation component in an infrared-safe way.

We can also notice, comparing Eqs. (III.77) and (III.78), that both criteria coincide at the outer cone ($r = R$, $\chi(R) = 1$), and due to the presence of the $\chi(r)$ function which verifies $0 \leq \chi(r) \leq 1$, the smooth cone isolation criterion is more restrictive than the standard one. For this reason, we expect smaller cross sections when one uses the smooth cone criterion compared to the case when one implements the standard one if the same parameters are imposed,

$$\sigma_{smooth}\{R, E_{Tmax}\} \leq \sigma_{Stand}\{R, E_{Tmax}\}. \quad (\text{III.80})$$

The smooth behaviour of the $\chi(r)$ function is the main obstacle to implement the new isolation criterion into the experimental situation. First, because of the finite size of the calorimeter cells used to measure the electromagnetic shower, the smooth cone criterion must be applied only beyond a minimum distance of approximately 0.1 (in $\{\Delta\eta, \Delta\phi\}$ plane). This allows a contribution from fragmentation in the innermost cone and one has to check to which extent the fragmentation component is still suppressed. In addition, the transverse energy in the experimental isolation cone is deposited in discrete cells of finite size. Thus concerning its experimental implementation, the continuity criterion, initially proposed by Frixione has to be replaced by a discretized version consisting of a finite number of nested cones, together with the collection of corresponding maximal values for the transverse energy allowed inside each of these cones.

As was previously noted, another interesting (theoretical) feature of the smooth cone isolation criterion is that it is free of the large logarithmic contributions of the type of $\ln(1/R)$ associated with the narrow cone.

11.2.3 Theoretical issues

As it was previously stated, the inclusion of the fragmentation contributions complicates the calculation. And in some cases, such as when one wants to reach NNLO accuracy in pQCD

²¹This could even lead to an unphysical result such as an isolated cross section larger than the inclusive one, thereby violating unitarity.

(like in diphoton production) it would make the calculation very unlikely for at least quite a few years since the machinery for such a computation is not available yet.

For those cases, one can find in the literature theoretical calculations in which the fragmentation component is considered at one perturbative level less than the direct component (*e.g.* the $\gamma\gamma$ and $W/Z\gamma$ production at NLO in pQCD in MCFM [159] or $\gamma\gamma$ + Jet at NLO in pQCD [493], etc.). This procedure, which is a way to approximate the full calculation where the fragmentation component is included at the same perturbative level that the direct component, could introduce unexpected (inconsistent) results in the presence of the standard cone isolation criterion. The following exercise shows how these problems can easily appear.

Let's consider diphoton production at the LHC ($\sqrt{s} = 8$ TeV) computed at NLO, the highest perturbative order at which both direct and fragmentation calculations are available. The acceptance criteria in this case requires: $p_T^{\text{harder}} \geq 40$ GeV and $p_T^{\text{softer}} \geq 30$ GeV. The rapidity of both photons is restricted to $|y_\gamma| \leq 2.5$ and $100 \text{ GeV} < M_{\gamma\gamma} < 160$ GeV. The isolation parameters are set to the values $n = 1$ (in the case of the smooth cone) and $R = 0.4$, and the minimum angular separation between the two photons is $R_{\gamma\gamma} = 0.5$. The remain isolation parameter $E_{T \text{ max}}$ (or ϵ) is varied in order to understand the cross section dependence on it. All the cross sections are obtained using the CTEQ6M set of parton distributions functions. We used for this analysis the DIPHOX code that includes the full NLO pQCD description.

First, we compare the calculation using the fragmentation at NLO with the case in which the fragmentation is considered only at LO (one perturbative order less than the direct NLO component). The results in Fig. III.49 (right) show that for the LO fragmentation one can obtain larger cross sections for more severe isolation cuts (smaller ϵ), which is clearly inconsistent. The same behaviour was reported in Ref. [493] for $\gamma\gamma$ + Jet at NLO, and we obtained similar features for $\gamma\gamma$, $W/Z\gamma$ production at NLO in pQCD with MCFM. On the other hand, the left panel in Fig. III.49 shows that the correct behaviour is found when one considers the full result in which the fragmentation contribution is computed at same perturbative level than the direct component (*i.e.*, NLO in this case).

The precedent comparison suggests that one has to be aware that approximating the fragmentation component at one order lower than the direct one can result in unphysical results. The situation can be even more serious when one looks at some extreme kinematical region where the cross section is dominated by higher order contributions.

In Table III.11 we present the results for the corresponding cross section with different isolation prescriptions and parameters. The values presented there help to understand the unexpected behaviour in Fig. III.49 (right). In this case, the results are obtained imposing the cuts used by CMS in a recent measurement of the production cross section for pairs of isolated photons in pp collisions at $\sqrt{s} = 7$ TeV [119]. Therefore, we require the harder photon to have a transverse momentum $p_T^{\text{hard}} \geq 40$ GeV while for the softer we choose $p_T^{\text{soft}} \geq 30$ GeV. The rapidity of both photons is restricted to $|y_\gamma| \leq 2.5$. Finally, we constrain the invariant mass of the diphotons to lie in the range $100 \text{ GeV} \leq M_{\gamma\gamma} \leq 160$ GeV. And to simulate the CMS crack, we reject photons with $1.442 \leq y_\gamma \leq 1.556$. In the cases in which the standard criterion was applied (*a-f* in Table III.11) we observe that as the isolation criterion turns out to be "loose" the NLO direct component becomes smaller and the NLO fragmentation (single and double) component larger. The sum of them behaves as expected with respect to the isolation parameters, since the increase in the fragmentation component overcompensates the decrease of the direct one. We remind the reader that in the standard isolation the theoretical separation between direct and fragmentation components is not physical and the results presented in this note correspond to the conventional \overline{MS} subtraction. On the other hand, if only the LO calculation is used for the fragmentation contributions, for which the QCD corrections are quite large (with K -factors exceeding 2), the mismatch in the perturbative order spoils the compensation between

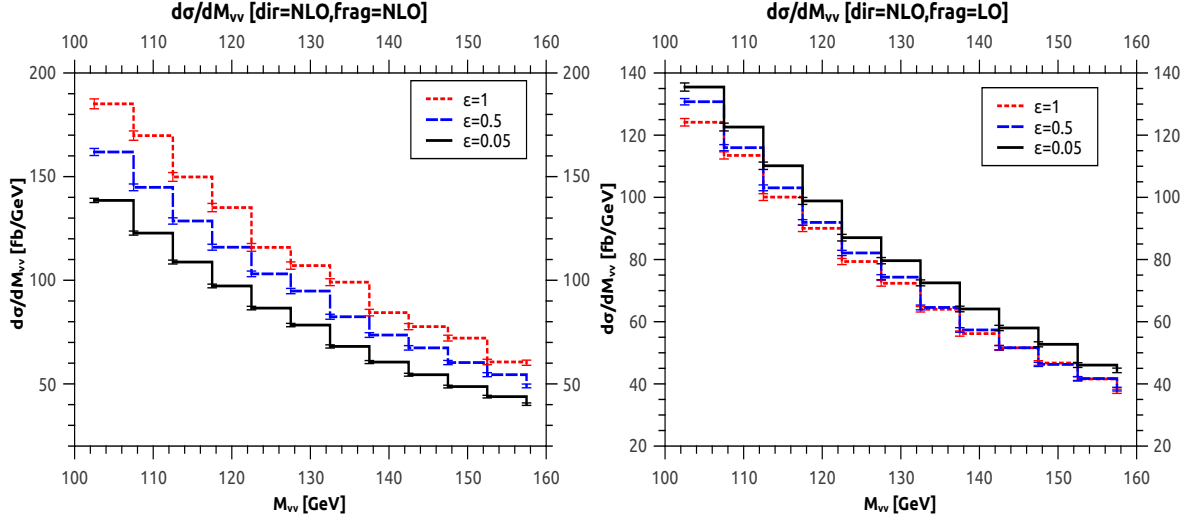


Fig. III.49: Diphoton cross section as a function of the invariant mass $M_{\gamma\gamma}$. (Left) With NLO fragmentation component. (Right) With LO fragmentation component.

the behaviour of the NLO direct and the LO fragmentation terms resulting in the unphysical behaviour observed in Fig. III.49 (right) as one considers less stringent isolation parameters.

Furthermore, from the cases in which the smooth cone criterion was applied ($h-m$ in Table III.11) we observed that, as expected, the result in the smooth cone case always provides a lower bound for the one obtained with the standard criterion when the same isolation parameters (energy in this case) are used. In the case of smooth cone isolation the (single and double) fragmentation components are identically null. Even more interestingly, and with one single exception, the results for the NLO cross sections computed using different isolation prescriptions differ by less than 1%. This result indicates that using the smooth cone prescription for a theoretical calculation (even when the data is analyzed using the standard one) provides an approximation that it is far much better than the one consisting in the standard prescription with a lowest order calculation for the fragmentation component. The only case where one can observe larger differences (of the order of 10%) corresponds to the use a very loose isolation, as for $\sum E_T^{had} \leq 0.5 p_T^\gamma$, where the fragmentation component in the standard case amounts more than half of the total cross section.

In all cases we have studied, the smooth cone provides an excellent approximation to the standard result as long as the isolation parameters are tight enough, i.e. $\sum E_T^{had} \leq 0.1 p_T^\gamma$ or $\sum E_T^{had} \leq 5$ GeV for the LHC at 7 TeV. Equivalently, one could define the isolation to be tight enough when the contribution from the fragmentation component does not exceeds $\sim 15 - 20\%$ of the total cross section.

While the previous analysis refers only to the fiducial cross section, it is known that the fragmentation contributions could be larger in kinematical regions far away from the back-to-back configuration²², and the approximation could in principle become less accurate for those distributions. In order to check that feature, in Fig. III.51 we compare the distributions for the full NLO calculation with the standard prescription, the one obtained using only the LO fragmentation component and the result for the smooth cone with $\sum E_T^{had} \leq 0.05 p_T^\gamma$ for $\cos \theta^*$ (left) and $\Delta\phi_{\gamma\gamma}$ (right). In both cases we observe that for all the bins the smooth cone provides

²²The low mass region in the invariant mass distribution, the low $\Delta\phi_{\gamma\gamma}$ distribution and the kinematical regions near to $\cos \theta^* = \pm 1$ belong to this case.

| | Code | $\sum E_T^{had} \leq$ | σ_{total}^{NLO} (fb) | σ_{dir}^{NLO} (fb) | σ_{onef}^{NLO} (fb) | σ_{twof}^{NLO} (fb) | Isolation |
|---|----------------|---------------------------|-----------------------------|---------------------------|----------------------------|----------------------------|-----------|
| a | DIPHOX | 2 GeV | 3756 | 3514 | 239 | 2.6 | Standard |
| b | DIPHOX | 3 GeV | 3776 | 3396 | 374 | 6 | Standard |
| c | DIPHOX | 4 GeV | 3796 | 3296 | 488 | 12 | Standard |
| d | DIPHOX | 5 GeV | 3825 | 3201 | 607 | 17 | Standard |
| e | DIPHOX | $0.05 p_T^\gamma$ | 3770 | 3446 | 320 | 4 | Standard |
| f | DIPHOX | $0.5 p_T^\gamma$ | 4474 | 2144 | 2104 | 226 | Standard |
| g | DIPHOX | <i>incl</i> | 6584 | 1186 | 3930 | 1468 | none |
| h | 2γ NNLO | $0.05 p_T^\gamma \chi(r)$ | 3768 | 3768 | 0 | 0 | Smooth |
| i | 2γ NNLO | $0.5 p_T^\gamma \chi(r)$ | 4074 | 4074 | 0 | 0 | Smooth |
| j | 2γ NNLO | 2 GeV $\chi(r)$ | 3754 | 3754 | 0 | 0 | Smooth |
| k | 2γ NNLO | 3 GeV $\chi(r)$ | 3776 | 3776 | 0 | 0 | Smooth |
| l | 2γ NNLO | 4 GeV $\chi(r)$ | 3795 | 3795 | 0 | 0 | Smooth |
| m | 2γ NNLO | 5 GeV $\chi(r)$ | 3814 | 3814 | 0 | 0 | Smooth |

Table III.11: Cross sections for the $pp \rightarrow \gamma\gamma + X$ process at the LHC at NLO. All these values are at 1% of statistical accuracy level.

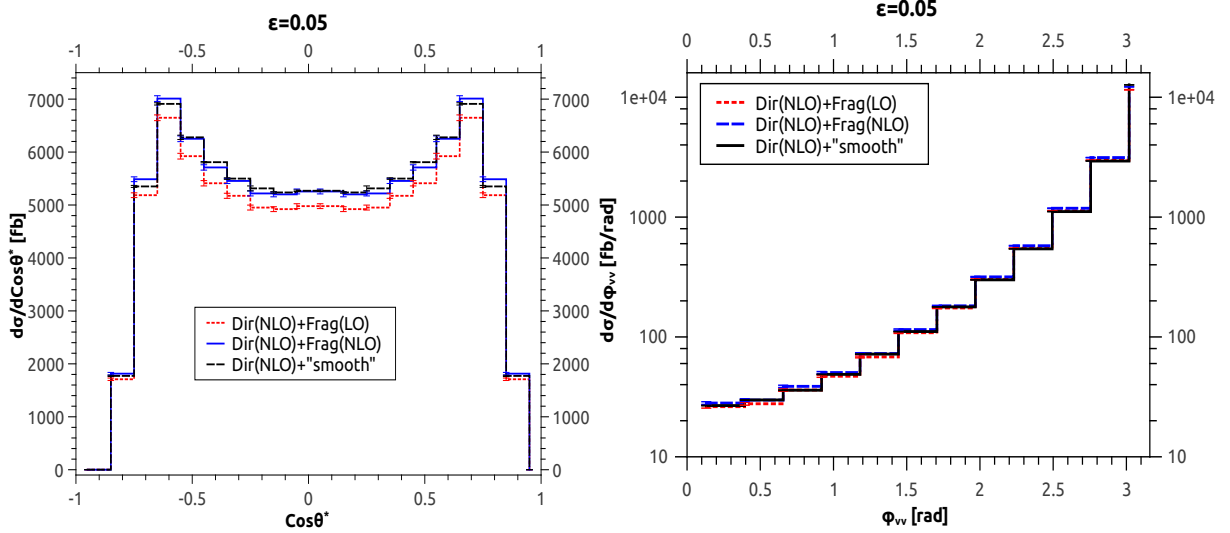


Fig. III.50: Diphoton cross section as a function of the $\cos\theta^*$ (Left), and the angular separation between the photons $\Delta\phi_{\gamma\gamma}$ (Right). A comparison between the different isolation criteria is showed. The applied cuts are the same as in Fig. III.49, and are described in the text.

the best approximation to the full result, always within a 2.5% accuracy. A more detailed analysis is presented in Fig. III.51 for the diphoton invariant mass distributions with two different isolation parameters, $\sum E_T^{had} \leq 0.05 p_T^\gamma$ (left) and $\sum E_T^{had} \leq 4$ GeV (right). Again, while using the LO fragmentation component fails to reproduce the full NLO result by up to 6%, the smooth cone approximation is always better than 1.5% in the same kinematical region.

The discrepancies between the full result and the smooth approach with the LO fragmentation approximation that evidently manifest in the invariant mass distribution (see Fig. III.51) or in kinematical regions far away from $\cos\theta^* = \pm 1$ (see Fig. III.50 (left)) are “hidden” in the $\Delta\phi_{\gamma\gamma}$ distribution, in the bin corresponding to $\Delta\phi_{\gamma\gamma} = \pi$ (the bin containing the back-to-back configurations). Moreover in the low $\Delta\phi_{\gamma\gamma}$ region we are dealing with events far away from the back-to-back configuration, and the only configuration that survives at NLO (in these

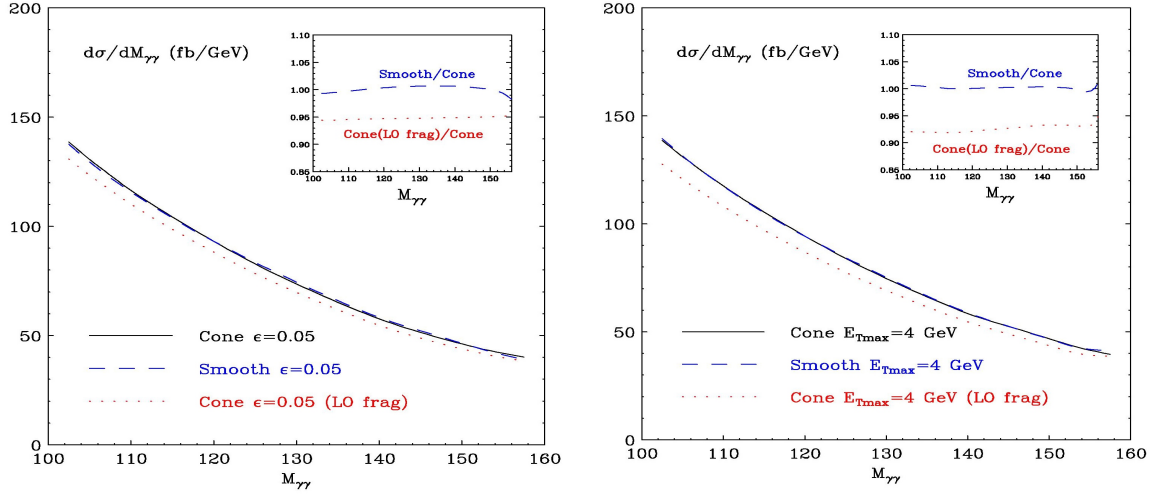


Fig. III.51: Diphoton cross section as a function of the invariant mass $M_{\gamma\gamma}$. Cross sections obtained with the standard cone isolation criterion (with LO and NLO fragmentation contributions) are compared with the cross section obtained with the smooth cone criterion using the same isolation parameters.

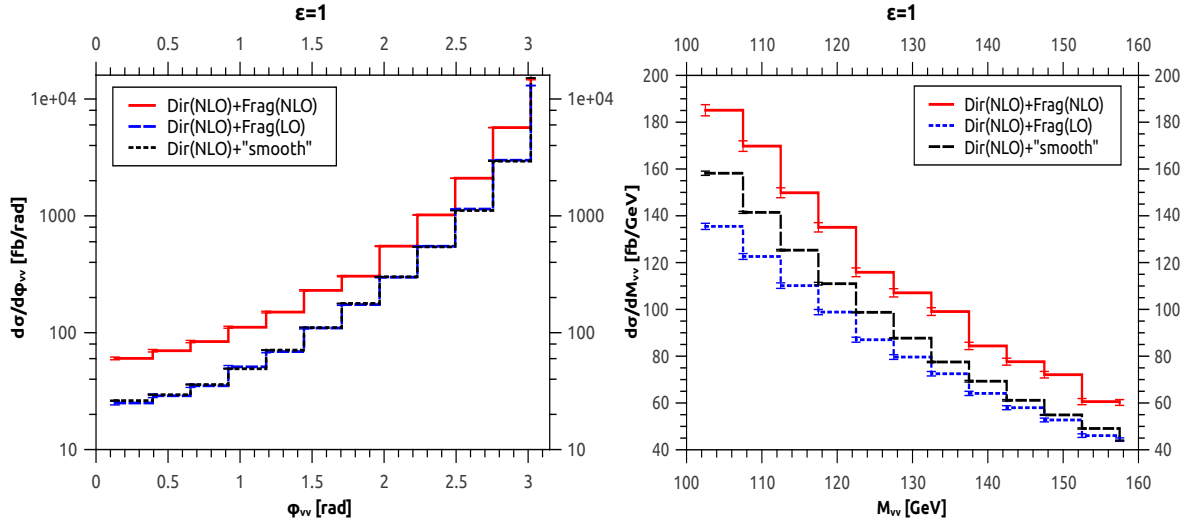


Fig. III.52: Diphoton cross section as a function of the angular separation between the photons $\Delta\phi_{\gamma\gamma}$ (Left), and the invariant mass of the diphoton system $M_{\gamma\gamma}$ (Right).

kinematical regions) is the real emission at LO which is for the three cases effectively the same contribution under these conditions.

If one relaxes the isolation and considers $\epsilon = 1$ (which is equivalent to $E_T^{max} > 40$ GeV, allowing for a huge amount of fragmentation contribution), the effects of fragmentation now strongly manifests at low $\Delta\phi_{\gamma\gamma}$ values, and the full result considerably differs from both the LO fragmentation approximation and the smooth cone criterion as we can observe in Fig. III.52 (azimuthal distribution in the upper plot and invariant mass in the lower one). Also we can see from Fig. III.52, in the bin corresponding to $\Delta\phi_{\gamma\gamma} = \pi$ (the bin containing the back-to-back configurations) the cross section obtained with the smooth cone criterion provides a better approximation than the LO fragmentation one.

11.3 Tight isolation accord

Finally, considering the results presented in the preceding sections we conclude this note by proposing a pragmatic accord in order to compare experimental data and theoretical calculations obtained at the highest possible perturbative order. Given the fact that matching experimental conditions to theoretical calculations always implies certain degree of approximation, we believe that considering the large QCD corrections to processes involving photons (with NNLO essential to understand diphoton data [488]) and the agreement (typically at the % level for the diphoton case studied here) between the standard and smooth cone TH calculations, the use of the later for TH purposes is well justified.

We call this approach "pragmatic", in the sense that we do not recommend the experiments to implement the smooth cone isolation, but to proceed to the analysis of the data with the usual standard isolation with cuts tight enough if the interesting observable needs to be an isolated cross section or distribution. While the definition of "tight enough" might slightly depend on the particular observable (that can always be checked by a lowest order calculation), our analysis shows that at the LHC isolation parameters as $E_T^{max} \leq 5$ GeV (or $\epsilon < 0.1$), $R \sim 0.4$ and $R_{\gamma\gamma} \sim 0.4$ are safe enough to proceed.

This procedure would allow to extend available NLO calculations to one order higher (NNLO) for a number of observables, since the direct component is always much simpler to evaluate than the fragmentation part, which identically vanishes under the smooth cone isolation.

We also refer to this approach as pragmatic in a numerical sense: we are certain that the smooth cone isolation applied for the TH calculation is NOT the one used in the experimental data, but considering that NNLO corrections are of the order of 50% for diphoton cross sections [488] and a few 100% for some distributions in extreme kinematical configurations, it is far better accepting a few % error arising from the isolation (less than the size of the expected NNNLO corrections and within any estimate of TH uncertainties!) than neglecting those huge QCD effects towards some "more pure implementation" of the isolation prescription.

We believe that a more detailed analysis of the profile function in the smooth cone isolation can be performed on a case by case basis in order to select, also in a pragmatic way, the most convenient for each observable, even though again, differences are expected to be very small as discussed before.

Acknowledgements

This work was supported in part by UBACYT, CONICET, ANPCyT, INFN and the Research Executive Agency (REA) of the European Union under the Grant Agreement number PITN-GA-2010-264564 (LHCPhenoNet, Initial Training Network).

12 Diphotons and jets at NLO²³

We study diphoton production in association with up to three jets at the LHC. In particular, we compare NLO predictions for up to two jets with leading order predictions matched to a parton shower. For the one-jet bin, we also include fragmentation contributions in the partonic calculation, which enables us to study the impact of different isolation criteria.

12.1 Introduction

Studies of the Higgs boson decay channel into two photons are of major importance in order to scrutinize the Higgs couplings and to be able to judge whether small deviations from the Standard Model predictions are hints of new physics.

²³N. Chanon, T. Gehrmann, N. Greiner, G. Heinrich

Measurements of the inclusive diphoton cross section by both ATLAS [118] and CMS [119] based on the $\sqrt{s} = 7$ TeV data set have been published recently. The production of photon pairs in association with jets are also very interesting processes, despite their smaller cross sections, as they constitute the main background to Higgs production in association with jets, where the higgs boson decays into two photons. In particular, the knowledge of diphoton production in association with two jets at next-to-leading order (NLO) accuracy allows to study the impact of vector boson fusion (VBF) cuts and thus helps to disentangle Higgs production in gluon fusion from the electroweak production mechanism.

Large- p_T photons in the final state can originate either from the hard interaction process itself or from the fragmentation of a large- p_T hadron. To single out the photons originating from the hard interaction from the secondary photons, photon isolation criteria need to be applied, which are typically formulated in the form of a maximum amount of hadronic energy allowed in the vicinity of the photon. The photons originating from fragmentation are, in a partonic calculation, described by fragmentation functions, which – in analogy to PDFs in the initial state – are non-perturbative objects that have to be determined from experimental data. To suppress the dependence of isolated photon cross sections on the fragmentation functions, a smooth cone isolation criterion has been proposed [494], where the allowed hadronic energy inside the isolation cone decreases with decreasing radial distance from the photon.

While diphoton production without extra jets has been calculated at NLO already some time ago, including also the fragmentation contribution at NLO in the public code DIPHOX [495], and even the NNLO corrections (without fragmentation contributions) have been calculated meanwhile [9], diphotons in association with jets at NLO have become available only recently. Photon pair plus one jet production at NLO has first been calculated in [496], using an isolation criterion [494] where the fragmentation component is eliminated. In Ref. [493], the fragmentation component has been included, allowing to study the impact of different isolation criteria at NLO, and the corresponding code is publicly available [497]. The virtual corrections are based on the automated one-loop program GOSAM [4], while the real corrections are built on the MADGRAPH/MADDIPOLE/MADEVENT [420–423] framework.

Photon pair plus two jet production at NLO has first been calculated in [498], also based on GOSAM+MADGRAPH/MADDIPOLE/MADEVENT, using a smooth isolation criterion. NLO results for $\gamma\gamma + 2$ jet production also have been presented in [499–501], and Ref. [500] in addition presents results for $\gamma\gamma + 3$ jet production at NLO.

12.2 Diphoton plus one jet production

In this section we consider diphoton production in association with one tagged jet. We compare the following samples:

1. NLO and LO samples produced by GOSAM+MADGRAPH/MADDIPOLE/MADEVENT (parton level). Renormalisation and factorisation scales μ and μ_F have been chosen as dynamical scales, with the default choice being $\mu_0 = \frac{1}{2}(m_{\gamma\gamma} + \sum_j p_T^{\text{jet}})$, $\mu = \mu_F$. The PDF set used is CT10. For the NLO sample based on GOSAM+MG we also compare cone isolation with Frixione [494] type isolation.
2. NLO samples produced by aMC@NLO [6] interfaced with a HERWIG6 shower [502], where the scale choice is $\mu_0 = \frac{1}{2}(m_{\gamma\gamma} + \sum p_T^{\text{partons}})$, $\mu = \mu_F$. The PDF set used here is CTEQ6M.
3. MADGRAPH LO samples with up to two jets at matrix element level, interfaced with a PYTHIA6 shower [288]. The scales are set to $\mu_0 = p_T^{\gamma_1} + p_T^{\gamma_2} + \sum p_T^{\text{partons}}$. The PDF set used is CTEQ6L1.

The LO computations based on MADGRAPH do not need any isolation criterion applied at parton level, as we require $R_{\gamma,j} > 0.5$. At NLO, however, collinear quark-photon configurations

due to extra radiation need to be taken care of. The singularities related to these configurations are cancelled by absorbing them into the “bare” fragmentation functions, analogous to the case of PDFs in the initial state. Therefore, the fragmentation part needs to be taken into account in an NLO calculation, unless it is completely suppressed by an isolation criterion like the one suggested by Frixione [494]. With this criterion, one considers smaller cones of radius r_γ inside the R -cone and calls the photon isolated if the energy in any sub-cone does not exceed

$$E_{\text{had,max}}(r_\gamma) = \epsilon p_T^\gamma \left(\frac{1 - \cos r_\gamma}{1 - \cos R} \right)^n .$$

When applying this criterion in our calculations, we use the isolation parameters $R = 0.4$, $n = 1$ and $\epsilon = 0.05$.

However, the latter criterion is difficult to implement in a realistic experimental environment, where the photon will always be accompanied by some amount of hadronic energy. Therefore, whenever we produce showered events, an isolation is applied at shower level which is a classical cone-type isolation: $GenIso < 0.05 \times p_T^\gamma$, where $GenIso$ is computed from the transverse momentum sum of all particles falling in a cone $\Delta R < 0.4$ around the photon. In the partonic NLO calculation labelled “GOSAM+MG NLO cone”, where the fragmentation component is included, we apply the same cone isolation parameters. Further we apply the following kinematic requirements on the two photons:

$$\begin{aligned} p_T^{\text{jet}} &> 30 \text{ GeV}, & p_T^{\gamma_1} &> 40 \text{ GeV}, & p_T^{\gamma_2} &> 25 \text{ GeV}, \\ m_{\gamma\gamma} &> 100 \text{ GeV}, & |\eta^\gamma| &\leq 2.5, & R_{\gamma,\gamma} &> 0.45. \end{aligned}$$

With GOSAM+MG, the jets are clustered with the anti- k_T algorithm using a cone of 0.5, applied to the QCD partons only. For the showered samples, the two hardest p_T photons in the event are selected as diphoton candidates, and they are removed from the list of particle candidates before the jet clustering algorithm is run. We then select the hardest jet in the event and require:

$$p_T^{\text{jet}} > 30 \text{ GeV}, \quad |\eta^j| \leq 4.7, \quad R_{\gamma,j} > 0.5 .$$

Differential distributions for the samples produced with different generators after kinematic and isolation requirements, for $\sqrt{s} = 8 \text{ TeV}$, are shown in Fig. III.53 for the leading photon and leading jet transverse momentum distributions. In particular, we compare, at NLO parton level, Frixione and cone-type isolation. We observe that for the rather tight isolation criteria considered here, the differences are quite small. In addition, we compare to showered samples with the same cone-type isolation. As expected, we observe that the effect of the isolation after the shower is considerably larger than at parton level. This can be seen particularly clearly in Fig. III.54, in distribution of the relative azimuthal angle $\Delta\phi_{\gamma_1\gamma_2}$ between the two photons. Note that the difference between GOSAM NLO with Frixione isolation and aMC@NLO with Frixione isolation at the LHE level can be attributed to the different scale choice (running over the partons for aMC@NLO and over the jets for GOSAM). The difference due to the different PDF set is negligible. Once the shower with Herwig6 is applied, the kinematic acceptance is reduced, giving a lower cross section.

12.3 Diphoton plus two jet production

For the production of two photons and two jets, we consider similar samples as for the one jet case, also adding SHERPA [166] LO samples with up to three jets at matrix element level. As the NLO calculation also contains up to three partons accompanying the photons in the final state, it makes sense to consider up to three jets at matrix element level in a LO sample. In the SHERPA sample, the box diagram $gg \rightarrow \gamma\gamma$, where the two additional jets are produced by the shower,

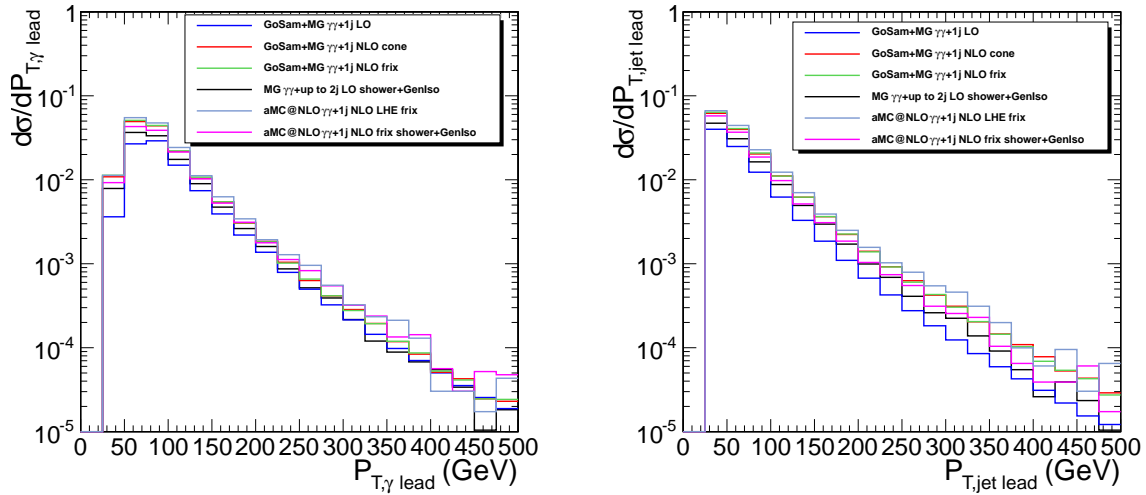


Fig. III.53: Transverse momentum distribution of the leading- p_T photon for the $\gamma\gamma+1$ jet process.

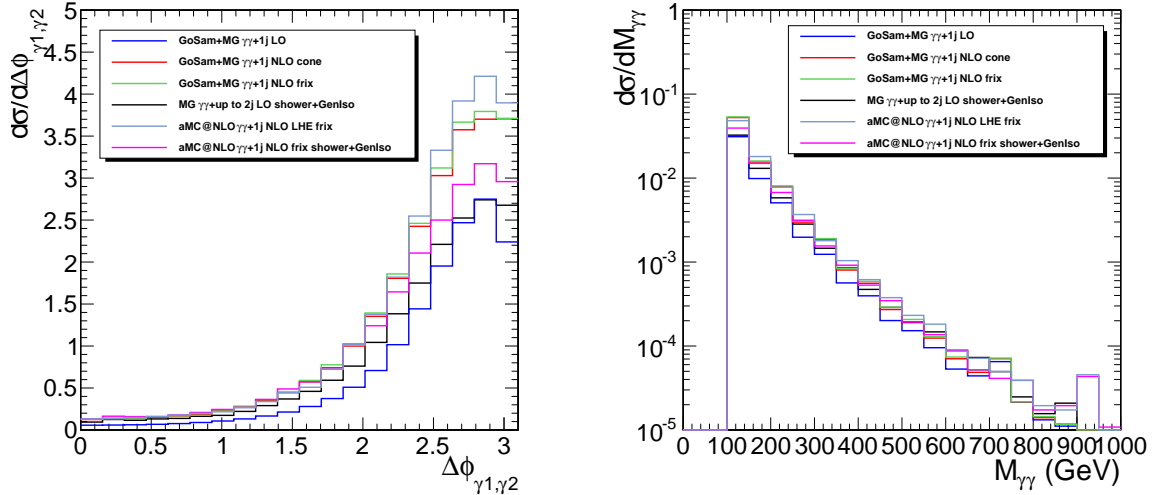


Fig. III.54: $\Delta\phi_{\gamma_1\gamma_2}$ and diphoton invariant mass distributions for the $\gamma\gamma+1$ jet process.

is also included, but its numerical impact is negligible. Factorisation and renormalisation scales are set by the METS scale, which uses a modified CKKW matching algorithm. The PDF set used is CT10. Differential distributions produced by the various generators after kinematic and isolation requirements are shown in Fig. III.55 for the leading photon and leading jet transverse momentum and in Fig. III.56 for the difference in azimuthal angle between the two photons and the diphoton invariant mass. One can see that the effect of the parton shower on the LO samples is different in the two-jet case: the kinematical and isolation cuts reduce the cross-section more strongly than in the one-jet case. This is easily understood by the fact that after the shower, the probability to identify two hard jets in addition to two isolated photons is much lower than the probability to identify just one hard jet.

12.4 Conclusions

We have studied the processes of diphoton production in association with one and two jets at the LHC. For the process $\gamma\gamma+1$ jet, we have compared partonic LO results, LO results matched

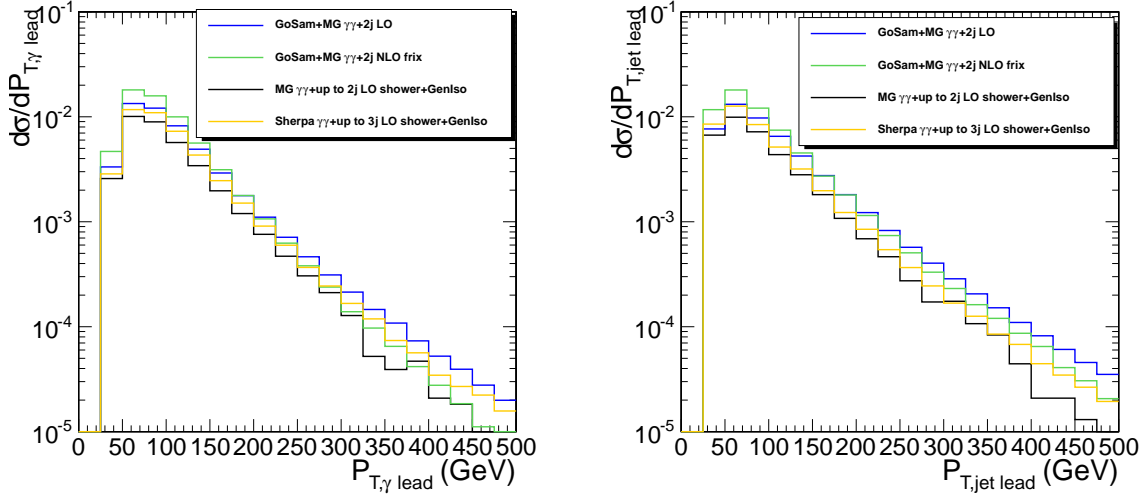


Fig. III.55: Transverse momentum distribution of the leading- p_T photon and jet for the $\gamma\gamma+2$ jets process.

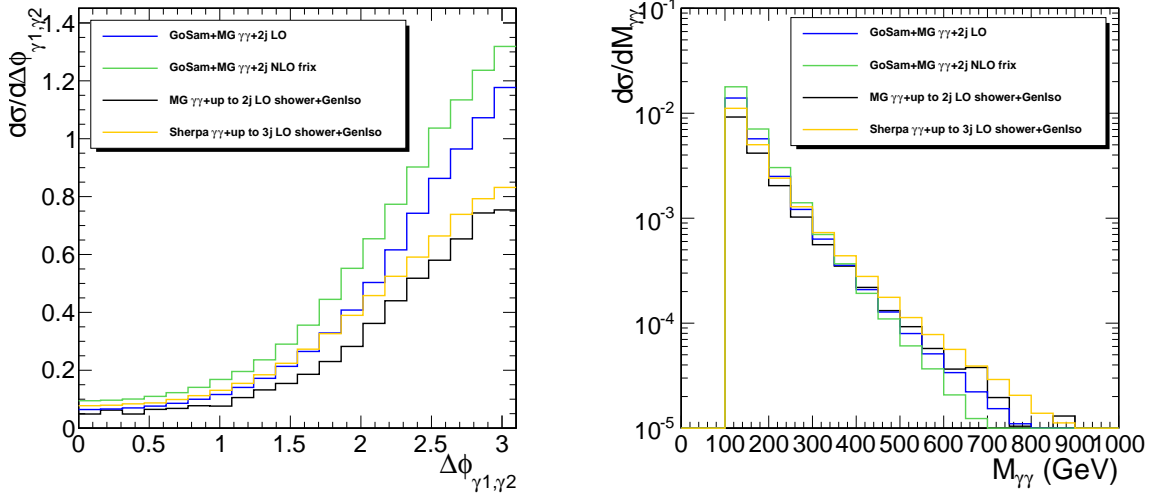


Fig. III.56: $\Delta\phi_{\gamma_1\gamma_2}$ and diphoton invariant mass distribution for the $\gamma\gamma+2$ jets process.

to a parton shower, NLO results at parton level with two different isolation criteria, and NLO results combined with a parton shower. As to be expected, we find that the NLO showered results lie between the LO results and the NLO partonic results. Comparing standard cone isolation with Frixione-type isolation at NLO at parton level, we observe that the difference is very small for the tight isolation criteria used in this study.

For the process $\gamma\gamma+2$ jets, we have compared LO and NLO samples at parton level produced with GoSAM+MadGraph/MadDipole/MadEvent to two different showered LO samples, produced with MadGraph or Sherpa. Comparing to the behaviour in the $\gamma\gamma+1$ jet case, we observe that in the presence of the additional tagged jet, switching on the parton shower leads to a considerably stronger reduction of the (LO) cross section, as the probability to identify two hard jets is reduced more strongly after the parton shower than in the one-jet case.

Acknowledgements

We would like to thank the organisers of “Les Houches 2013” for the stimulating workshop. We are also grateful to all members of the GOSAM project for their contributions to code development. This work is supported by the Sinergia program of the Swiss National Science Foundation (SNF) under grant number CRSII2-141847.

Chapter IV

MC tuning and output formats

1 Extensions to the Les Houches Event Format¹

1.1 Background

The LHE file format has been around since 2006 and has been very successful. At the Les Houches workshop in 2009 an update was suggested, mainly to improve the handling of NLO and matching/merging. The proposal was published in the proceedings (arXiv:1003.1643), but have never really been properly used. Nevertheless, some shortcomings have been noticed and some superfluous features identified, both of which issues we attempt to address in this contribution.

In the discussions at this years workshop some ideas on how to better specify weights were suggested, and also some other new features were suggested and old features were suggested to be dropped. Here we summarise the discussion as a set of agreed-upon proposals to define version 3.0 of the LHE format.

1.2 Changes in the format of 2009

Some XML tags that were introduced in 2009 were not adopted by the community, possibly because their usefulness was very limited. In order not to clutter the new proposal with unnecessary features, we recommend that the following XML tags be removed.

In the `<init>` block, we recommend that

`<mergeinfo>` Should be removed due to very limited usability.

In the `<event>` block, we recommend that

`<weight>` Should be removed and replaced by `<weights>` (see below), to avoid clashes with the *new* weight tag defined below.

`<clustering>` Should be removed due to very limited usability.

`<pdfinfo>` Should be removed due to unclear purpose.

None of these XML tags seem to have been used. Thus, we do not expect backward-compatibility problems if they were to be removed, and hence propose that they be simply ignored by future parsers, as per the normally defined LHE parsing behaviour for unknown XML tags. Any new LHE-parsing/writing code should be based on this definition rather than the previous one.

In discussions before and during the Les Houches workshop, it became obvious that the LHEF standard should be updated. This mainly concerns the handling of multiple event weights per phase space point. Allowing for multiple weights can significantly speed up the assessment of uncertainties as well as performing finely-grained parameter scans. For a well-defined handling of multiple weights, two proposals for extending the LHEF format were made, and were later combined into a single definition agreed on by the authors of the MC generator codes (both matrix element and parton shower) actively using the format.

¹A. Buckley, J. Butterworth, R. Frederix, B. Fuks, F. Krauss, L. Lonnblad, O. Mattelaer, P. Nason, C. Oleari, S. Padhi, S. Plätzer, S. Prestel

1.3 Additions to the LHEF format for dealing with multiple weights

The main improvement to the LHEF format is the need to deal with multiple event weights. We therefore describe the additional XML tags dealing with them first.

1.3.1 Multiple weight definition in the event file header

In the case where additional event weights are computed by the code that generates the event file, the header of that file should contain a new block, `<initrwgt>`, which syntax should follow this example:

```
<initrwgt>
  <weight id='1'> This is the original event weight </weight>
  <weightgroup name='scale variation' combine='envelope'>
    <weight id='2'> muR = 2.0 </weight>
    <weight id='3'> muR = 0.5 </weight>
  </weightgroup>
  <weightgroup name="MRST2008 PDF uncertainty" combine="hessian">
    <weight id='4'> set 01 </weight>
    <weight id='5'> set 02 </weight>
    ...
  </weightgroup>
  <weightgroup name='Qmatch variation' combine='envelope'>
    <weight id='44'> Qmatch=20 </weight>
    <weight id='my_own_id'> Qmatch=40 </weight>
  </weightgroup>
  <weight id='46'> BSM benchmark point number 42B </weight>
</initrwgt>
```

The information in the `<weight>` tags should be human-readable and explain what the weights mean. It can simply contain all the parameters that were used in to generate this weight; or only the ones that were changed compared to the original run; or simply a sentence explaining what this number means. It is up to the user that is doing the analysis to make sure that this information is correctly used (and up to the authors of the codes to make sure that the user has enough information to understand what the weights correspond to). The `<weight>` tag has the weight name `id` as mandatory argument. Suggested optional arguments are

- muf** The factor multiplying the nominal factorization scale for the event for the given weight
- mur** The factor multiplying the nominal renormalization scale for the event for the given weight
- pdf** The LHAPDF code corresponding to the given weight
- pdf2** The LHAPDF code corresponding to the given weight for the second beam if different from `pdf`

These arguments can be useful to concatenate a helpful string identifier when parsing the information through events in HepMC format. In this context, it is also helpful to choose a descriptive value for `id`.

The `<weightgroup>` tag allows to group several weights together and to have the information about how to combine weights to obtain, *e.g.*, scale variation or pdf uncertainties. The attribute `name` is mandatory and should define the name of the group. The attribute `combine` is optional and it indicates how the weights should be combined to define the associated uncertainties. Possible arguments are `none`, `hessian`, `envelope` or `gaussian`. If not specified, the default choice is `combine='none'`, all the curves associated with each weights being kept independent. For `combine='hessian'`, the first weight is the central value and the next weights correspond respectively to the positive and negative variations along a specific direction of the parameter space.

1.3.2 Multiple weights in the <event> block

As already hinted above, there are two formats for the inclusions of the weights in each of the events in the <event> block: a compressed format and a detailed format. The compressed format is designed to be memory-efficient, by avoiding repetition of identical strings for each event as much as possible. It amounts to adding a single <weights> tag to each event. The <weights> tag contains a space-separated list of weights for the events given in the order they are defined by the <weight> tags in the <initrwgt> block. If for some obscure reason a weight source is absent, its position in the list should be filled with a zero weight entry. In this case, a typical event will look like:

```
<event>
7 100 0.100E+01 0.200E+00 0.000E+00 0.000E+00
-2 -1 0 0 0 0 0.126E+01 0.554E+01 0.576E+02 0.579E+02 0.000E+00 0. 0.
 2 -1 0 0 0 0 -.913E+00 0.131E+01 -.349E+02 0.350E+02 0.000E+00 0. 0.
23 2 1 1 0 0 0.356E+00 0.685E+01 0.226E+02 0.929E+02 0.898E+02 0. 0.
-13 2 3 3 0 0 0.516E+01 0.211E+02 0.539E+02 0.581E+02 0.105E+00 0. 0.
 13 2 3 3 0 0 -.480E+01 -.142E+02 -.312E+02 0.347E+02 0.105E+00 0. 0.
-13 1 0 0 0 0 0.516E+01 0.211E+02 0.539E+02 0.581E+02 0.105E+00 0. 0.
 13 1 0 0 0 0 -.480E+01 -.142E+02 -.312E+02 0.347E+02 0.105E+00 0. 0.
<weights> 1.000e+00 0.204e+00 ... 1.564e+00 </weights>
</event>
```

In <http://home.thep.lu.se/~leif/LHEF> there is a small example class which is able to read and write this representation of the suggested new format. Future development and documentation of the format will take place at <http://lhcf.hepforge.org>.

For the detailed format the weights are put in <wgt> tags and are identified by their identifier id; their order is not of relevance. The list of weights should be put in the <rwgt> block, and each weight should be on a separate line. In this case a typical example event looks like:

```
<event>
7 100 0.100E+01 0.200E+00 0.000E+00 0.000E+00
-2 -1 0 0 0 0 0.126E+01 0.554E+01 0.576E+02 0.579E+02 0.000E+00 0. 0.
 2 -1 0 0 0 0 -.913E+00 0.131E+01 -.349E+02 0.350E+02 0.000E+00 0. 0.
23 2 1 1 0 0 0.356E+00 0.685E+01 0.226E+02 0.929E+02 0.898E+02 0. 0.
-13 2 3 3 0 0 0.516E+01 0.211E+02 0.539E+02 0.581E+02 0.105E+00 0. 0.
 13 2 3 3 0 0 -.480E+01 -.142E+02 -.312E+02 0.347E+02 0.105E+00 0. 0.
-13 1 0 0 0 0 0.516E+01 0.211E+02 0.539E+02 0.581E+02 0.105E+00 0. 0.
 13 1 0 0 0 0 -.480E+01 -.142E+02 -.312E+02 0.347E+02 0.105E+00 0. 0.
<rwgt>
  <wgt id='1'> 1.000e+00 </wgt>
  <wgt id='2'> 0.204e+00 </wgt>
  <wgt id='3'> 1.564e+00 </wgt>
  <wgt id='4'> 2.248e+00 </wgt>
  <wgt id='5'> 1.486e+00 </wgt>
  ...
  <wgt id='my_own_id'> -0.839e+00 </wgt>
  <wgt id='46'> -0.899e+00 </wgt>
</rwgt>
</event>
```

This representation of the proposed format has been implemented in the MADGRAPH5_AMC@NLO, MADANALYSIS5 and POWHEG BOX V2 packages.

Note that for both formats the weight for the nominal event is still also given by XWGTUP entry.

1.4 Additional new tags not related to multiple event weights

We agreed upon two more tags to become part of the LHEFv3.0 accord. The first one should be put in the `<init>` block and helps to transfer the program version with which the LHEF has been generated:

<generator> There should be at least one such tag (potentially more) with a `name` and a `version` attribute in the `<init>` section.

A typical example is

```
<generator name='SomeGen' version='1.2.3'> some additional comments </generator>
```

The additional comments can either identify sub-modules or libraries, or other information, like an arXiv number.

The second tag, `<scales>`, is optional and should be put within the `<event>` block. It is defined as:

<scales> contains information about different scales used by the matrix element generator in the given event. The scales are given as attributes, and any attribute name is allowed. However, only the following attributes have a pre-defined meaning:

muf The factorization scale (in GeV)

mur The renormalization scale (in GeV)

mups Suggested shower starting scale (in GeV)

If any of these attributes are missing, then the value in `SCALUP` is to be assumed for the missing attribute.

Acknowledgements

The authors thank the Les Houches workshop once again for the hospitality and enjoyable/productive working environment in the Chamonix valley. AB acknowledges support from a Royal Society University Research Fellowship, a CERN Scientific Associateship, an IPPP Associateship, and the University of Glasgow's Leadership Fellow programme.

2 Proposed updates for HepMC event record²

2.1 GenRun

There is a need to store the names and version numbers of all generators used in producing an event. We propose to define a `GenRun` object to contain cross-section (`GenCrossSection`) and other run-level quantities discussed below. Each `GenEvent` should link to the `GenRun`.

2.2 Generator names and versions

Add string array to `GenRun` with pairs of strings specifying (generator name, generator version). All generators used in the production should be listed, in order of processing, with full version numbers.

2.3 Vertex ID

The `GenVertex.id()` is not currently used/specified. We propose to define six codes:

- 0** undefined (no information)
- 1** matrix element vertex (i.e. the hard process which defines the PDF arguments). (Must be the same as the `GenEvent::signal_vertex()`);
- 2** secondary partonic scatters (useful for studies of MPI jet production, e.g. for suppressing jets from MPI while retaining the low p_{\perp} tail of the underlying event);
- 3** hard decay (prehadronisation) e.g. of W , H , Z , t . Useful e.g. for optimisation studies of mass resolution;
- 4** parton shower (including QED radiation) useful for e.g. identifying $g \rightarrow b\bar{b}$ splitting probability; ME/PS matching studies; identifying photons for dressing leptons. Note: any parton shower after a hadronisation is ignored, and the hadrons from it are flagged as being produced in a hadron decay;
- 5** primary hadron formation. Useful for e.g re-doing hadronisation, applying BEC corrections, studying/tracking decay chains;
- 6** hadron, tau and muon decays

We propose that 10–99 be reserved for generator-specific types. Use of this information must be made carefully, to avoid generator-specific physics conclusions.

2.4 Weight names

Some standardisation of weight names is desirable. We propose several standard weight name components, to be separated from each other by single underscore characters:

MUF0.5, **MUF2** factorization scale multiplication. Any float may occur between **MUF** and the underscore divider / end of string;

MUR0.5, **MUR1.414** renormalization scale multiplication. Any float may occur between **MUR** and the underscore divider / end of string;

PDF10801, **PDF20123** PDF variations, with the number following PDF up to the underscore/end being the LHAPDF/PDFLIB unique PDF member ID.

The potentially composite names for each weight are proposed to be stored in the `GenRun`, linked to the `WeightContainer` to avoid replication in the ASCII event format.

²A. Buckley, J. Butterworth, F. Krauss, L. Lonnblad, S. Plätzer, S. Prestel

Acknowledgements

All authors thank the Les Houches workshop once again for the hospitality and enjoyable/productive working environment in the Chamonix valley. AB acknowledges support from a Royal Society University Research Fellowship, a CERN Scientific Associateship, an IPPP Associateship, and the University of Glasgow's Leadership Fellow programme.

3 Improvements in the Rivet MC analysis toolkit³

Rivet [379] is the de facto analysis toolkit used for phenomenology and experimental MC analysis at the LHC. It comprises a steering system for efficiently processing events (as HepMC [503] code objects) through a user-specified set of analysis routines, each of which outputs a set of histograms for comparison to data or to other MC predictions. User-written analyses can be easily run without rebuilding Rivet, or any of the currently 250 built-in analyses may be used.

Rivet makes a major point of portability between any parton shower MC generators by reconstructing all quantities from physically reliable final-state (or decayed hadron) quantities, i.e. those which are at least in principle measurable and are not subject to the computational ambiguities of perhaps interfering quantum amplitudes. This has had the side-effect of making Rivet a useful “straw man” system for development of more robust definitions of physical quantities at “MC truth” level.

In this contribution I describe several major updates made to data processing and physics observable features in the Rivet MC analysis toolkit, which defined the step from the long-established Rivet version 1 to version 2, and the planned / in-development features for the next major release.

3.1 Histogramming and run merging

Partially as an historical accident of its genesis, Rivet has never been able to fully merge generator runs. Primarily this is because it converts all histograms (i.e. objects which preserve the history of their fills somehow) into simple “scatter” plots of x and y points with associated error bars. Histograms typically compute the visual heights of their bins from stored weighted moments like $\sum w_i$, $\sum w_i^2$, $\sum w_i x_i$, etc. (where w_i is the weight of the i th histogram fill and x_i the value in that fill), by standard statistical rules (and of course the width of each bin to preserve the shape invariance of the observable under rebinning). It is therefore possible to merge runs by simply adding the summed moments, either directly if the process type in the different runs is the same, or with a cross-section scaling if they are different or contain the same process but with complementary kinematic generation cuts, cf. the classic “jet slices” beloved of experiment MC productions. It is not possible to get the same exact merging behaviour from “scatter” graphs, and hence Rivet’s run merging has always relied on asymptotic scaling which break down on unpopulated distribution tails.

In Rivet version 2, a major redevelopment of the histogramming system was made, replacing the formerly used AIDA system (in a much-hacked implementation called LWH) with a new histogramming system, YODA [504]. This was written specifically to support MC analysis idioms and issues but intentionally does not contain any specific binding to particle physics concepts or usage. Usage of the ubiquitous ROOT [505] system was also extensively considered, but ROOT’s pervasive global state / threading unfriendliness and issues with object ownership and histogram behaviour convinced us that it was better to start from scratch and attempt to “do it right”. YODA precisely stores the sorts of weighted moments discussed above, for 1D and 2D histograms and profile histograms, as well as 1D, 2D, and 3D scatters and functions for conversion between these objects and to their ROOT equivalents.

The YODA statistics implementations are based on those from our LWH code, and are extremely careful in their treatments of low statistics errors, unfilled bins, overflow/underflow bins and whole distribution properties, as well as permitting gaps in binning as required by many historical public datasets in the HepData system. Extensions to the YODA binning system are intended to allow *any* type of object to be stored and looked up in an efficient binning representation. YODA histogram objects can be arbitrarily “annotated” with key–value pairs,

³A. Buckley

which proves extremely useful for e.g. storing information about scaling operations applied to histograms, as well as style information to be used by the Rivet plotting system. Unlike in ROOT and AIDA, YODA histograms do not need to be immediately registered with a unique path or name string: it is perfectly allowed to handle YODA histograms which are unknown to the system, and paths are purely used for identification of analysis objects when writing to or reading from a data file. The main YODA data format is a plain text one closely related to the simple format previously used by Rivet’s plotting system, and is far simpler and more compact to handle than the verbose AIDA XML format. Several scripts are provided for merging YODA data files, or for converting them to or from other formats, including ROOT to the extent that ROOT can encode all the information stored by YODA’s data objects.

Converting Rivet’s 200+ built-in analyses to use YODA was an extremely lengthy and difficult process. The actual conversion of the code was mostly straightforward, as the majority of analyses do not do anything more complex than filling and normalisation of histograms and the necessary class renamings were trivial. Subtractions and additions of histograms were also easily converted. Some, however, performed quite complex operations and these required extensive work. This conversion process, and the motivation to keep simple things simple while making complex ones not unpleasant, was of great help in designing and iterating the YODA interface. We are confident that the new YODA mechanisms in every non-trivial case made histogramming in Rivet more intuitive and expressive than previously.

Simply converting the code was not the whole story, of course: the Herwig++ [164] Rivet-based internal validation system was used to run sets of pre-generated events through both the AIDA- and YODA-based Rivet versions, and numerical agreement of better than one part in 10^5 was required. Such a stringent test unavoidably threw up many false positives and a great deal of time was spent individually going through the discrepant cases and understanding the source of the disagreement. Again this helped to improve the YODA design and behaviour, and in several cases bugs were found (and fixed) in the original Rivet analyses.

3.2 Lepton dressing

During the Rivet 2 development process, discussions arose relating to the definition of how charged leptons are to be “dressed” with photons in Rivet. The discussion of lepton dressing, with the primary intention of capturing the physical effects of QED final state radiation (FSR) in W and Z decays, without introducing generator-dependent analysis code, was previously discussed in the 2009 Les Houches proceedings [506].

The definition of dressing used in that note noted that “near-Born” performance could be achieved by clustering photons in a narrow cone around the lepton – the radius of the cone being of order $R = 0.1$ to reflect the typical granularity of a collider experiment EM calorimeter. This neglects the effect of wide-angle FSR, which cannot be distinguished from other photons unrelated to the EW hard process.

The refinement made in Rivet 2 (and backported to 1.9.0, the final release in the 1.x series) is to by default restrict the clustered photons to those which do not have a hadron or tau parent. This classification is made by recursively walking the HepMC decay chain from final state photons: if any hadrons or tau leptons with status = 2 are found in a photon’s history then it is considered of hadronic origin and hence emitted on a timescale entirely factorized from that of the hard-process. This change to the clustering achieves an accuracy for EW precision observables (e.g. $Z p_{\perp}$) of order a few per-mille as opposed to 1%.

Alternative refinements have also been proposed, particularly those involving a use of a jet clustering algorithm for photon gathering. Studies so far indicate no significant advantage to be gained from such an approach. Other suggestions have included process dependent distinguishing

of QED ISR from FSR which, even if considered desirable, is not sufficiently generic for use in a system like Rivet.

This change to clustering once again shows the value of Rivet as a concrete example of a generator-agnostic standard analysis system for driving physically motivated observable definitions. Isolation of hard leptons is still important, of course: if two leptons are close enough for their clustering cones to overlap, then duplicate clusterings and double countings are avoided, but most likely the photon-to-lepton identifications are not reliable. (This is similar to the treatment of b -tagging with boosted jets, another area where we hope that Rivet will prove a useful testing ground.)

The charged leptons considered so far just include stable electrons and muons. Taus are much more troublesome, since they decay (both hadronically and leptonically) and the decay itself is a source of photon emission, albeit one unrelated to the hard process of the EW boson decay. Rivet’s treatment of taus will be improved in future, in connection with the evolving experimental treatment of tau issues.

3.3 Status, plans and prospects

Rivet 2.0.0 was finally released in November 2013, using YODA for all histogramming. It was followed by a catch-up release 1.9.0 to include analyses provided during the final stages of the v2 development, and shortly thereafter by an equivalent 2.1.0. No further releases will be made in the Rivet v1 series. All versions of Rivet can be downloaded from the website at <http://rivet.hepforge.org>, along with (updated) bootstrap scripts to help with installation on systems both with and without CERN AFS available.

Version 2.2 of Rivet is envisaged to contain the following important new features, all of which have already been significantly developed:

- **FastJet integration:** Since Rivet development began concurrently with the development of FastJet [283], the original jet clustering tools were not based on FastJet but rather on independent implementations. In the intervening years FastJet has become the de facto package for jet studies (and other IRC-safe clustering applications), and in particular contains many powerful features for jet grooming, pile-up/underlying event subtraction, jet substructure, etc. While these can be accessed from within Rivet, it does not currently integrate well with the Rivet `Jet` objects. This will be improved by basing the Rivet `Jet` on FastJet’s `PseudoJet` and providing conversion operators between them. FastJet v3 is now required by Rivet, meaning that Rivet’s jet objects will also now automatically hold connections to the clustering sequence for jet deconstruction studies. The deeper integration with FastJet will also permit more physical b , c and tau tagging, using new projections developed for finding heavy hadrons immediately before their weak decays.
- **Kinematic cuts:** The interfaces of many Rivet tools involve calling constructors or class methods with arguments expressing the values of kinematic cuts, such as p_{\perp} or pseudo-rapidity thresholds. All these are currently expressed as floating point numbers, meaning that a) it is easy to forget the correct orderings and the compiler cannot distinguish between the intended meanings of several `double` s, and b) it is not possible to have methods which take arguments of e.g. $(\eta_{\min}, \eta_{\max}, p_{\perp}^{\min})$ and $(y_{\min}, y_{\max}, E_{\perp}^{\min})$ because again all the compiler sees is three `double` s. Expressing complex cuts such as several disjoint ranges of rapidity is also awkward. This has been addressed by creation of an object-based “cuts” system, where only one argument needs to be passed to represent a collection of kinematic selections. Rather than use a pre-approved set of combined cuts, users can build them “inline” as desired, using logical operators, e.g. `ptMin(10*GeV) & (etaIn(-2,-1) | etaIn(-0.5,0.5) | etaIn(1,2))`. This will make analysis code both

more powerful/expressive, and easier to read.

- **“Re-entrant” analysis and general run merging:** While the developments of YODA and Rivet 2 have made “normal” merging of MC runs possible, they cannot handle all observables. While YODA has the advantage that normalized and scaled plots can be combined (which is not normally the case, but YODA stores the scaling factor so it can be temporarily undone during the combination), it still cannot combine more complex observables such as histogram divisions A/B or asymmetries $(A - B)/(A + B)$ constructed in the `finalize` step of the analysis. These objects cease to be histograms in the division step – i.e. it would not make sense to continue calling `fill` on them, and their weighted moments are lost – hence they cannot be combined to get the equivalent result to one large run.

The solution to this is to write out both the finalized histogram objects *and* any temporary objects used to construct them: this latter group includes the A and B intermediate histograms above and any weight counters, in their state at the start of `finalize`, after the event loop has run. Some machinery is needed to make sure that the necessary information is all stored in the YODA data files, and that declarations are passed through the processing chain to avoid unwanted plotting of temporary histograms. It is envisaged that extra bookkeeping information such as the estimated cross-section, number of events, and perhaps a process ID code will also be automatically stored to aid automatic run combination.

The resulting data files, containing a mix of temporary and final analysis data objects, will then be combinable using the usual YODA merging mechanisms – although of course only the intermediate object will be correctly combinable. The final step in the process will then be to re-run Rivet with the merged histogram file as a starting point for the statistical aggregation, and usually to jump immediately to the `finalize` method(s) to create the fully merged complex observables. The ability to re-start the Rivet event loop based on a previous run obviously has other benefits, such as the ability to trivially extend run statistics should they be found to be insufficient, and to periodically write out finalized histograms during a run: it is for this reason that we call the system “re-entrant” analysis.

- **NLO and multi-weighted event handling:** The re-entrant system described above also provides a clean route for handling awkward event streams in which NLO generators place several counter-events in order, requiring that each counter-event group be treated as a single statistical unit, or the increasing phenomenon of events with very many weights representing systematic variations of scales, PDFs, etc. calculated during the generator run. Rivet (nor any other analysis system) cannot currently handle such situations automatically, and we strongly wish to avoid burdening all authors of analysis codes with the need to understand and implement a complex data processing procedure which most likely does not apply to their personal usage of the system.

The planned development is that the histogram objects used in the analysis routine are in fact proxies for the permanent histograms (both intermediate and final) which will be written out at the end of the run. The user should be mainly oblivious to this distinction, but behind the scenes the analysis histograms are used automatically for filling an ensemble of histograms for each event weight, automatically combined according to the counter-event grouping. This places a requirement on the user to register temporary histograms with the Rivet histogram booking system, but this requirement already exists for the re-entrant histogramming. Conveniently, this development will also remove the need for users to explicitly make use of event weights when filling histograms, as this will be done automatically by the Rivet system.

A final development for NLO counter-events is the optional use of “fuzzy” histogramming. It is well known that NLO predictions only remain finite when a resolution parameter of

some form is used, since perfect resolution of soft or collinear emissions breaks the necessary cancellation of divergences between real and virtual terms in the calculation [148, 149]. While histogram bins themselves implement this finite resolution, the boundaries between them are in a sense perfectly sharp and so can re-introduce problems. The classic case of this is when two counter-events fall just on opposite sides of a bin boundary, producing a large positive contribution in one bin and a large negative entry in its neighbour: the required cancellation fails to occur. To handle this situation, we have developed a “fuzzy binning” procedure, whereby a single fill operation will actually fill two bins, identified by and in proportion to the position of the fill within a bin: a fill in the middle of a bin will only fill that bin, but one close to a bin edge will proportionally contribute both to that bin and to its neighbour on the other side of the bin edge. It has not yet been decided whether this feature should be implemented in YODA itself, or be performed by Rivet using YODA objects.

- **Decay chain tools:** Finally, we mention that Rivet will acquire tools to assist with analysis of (mainly hadron) decay chains – a topic of interest for flavour physics analyses in particular but for which Rivet provides little assistance, requiring the user to drop into the raw HepMC event record. This, as with the need for better tau lepton decay handling mentioned above, reflects the increasing trend toward dealing with details of event properties and modelling in LHC Run 2.

Rivet continues to be heavily used in the LHC experimental and phenomenological communities for a variety of analysis types. Limitations of our histogramming capabilities have long been lamented, and we are pleased to have substantially improved this area. Work remains to be done, of course, in particular to support the rise in fully exclusive event simulation with NLO-subtracted matrix elements and use of internal event reweighting for modelling systematics. Developments such as incremental improvements in lepton dressing and flavour tagging algorithms in Rivet are well connected to LHC experiment discussions on the same topics of truth object definition, which are of key importance as the LHC enters its precision physics era.

Acknowledgements

AB thanks the Les Houches workshop once again for the hospitality and enjoyable/productive working environment in the Chamonix valley, and acknowledges support from a Royal Society University Research Fellowship, a CERN Scientific Associateship, an IPPP Associateship, and the University of Glasgow’s Leadership Fellow programme. Much of the key final development and testing of Rivet2, as well as the now-traditional Rivet tutorials, was performed during Les Houches 2013.

References

- [1] S. Badger, B. Biedermann, P. Uwer, and V. Yundin, *Next-to-leading order QCD corrections to five jet production at the LHC*, Phys.Rev. **D89** (2014) 034019, [arXiv:1309.6585 \[hep-ph\]](#).
- [2] Z. Bern, L. Dixon, F. Febres Cordero, S. Hoeche, H. Ita, et al., *Next-to-Leading Order $W + 5$ -Jet Production at the LHC*, Phys.Rev. **D88** (2013) 014025, [arXiv:1304.1253 \[hep-ph\]](#).
- [3] G. Cullen, H. van Deurzen, N. Greiner, G. Luisoni, P. Mastrolia, et al., *NLO QCD corrections to Higgs boson production plus three jets in gluon fusion*, Phys.Rev.Lett. **111** (2013) 131801, [arXiv:1307.4737 \[hep-ph\]](#).
- [4] G. Cullen, N. Greiner, G. Heinrich, G. Luisoni, P. Mastrolia, et al., *Automated One-Loop Calculations with GoSam*, Eur.Phys.J. **C72** (2012) 1889, [arXiv:1111.2034 \[hep-ph\]](#).
- [5] G. Bevilacqua, M. Czakon, M. Garzelli, A. van Hameren, A. Kardos, et al., *HELAC-NLO*, Comput.Phys.Commun. **184** (2013) 986–997, [arXiv:1110.1499 \[hep-ph\]](#).
- [6] V. Hirschi, R. Frederix, S. Frixione, M. V. Garzelli, F. Maltoni, et al., *Automation of one-loop QCD corrections*, JHEP **1105** (2011) 044, [arXiv:1103.0621 \[hep-ph\]](#).
- [7] F. Cascioli, P. Maierhofer, and S. Pozzorini, *Scattering Amplitudes with Open Loops*, Phys.Rev.Lett. **108** (2012) 111601, [arXiv:1111.5206 \[hep-ph\]](#).
- [8] S. Actis, A. Denner, L. Hofer, A. Scharf, and S. Uccirati, *Recursive generation of one-loop amplitudes in the Standard Model*, JHEP **1304** (2013) 037, [arXiv:1211.6316 \[hep-ph\]](#).
- [9] S. Catani, L. Cieri, D. de Florian, G. Ferrera, and M. Grazzini, *Diphoton production at hadron colliders: a fully-differential QCD calculation at NNLO*, Phys.Rev.Lett. **108** (2012) 072001, [arXiv:1110.2375 \[hep-ph\]](#).
- [10] M. Grazzini, S. Kallweit, D. Rathlev, and A. Torre, *$Z\gamma$ production at hadron colliders in NNLO QCD*, [arXiv:1309.7000 \[hep-ph\]](#).
- [11] P. Baernreuther, M. Czakon, and A. Mitov, *Percent Level Precision Physics at the Tevatron: First Genuine NNLO QCD Corrections to $q\bar{q} \rightarrow t\bar{t} + X$* , Phys.Rev.Lett. **109** (2012) 132001, [arXiv:1204.5201 \[hep-ph\]](#).
- [12] M. Czakon and A. Mitov, *NNLO corrections to top-pair production at hadron colliders: the all-fermionic scattering channels*, JHEP **1212** (2012) 054, [arXiv:1207.0236 \[hep-ph\]](#).
- [13] M. Czakon and A. Mitov, *NNLO corrections to top pair production at hadron colliders: the quark-gluon reaction*, JHEP **1301** (2013) 080, [arXiv:1210.6832 \[hep-ph\]](#).
- [14] M. Czakon, P. Fiedler, and A. Mitov, *The total top quark pair production cross-section at hadron colliders through $O(\alpha_s^4)$* , [arXiv:1303.6254 \[hep-ph\]](#).
- [15] A. Gehrmann-De Ridder, T. Gehrmann, E. Glover, and J. Pires, *Second order QCD corrections to jet production at hadron colliders: the all-gluon contribution*, Phys. Rev. Lett. **110** (2013) no. 16, 162003, [arXiv:1301.7310 \[hep-ph\]](#).
- [16] J. Currie, A. Gehrmann-De Ridder, E. Glover, and J. Pires, *NNLO QCD corrections to jet production at hadron colliders from gluon scattering*, JHEP **1401** (2014) 110, [arXiv:1310.3993 \[hep-ph\]](#).
- [17] R. Boughezal, F. Caola, K. Melnikov, F. Petriello, and M. Schulze, *Higgs boson production in association with a jet at next-to-next-to-leading order in perturbative QCD*, JHEP **1306** (2013) 072, [arXiv:1302.6216 \[hep-ph\]](#).
- [18] M. Czakon, *A novel subtraction scheme for double-real radiation at NNLO*, Phys.Lett. **B693** (2010) 259–268, [arXiv:1005.0274 \[hep-ph\]](#).

- [19] A. Gehrmann-De Ridder, T. Gehrmann, and E. N. Glover, *Antenna subtraction at NNLO*, JHEP **0509** (2005) 056, arXiv:hep-ph/0505111 [hep-ph].
- [20] R. Boughezal, K. Melnikov, and F. Petriello, *A subtraction scheme for NNLO computations*, Phys.Rev. **D85** (2012) 034025, arXiv:1111.7041 [hep-ph].
- [21] R. D. Ball, M. Bonvini, S. Forte, S. Marzani, and G. Ridolfi, *Higgs production in gluon fusion beyond NNLO*, Nucl.Phys. **B874** (2013) 746–772, arXiv:1303.3590 [hep-ph].
- [22] S. Buehler and A. Lazopoulos, *Scale dependence and collinear subtraction terms for Higgs production in gluon fusion at N³LO*, JHEP **1310** (2013) 096, arXiv:1306.2223 [hep-ph].
- [23] C. Anastasiou, C. Duhr, F. Dulat, and B. Mistlberger, *Soft triple-real radiation for Higgs production at N³LO*, JHEP **1307** (2013) 003, arXiv:1302.4379 [hep-ph].
- [24] C. Anastasiou, C. Duhr, F. Dulat, F. Herzog, and B. Mistlberger, *Real-virtual contributions to the inclusive Higgs cross-section at N³LO*, JHEP **1312** (2013) 088, arXiv:1311.1425 [hep-ph].
- [25] C. Anastasiou, C. Duhr, F. Dulat, E. Furlan, T. Gehrmann, et al., *Higgs boson gluon-fusion production at threshold in N³LO QCD*, arXiv:1403.4616 [hep-ph].
- [26] S. Alioli, P. Nason, C. Oleari, and E. Re, *A general framework for implementing NLO calculations in shower Monte Carlo programs: the POWHEG BOX*, JHEP **1006** (2010) 043, arXiv:1002.2581 [hep-ph].
- [27] S. Hoche, F. Krauss, M. Schonherr, and F. Siegert, *Automating the POWHEG method in Sherpa*, JHEP **1104** (2011) 024, arXiv:1008.5399 [hep-ph].
- [28] S. Plätzer and S. Gieseke, *Dipole Showers and Automated NLO Matching in Herwig++*, Eur.Phys.J. **C72** (2012) 2187, arXiv:1109.6256 [hep-ph].
- [29] S. Höche, F. Krauss, M. Schönerr, and F. Siegert, *A critical appraisal of NLO+PS matching methods*, JHEP **1209** (2012) 049, arXiv:1111.1220 [hep-ph].
- [30] S. Höche, F. Krauss, M. Schönerr, and F. Siegert, *QCD matrix elements + parton showers: The NLO case*, JHEP **1304** (2013) 027, arXiv:1207.5030 [hep-ph].
- [31] L. Lönnblad and S. Prestel, *Unitarising Matrix Element + Parton Shower merging*, JHEP **1302** (2013) 094, arXiv:1211.4827 [hep-ph].
- [32] K. Hamilton, P. Nason, and G. Zanderighi, *MINLO: Multi-Scale Improved NLO*, JHEP **1210** (2012) 155, arXiv:1206.3572 [hep-ph].
- [33] K. Hamilton, P. Nason, C. Oleari, and G. Zanderighi, *Merging H/W/Z + 0 and 1 jet at NLO with no merging scale: a path to parton shower + NNLO matching*, JHEP **1305** (2013) 082, arXiv:1212.4504.
- [34] K. Hamilton, P. Nason, E. Re, and G. Zanderighi, *NNLOPS simulation of Higgs boson production*, JHEP **1310** (2013) 222, arXiv:1309.0017 [hep-ph].
- [35] L. Lönnblad and S. Prestel, *Merging Multi-leg NLO Matrix Elements with Parton Showers*, JHEP **1303** (2013) 166, arXiv:1211.7278 [hep-ph].
- [36] S. Frixione and B. R. Webber, *Matching NLO QCD computations and parton shower simulations*, JHEP **0206** (2002) 029, arXiv:hep-ph/0204244 [hep-ph].
- [37] S. Frixione, P. Nason, and C. Oleari, *Matching NLO QCD computations with Parton Shower simulations: the POWHEG method*, JHEP **0711** (2007) 070, arXiv:0709.2092 [hep-ph].
- [38] LHC Higgs Cross Section Working Group Collaboration, S. Dittmaier et al., *Handbook of LHC Higgs Cross Sections: 1. Inclusive Observables*, arXiv:1101.0593 [hep-ph].
- [39] S. Dittmaier, C. Mariotti, G. Passarino, R. Tanaka, et al., *Handbook of LHC Higgs Cross Sections: 2. Differential Distributions*, arXiv:1201.3084 [hep-ph].

- [40] LHC Higgs Cross Section Working Group Collaboration, S. Heinemeyer, C. Mariotti, G. Passarino, R. Tanaka, et al., *Handbook of LHC Higgs Cross Sections: 3. Higgs Properties*, arXiv:1307.1347 [hep-ph].
- [41] S. Dittmaier and M. Schumacher, *The Higgs Boson in the Standard Model - From LEP to LHC: Expectations, Searches, and Discovery of a Candidate*, Prog.Part.Nucl.Phys. **70** (2013) 1–54, arXiv:1211.4828 [hep-ph].
- [42] S. Dawson, A. Gritsan, H. Logan, J. Qian, C. Tully, et al., *Higgs Working Group Report of the Snowmass 2013 Community Planning Study*, arXiv:1310.8361 [hep-ex].
- [43] T. A. collaboration, *Differential cross sections of the Higgs boson measured in the diphoton decay channel using 8 TeV pp collisions*, .
- [44] J. M. Campbell, R. K. Ellis, and C. Williams, *Hadronic production of a Higgs boson and two jets at next-to-leading order*, Phys.Rev. **D81** (2010) 074023, arXiv:1001.4495 [hep-ph].
- [45] H. van Deurzen, N. Greiner, G. Luisoni, P. Mastrolia, E. Mirabella, et al., *NLO QCD corrections to the production of Higgs plus two jets at the LHC*, Phys.Lett. **B721** (2013) 74–81, arXiv:1301.0493 [hep-ph].
- [46] G. Ferrera, M. Grazzini, and F. Tramontano, *Associated WH production at hadron colliders: a fully exclusive QCD calculation at NNLO*, Phys.Rev.Lett. **107** (2011) 152003, arXiv:1107.1164 [hep-ph].
- [47] A. Denner, S. Dittmaier, S. Kallweit, and A. Muck, *Electroweak corrections to Higgs-strahlung off W/Z bosons at the Tevatron and the LHC with HAWK*, JHEP **1203** (2012) 075, arXiv:1112.5142 [hep-ph].
- [48] L. Altenkamp, S. Dittmaier, R. V. Harlander, H. Rzehak, and T. J. Zirke, *Gluon-induced Higgs-strahlung at next-to-leading order QCD*, JHEP **1302** (2013) 078, arXiv:1211.5015 [hep-ph].
- [49] G. Ferrera, M. Grazzini, and F. Tramontano, *Higher-order QCD effects for associated WH production and decay at the LHC*, arXiv:1312.1669 [hep-ph].
- [50] C. Anastasiou, F. Herzog, and A. Lazopoulos, *The fully differential decay rate of a Higgs boson to bottom-quarks at NNLO in QCD*, JHEP **1203** (2012) 035, arXiv:1110.2368 [hep-ph].
- [51] J. Ellis, D. S. Hwang, K. Sakurai, and M. Takeuchi, *Disentangling Higgs-Top Couplings in Associated Production*, arXiv:1312.5736 [hep-ph].
- [52] S. Dawson, S. Dittmaier, and M. Spira, *Neutral Higgs boson pair production at hadron colliders: QCD corrections*, Phys.Rev. **D58** (1998) 115012, arXiv:hep-ph/9805244 [hep-ph].
- [53] J. Grigo, J. Hoff, K. Melnikov, and M. Steinhauser, *On the Higgs boson pair production at the LHC*, Nucl.Phys. **B875** (2013) 1–17, arXiv:1305.7340 [hep-ph].
- [54] D. de Florian and J. Mazzitelli, *Higgs Boson Pair Production at Next-to-Next-to-Leading Order in QCD*, Phys. Rev. Lett. **111**, **201801** (2013) 201801, arXiv:1309.6594 [hep-ph].
- [55] J. Baglio, A. Djouadi, R. Gr uber, M. M ajhleitner, J. Quevillon, et al., *The measurement of the Higgs self-coupling at the LHC: theoretical status*, JHEP **1304** (2013) 151, arXiv:1212.5581 [hep-ph].
- [56] R. Frederix, S. Frixione, V. Hirschi, F. Maltoni, O. Mattelaer, et al., *Higgs pair production at the LHC with NLO and parton-shower effects*, arXiv:1401.7340 [hep-ph].
- [57] ATLAS Collaboration Collaboration, G. Aad et al., *Measurement of the cross section for*

- top-quark pair production in pp collisions at $\sqrt{s} = 7$ TeV with the ATLAS detector using final states with two high-pt leptons*, JHEP **1205** (2012) 059, arXiv:1202.4892 [hep-ex].
- [58] CMS Collaboration, S. Chatrchyan et al., *Measurement of the $t\bar{t}$ production cross section in the dilepton channel in pp collisions at $\sqrt{s} = 7$ TeV*, JHEP **1211** (2012) 067, arXiv:1208.2671 [hep-ex].
- [59] J. KÅijhn, A. Scharf, and P. Uwer, *Weak Interactions in Top-Quark Pair Production at Hadron Colliders: An Update*, arXiv:1305.5773 [hep-ph].
- [60] K. Melnikov and M. Schulze, *NLO QCD corrections to top quark pair production and decay at hadron colliders*, JHEP **0908** (2009) 049, arXiv:0907.3090 [hep-ph].
- [61] A. Denner, S. Dittmaier, S. Kallweit, and S. Pozzorini, *NLO QCD corrections to WWbb production at hadron colliders*, Phys.Rev.Lett. **106** (2011) 052001, arXiv:1012.3975 [hep-ph].
- [62] G. Bevilacqua, M. Czakon, A. van Hameren, C. G. Papadopoulos, and M. Worek, *Complete off-shell effects in top quark pair hadroproduction with leptonic decay at next-to-leading order*, JHEP **1102** (2011) 083, arXiv:1012.4230 [hep-ph].
- [63] A. Denner, S. Dittmaier, S. Kallweit, and S. Pozzorini, *NLO QCD corrections to off-shell top-antitop production with leptonic decays at hadron colliders*, JHEP **1210** (2012) 110, arXiv:1207.5018 [hep-ph].
- [64] F. Cascioli, S. Kallweit, P. MaierhÄufer, and S. Pozzorini, *A unified NLO description of top-pair and associated Wt production*, arXiv:1312.0546 [hep-ph].
- [65] S. Dittmaier, P. Uwer, and S. Weinzierl, *NLO QCD corrections to t anti-t + jet production at hadron colliders*, Phys.Rev.Lett. **98** (2007) 262002, arXiv:hep-ph/0703120 [HEP-PH].
- [66] S. Dittmaier, P. Uwer, and S. Weinzierl, *Hadronic top-quark pair production in association with a hard jet at next-to-leading order QCD: Phenomenological studies for the Tevatron and the LHC*, Eur.Phys.J. **C59** (2009) 625–646, arXiv:0810.0452 [hep-ph].
- [67] K. Melnikov and M. Schulze, *NLO QCD corrections to top quark pair production in association with one hard jet at hadron colliders*, Nucl.Phys. **B840** (2010) 129–159, arXiv:1004.3284 [hep-ph].
- [68] A. Kardos, C. Papadopoulos, and Z. Trocsanyi, *Top quark pair production in association with a jet with NLO parton showering*, Phys.Lett. **B705** (2011) 76–81, arXiv:1101.2672 [hep-ph].
- [69] K. Melnikov, A. Scharf, and M. Schulze, *Top quark pair production in association with a jet: QCD corrections and jet radiation in top quark decays*, Phys.Rev. **D85** (2012) 054002, arXiv:1111.4991 [hep-ph].
- [70] G. Bevilacqua, M. Czakon, C. Papadopoulos, and M. Worek, *Dominant QCD Backgrounds in Higgs Boson Analyses at the LHC: A Study of $pp \rightarrow t\bar{t} + 2\text{jets}$ at Next-To-Leading Order*, Phys.Rev.Lett. **104** (2010) 162002, arXiv:1002.4009 [hep-ph].
- [71] G. Bevilacqua, M. Czakon, C. Papadopoulos, and M. Worek, *Hadronic top-quark pair production in association with two jets at Next-to-Leading Order QCD*, Phys.Rev. **D84** (2011) 114017, arXiv:1108.2851 [hep-ph].
- [72] S. Hoeche, F. Krauss, P. Maierhoefer, S. Pozzorini, M. Schonherr, et al., *Next-to-leading order QCD predictions for top-quark pair production with up to two jets merged with a parton shower*, arXiv:1402.6293 [hep-ph].
- [73] A. Kardos, Z. Trocsanyi, and C. Papadopoulos, *Top quark pair production in association*

- with a Z -boson at NLO accuracy, Phys.Rev. **D85** (2012) 054015, arXiv:1111.0610 [hep-ph].
- [74] M. Garzelli, A. Kardos, C. Papadopoulos, and Z. Trocsanyi, $Z0$ - boson production in association with a top anti-top pair at NLO accuracy with parton shower effects, Phys.Rev. **D85** (2012) 074022, arXiv:1111.1444 [hep-ph].
- [75] J. M. Campbell and R. K. Ellis, $t\bar{t}W^{+-}$ production and decay at NLO , JHEP **1207** (2012) 052, arXiv:1204.5678 [hep-ph].
- [76] M. Garzelli, A. Kardos, C. Papadopoulos, and Z. Trocsanyi, $t\bar{t}W^{+-}$ and $t\bar{t}Z$ Hadroproduction at NLO accuracy in QCD with Parton Shower and Hadronization effects, JHEP **1211** (2012) 056, arXiv:1208.2665 [hep-ph].
- [77] A. Lazopoulos, T. McElmurry, K. Melnikov, and F. Petriello, Next-to-leading order QCD corrections to $t\bar{t}Z$ production at the LHC, Phys.Lett. **B666** (2008) 62–65, arXiv:0804.2220 [hep-ph].
- [78] CMS Collaboration Collaboration, S. Chatrchyan et al., Measurement of associated production of vector bosons and top quark-antiquark pairs at $\sqrt{s} = 7$ TeV, Phys.Rev.Lett. **110** (2013) 172002, arXiv:1303.3239 [hep-ex].
- [79] Top Quark Working Group Collaboration, K. Agashe et al., Snowmass 2013 Top quark working group report, arXiv:1311.2028 [hep-ph].
- [80] ATLAS Collaboration Collaboration, G. Aad et al., Evidence for the associated production of a W boson and a top quark in ATLAS at $\sqrt{s} = 7$ TeV, Phys.Lett. **B716** (2012) 142–159, arXiv:1205.5764 [hep-ex].
- [81] CMS Collaboration Collaboration, S. Chatrchyan et al., Evidence for associated production of a single top quark and W boson in pp collisions at $\sqrt{s} = 7$ TeV, Phys.Rev.Lett. **110** (2013) 022003, arXiv:1209.3489 [hep-ex].
- [82] B. Harris, E. Laenen, L. Phaf, Z. Sullivan, and S. Weinzierl, The Fully differential single top quark cross-section in next to leading order QCD, Phys.Rev. **D66** (2002) 054024, arXiv:hep-ph/0207055 [hep-ph].
- [83] J. M. Campbell, R. K. Ellis, and F. Tramontano, Single top production and decay at next-to-leading order, Phys.Rev. **D70** (2004) 094012, arXiv:hep-ph/0408158 [hep-ph].
- [84] J. Campbell, R. K. Ellis, and R. Rontsch, Single top production in association with a Z boson at the LHC, Phys.Rev. **D87** (2013) 114006, arXiv:1302.3856 [hep-ph].
- [85] N. Kidonakis, Single top production at the Tevatron: Threshold resummation and finite-order soft gluon corrections, Phys.Rev. **D74** (2006) 114012, arXiv:hep-ph/0609287 [hep-ph].
- [86] N. Kidonakis, Next-to-next-to-leading-order collinear and soft gluon corrections for t -channel single top quark production, Phys.Rev. **D83** (2011) 091503, arXiv:1103.2792 [hep-ph].
- [87] S. Dittmaier, A. Huss, and C. Speckner, Weak radiative corrections to dijet production at hadron colliders, JHEP **1211** (2012) 095, arXiv:1210.0438 [hep-ph].
- [88] ATLAS Collaboration, G. Aad et al., Measurement of inclusive jet and dijet production in pp collisions at $\sqrt{s} = 7$ TeV using the ATLAS detector, Phys.Rev. **D86** (2012) 014022, arXiv:1112.6297 [hep-ex].
- [89] ATLAS Collaboration Collaboration, G. Aad et al., Measurement of dijet cross sections in pp collisions at 7 TeV centre-of-mass energy using the ATLAS detector, arXiv:1312.3524 [hep-ex].
- [90] CMS Collaboration Collaboration, S. Chatrchyan et al., Measurements of differential jet cross sections in proton-proton collisions at $\sqrt{s} = 7$ TeV with the CMS detector,

- Phys.Rev. **D87** (2013) 112002, arXiv:1212.6660 [hep-ex].
- [91] CMS Collaboration Collaboration, S. Chatrchyan et al., *Measurement of the ratio of the inclusive 3-jet cross section to the inclusive 2-jet cross section in pp collisions at $\sqrt{s} = 7$ TeV and first determination of the strong coupling constant in the TeV range*, Eur.Phys.J. **C73** (2013) 2604, arXiv:1304.7498 [hep-ex].
- [92] Z. Nagy, *Three jet cross-sections in hadron hadron collisions at next-to-leading order*, Phys. Rev. Lett. **88** (2002) 122003, arXiv:hep-ph/0110315.
- [93] Z. Nagy, *Next-to-leading order calculation of three jet observables in hadron hadron collision*, Phys. Rev. D **68** (2003) 094002, arXiv:hep-ph/0307268.
- [94] ATLAS Collaboration, G. Aad et al., *Measurement of the inclusive W^\pm and Z/gamma cross sections in the electron and muon decay channels in pp collisions at $\sqrt{s} = 7$ TeV with the ATLAS detector*, Phys.Rev. **D85** (2012) 072004, arXiv:1109.5141 [hep-ex].
- [95] CMS Collaboration Collaboration, S. Chatrchyan et al., *Measurement of inclusive W and Z boson production cross sections in pp collisions at $\sqrt{s} = 8$ TeV*, arXiv:1402.0923 [hep-ex].
- [96] R. Boughezal, Y. Li, and F. Petriello, *Disentangling radiative corrections using high-mass Drell-Yan at the LHC*, Phys.Rev. **D89** (2014) 034030, arXiv:1312.3972 [hep-ph].
- [97] ATLAS Collaboration Collaboration, G. Aad et al., *Determination of the strange quark density of the proton from ATLAS measurements of the $W \rightarrow l\nu$ and $Z \rightarrow \ell\ell$ cross sections*, Phys.Rev.Lett. **109** (2012) 012001, arXiv:1203.4051 [hep-ex].
- [98] A. Denner, S. Dittmaier, T. Kasprzik, and A. Mück, *Electroweak corrections to $W + jet$ hadroproduction including leptonic W-boson decays*, JHEP **0908** (2009) 075, arXiv:0906.1656 [hep-ph].
- [99] A. Denner, S. Dittmaier, T. Kasprzik, and A. Mück, *Electroweak corrections to dilepton + jet production at hadron colliders*, JHEP **1106** (2011) 069, arXiv:1103.0914 [hep-ph].
- [100] A. Denner, S. Dittmaier, T. Kasprzik, and A. Mück, *Electroweak corrections to monojet production at the LHC*, Eur.Phys.J. **C73** (2013) 2297, arXiv:1211.5078 [hep-ph].
- [101] A. Denner, L. Hofer, A. Scharf, and S. Uccirati, *Electroweak corrections to $Z + 2 jets$ production at the LHC*, arXiv:1311.5336 [hep-ph].
- [102] ATLAS Collaboration Collaboration, G. Aad et al., *Measurement of the production cross section of jets in association with a Z boson in pp collisions at $\sqrt{s} = 7$ TeV with the ATLAS detector*, JHEP **1307** (2013) 032, arXiv:1304.7098 [hep-ex].
- [103] ATLAS Collaboration Collaboration, G. Aad et al., *Measurement of WZ production in proton-proton collisions at $\sqrt{s} = 7$ TeV with the ATLAS detector*, Eur.Phys.J. **C72** (2012) 2173, arXiv:1208.1390 [hep-ex].
- [104] CMS Collaboration Collaboration, S. Chatrchyan et al., *Measurement of the W^+W^- Cross section in pp Collisions at $\sqrt{s} = 7$ TeV and Limits on Anomalous $WW\gamma$ and WWZ couplings*, Eur.Phys.J. **C73** (2013) 2610, arXiv:1306.1126 [hep-ex].
- [105] A. Bierweiler, T. Kasprzik, J. H. Kühn, and S. Uccirati, *Electroweak corrections to W-boson pair production at the LHC*, JHEP **1211** (2012) 093, arXiv:1208.3147 [hep-ph].
- [106] A. Bierweiler, T. Kasprzik, and J. H. Kühn, *Vector-boson pair production at the LHC to $\mathcal{O}(\alpha^3)$ accuracy*, JHEP **1312** (2013) 071, arXiv:1305.5402 [hep-ph].
- [107] J. Baglio, L. D. Ninh, and M. M. Weber, *Massive gauge boson pair production at the LHC: a next-to-leading order story*, Phys.Rev. **D88** (2013) 113005, arXiv:1307.4331.
- [108] M. Billoni, S. Dittmaier, B. Jäger, and C. Speckner, *Next-to-leading order electroweak*

- corrections to $pp \rightarrow W^+W^- \rightarrow 4 \text{ leptons}$ at the LHC in double-pole approximation, JHEP **1312** (2013) 043, arXiv:1310.1564 [hep-ph].
- [109] S. Gieseke, T. Kasprzik, and J. H. Kühn, *Vector-boson pair production and electroweak corrections in HERWIG++*, arXiv:1401.3964 [hep-ph].
- [110] ATLAS Collaboration Collaboration, G. Aad et al., *Measurement of W^+W^- production in pp collisions at $\sqrt{s} = 7$ TeV with the ATLAS detector and limits on anomalous WWZ and $WW\gamma$ couplings*, Phys.Rev. **D87** (2013) 112001, arXiv:1210.2979 [hep-ex].
- [111] ATLAS Collaboration Collaboration, G. Aad et al., *Measurement of ZZ production in pp collisions at $\sqrt{s} = 7$ TeV and limits on anomalous ZZZ and $ZZ\gamma$ couplings with the ATLAS detector*, JHEP **1303** (2013) 128, arXiv:1211.6096 [hep-ex].
- [112] CMS Collaboration Collaboration, S. Chatrchyan et al., *Measurement of the ZZ production cross section and search for anomalous couplings in $2l2l'$ final states in pp collisions at $\sqrt{s} = 7$ TeV*, JHEP **1301** (2013) 063, arXiv:1211.4890 [hep-ex].
- [113] CMS Collaboration Collaboration, S. Chatrchyan et al., *Measurement of W^+W^- and ZZ production cross sections in pp collisions at $\sqrt{s} = 8$ TeV*, Phys.Lett. **B721** (2013) 190–211, arXiv:1301.4698 [hep-ex].
- [114] M. Bonvini, F. Caola, S. Forte, K. Melnikov, and G. Ridolfi, *Signal-background interference effects for $gg \rightarrow H \rightarrow W^+W^-$ beyond leading order*, Phys.Rev. **D88** (2013) 034032, arXiv:1304.3053 [hep-ph].
- [115] ATLAS Collaboration Collaboration, G. Aad et al., *Measurements of $W\gamma$ and $Z\gamma$ production in pp collisions at $\sqrt{s} = 7$ TeV with the ATLAS detector at the LHC*, Phys.Rev. **D87** (2013) 112003, arXiv:1302.1283 [hep-ex].
- [116] CMS Collaboration Collaboration, S. Chatrchyan et al., *Measurement of the production cross section for $Z\gamma \rightarrow \nu\bar{\nu}\gamma$ in pp collisions at $\sqrt{s} = 7$ TeV and limits on $ZZ\gamma$ and $Z\gamma\gamma$ triple gauge boson couplings*, JHEP **1310** (2013) 164, arXiv:1309.1117 [hep-ex].
- [117] D. T. Nhung, L. D. Ninh, and M. M. Weber, *NLO corrections to WWZ production at the LHC*, JHEP **1312** (2013) 096, arXiv:1307.7403 [hep-ph].
- [118] ATLAS Collaboration, G. Aad et al., *Measurement of isolated-photon pair production in pp collisions at $\sqrt{s} = 7$ TeV with the ATLAS detector*, JHEP **1301** (2013) 086, arXiv:1211.1913 [hep-ex].
- [119] CMS Collaboration, S. Chatrchyan et al., *Measurement of the Production Cross Section for Pairs of Isolated Photons in pp collisions at $\sqrt{s} = 7$ TeV*, JHEP **1201** (2012) 133, arXiv:1110.6461 [hep-ex].
- [120] A. Denner, *Techniques for calculation of electroweak radiative corrections at the one loop level and results for W physics at LEP-200*, Fortsch.Phys. **41** (1993) 307–420, arXiv:0709.1075 [hep-ph].
- [121] S. Eidelman and F. Jegerlehner, *Hadronic contributions to $g-2$ of the leptons and to the effective fine structure constant $\alpha(M_Z^2)$* , Z.Phys. **C67** (1995) 585–602, arXiv:hep-ph/9502298 [hep-ph].
- [122] A. Sirlin, *Radiative Corrections in the $SU(2)_L \times U(1)$ Theory: A Simple Renormalization Framework*, Phys.Rev. **D22** (1980) 971–981.
- [123] M. Consoli, W. Hollik, and F. Jegerlehner, *The Effect of the Top Quark on the $M_W - M_Z$ Interdependence and Possible Decoupling of Heavy Fermions from Low-Energy Physics*, Phys.Lett. **B227** (1989) 167.
- [124] S. Dittmaier and M. Krämer, *Electroweak radiative corrections to W boson production at hadron colliders*, Phys.Rev. **D65** (2002) 073007, arXiv:hep-ph/0109062 [hep-ph].
- [125] S. Bremsing, S. Dittmaier, M. Krämer, and A. Mück, *Radiative corrections to W^- boson*

- hadroproduction: Higher-order electroweak and supersymmetric effects*, Phys.Rev. **D77** (2008) 073006, arXiv:0710.3309 [hep-ph].
- [126] S. Dittmaier and M. Huber, *Radiative corrections to the neutral-current Drell-Yan process in the Standard Model and its minimal supersymmetric extension*, JHEP **1001** (2010) 060, arXiv:0911.2329 [hep-ph].
- [127] V. S. Fadin, L. Lipatov, A. D. Martin, and M. Melles, *Resummation of double logarithms in electroweak high-energy processes*, Phys.Rev. **D61** (2000) 094002, arXiv:hep-ph/9910338 [hep-ph].
- [128] J. H. Kühn, A. Penin, and V. A. Smirnov, *Summing up subleading Sudakov logarithms*, Eur.Phys.J. **C17** (2000) 97–105, arXiv:hep-ph/9912503 [hep-ph].
- [129] M. Ciafaloni, P. Ciafaloni, and D. Comelli, *Bloch-Nordsieck violating electroweak corrections to inclusive TeV scale hard processes*, Phys.Rev.Lett. **84** (2000) 4810–4813, arXiv:hep-ph/0001142 [hep-ph].
- [130] M. Hori, H. Kawamura, and J. Kodaira, *Electroweak Sudakov at two loop level*, Phys.Lett. **B491** (2000) 275–279, arXiv:hep-ph/0007329 [hep-ph].
- [131] A. Denner and S. Pozzorini, *One loop leading logarithms in electroweak radiative corrections. 2. Factorization of collinear singularities*, Eur.Phys.J. **C21** (2001) 63–79, arXiv:hep-ph/0104127 [hep-ph].
- [132] M. Melles, *Resummation of angular dependent corrections in spontaneously broken gauge theories*, Eur.Phys.J. **C24** (2002) 193–204, arXiv:hep-ph/0108221 [hep-ph].
- [133] W. Beenakker and A. Werthenbach, *Electroweak two loop Sudakov logarithms for on-shell fermions and bosons*, Nucl.Phys. **B630** (2002) 3–54, arXiv:hep-ph/0112030 [hep-ph].
- [134] A. Denner, M. Melles, and S. Pozzorini, *Two loop electroweak angular dependent logarithms at high-energies*, Nucl.Phys. **B662** (2003) 299–333, arXiv:hep-ph/0301241 [hep-ph].
- [135] B. Jantzen, J. H. Kühn, A. A. Penin, and V. A. Smirnov, *Two-loop electroweak logarithms*, Phys.Rev. **D72** (2005) 051301, arXiv:hep-ph/0504111 [hep-ph].
- [136] B. Jantzen, J. H. Kühn, A. A. Penin, and V. A. Smirnov, *Two-loop electroweak logarithms in four-fermion processes at high energy*, Nucl.Phys. **B731** (2005) 188–212, arXiv:hep-ph/0509157 [hep-ph].
- [137] A. Denner, B. Jantzen, and S. Pozzorini, *Two-loop electroweak next-to-leading logarithmic corrections to massless fermionic processes*, Nucl.Phys. **B761** (2007) 1–62, arXiv:hep-ph/0608326 [hep-ph].
- [138] J. R. Christiansen and Sjöstrand, Torbjörn, *Weak Gauge Boson Radiation in Parton Showers*, arXiv:1401.5238 [hep-ph].
- [139] P. Ciafaloni and D. Comelli, *The Importance of weak bosons emission at LHC*, JHEP **0609** (2006) 055, arXiv:hep-ph/0604070 [hep-ph].
- [140] U. Baur, *Weak Boson Emission in Hadron Collider Processes*, Phys.Rev. **D75** (2007) 013005, arXiv:hep-ph/0611241 [hep-ph].
- [141] G. Bell, J. Kühn, and J. Rittinger, *Electroweak Sudakov Logarithms and Real Gauge-Boson Radiation in the TeV Region*, Eur.Phys.J. **C70** (2010) 659–671, arXiv:1004.4117 [hep-ph].
- [142] M. Chiesa, G. Montagna, L. BarzÁl, M. Moretti, O. Nicrosini, et al., *Electroweak Sudakov Corrections to New Physics Searches at the LHC*, Phys.Rev.Lett. **111** (2013) 121801, arXiv:1305.6837 [hep-ph].
- [143] W. Beenakker et al., *WW cross-sections and distributions*, arXiv:hep-ph/9602351 [hep-ph].

- [144] A. Arbuzov, *Nonsinglet splitting functions in QED*, Phys.Lett. **B470** (1999) 252–258, [arXiv:hep-ph/9908361](#) [hep-ph].
- [145] W. Placzek and S. Jadach, *Multiphoton radiation in leptonic W boson decays*, Eur.Phys.J. **C29** (2003) 325–339, [arXiv:hep-ph/0302065](#) [hep-ph].
- [146] C. Carloni Calame, G. Montagna, O. Nicrosini, and M. Treccani, *Higher order QED corrections to W boson mass determination at hadron colliders*, Phys.Rev. **D69** (2004) 037301, [arXiv:hep-ph/0303102](#) [hep-ph].
- [147] P. Golonka and Z. Was, *Next to Leading Logarithms and the PHOTOS Monte Carlo*, Eur.Phys.J. **C50** (2007) 53–62, [arXiv:hep-ph/0604232](#) [hep-ph].
- [148] T. Kinoshita, *Mass singularities of Feynman amplitudes*, J.Math.Phys. **3** (1962) 650–677.
- [149] T. Lee and M. Nauenberg, *Degenerate Systems and Mass Singularities*, Phys.Rev. **133** (1964) B1549–B1562.
- [150] ATLAS Collaboration Collaboration, G. Aad et al., *Measurement of the transverse momentum distribution of Z/ γ^* bosons in proton-proton collisions at $\sqrt{s} = 7$ TeV with the ATLAS detector*, Phys.Lett. **B705** (2011) 415–434, [arXiv:1107.2381](#) [hep-ex].
- [151] A. Martin, R. Roberts, W. Stirling, and R. Thorne, *Parton distributions incorporating QED contributions*, Eur.Phys.J. **C39** (2005) 155–161, [arXiv:hep-ph/0411040](#) [hep-ph].
- [152] NNPDF Collaboration, R. D. Ball et al., *Parton distributions with QED corrections*, Nucl.Phys. **B877** (2013) no. 2, 290–320, [arXiv:1308.0598](#) [hep-ph].
- [153] K.-P. Diener, S. Dittmaier, and W. Hollik, *Electroweak higher-order effects and theoretical uncertainties in deep-inelastic neutrino scattering*, Phys.Rev. **D72** (2005) 093002, [arXiv:hep-ph/0509084](#) [hep-ph].
- [154] C. Carloni Calame, G. Montagna, O. Nicrosini, and A. Vicini, *Precision electroweak calculation of the production of a high transverse-momentum lepton pair at hadron colliders*, JHEP **0710** (2007) 109, [arXiv:0710.1722](#) [hep-ph].
- [155] A. Denner, S. Dittmaier, T. Gehrmann, and C. Kurz, *Electroweak corrections to hadronic event shapes and jet production in e^+e^- annihilation*, Nucl.Phys. **B836** (2010) 37–90, [arXiv:1003.0986](#) [hep-ph].
- [156] E. N. Glover and A. Morgan, *Measuring the photon fragmentation function at LEP*, Z.Phys. **C62** (1994) 311–322.
- [157] ALEPH Collaboration Collaboration, D. Buskulic et al., *First measurement of the quark to photon fragmentation function*, Z.Phys. **C69** (1996) 365–378.
- [158] S. Frixione, *Isolated photons in perturbative QCD*, Phys.Lett. **B429** (1998) 369–374, [arXiv:hep-ph/9801442](#) [hep-ph].
- [159] J. M. Campbell, R. K. Ellis, and C. Williams, *Vector boson pair production at the LHC*, JHEP **1107** (2011) 018, [arXiv:1105.0020](#) [hep-ph].
- [160] SM and NLO Multileg Working Group Collaboration, J. Andersen et al., *The SM and NLO Multileg Working Group: Summary report*, [arXiv:1003.1241](#) [hep-ph].
- [161] G. Corcella et al., *HERWIG 6.5 release note*, [arXiv:hep-ph/0210213](#) [hep-ph].
- [162] M. Ciccolini, A. Denner, and S. Dittmaier, *Strong and electroweak corrections to the production of Higgs + 2jets via weak interactions at the LHC*, Phys.Rev.Lett. **99** (2007) 161803, [arXiv:0707.0381](#) [hep-ph].
- [163] M. Ciccolini, A. Denner, and S. Dittmaier, *Electroweak and QCD corrections to Higgs production via vector-boson fusion at the LHC*, Phys.Rev. **D77** (2008) 013002, [arXiv:0710.4749](#) [hep-ph].
- [164] M. Bahr, S. Gieseke, M. Gigg, D. Grellscheid, K. Hamilton, et al., *Herwig++ Physics*

- and *Manual*, Eur.Phys.J. **C58** (2008) 639–707, arXiv:0803.0883 [hep-ph].
- [165] K. Arnold et al., *Herwig++ 2.6 Release Note*, arXiv:1205.4902 [hep-ph].
- [166] T. Gleisberg, S. Höche, F. Krauss, M. Schönherr, S. Schumann, et al., *Event generation with SHERPA 1.1*, JHEP **0902** (2009) 007, arXiv:0811.4622 [hep-ph].
- [167] Q.-H. Cao and C. Yuan, *Combined effect of QCD resummation and QED radiative correction to W boson observables at the Tevatron*, Phys.Rev.Lett. **93** (2004) 042001, arXiv:hep-ph/0401026 [hep-ph].
- [168] G. Balossini et al., *Combination of electroweak and QCD corrections to single W production at the Fermilab Tevatron and the CERN LHC*, JHEP **1001** (2010) 013, arXiv:0907.0276 [hep-ph].
- [169] W. PáĆaczek, S. Jadach, and M. Krasny, *Drell-Yan processes with WINHAC*, Acta Phys.Polon. **B44** (2013) no. 11, 2171–2178, arXiv:1310.5994 [hep-ph].
- [170] P. Nason, *A New method for combining NLO QCD with shower Monte Carlo algorithms*, JHEP **0411** (2004) 040, arXiv:hep-ph/0409146 [hep-ph].
- [171] C. Bernaciak and D. Wackerroth, *Combining NLO QCD and Electroweak Radiative Corrections to W boson Production at Hadron Colliders in the POWHEG Framework*, Phys.Rev. **D85** (2012) 093003, arXiv:1201.4804 [hep-ph].
- [172] L. Barze, G. Montagna, P. Nason, O. Nicrosini, and F. Piccinini, *Implementation of electroweak corrections in the POWHEG BOX: single W production*, JHEP **1204** (2012) 037, arXiv:1202.0465 [hep-ph].
- [173] L. Barze, G. Montagna, P. Nason, O. Nicrosini, F. Piccinini, et al., *Neutral current Drell-Yan with combined QCD and electroweak corrections in the POWHEG BOX*, Eur.Phys.J. **C73** (2013) 2474, arXiv:1302.4606 [hep-ph].
- [174] N. Kauer, *Narrow-width approximation limitations*, Phys.Lett. **B649** (2007) 413–416, arXiv:hep-ph/0703077 [hep-ph].
- [175] D. Berdine, N. Kauer, and D. Rainwater, *Breakdown of the Narrow Width Approximation for New Physics*, Phys.Rev.Lett. **99** (2007) 111601, arXiv:hep-ph/0703058 [hep-ph].
- [176] P. Gambino and P. A. Grassi, *The Nielsen identities of the SM and the definition of mass*, Phys.Rev. **D62** (2000) 076002, arXiv:hep-ph/9907254 [hep-ph].
- [177] P. A. Grassi, B. A. Kniehl, and A. Sirlin, *Width and partial widths of unstable particles in the light of the Nielsen identities*, Phys.Rev. **D65** (2002) 085001, arXiv:hep-ph/0109228 [hep-ph].
- [178] D. Y. Bardin, A. Leike, T. Riemann, and M. Sachwitz, *Energy Dependent Width Effects in e^+e^- Annihilation Near the Z Boson Pole*, Phys.Lett. **B206** (1988) 539–542.
- [179] W. Beenakker et al., *The Fermion loop scheme for finite width effects in e^+e^- annihilation into four fermions*, Nucl.Phys. **B500** (1997) 255–298, arXiv:hep-ph/9612260 [hep-ph].
- [180] A. Denner, S. Dittmaier, M. Roth, and D. Wackerroth, *Predictions for all processes $e^+e^- \rightarrow 4 \text{ fermions} + \gamma$* , Nucl.Phys. **B560** (1999) 33–65, arXiv:hep-ph/9904472 [hep-ph].
- [181] S. Dittmaier and M. Roth, *LUSIFER: A LUCid approach to six FERMion production*, Nucl.Phys. **B642** (2002) 307–343, arXiv:hep-ph/0206070 [hep-ph].
- [182] R. G. Stuart, *Gauge invariance, analyticity and physical observables at the Z^0 resonance*, Phys.Lett. **B262** (1991) 113–119.
- [183] A. Aepli, G. J. van Oldenborgh, and D. Wyler, *Unstable particles in one loop calculations*, Nucl.Phys. **B428** (1994) 126–146, arXiv:hep-ph/9312212 [hep-ph].
- [184] G. Passarino, C. Sturm, and S. Uccirati, *Higgs Pseudo-Observables, Second Riemann*

- Sheet and All That*, Nucl.Phys. **B834** (2010) 77–115, arXiv:1001.3360 [hep-ph].
- [185] S. Goria, G. Passarino, and D. Rosco, *The Higgs Boson Lineshape*, Nucl.Phys. **B864** (2012) 530–579, arXiv:1112.5517 [hep-ph].
- [186] G. M. W. et al., *Reports of the Working Groups on Precision Calculations for LEP2 Physics: Proceedings. Four fermion production in electron positron collisions*, arXiv:hep-ph/0005309 [hep-ph].
- [187] M. Beneke, A. Chapovsky, A. Signer, and G. Zanderighi, *Effective theory approach to unstable particle production*, Phys.Rev.Lett. **93** (2004) 011602, arXiv:hep-ph/0312331 [hep-ph].
- [188] M. Beneke, A. Chapovsky, A. Signer, and G. Zanderighi, *Effective theory calculation of resonant high-energy scattering*, Nucl.Phys. **B686** (2004) 205–247, arXiv:hep-ph/0401002 [hep-ph].
- [189] A. H. Hoang and C. J. Reisser, *Electroweak absorptive parts in NRQCD matching conditions*, Phys.Rev. **D71** (2005) 074022, arXiv:hep-ph/0412258 [hep-ph].
- [190] M. Beneke, P. Falgari, C. Schwinn, A. Signer, and G. Zanderighi, *Four-fermion production near the W pair production threshold*, Nucl.Phys. **B792** (2008) 89–135, arXiv:0707.0773 [hep-ph].
- [191] P. Falgari, A. Papanastasiou, and A. Signer, *Finite-width effects in unstable-particle production at hadron colliders*, JHEP **1305** (2013) 156, arXiv:1303.5299 [hep-ph].
- [192] A. Denner, S. Dittmaier, M. Roth, and L. Wieders, *Electroweak corrections to charged-current $e^+e^- \rightarrow 4$ fermion processes: Technical details and further results*, Nucl.Phys. **B724** (2005) 247–294, arXiv:hep-ph/0505042 [hep-ph].
- [193] A. Bredenstein, A. Denner, S. Dittmaier, and M. Weber, *Precise predictions for the Higgs-boson decay $H \rightarrow WW/ZZ \rightarrow 4$ leptons*, Phys.Rev. **D74** (2006) 013004, arXiv:hep-ph/0604011 [hep-ph].
- [194] A. Bredenstein, A. Denner, S. Dittmaier, and M. Weber, *Radiative corrections to the semileptonic and hadronic Higgs-boson decays $H \rightarrow WW/ZZ \rightarrow 4$ fermions*, JHEP **0702** (2007) 080, arXiv:hep-ph/0611234 [hep-ph].
- [195] S. Actis, G. Passarino, C. Sturm, and S. Uccirati, *NLO Electroweak Corrections to Higgs Boson Production at Hadron Colliders*, Phys.Lett. **B670** (2008) 12–17, arXiv:0809.1301 [hep-ph].
- [196] S. Actis, G. Passarino, C. Sturm, and S. Uccirati, *Two-Loop Threshold Singularities, Unstable Particles and Complex Masses*, Phys.Lett. **B669** (2008) 62–68, arXiv:0809.1302 [hep-ph].
- [197] G. Passarino, *Higgs CAT*, arXiv:1312.2397 [hep-ph].
- [198] T. Binoth, F. Boudjema, G. Dissertori, A. Lazopoulos, A. Denner, et al., *A Proposal for a standard interface between Monte Carlo tools and one-loop programs*, Comput.Phys.Commun. **181** (2010) 1612–1622, arXiv:1001.1307 [hep-ph].
- [199] S. Alioli, S. Badger, J. Bellm, B. Biedermann, F. Boudjema, et al., *Update of the Binoth Les Houches Accord for a standard interface between Monte Carlo tools and one-loop programs*, Comput.Phys.Commun. **185** (2014) 560–571, arXiv:1308.3462 [hep-ph].
- [200] S. Catani and M. Seymour, *A General algorithm for calculating jet cross-sections in NLO QCD*, Nucl.Phys. **B485** (1997) 291–419, arXiv:hep-ph/9605323 [hep-ph].
- [201] S. Badger, B. Biedermann, P. Uwer, and V. Yundin, *Numerical evaluation of virtual corrections to multi-jet production in massless QCD*, arXiv:1209.0100 [hep-ph].
- [202] J. Kotanski, J. Katzy, S. Plätzer, and Z. Nagy, *Interfacing nlojet++ and Herwig++/Matchbox*, unpublished, .

- [203] J. Bellm, S. Gieseke, N. Greiner, G. Heinrich, S. Plätzer, C. Reuschle, and J. von Soden-Fraunhofen, *GoSam plus Herwig++/Matchbox, these proceedings*, .
- [204] M. Czakon, C. Papadopoulos, and M. Worek, *Polarizing the Dipoles*, JHEP **0908** (2009) 085, arXiv:0905.0883 [hep-ph].
- [205] S. Plätzer and M. Sjö Dahl, *Subleading Nc improved Parton Showers*, JHEP **1207** (2012) 042, arXiv:1201.0260 [hep-ph].
- [206] S. Plätzer, *Summing Large-N Towers in Colour Flow Evolution*, arXiv:1312.2448 [hep-ph].
- [207] C. Berger, Z. Bern, L. Dixon, F. Febres Cordero, D. Forde, et al., *An Automated Implementation of On-Shell Methods for One-Loop Amplitudes*, Phys.Rev. **D78** (2008) 036003, arXiv:0803.4180 [hep-ph].
- [208] T. Hahn, *Feynman Diagram Calculations with FeynArts, FormCalc, and LoopTools*, PoS **ACAT2010** (2010) 078, arXiv:1006.2231 [hep-ph].
- [209] J. M. Campbell and R. Ellis, *MCFM for the Tevatron and the LHC*, Nucl.Phys.Proc.Suppl. **205-206** (2010) 10–15, arXiv:1007.3492 [hep-ph].
- [210] K. Arnold, J. Bellm, G. Bozzi, M. Brieg, F. Campanario, et al., *VBFNLO: A Parton Level Monte Carlo for Processes with Electroweak Bosons – Manual for Version 2.5.0*, arXiv:1107.4038 [hep-ph].
- [211] S. Plätzer, *Controlling inclusive cross sections in parton shower + matrix element merging*, JHEP **1308** (2013) 114, arXiv:1211.5467 [hep-ph].
- [212] J. Bellm, S. Gieseke, D. Grellscheid, A. Papaefstathiou, S. Plätzer, et al., *Herwig++ 2.7 Release Note*, arXiv:1310.6877 [hep-ph].
- [213] C. Degrande, C. Duhr, B. Fuks, D. Grellscheid, O. Mattelaer, et al., *UFO - The Universal FeynRules Output*, Comput.Phys.Commun. **183** (2012) 1201–1214, arXiv:1108.2040 [hep-ph].
- [214] P. Z. Skands, B. Allanach, H. Baer, C. Balazs, G. Belanger, et al., *SUSY Les Houches accord: Interfacing SUSY spectrum calculators, decay packages, and event generators*, JHEP **0407** (2004) 036, arXiv:hep-ph/0311123 [hep-ph].
- [215] S. Plätzer and S. Gieseke, *Coherent Parton Showers with Local Recoils*, JHEP **01** (2011) 024, arXiv:0909.5593 [hep-ph].
- [216] S. Badger, S. Plätzer, and V. Yundin, *The first use case for BLHA2 extensions: NJet plus Herwig++/Matchbox, these proceedings*, .
- [217] R. D. Ball, S. Carrazza, L. Del Debbio, S. Forte, J. Gao, et al., *Parton Distribution Benchmarking with LHC Data*, JHEP **1304** (2013) 125, arXiv:1211.5142 [hep-ph].
- [218] M. Botje et al., *The PDF4LHC Working Group Interim Recommendations*, arXiv:1101.0538 [hep-ph].
- [219] W. Giele, E. N. Glover, I. Hinchliffe, J. Huston, E. Laenen, et al., *The QCD / SM working group: Summary report*, arXiv:hep-ph/0204316 [hep-ph].
- [220] G. P. Salam and J. Rojo, *A Higher Order Perturbative Parton Evolution Toolkit (HOPPET)*, Comput.Phys.Commun. **180** (2009) 120–156, arXiv:0804.3755 [hep-ph].
- [221] A. Vogt, *Efficient evolution of unpolarized and polarized parton distributions with QCD-PEGASUS*, Comput.Phys.Commun. **170** (2005) 65–92, arXiv:hep-ph/0408244 [hep-ph].
- [222] M. Dittmar, S. Forte, A. Glazov, S. Moch, S. Alekhin, et al., *Working Group I: Parton distributions: Summary report for the HERA LHC Workshop Proceedings*, arXiv:hep-ph/0511119 [hep-ph].
- [223] F. Demartin, S. Forte, E. Mariani, J. Rojo, and A. Vicini, *The impact of PDF and alphas*

- uncertainties on Higgs Production in gluon fusion at hadron colliders*, Phys.Rev. **D82** (2010) 014002, arXiv:1004.0962 [hep-ph].
- [224] G. Watt, *Parton distribution function dependence of benchmark Standard Model total cross sections at the 7 TeV LHC*, JHEP **1109** (2011) 069, arXiv:1106.5788 [hep-ph].
- [225] S. Alekhin, S. Alioli, R. D. Ball, V. Bertone, J. Blumlein, et al., *The PDF4LHC Working Group Interim Report*, arXiv:1101.0536 [hep-ph].
- [226] S. Alekhin, J. Blumlein, P. Jimenez-Delgado, S. Moch, and E. Reya, *NNLO Benchmarks for Gauge and Higgs Boson Production at TeV Hadron Colliders*, Phys.Lett. **B697** (2011) 127–135, arXiv:1011.6259 [hep-ph].
- [227] S. Alekhin, J. Blumlein, and S. Moch, *Parton Distribution Functions and Benchmark Cross Sections at NNLO*, Phys.Rev. **D86** (2012) 054009, arXiv:1202.2281 [hep-ph].
- [228] A. M. Cooper-Sarkar, *Including heavy flavour production in PDF fits*, arXiv:0709.0191 [hep-ph].
- [229] R. Thorne, *Effect of changes of variable flavor number scheme on parton distribution functions and predicted cross sections*, Phys.Rev. **D86** (2012) 074017, arXiv:1201.6180 [hep-ph].
- [230] The NNPDF Collaboration, R. D. Ball et al., *Theoretical issues in PDF determination and associated uncertainties*, Phys.Lett. **B723** (2013) 330–339, arXiv:1303.1189 [hep-ph].
- [231] R. Thorne, *The effect on PDFs and $\alpha_s(M_Z^2)$ due to changes in flavour scheme and higher twist contributions*, arXiv:1402.3536 [hep-ph].
- [232] S. Alekhin, J. Blumlein, and S.-O. Moch, *ABM news and benchmarks*, PoS **DIS2013** (2013) 039, arXiv:1308.5166 [hep-ph].
- [233] J. Gao, M. Guzzi, J. Huston, H.-L. Lai, Z. Li, et al., *The CT10 NNLO Global Analysis of QCD*, arXiv:1302.6246 [hep-ph].
- [234] H1 and ZEUS Collaboration, A. Cooper-Sarkar, *PDF Fits at HERA*, PoS **EPS-HEP2011** (2011) 320, arXiv:1112.2107 [hep-ph].
- [235] A. Martin, W. Stirling, R. Thorne, and G. Watt, *Parton distributions for the LHC*, Eur.Phys.J. **C63** (2009) 189–285, arXiv:0901.0002 [hep-ph].
- [236] R. D. Ball, V. Bertone, S. Carrazza, C. S. Deans, L. Del Debbio, et al., *Parton distributions with LHC data*, Nucl.Phys. **B867** (2013) 244–289, arXiv:1207.1303 [hep-ph].
- [237] H1 and ZEUS Collaboration, F. Aaron et al., *Combined Measurement and QCD Analysis of the Inclusive e^+p Scattering Cross Sections at HERA*, JHEP **1001** (2010) 109, arXiv:0911.0884 [hep-ex].
- [238] S. Dulat, T.-J. Hou, J. Gao, J. Huston, P. Nadolsky, et al., *Higgs Boson Cross Section from CTEQ-TEA Global Analysis*, arXiv:1310.7601 [hep-ph].
- [239] H1, ZEUS Collaboration, H. Abramowicz et al., *Combination and QCD Analysis of Charm Production Cross Section Measurements in Deep-Inelastic ep Scattering at HERA*, Eur.Phys.J. **C73** (2013) 2311, arXiv:1211.1182 [hep-ex].
- [240] C. Anastasiou, S. Buehler, F. Herzog, and A. Lazopoulos, *Total cross-section for Higgs boson hadroproduction with anomalous Standard Model interactions*, JHEP **1112** (2011) 058, arXiv:1107.0683 [hep-ph].
- [241] M. Guzzi, P. M. Nadolsky, H.-L. Lai, and C.-P. Yuan, *General-Mass Treatment for Deep Inelastic Scattering at Two-Loop Accuracy*, Phys.Rev. **D86** (2012) 053005, arXiv:1108.5112 [hep-ph].
- [242] R. Thorne, *A Variable-flavor number scheme for NNLO*, Phys.Rev. **D73** (2006) 054019,

- arXiv:hep-ph/0601245 [hep-ph].
- [243] S. Forte, E. Laenen, P. Nason, and J. Rojo, *Heavy quarks in deep-inelastic scattering*, Nucl.Phys. **B834** (2010) 116–162, arXiv:1001.2312 [hep-ph].
 - [244] V. Bertone, S. Carrazza, and J. Rojo, *APFEL: A PDF Evolution Library with QED corrections*, arXiv:1310.1394 [hep-ph].
 - [245] Herafitter program (2012), www.herafitter.org.
 - [246] M. Botje, *QCDNUM: Fast QCD Evolution and Convolution*, Comput.Phys.Commun. **182** (2011) 490–532, arXiv:1005.1481 [hep-ph].
 - [247] H1 Collaboration, F. Aaron et al., *A Precision Measurement of the Inclusive ep Scattering Cross Section at HERA*, Eur.Phys.J. **C64** (2009) 561–587, arXiv:0904.3513 [hep-ex].
 - [248] S. Riemersma, J. Smith, and W. van Neerven, *Rates for inclusive deep inelastic electroproduction of charm quarks at HERA*, Phys.Lett. **B347** (1995) 143–151, arXiv:hep-ph/9411431 [hep-ph].
 - [249] J. Pumplin, *Parametrization dependence and Delta Chi**2 in parton distribution fitting*, Phys.Rev. **D82** (2010) 114020, arXiv:0909.5176 [hep-ph].
 - [250] A. Martin, A. T. Mathijssen, W. Stirling, R. Thorne, B. Watt, et al., *Extended Parameterisations for MSTW PDFs and their effect on Lepton Charge Asymmetry from W Decays*, Eur.Phys.J. **C73** (2013) 2318, arXiv:1211.1215 [hep-ph].
 - [251] J. Pumplin, D. Stump, J. Huston, H. Lai, P. M. Nadolsky, et al., *New generation of parton distributions with uncertainties from global QCD analysis*, JHEP **0207** (2002) 012, arXiv:hep-ph/0201195 [hep-ph].
 - [252] J. Pumplin, D. Stump, R. Brock, D. Casey, J. Huston, et al., *Uncertainties of predictions from parton distribution functions. 2. The Hessian method*, Phys.Rev. **D65** (2001) 014013, arXiv:hep-ph/0101032 [hep-ph].
 - [253] G. D’Agostini, *On the use of the covariance matrix to fit correlated data*, Nucl.Instrum.Meth. **A346** (1994) 306–311.
 - [254] NNPDF Collaboration, R. D. Ball et al., *Fitting Parton Distribution Data with Multiplicative Normalization Uncertainties*, JHEP **1005** (2010) 075, arXiv:0912.2276 [hep-ph].
 - [255] D. Stump, J. Pumplin, R. Brock, D. Casey, J. Huston, et al., *Uncertainties of predictions from parton distribution functions. 1. The Lagrange multiplier method*, Phys.Rev. **D65** (2001) 014012, arXiv:hep-ph/0101051 [hep-ph].
 - [256] A. Martin, W. Stirling, R. Thorne, and G. Watt, *Heavy-quark mass dependence in global PDF analyses and 3- and 4-flavour parton distributions*, Eur.Phys.J. **C70** (2010) 51–72, arXiv:1007.2624 [hep-ph].
 - [257] J. Gao, M. Guzzi, and P. M. Nadolsky, *Charm quark mass dependence in a global QCD analysis*, Eur.Phys.J. **C73** (2013) 2541, arXiv:1304.3494 [hep-ph].
 - [258] P. M. Nadolsky and W.-K. Tung, *Improved Formulation of Global QCD Analysis with Zero-mass Matrix Elements*, Phys.Rev. **D79** (2009) 113014, arXiv:0903.2667 [hep-ph].
 - [259] D. d’Enterria and J. Rojo, *Quantitative constraints on the gluon distribution function in the proton from collider isolated-photon data*, Nucl.Phys. **B860** (2012) 311–338, arXiv:1202.1762 [hep-ph].
 - [260] L. Carminati, G. Costa, D. D’Enterria, I. Koletsou, G. Marchiori, et al., *Sensitivity of the LHC isolated-gamma+jet data to the parton distribution functions of the proton*, EPL **101** (2013) 61002, arXiv:1212.5511.

- [261] S. A. Malik and G. Watt, *Ratios of W and Z cross sections at large boson p_T as a constraint on PDFs and background to new physics*, JHEP **1402** (2014) 025, arXiv:1304.2424 [hep-ph].
- [262] M. Czakon, M. L. Mangano, A. Mitov, and J. Rojo, *Constraints on the gluon PDF from top quark pair production at hadron colliders*, JHEP **1307** (2013) 167, arXiv:1303.7215 [hep-ph].
- [263] B. Watt, P. Motylinski, and R. Thorne, *The Effect of LHC Jet Data on MSTW PDFs*, arXiv:1311.5703 [hep-ph].
- [264] Particle Data Group Collaboration, J. Beringer et al., *Review of Particle Physics (RPP)*, Phys.Rev. **D86** (2012) 010001.
- [265] NNPDF Collaboration Collaboration, R. D. Ball et al., *Unbiased global determination of parton distributions and their uncertainties at NNLO and at LO*, Nucl.Phys. **B855** (2012) 153–221, arXiv:1107.2652 [hep-ph].
- [266] R. D. Ball, V. Bertone, L. Del Debbio, S. Forte, A. Guffanti, et al., *Precision NNLO determination of $\alpha_s(M_Z)$ using an unbiased global parton set*, Phys.Lett. **B707** (2012) 66–71, arXiv:1110.2483 [hep-ph].
- [267] S. Lionetti, R. D. Ball, V. Bertone, F. Cerutti, L. Del Debbio, et al., *Precision determination of α_s using an unbiased global NLO parton set*, Phys.Lett. **B701** (2011) 346–352, arXiv:1103.2369 [hep-ph].
- [268] C. Anastasiou, S. Buehler, F. Herzog, and A. Lazopoulos, *Inclusive Higgs boson cross-section for the LHC at 8 TeV*, JHEP **1204** (2012) 004, arXiv:1202.3638 [hep-ph].
- [269] R. Thorne and G. Watt, *PDF dependence of Higgs cross sections at the Tevatron and LHC: Response to recent criticism*, JHEP **1108** (2011) 100, arXiv:1106.5789 [hep-ph].
- [270] NNPDF Collaboration, R. D. Ball et al., *Reweighting NNPDFs: the W lepton asymmetry*, Nucl.Phys. **B849** (2011) 112–143, arXiv:1012.0836 [hep-ph].
- [271] R. D. Ball, V. Bertone, F. Cerutti, L. Del Debbio, S. Forte, et al., *Reweighting and Unweighting of Parton Distributions and the LHC W lepton asymmetry data*, Nucl.Phys. **B855** (2012) 608–638, arXiv:1108.1758 [hep-ph].
- [272] M. L. Mangano and J. Rojo, *Cross Section Ratios between different CM energies at the LHC: opportunities for precision measurements and BSM sensitivity*, JHEP **1208** (2012) 010, arXiv:1206.3557 [hep-ph].
- [273] M. Whalley, D. Bourilkov, and R. Group, *The Les Houches accord PDFs (LHAPDF) and LHAGLUE*, arXiv:hep-ph/0508110 [hep-ph].
- [274] <http://yaml.org/>.
- [275] <https://zlibc.linux.lu/>.
- [276] <http://lhapdf.hepforge.org/>.
- [277] S. D. Ellis, Z. Kunszt, and D. E. Soper, *One-Jet Inclusive Cross Section at Order α_s^3 : Quarks and Gluons*, Phys. Rev. Lett. **64** (1990) 2121.
- [278] S. D. Ellis, Z. Kunszt, and D. E. Soper, *Two-Jet Production in Hadron Collisions at Order α_s^3 in QCD*, Phys. Rev. Lett. **69** (1992) 1496.
- [279] W. Giele, E. N. Glover, and D. A. Kosower, *The Two-Jet Differential Cross Section at $\mathcal{O}(\alpha_s^3)$ in Hadron Collisions*, Phys. Rev. Lett. **73** (1994) 2019, arXiv:hep-ph/9403347 [hep-ph].
- [280] S. Moretti, M. Nolten, and D. Ross, *Weak corrections to four-parton processes*, Nucl. Phys. B **759** (2006) 50, arXiv:hep-ph/0606201 [hep-ph].
- [281] A. Scharf, *Electroweak corrections to b -jet and di-jet production*, arXiv:0910.0223

- [hep-ph].
- [282] CMS Collaboration, S. Chatrchyan et al., *The CMS experiment at the CERN LHC*, JINST **3** (2008) S08004.
- [283] M. Cacciari, G. P. Salam, and G. Soyez, *FastJet User Manual*, Eur.Phys.J. **C72** (2012) 1896, arXiv:1111.6097 [hep-ph].
- [284] M. Cacciari, G. P. Salam, and G. Soyez, *The Anti- $k(t)$ jet clustering algorithm*, JHEP **0804** (2008) 063, arXiv:0802.1189 [hep-ph].
- [285] M. Whalley, *The Durham-RAL high-energy physics databases: HEPDATA*, Comput. Phys. Commun. **57** (1989) 536–537. <http://durpdg.dur.ac.uk/>.
- [286] A. Buckley and M. Whalley, *HepData reloaded: Reinventing the HEP data archive*, PoS **ACAT2010** (2010) 067, arXiv:1006.0517 [hep-ex].
- [287] fastNLO Collaboration, D. Britzger, K. Rabbertz, F. Stober, and M. Wobisch, *New features in version 2 of the fastNLO project*, arXiv:1208.3641 [hep-ph].
- [288] T. Sjostrand, S. Mrenna, and P. Z. Skands, *PYTHIA 6.4 Physics and Manual*, JHEP **0605** (2006) 026, arXiv:hep-ph/0603175 [hep-ph].
- [289] H.-L. Lai, M. Guzzi, J. Huston, Z. Li, P. M. Nadolsky, et al., *New parton distributions for collider physics*, Phys.Rev. **D82** (2010) 074024, arXiv:1007.2241 [hep-ph].
- [290] R. D. Ball, V. Bertone, F. Cerutti, L. Del Debbio, S. Forte, et al., *Impact of Heavy Quark Masses on Parton Distributions and LHC Phenomenology*, Nucl. Phys. B **849** (2011) 296, arXiv:1101.1300 [hep-ph].
- [291] ATLAS Collaboration, G. Aad et al., *Search for high-mass dilepton resonances in 20/fb of pp collisions at $\sqrt{s} = 8$ TeV with the ATLAS experiment*, ATLAS-CONF-2013-017.
- [292] R. Gavin, Y. Li, F. Petriello, and S. Quackenbush, *FEWZ 2.0: A code for hadronic Z production at next-to-next-to-leading order*, Comput.Phys.Commun. **182** (2011) 2388–2403, arXiv:1011.3540 [hep-ph].
- [293] R. Gavin, Y. Li, F. Petriello, and S. Quackenbush, *W Physics at the LHC with FEWZ 2.1*, arXiv:1201.5896 [hep-ph].
- [294] Y. Li and F. Petriello, *Combining QCD and electroweak corrections to dilepton production in FEWZ*, arXiv:1208.5967 [hep-ph].
- [295] S. Catani and M. Grazzini, *An NNLO subtraction formalism in hadron collisions and its application to Higgs boson production at the LHC*, Phys.Rev.Lett. **98** (2007) 222002, arXiv:hep-ph/0703012 [hep-ph].
- [296] S. Catani, L. Cieri, G. Ferrera, D. de Florian, and M. Grazzini, *Vector boson production at hadron colliders: A Fully exclusive QCD calculation at NNLO*, Phys.Rev.Lett. **103** (2009) 082001, arXiv:0903.2120 [hep-ph].
- [297] R. Hamberg, W. L. van Neerven, and T. Matsuura, *A Complete Calculation Of The Order α_s^2 Correction To The Drell-Yan K Factor*, Nucl. Phys. B **359** (1991) 343.
- [298] C. Anastasiou, L. Dixon, K. Melnikov, and F. Petriello, *High precision QCD at hadron colliders: Electroweak gauge boson rapidity distributions at NNLO*, Phys. Rev. D **69** (2004) 094008. v0.9 including LHAPDF interface by D. Maitre.
- [299] M. Grazzini, *private communications*, 2013.
- [300] D. Bardin, S. Bondarenko, P. Christova, L. Kalinovskaya, L. Romyantsev, et al., *SANC integrator in the progress: QCD and EW contributions*, JETP Lett. **96** (2012) 285–289, arXiv:1207.4400 [hep-ph].
- [301] Particle Data Group Collaboration, J. Beringer et al., *Review of Particle Physics*, vol. 86. 2012.

- [302] S. G. Bondarenko and A. A. Sapronov, *NLO EW and QCD proton-proton cross section calculations with mcsanc-v1.01*, Comput.Phys.Commun. **184** (2013) 2343–2350, arXiv:1301.3687 [hep-ph].
- [303] P. Golonka and Z. Was, *PHOTOS Monte Carlo: a precision tool for QED corrections in Z and W decays*, Eur. Phys. J. **C45** (2006) 97–107.
- [304] A. Arbuzov, R. Sadykov, and Z. Was, *QED Bremsstrahlung in decays of electroweak bosons*, Eur.Phys.J. **C73** (2013) 2625, arXiv:1212.6783 [hep-ph].
- [305] F. Petriello and Y. Li, *FEWZ 3.1.a3 EW flags resulting from a private communication*, July 2012.
- [306] A. Belloni and U. Klein, *Talk at LPCC EW WG meeting, 27.04.2012*, <https://indico.cern.ch/getFile.py/access?contribId=3&resId=0&materialId=slides&confId=188020>.
- [307] U. Klein, *Talk at LPCC EW WG meeting, 9.10.2012*, <https://indico.cern.ch/getFile.py/access?contribId=14&sessionId=2&resId=0&materialId=slides&confId=203748>.
- [308] ATLAS Collaboration, G. Aad et al., *Measurement of the high-mass Drell-Yan differential cross-section in pp collisions at $\sqrt{s}=7$ TeV with the ATLAS detector*, Phys.Lett. **B725** (2013) 223–242, arXiv:1305.4192 [hep-ex].
- [309] R. Roberts and G. Watt, *private communication at PDF4LHC meeting*, December 2012.
- [310] ATLAS Collaboration Collaboration, G. Aad et al., *Search for squarks and gluinos using final states with jets and missing transverse momentum with the ATLAS detector in $\sqrt{s} = 7$ TeV proton-proton collisions*, Phys.Lett. **B710** (2012) 67–85, arXiv:1109.6572 [hep-ex].
- [311] CMS Collaboration Collaboration, S. Chatrchyan et al., *Search for New Physics with Jets and Missing Transverse Momentum in pp collisions at $\sqrt{s} = 7$ TeV*, JHEP **1108** (2011) 155, arXiv:1106.4503 [hep-ex].
- [312] CMS Collaboration Collaboration, S. Chatrchyan et al., *Search for new physics in the multijet and missing transverse momentum final state in proton-proton collisions at $\sqrt{s} = 7$ TeV*, Phys.Rev.Lett. **109** (2012) 171803, arXiv:1207.1898 [hep-ex].
- [313] S. Ask, M. Parker, T. Sandoval, M. Shea, and W. Stirling, *Using gamma+jets Production to Calibrate the Standard Model Z(nunu)+jets Background to New Physics Processes at the LHC*, JHEP **1110** (2011) 058, arXiv:1107.2803 [hep-ph].
- [314] Z. Bern, G. Diana, L. Dixon, F. Febres Cordero, S. Hoche, et al., *Driving Missing Data at Next-to-Leading Order*, Phys.Rev. **D84** (2011) 114002, arXiv:1106.1423 [hep-ph].
- [315] Z. Bern, G. Diana, L. Dixon, F. Febres Cordero, S. Hoeche, et al., *Missing Energy and Jets for Supersymmetry Searches*, Phys.Rev. **D87** (2013) no. 3, 034026, arXiv:1206.6064 [hep-ph].
- [316] J. H. Kuhn, A. Kulesza, S. Pozzorini, and M. Schulze, *Electroweak corrections to hadronic photon production at large transverse momenta*, JHEP **0603** (2006) 059, arXiv:hep-ph/0508253 [hep-ph].
- [317] E. Maina, S. Moretti, and D. A. Ross, *One loop weak corrections to gamma / Z hadroproduction at finite transverse momentum*, Phys.Lett. **B593** (2004) 143–150, arXiv:hep-ph/0403050 [hep-ph].
- [318] W. Stirling and E. Vryonidou, *Electroweak corrections and Bloch-Nordsieck violations in 2-to-2 processes at the LHC*, JHEP **1304** (2013) 155, arXiv:1212.6537 [hep-ph].
- [319] P. Ciafaloni and D. Comelli, *Sudakov enhancement of electroweak corrections*, Phys.Lett. **B446** (1999) 278–284, arXiv:hep-ph/9809321 [hep-ph].

- [320] M. Beccaria, P. Ciafaloni, D. Comelli, F. Renard, and C. Verzegnassi, *Logarithmic expansion of electroweak corrections to four-fermion processes in the TeV region*, Phys.Rev. **D61** (2000) 073005, arXiv:hep-ph/9906319 [hep-ph].
- [321] M. Ciafaloni, P. Ciafaloni, and D. Comelli, *Electroweak Bloch-Nordsieck violation at the TeV scale: 'Strong' weak interactions?*, Nucl.Phys. **B589** (2000) 359–380, arXiv:hep-ph/0004071 [hep-ph].
- [322] A. Denner and S. Pozzorini, *One loop leading logarithms in electroweak radiative corrections. 1. Results*, Eur.Phys.J. **C18** (2001) 461–480, arXiv:hep-ph/0010201 [hep-ph].
- [323] M. Ciafaloni, P. Ciafaloni, and D. Comelli, *Bloch-Nordsieck violation in spontaneously broken Abelian theories*, Phys.Rev.Lett. **87** (2001) 211802, arXiv:hep-ph/0103315 [hep-ph].
- [324] J. H. Kuhn, A. Kulesza, S. Pozzorini, and M. Schulze, *Logarithmic electroweak corrections to hadronic Z+1 jet production at large transverse momentum*, Phys.Lett. **B609** (2005) 277–285, arXiv:hep-ph/0408308 [hep-ph].
- [325] J. H. Kuhn, A. Kulesza, S. Pozzorini, and M. Schulze, *One-loop weak corrections to hadronic production of Z bosons at large transverse momenta*, Nucl.Phys. **B727** (2005) 368–394, arXiv:hep-ph/0507178 [hep-ph].
- [326] J. H. Kuhn, A. Kulesza, S. Pozzorini, and M. Schulze, *Electroweak corrections to large transverse momentum production of W bosons at the LHC*, Phys.Lett. **B651** (2007) 160–165, arXiv:hep-ph/0703283 [hep-ph].
- [327] E. Accomando, A. Denner, and S. Pozzorini, *Logarithmic electroweak corrections to $e^+e^- \rightarrow \nu_e\bar{\nu}_e W^+W^-$* , JHEP **0703** (2007) 078, arXiv:hep-ph/0611289 [hep-ph].
- [328] S. Pozzorini, *Electroweak radiative corrections at high-energies*, arXiv:hep-ph/0201077 [hep-ph].
- [329] M. L. Mangano, M. Moretti, F. Piccinini, R. Pittau, and A. D. Polosa, *ALPGEN, a generator for hard multiparton processes in hadronic collisions*, JHEP **0307** (2003) 001, arXiv:hep-ph/0206293 [hep-ph].
- [330] E. Gerwick, *Recursive prescription for logarithmic jet rate coefficients*, Phys.Rev. **D88** (2013) 094009, arXiv:1305.6319 [hep-ph].
- [331] E. Gerwick, S. Schumann, B. Gripaios, and B. Webber, *QCD Jet Rates with the Inclusive Generalized kt Algorithms*, JHEP **1304** (2013) 089, arXiv:1212.5235.
- [332] S. Schumann and F. Krauss, *A Parton shower algorithm based on Catani-Seymour dipole factorisation*, JHEP **0803** (2008) 038, arXiv:0709.1027 [hep-ph].
- [333] T. Sjöstrand, S. Mrenna, and P. Z. Skands, *A Brief Introduction to PYTHIA 8.1*, Comput.Phys.Commun. **178** (2008) 852–867, arXiv:0710.3820 [hep-ph].
- [334] C. W. Bauer and F. J. Tackmann, *Gaining analytic control of parton showers*, Phys.Rev. **D76** (2007) 114017, arXiv:0705.1719 [hep-ph].
- [335] C. W. Bauer and M. D. Schwartz, *Event Generation from Effective Field Theory*, Phys.Rev. **D76** (2007) 074004, arXiv:hep-ph/0607296 [hep-ph].
- [336] B. R. Webber, *QCD Jets and Parton Showers*, arXiv:1009.5871 [hep-ph].
- [337] J. R. Andersen and J. M. Smillie, *Constructing All-Order Corrections to Multi-Jet Rates*, JHEP **1001** (2010) 039, arXiv:0908.2786 [hep-ph].
- [338] J. R. Andersen and J. M. Smillie, *The Factorisation of the t-channel Pole in Quark-Gluon Scattering*, Phys.Rev. **D81** (2010) 114021, arXiv:0910.5113 [hep-ph].
- [339] J. R. Andersen and J. M. Smillie, *Multiple Jets at the LHC with High Energy Jets*, JHEP **1106** (2011) 010, arXiv:1101.5394 [hep-ph].

- [340] C. Berger, Z. Bern, L. J. Dixon, F. Febres Cordero, D. Forde, H. Ita, D. A. Kosower, and D. Maître, *An automated implementation of on-shell methods for one-loop amplitudes*, Phys. Rev. **D78** (2008) 036003, arXiv:0803.4180 [hep-ph].
- [341] Z. Bern, G. Diana, L. J. Dixon, F. Febres Cordero, S. Höche, H. Ita, D. A. Kosower, D. Maître, and K. Ozeren, *Four-jet production at the Large Hadron Collider at next-to-leading order in QCD*, Phys. Rev. Lett. **109** (2011) 042001, arXiv:1112.3940 [hep-ph].
- [342] T. Gleisberg, S. Höche, F. Krauss, A. Schälicke, S. Schumann, and J. Winter, *SHERPA 1.α: A proof of concept version*, JHEP **0402** (2004) 056, arXiv:hep-ph/0311263 [hep-ph].
- [343] T. Gleisberg, S. Höche, F. Krauss, M. Schönherr, S. Schumann, F. Siegert, and J. Winter, *Event generation with SHERPA 1.1*, JHEP **0902** (2009) 007, arXiv:0811.4622 [hep-ph].
- [344] F. Krauss, R. Kuhn, and G. Soff, *AMEGIC++ 1.0: A matrix element generator in C++*, JHEP **0202** (2002) 044, arXiv:hep-ph/0109036 [hep-ph].
- [345] T. Gleisberg and F. Krauss, *Automating dipole subtraction for QCD NLO calculations*, Eur. Phys. J. **C53** (2008) 501–523, arXiv:0709.2881 [hep-ph].
- [346] ATLAS Collaboration Collaboration, G. Aad et al., *Measurement of dijet production with a veto on additional central jet activity in pp collisions at $\sqrt{s} = 7$ TeV using the ATLAS detector*, JHEP **1109** (2011) 053, arXiv:1107.1641 [hep-ex].
- [347] J. Andersen, T. Binoth, G. Heinrich, and J. Smillie, *Loop induced interference effects in Higgs Boson plus two jet production at the LHC*, JHEP **0802** (2008) 057, arXiv:0709.3513 [hep-ph].
- [348] A. Bredenstein, K. Hagiwara, and B. Jäger, *Mixed QCD-electroweak contributions to Higgs-plus-dijet production at the LHC*, Phys.Rev. **D77** (2008) 073004, arXiv:0801.4231 [hep-ph].
- [349] L. J. Dixon and Y. Sofianatos, *Analytic one-loop amplitudes for a Higgs boson plus four partons*, JHEP **0908** (2009) 058, arXiv:0906.0008 [hep-ph].
- [350] T. Plehn, D. L. Rainwater, and D. Zeppenfeld, *Determining the structure of Higgs couplings at the LHC*, Phys.Rev.Lett. **88** (2002) 051801, arXiv:hep-ph/0105325 [hep-ph].
- [351] G. Klamke and D. Zeppenfeld, *Higgs plus two jet production via gluon fusion as a signal at the CERN LHC*, JHEP **0704** (2007) 052, arXiv:hep-ph/0703202 [HEP-PH].
- [352] Y. L. Dokshitzer, S. Troian, and V. A. Khoze, *Collective QCD Effects in the Structure of Final Multi - Hadron States. (In Russian)*, Sov.J.Nucl.Phys. **46** (1987) 712–719.
- [353] Y. L. Dokshitzer, V. A. Khoze, and T. Sjöstrand, *Rapidity gaps in Higgs production*, Phys.Lett. **B274** (1992) 116–121.
- [354] J. R. Andersen, K. Arnold, and D. Zeppenfeld, *Azimuthal Angle Correlations for Higgs Boson plus Multi-Jet Events*, JHEP **1006** (2010) 091, arXiv:1001.3822 [hep-ph].
- [355] J. Alwall, M. Herquet, F. Maltoni, O. Mattelaer, and T. Stelzer, *MadGraph 5 : Going Beyond*, JHEP **1106** (2011) 128, arXiv:1106.0522 [hep-ph].
- [356] J. M. Campbell, R. K. Ellis, and G. Zanderighi, *Next-to-Leading order Higgs + 2 jet production via gluon fusion*, JHEP **0610** (2006) 028, arXiv:hep-ph/0608194 [hep-ph].
- [357] R. Frederix and S. Frixione, *Merging meets matching in MC@NLO*, JHEP **1212** (2012) 061, arXiv:1209.6215 [hep-ph].
- [358] J. R. Andersen and C. D. White, *A New Framework for Multijet Predictions and its application to Higgs Boson production at the LHC*, Phys.Rev. **D78** (2008) 051501,

- arXiv:0802.2858 [hep-ph].
- [359] J. R. Andersen, V. Del Duca, and C. D. White, *Higgs Boson Production in Association with Multiple Hard Jets*, JHEP **0902** (2009) 015, arXiv:0808.3696 [hep-ph].
 - [360] J. R. Andersen, T. A. Hapola, and J. M. Smillie To appear .
 - [361] ATLAS Collaboration, *Further ATLAS tunes of PYTHIA6 and Pythia 8*, ATL-PHYS-PUB-2011-014, ATL-COM-PHYS-2011-1507 (2011) .
 - [362] ATLAS Collaboration, *Summary of ATLAS Pythia 8 tunes*, ATL-PHYS-PUB-2012-003, ATL-COM-PHYS-2012-738 (2012) .
 - [363] S. Alioli, P. Nason, C. Oleari, and E. Re, *NLO Higgs boson production via gluon fusion matched with shower in POWHEG*, JHEP **0904** (2009) 002, arXiv:0812.0578 [hep-ph].
 - [364] J. M. Campbell, R. K. Ellis, R. Frederix, P. Nason, C. Oleari, et al., *NLO Higgs Boson Production Plus One and Two Jets Using the POWHEG BOX, MadGraph4 and MCFM*, JHEP **1207** (2012) 092, arXiv:1202.5475 [hep-ph].
 - [365] F. Maltoni and T. Stelzer, *MadEvent: Automatic event generation with MadGraph*, JHEP **0302** (2003) 027, arXiv:hep-ph/0208156 [hep-ph].
 - [366] L. Lönnblad, *Correcting the color dipole cascade model with fixed order matrix elements*, JHEP **0205** (2002) 046, arXiv:hep-ph/0112284 [hep-ph].
 - [367] N. Lavesson and L. Lonnblad, *W+jets matrix elements and the dipole cascade*, JHEP **0507** (2005) 054, arXiv:hep-ph/0503293 [hep-ph].
 - [368] L. Lönnblad and S. Prestel, *Matching Tree-Level Matrix Elements with Interleaved Showers*, JHEP **1203** (2012) 019, arXiv:1109.4829 [hep-ph].
 - [369] T. Gehrmann, S. Höche, F. Krauss, M. Schönherr, and F. Siegert, *NLO QCD matrix elements + parton showers in $e^+e^- \rightarrow$ hadrons*, JHEP **1301** (2013) 144, arXiv:1207.5031 [hep-ph].
 - [370] F. Cascioli, S. Höche, F. Krauss, P. Maierhöfer, S. Pozzorini, et al., *Precise Higgs-background predictions: merging NLO QCD and squared quark-loop corrections to four-lepton + 0,1 jet production*, JHEP **1401** (2014) 046, arXiv:1309.0500 [hep-ph].
 - [371] F. Cascioli, P. Maierhöfer, N. Moretti, S. Pozzorini, and F. Siegert, *NLO matching for $t\bar{t}b\bar{b}$ production with massive b -quarks*, arXiv:1309.5912 [hep-ph].
 - [372] S. Höche, F. Krauss, and M. Schönherr, *Uncertainties in MEPS@NLO calculations of h +jets*, arXiv:1401.7971 [hep-ph].
 - [373] S. Dawson, *Radiative corrections to Higgs boson production*, Nucl.Phys. **B359** (1991) 283–300.
 - [374] A. Djouadi, M. Spira, and P. Zerwas, *Production of Higgs bosons in proton colliders: QCD corrections*, Phys.Lett. **B264** (1991) 440–446.
 - [375] D. de Florian, M. Grazzini, and Z. Kunszt, *Higgs production with large transverse momentum in hadronic collisions at next-to-leading order*, Phys.Rev.Lett. **82** (1999) 5209–5212, arXiv:hep-ph/9902483 [hep-ph].
 - [376] V. Ravindran, J. Smith, and W. Van Neerven, *Next-to-leading order QCD corrections to differential distributions of Higgs boson production in hadron hadron collisions*, Nucl.Phys. **B634** (2002) 247–290, arXiv:hep-ph/0201114 [hep-ph].
 - [377] S. Höche and M. Schönherr, *Uncertainties in next-to-leading order plus parton shower matched simulations of inclusive jet and dijet production*, Phys.Rev. **D86** (2012) 094042, arXiv:1208.2815 [hep-ph].
 - [378] SM AND NLO MULTILEG and SM MC Working Groups Collaboration, J. Alcaraz Maestre et al., *The SM and NLO Multileg and SM MC Working Groups:*

- Summary Report*, arXiv:1203.6803 [hep-ph].
- [379] A. Buckley, J. Butterworth, L. Lönnblad, D. Grellscheid, H. Hoeth, et al., *Rivet user manual*, Comput.Phys.Comm. **184** (2013) 2803–2819, arXiv:1003.0694 [hep-ph].
- [380] The analysis can be found at <http://phystev.in2p3.fr/wiki/2013:groups:sm:higgs:hdijets>.
- [381] ATLAS Collaboration, G. Aad et al., *Measurement of the electroweak production of dijets in association with a Z-boson and distributions sensitive to vector boson fusion in proton-proton collisions at $\sqrt{s} = 8$ TeV using the ATLAS detector*, arXiv:1401.7610 [hep-ex].
- [382] V. Del Duca, W. Kilgore, C. Oleari, C. Schmidt, and D. Zeppenfeld, *Higgs + 2 jets via gluon fusion*, Phys.Rev.Lett. **87** (2001) 122001, arXiv:hep-ph/0105129 [hep-ph].
- [383] V. Del Duca, W. Kilgore, C. Oleari, C. Schmidt, and D. Zeppenfeld, *Gluon fusion contributions to $H + 2$ jet production*, Nucl.Phys. **B616** (2001) 367–399, arXiv:hep-ph/0108030 [hep-ph].
- [384] F. Campanario and M. Kubocz, *Higgs boson production in association with three jets via gluon fusion at the LHC: Gluonic contributions*, arXiv:1306.1830 [hep-ph].
- [385] H. van Deurzen, N. Greiner, G. Luisoni, P. Mastrolia, E. Mirabella, et al., *NLO QCD corrections to the production of Higgs plus two jets at the LHC*, Phys.Lett. **B721** (2013) 74–81, arXiv:1301.0493 [hep-ph].
- [386] V. Del Duca, A. Frizzo, and F. Maltoni, *Higgs boson production in association with three jets*, JHEP **0405** (2004) 064, arXiv:hep-ph/0404013 [hep-ph].
- [387] L. J. Dixon, E. N. Glover, and V. V. Khoze, *MHV rules for Higgs plus multi-gluon amplitudes*, JHEP **0412** (2004) 015, arXiv:hep-th/0411092 [hep-th].
- [388] S. Badger, E. N. Glover, and V. V. Khoze, *MHV rules for Higgs plus multi-parton amplitudes*, JHEP **0503** (2005) 023, arXiv:hep-th/0412275 [hep-th].
- [389] R. K. Ellis, W. Giele, and G. Zanderighi, *Virtual QCD corrections to Higgs boson plus four parton processes*, Phys.Rev. **D72** (2005) 054018, arXiv:hep-ph/0506196 [hep-ph].
- [390] R. K. Ellis, W. Giele, and G. Zanderighi, *Semi-numerical evaluation of one-loop corrections*, Phys.Rev. **D73** (2006) 014027, arXiv:hep-ph/0508308 [hep-ph].
- [391] C. F. Berger, V. Del Duca, and L. J. Dixon, *Recursive Construction of Higgs-Plus-Multiparton Loop Amplitudes: The Last of the Phi-nite Loop Amplitudes*, Phys.Rev. **D74** (2006) 094021, arXiv:hep-ph/0608180 [hep-ph].
- [392] S. Badger and E. N. Glover, *One-loop helicity amplitudes for $H \rightarrow$ gluons: The All-minus configuration*, Nucl.Phys.Proc.Suppl. **160** (2006) 71–75, arXiv:hep-ph/0607139 [hep-ph].
- [393] S. Badger, E. N. Glover, and K. Risager, *One-loop phi-MHV amplitudes using the unitarity bootstrap*, JHEP **0707** (2007) 066, arXiv:0704.3914 [hep-ph].
- [394] E. N. Glover, P. Mastrolia, and C. Williams, *One-loop phi-MHV amplitudes using the unitarity bootstrap: The General helicity case*, JHEP **0808** (2008) 017, arXiv:0804.4149 [hep-ph].
- [395] S. Badger, E. Nigel Glover, P. Mastrolia, and C. Williams, *One-loop Higgs plus four gluon amplitudes: Full analytic results*, JHEP **1001** (2010) 036, arXiv:0909.4475 [hep-ph].
- [396] S. Badger, J. M. Campbell, R. K. Ellis, and C. Williams, *Analytic results for the one-loop NMHV Hqgg amplitude*, JHEP **0912** (2009) 035, arXiv:0910.4481 [hep-ph].
- [397] P. Mastrolia, E. Mirabella, and T. Peraro, *Integrand reduction of one-loop scattering amplitudes through Laurent series expansion*, JHEP **1206** (2012) 095, arXiv:1203.0291 [hep-ph].

- [398] P. Nogueira, *Automatic Feynman graph generation*, J.Comput.Phys. **105** (1993) 279–289.
- [399] J. Vermaseren, *New features of FORM*, arXiv:math-ph/0010025 [math-ph].
- [400] T. Reiter, *Optimising Code Generation with haggies*, Comput.Phys.Commun. **181** (2010) 1301–1331, arXiv:0907.3714 [hep-ph].
- [401] G. Cullen, M. Koch-Janusz, and T. Reiter, *Spinney: A Form Library for Helicity Spinors*, Comput.Phys.Commun. **182** (2011) 2368–2387, arXiv:1008.0803 [hep-ph].
- [402] G. Ossola, C. G. Papadopoulos, and R. Pittau, *Reducing full one-loop amplitudes to scalar integrals at the integrand level*, Nucl.Phys. **B763** (2007) 147–169, arXiv:hep-ph/0609007 [hep-ph].
- [403] G. Ossola, C. G. Papadopoulos, and R. Pittau, *Numerical evaluation of six-photon amplitudes*, JHEP **0707** (2007) 085, arXiv:0704.1271 [hep-ph].
- [404] R. Ellis, W. Giele, and Z. Kunszt, *A Numerical Unitarity Formalism for Evaluating One-Loop Amplitudes*, JHEP **0803** (2008) 003, arXiv:0708.2398 [hep-ph].
- [405] G. Ossola, C. G. Papadopoulos, and R. Pittau, *On the Rational Terms of the one-loop amplitudes*, JHEP **0805** (2008) 004, arXiv:0802.1876 [hep-ph].
- [406] P. Mastrolia, G. Ossola, C. Papadopoulos, and R. Pittau, *Optimizing the Reduction of One-Loop Amplitudes*, JHEP **0806** (2008) 030, arXiv:0803.3964 [hep-ph].
- [407] P. Mastrolia, E. Mirabella, G. Ossola, and T. Peraro, *Scattering Amplitudes from Multivariate Polynomial Division*, Phys.Lett. **B718** (2012) 173–177, arXiv:1205.7087 [hep-ph].
- [408] P. Mastrolia, G. Ossola, T. Reiter, and F. Tramontano, *Scattering AMplitudes from Unitarity-based Reduction Algorithm at the Integrand-level*, JHEP **1008** (2010) 080, arXiv:1006.0710 [hep-ph].
- [409] P. Mastrolia, E. Mirabella, G. Ossola, T. Peraro, and H. van Deurzen, *The Integrand Reduction of One- and Two-Loop Scattering Amplitudes*, PoS **LL2012** (2012) 028, arXiv:1209.5678 [hep-ph].
- [410] H. van Deurzen, *Associated Higgs Production at NLO with GoSam*, Acta Phys.Polon. **B44** (2013) no. 11, 2223–2230.
- [411] T. Peraro, *Ninja: Automated Integrand Reduction via Laurent Expansion for One-Loop Amplitudes*, arXiv:1403.1229 [hep-ph].
- [412] H. van Deurzen, G. Luisoni, P. Mastrolia, E. Mirabella, G. Ossola, et al., *Multi-leg One-loop Massive Amplitudes from Integrand Reduction via Laurent Expansion*, arXiv:1312.6678 [hep-ph].
- [413] T. Peraro, *Integrand-level Reduction at One and Higher Loops*, Acta Phys.Polon. **B44** (2013) 2215–2221.
- [414] G. Cullen, J. P. Guillet, G. Heinrich, T. Kleinschmidt, E. Pilon, et al., *Golem95C: A library for one-loop integrals with complex masses*, Comput.Phys.Commun. **182** (2011) 2276–2284, arXiv:1101.5595 [hep-ph].
- [415] J. P. Guillet, G. Heinrich, and J. von Soden-Fraunhofen, *Tools for NLO automation: extension of the golem95C integral library*, arXiv:1312.3887 [hep-ph].
- [416] A. van Hameren, *OneLOop: For the evaluation of one-loop scalar functions*, Comput.Phys.Commun. **182** (2011) 2427–2438, arXiv:1007.4716 [hep-ph].
- [417] J. Kuipers, T. Ueda, J. Vermaseren, and J. Vollinga, *FORM version 4.0*, Comput.Phys.Commun. **184** (2013) 1453–1467, arXiv:1203.6543 [cs.SC].
- [418] F. Krauss, R. Kuhn, and G. Soff, *AMEGIC++ 1.0: A Matrix element generator in C++*, JHEP **0202** (2002) 044, arXiv:hep-ph/0109036 [hep-ph].
- [419] T. Gleisberg and F. Krauss, *Automating dipole subtraction for QCD NLO calculations*,

- Eur.Phys.J. **C53** (2008) 501–523, [arXiv:0709.2881 \[hep-ph\]](#).
- [420] T. Stelzer and W. Long, *Automatic generation of tree level helicity amplitudes*, *Comput.Phys.Commun.* **81** (1994) 357–371, [arXiv:hep-ph/9401258 \[hep-ph\]](#).
- [421] J. Alwall, P. Demin, S. de Visscher, R. Frederix, M. Herquet, et al., *MadGraph/MadEvent v4: The New Web Generation*, *JHEP* **0709** (2007) 028, [arXiv:0706.2334 \[hep-ph\]](#).
- [422] R. Frederix, T. Gehrmann, and N. Greiner, *Automation of the Dipole Subtraction Method in MadGraph/MadEvent*, *JHEP* **0809** (2008) 122, [arXiv:0808.2128 \[hep-ph\]](#).
- [423] R. Frederix, T. Gehrmann, and N. Greiner, *Integrated dipoles with MadDipole in the MadGraph framework*, *JHEP* **1006** (2010) 086, [arXiv:1004.2905 \[hep-ph\]](#).
- [424] M. Cacciari and G. P. Salam, *Dispelling the N^3 myth for the k_t jet-finder*, *Phys.Lett.* **B641** (2006) 57–61, [arXiv:hep-ph/0512210 \[hep-ph\]](#).
- [425] ATLAS Collaboration, G. Aad et al., *Observation of a new particle in the search for the Standard Model Higgs boson with the ATLAS detector at the LHC*, *Phys.Lett.* **B716** (2012) 1–29, [arXiv:1207.7214 \[hep-ex\]](#).
- [426] CMS Collaboration, S. Chatrchyan et al., *Observation of a new boson at a mass of 125 GeV with the CMS experiment at the LHC*, *Phys.Lett.* **B716** (2012) 30–61, [arXiv:1207.7235 \[hep-ex\]](#).
- [427] A. Banfi, G. P. Salam, and G. Zanderighi, *NLL+NNLO predictions for jet-veto efficiencies in Higgs-boson and Drell-Yan production*, *JHEP* **1206** (2012) 159, [arXiv:1203.5773 \[hep-ph\]](#).
- [428] A. Banfi, P. F. Monni, G. P. Salam, and G. Zanderighi, *Higgs and Z-boson production with a jet veto*, *Phys.Rev.Lett.* **109** (2012) 202001, [arXiv:1206.4998 \[hep-ph\]](#).
- [429] T. Becher and M. Neubert, *Factorization and NNLL Resummation for Higgs Production with a Jet Veto*, *JHEP* **1207** (2012) 108, [arXiv:1205.3806 \[hep-ph\]](#).
- [430] I. W. Stewart, F. J. Tackmann, J. R. Walsh, and S. Zuberi, *Jet p_T Resummation in Higgs Production at NNLL'+NNLO*, [arXiv:1307.1808](#).
- [431] T. Becher, M. Neubert, and L. Rothen, *Factorization and N^3LL_p +NNLO predictions for the Higgs cross section with a jet veto*, *JHEP* **1310** (2013) 125, [arXiv:1307.0025 \[hep-ph\]](#).
- [432] A. Banfi, P. F. Monni, and G. Zanderighi, *Quark masses in Higgs production with a jet veto*, *JHEP* **1401** (2014) 097, [arXiv:1308.4634 \[hep-ph\]](#).
- [433] M. Grazzini and H. Sargsyan, *Heavy-quark mass effects in Higgs boson production at the LHC*, *JHEP* **1309** (2013) 129, [arXiv:1306.4581 \[hep-ph\]](#).
- [434] A. Banfi, G. Marchesini, and G. Smye, *Away from jet energy flow*, *JHEP* **0208** (2002) 006, [arXiv:hep-ph/0206076 \[hep-ph\]](#).
- [435] M. Dasgupta and G. Salam, *Resummation of nonglobal QCD observables*, *Phys.Lett.* **B512** (2001) 323–330, [arXiv:hep-ph/0104277 \[hep-ph\]](#).
- [436] X. Liu and F. Petriello, *Reducing theoretical uncertainties for exclusive Higgs-boson plus one-jet production at the LHC*, *Phys.Rev.* **D87** (2013) no. 9, 094027, [arXiv:1303.4405 \[hep-ph\]](#).
- [437] I. W. Stewart and F. J. Tackmann, *Theory Uncertainties for Higgs and Other Searches Using Jet Bins*, *Phys.Rev.* **D85** (2012) 034011, [arXiv:1107.2117 \[hep-ph\]](#).
- [438] R. Boughezal, X. Liu, F. Petriello, F. J. Tackmann, and J. R. Walsh, *Combining Resummed Higgs Predictions Across Jet Bins*, [arXiv:1312.4535 \[hep-ph\]](#).
- [439] L. Reina and S. Dawson, *Next-to-leading order results for t anti- t h production at the Tevatron*, *Phys.Rev.Lett.* **87** (2001) 201804, [arXiv:hep-ph/0107101 \[hep-ph\]](#).

- [440] L. Reina, S. Dawson, and D. Wackerroth, *QCD corrections to associated t anti- t h production at the Tevatron*, Phys.Rev. **D65** (2002) 053017, arXiv:hep-ph/0109066 [hep-ph].
- [441] S. Dawson, L. Orr, L. Reina, and D. Wackerroth, *Associated top quark Higgs boson production at the LHC*, Phys.Rev. **D67** (2003) 071503, arXiv:hep-ph/0211438 [hep-ph].
- [442] S. Dawson, C. Jackson, L. Orr, L. Reina, and D. Wackerroth, *Associated Higgs production with top quarks at the large hadron collider: NLO QCD corrections*, Phys.Rev. **D68** (2003) 034022, arXiv:hep-ph/0305087 [hep-ph].
- [443] ATLAS Collaboration, *Search for the Standard Model Higgs boson produced in association with top quarks in proton-proton collisions at $\sqrt{s} = 7$ TeV using the ATLAS detector*, Tech. Rep. ATLAS-CONF-2012-135, ATLAS-COM-CONF-2012-162, CERN, Geneva, Sep, 2012.
- [444] CMS Collaboration, S. Chatrchyan et al., *Search for the standard model Higgs boson produced in association with a top-quark pair in pp collisions at the LHC*, JHEP **1305** (2013) 145, arXiv:1303.0763 [hep-ex].
- [445] ATLAS Collaboration, *Search for $t\bar{t}H$ production in the $H \rightarrow \gamma\gamma$ channel at $\sqrt{s} = 8$ TeV with the ATLAS detector*, Tech. Rep. ATLAS-CONF-2013-080, ATLAS-COM-CONF-2013-089, CERN, Geneva, Jul, 2013.
- [446] CMS Collaboration, *Search for Higgs Boson Production in Association with a Top-Quark Pair and Decaying to Bottom Quarks or Tau Leptons*, Tech. Rep. CMS-PAS-HIG-13-019, CERN, Geneva, 2013.
- [447] W. Beenakker et al., *Higgs radiation off top quarks at the Tevatron and the LHC*, Phys. Rev. Lett. **87** (2001) 201805, arXiv:hep-ph/0107081.
- [448] W. Beenakker et al., *NLO QCD corrections to $t\bar{t}H$ production in hadron collisions. (U)*, Nucl. Phys. **B653** (2003) 151–203, arXiv:hep-ph/0211352.
- [449] R. Frederix, S. Frixione, V. Hirschi, F. Maltoni, R. Pittau, et al., *Scalar and pseudoscalar Higgs production in association with a top-antitop pair*, Phys.Lett. **B701** (2011) 427–433, arXiv:1104.5613 [hep-ph].
- [450] M. Garzelli, A. Kardos, C. Papadopoulos, and Z. Trocsanyi, *Standard Model Higgs boson production in association with a top anti-top pair at NLO with parton showering*, Europhys.Lett. **96** (2011) 11001, arXiv:1108.0387 [hep-ph].
- [451] T. Gleisberg, S. Hoeche, F. Krauss, A. Schalicke, S. Schumann, et al., *SHERPA 1. alpha: A Proof of concept version*, JHEP **0402** (2004) 056, arXiv:hep-ph/0311263 [hep-ph].
- [452] A. Cafarella, C. G. Papadopoulos, and M. Worek, *Helac-Phegas: A Generator for all parton level processes*, Comput.Phys.Commun. **180** (2009) 1941–1955, arXiv:0710.2427 [hep-ph].
- [453] A. van Hameren, C. Papadopoulos, and R. Pittau, *Automated one-loop calculations: A Proof of concept*, JHEP **0909** (2009) 106, arXiv:0903.4665 [hep-ph].
- [454] P. Draggiotis, M. Garzelli, C. Papadopoulos, and R. Pittau, *Feynman Rules for the Rational Part of the QCD 1-loop amplitudes*, JHEP **0904** (2009) 072, arXiv:0903.0356 [hep-ph].
- [455] G. Bevilacqua, M. Czakon, M. Garzelli, A. van Hameren, Y. Malamos, et al., *NLO QCD calculations with HELAC-NLO*, Nucl.Phys.Proc.Suppl. **205-206** (2010) 211–217, arXiv:1007.4918 [hep-ph].
- [456] S. Frixione, Z. Kunszt, and A. Signer, *Three jet cross-sections to next-to-leading order*, Nucl.Phys. **B467** (1996) 399–442, arXiv:hep-ph/9512328 [hep-ph].

- [457] J. Alwall, A. Ballestrero, P. Bartalini, S. Belov, E. Boos, et al., *A Standard format for Les Houches event files*, Comput.Phys.Commun. **176** (2007) 300–304, arXiv:hep-ph/0609017 [hep-ph].
- [458] M. Garzelli, A. Kardos, and Z. Trocsanyi, *NLO Event Samples for the LHC*, PoS **EPS-HEP2011** (2011) 282, arXiv:1111.1446 [hep-ph].
- [459] P. Z. Skands, *Tuning Monte Carlo Generators: The Perugia Tunes*, Phys.Rev. **D82** (2010) 074018, arXiv:1005.3457 [hep-ph].
- [460] F. Englert and R. Brout, *Broken Symmetry and the Mass of Gauge Vector Mesons*, Phys.Rev.Lett. **13** (1964) 321–323.
- [461] P. W. Higgs, *Broken Symmetries and the Masses of Gauge Bosons*, Phys.Rev.Lett. **13** (1964) 508–509.
- [462] P. W. Higgs, *Broken symmetries, massless particles and gauge fields*, Phys.Lett. **12** (1964) 132–133.
- [463] U. Baur, T. Plehn, and D. L. Rainwater, *Determining the Higgs boson selfcoupling at hadron colliders*, Phys.Rev. **D67** (2003) 033003, arXiv:hep-ph/0211224 [hep-ph].
- [464] M. J. Dolan, C. Englert, and M. Spannowsky, *Higgs self-coupling measurements at the LHC*, JHEP **1210** (2012) 112, arXiv:1206.5001 [hep-ph].
- [465] A. Papaefstathiou, L. L. Yang, and J. Zurita, *Higgs boson pair production at the LHC in the $b\bar{b}W^+W^-$ channel*, Phys.Rev. **D87** (2013) 011301, arXiv:1209.1489 [hep-ph].
- [466] U. Baur, T. Plehn, and D. L. Rainwater, *Probing the Higgs selfcoupling at hadron colliders using rare decays*, Phys.Rev. **D69** (2004) 053004, arXiv:hep-ph/0310056 [hep-ph].
- [467] M. J. Dolan, C. Englert, and M. Spannowsky, *New Physics in LHC Higgs boson pair production*, Phys.Rev. **D87** (2013) no. 5, 055002, arXiv:1210.8166 [hep-ph].
- [468] F. Goertz, A. Papaefstathiou, L. L. Yang, and J. Zurita, *Higgs Boson self-coupling measurements using ratios of cross sections*, JHEP **1306** (2013) 016, arXiv:1301.3492 [hep-ph].
- [469] D. Y. Shao, C. S. Li, H. T. Li, and J. Wang, *Threshold resummation effects in Higgs boson pair production at the LHC*, arXiv:1301.1245 [hep-ph].
- [470] M. Gouzevitch, A. Oliveira, J. Rojo, R. Rosenfeld, G. P. Salam, et al., *Scale-invariant resonance tagging in multijet events and new physics in Higgs pair production*, JHEP **1307** (2013) 148, arXiv:1303.6636 [hep-ph].
- [471] E. N. Glover and J. van der Bij, *HIGGS BOSON PAIR PRODUCTION VIA GLUON FUSION*, Nucl.Phys. **B309** (1988) 282.
- [472] O. J. Eboli, G. Marques, S. Novaes, and A. Natale, *TWIN HIGGS BOSON PRODUCTION*, Phys.Lett. **B197** (1987) 269.
- [473] T. Plehn, M. Spira, and P. Zerwas, *Pair production of neutral Higgs particles in gluon-gluon collisions*, Nucl.Phys. **B479** (1996) 46–64, arXiv:hep-ph/9603205 [hep-ph].
- [474] M. Kramer, E. Laenen, and M. Spira, *Soft gluon radiation in Higgs boson production at the LHC*, Nucl.Phys. **B511** (1998) 523–549, arXiv:hep-ph/9611272 [hep-ph].
- [475] K. Chetyrkin, B. A. Kniehl, and M. Steinhauser, *Hadronic Higgs decay to order α_s^4* , Phys.Rev.Lett. **79** (1997) 353–356, arXiv:hep-ph/9705240 [hep-ph].
- [476] R. V. Harlander and W. B. Kilgore, *Next-to-next-to-leading order Higgs production at hadron colliders*, Phys.Rev.Lett. **88** (2002) 201801, arXiv:hep-ph/0201206 [hep-ph].
- [477] C. Anastasiou and K. Melnikov, *Higgs boson production at hadron colliders in NNLO QCD*, Nucl.Phys. **B646** (2002) 220–256, arXiv:hep-ph/0207004 [hep-ph].

- [478] V. Ravindran, J. Smith, and W. L. van Neerven, *NNLO corrections to the total cross-section for Higgs boson production in hadron hadron collisions*, Nucl.Phys. **B665** (2003) 325–366, arXiv:hep-ph/0302135 [hep-ph].
- [479] D. de Florian and J. Mazzitelli, *Two-loop virtual corrections to Higgs pair production*, Phys.Lett. **B724** (2013) 306–309, arXiv:1305.5206 [hep-ph].
- [480] T. Hahn, *Generating Feynman diagrams and amplitudes with FeynArts 3*, Comput.Phys.Commun. **140** (2001) 418–431, arXiv:hep-ph/0012260 [hep-ph].
- [481] R. Mertig, M. Bohm, and A. Denner, *FEYN CALC: Computer algebraic calculation of Feynman amplitudes*, Comput.Phys.Commun. **64** (1991) 345–359.
- [482] A. Martin, W. Stirling, R. Thorne, and G. Watt, *Uncertainties on $\alpha(S)$ in global PDF analyses and implications for predicted hadronic cross sections*, Eur.Phys.J. **C64** (2009) 653–680, arXiv:0905.3531 [hep-ph].
- [483] R. Blair, B. Brelier, F. Bucci, S. Chekanov, M. Stockton, and M. Tripijana, *NLO Theoretical Predictions for Photon Measurements Using the PHOX Generators*, Tech. Rep. CERN-OPEN-2011-041, CERN, Geneva, Sep, 2011.
- [484] M. Wielers, *Isolation of Photons*, Tech. Rep. ATL-PHYS-2002-004, ATL-COM-PHYS-2001-024, CERN-ATL-PHYS-2002-004, 2001.
- [485] OPAL Collaboration Collaboration, G. Abbiendi et al., *Measurement of isolated prompt photon production in photon photon collisions at $s(ee)^{1/2} = 183 \text{ GeV} - 209\text{-GeV}$* , Eur.Phys.J. **C31** (2003) 491–502, arXiv:hep-ex/0305075 [hep-ex].
- [486] T. Binoth, J. Guillet, E. Pilon, and M. Werlen, *A Full next-to-leading order study of direct photon pair production in hadronic collisions*, Eur.Phys.J. **C16** (2000) 311–330, arXiv:hep-ph/9911340 [hep-ph].
- [487] S. Catani, M. Fontannaz, J. Guillet, and E. Pilon, *Cross-section of isolated prompt photons in hadron hadron collisions*, JHEP **0205** (2002) 028, arXiv:hep-ph/0204023 [hep-ph].
- [488] S. Catani, L. Cieri, D. de Florian, G. Ferrera, and M. Grazzini, *Diphoton production at hadron colliders: a fully-differential QCD calculation at NNLO*, Phys.Rev.Lett. **108** (2012) 072001, arXiv:1110.2375 [hep-ph].
- [489] S. Catani, M. Fontannaz, J. Guillet, and E. Pilon, *Cross-section of isolated prompt photons in hadron hadron collisions*, JHEP **0205** (2002) 028, arXiv:hep-ph/0204023 [hep-ph].
- [490] S. Catani, M. Fontannaz, J. P. Guillet, and E. Pilon, *Isolating Prompt Photons with Narrow Cones*, JHEP **1309** (2013) 007, arXiv:1306.6498 [hep-ph].
- [491] S. Frixione and W. Vogelsang, *Isolated photon production in polarized pp collisions*, Nucl.Phys. **B568** (2000) 60–92, arXiv:hep-ph/9908387 [hep-ph].
- [492] S. Catani, M. Dittmar, D. Soper, W. J. Stirling, S. Tapprogge, et al., *QCD*, arXiv:hep-ph/0005025 [hep-ph].
- [493] T. Gehrmann, N. Greiner, and G. Heinrich, *Photon isolation effects at NLO in gamma gamma + jet final states in hadronic collisions*, JHEP **1306** (2013) 058, arXiv:1303.0824 [hep-ph].
- [494] S. Frixione, *Isolated photons in perturbative QCD*, Phys.Lett. **B429** (1998) 369–374, arXiv hep-ph/9801442.
- [495] T. Binoth, J. Guillet, E. Pilon, and M. Werlen, *A Full next-to-leading order study of direct photon pair production in hadronic collisions*, Eur.Phys.J. **C16** (2000) 311–330, arXiv:hep-ph/9911340 [hep-ph].
- [496] V. Del Duca, F. Maltoni, Z. Nagy, and Z. Trocsanyi, *QCD radiative corrections to*

- prompt diphoton production in association with a jet at hadron colliders*, JHEP **0304** (2003) 059, [arXiv:hep-ph/0303012](#) [hep-ph].
- [497] <http://www.gosam.hepforge.org/diphoton>.
- [498] T. Gehrmann, N. Greiner, and G. Heinrich, *Precise QCD Predictions for the Production of a Photon Pair in Association with Two Jets*, Phys. Rev. Lett. **111** (2013) 222002, [arXiv:1308.3660](#) [hep-ph].
<http://link.aps.org/doi/10.1103/PhysRevLett.111.222002>.
- [499] Z. Bern, L. Dixon, F. Febres Cordero, S. Hoeche, H. Ita, et al., *Next-to-leading order diphoton+2-jet production at the LHC*, [arXiv:1312.0592](#) [hep-ph].
- [500] S. Badger, A. Guffanti, and V. Yundin, *Next-to-leading order QCD corrections to di-photon production in association with up to three jets at the Large Hadron Collider*, [arXiv:1312.5927](#) [hep-ph].
- [501] Z. Bern, L. Dixon, F. Febres Cordero, S. Hoeche, H. Ita, et al., *Next-to-Leading Order Gamma Gamma + 2-Jet Production at the LHC*, [arXiv:1402.4127](#) [hep-ph].
- [502] G. Corcella, I. Knowles, G. Marchesini, S. Moretti, K. Odagiri, et al., *HERWIG 6: An Event generator for hadron emission reactions with interfering gluons (including supersymmetric processes)*, JHEP **0101** (2001) 010, [arXiv:hep-ph/0011363](#) [hep-ph].
- [503] M. Dobbs and J. B. Hansen, *The HepMC C++ Monte Carlo event record for High Energy Physics*, Comput.Phys.Commun. **134** (2001) 41–46.
- [504] <http://yoda.hepforge.org/>.
- [505] R. Brun and F. Rademakers, *ROOT: An object oriented data analysis framework*, Nucl.Instrum.Meth. **A389** (1997) 81–86.
- [506] J. Butterworth, A. Arbey, L. Basso, S. Belov, A. Bharucha, et al., *The Tools and Monte Carlo working group Summary Report*, [arXiv:1003.1643](#) [hep-ph].